

Cover Page



Universiteit Leiden



The handle <http://hdl.handle.net/1887/37161> holds various files of this Leiden University dissertation

Author: Boas, Sonja E.M.

Title: Computational modeling of angiogenesis : from matrix invasion to lumen formation

Issue Date: 2015-12-22

Computational modeling of angiogenesis

from matrix invasion to lumen formation

Sonja E.M. Boas



Cover: Photograph of the blood vessels in Sonja Boas' retina.

ISBN: 978-94-6299-241-2

Copyright © Sonja Boas

Printed by Ridderprint

Computational modeling of angiogenesis

from matrix invasion to lumen formation

Proefschrift

ter verkrijging van
de graad van Doctor aan de Universiteit Leiden,
op gezag van Rector Magnificus prof.mr. C.J.J.M. Stolker,
volgens besluit van het College voor Promoties
te verdedigen op dinsdag 22 december 2015
klokke 16.15 uur

door

Sonja Elisabeth Maria Boas
geboren te Maastricht
in 1987

Promotor: prof. dr. Roeland M.H. Merks

Voorzitter: prof. dr. Aad van der Vaart

Promotiecommissie: prof. dr. Marie-José Goumans
prof. dr. Frank den Hollander
dr. Pieter Koolwijk (Vrije Universiteit Amsterdam)
dr. Kirsten ten Tusscher (Universiteit Utrecht)

This research has been carried out at Centrum Wiskunde & Informatica (CWI) in the Life Sciences group. The investigations were supported by the Division for Earth and Life Sciences (ALW; Vidi 864.10.009) with financial aid from the Netherlands Organization for Scientific Research (NWO).

Contents

1	Introduction	1
1.1	Angiogenesis and vasculogenesis	2
1.2	The mechanisms of angiogenesis	2
1.3	Experimental models of angiogenesis and vasculogenesis . . .	5
1.4	Computational models of angiogenesis and vasculogenesis . .	7
1.5	CPM-based models of vasculogenesis and angiogenesis	10
1.6	Thesis outline	14
2	A local uPAR-plasmin-TGFβ1 positive feedback loop in a computational model of angiogenic sprouting explains the <i>in vitro</i> effect of fibrinogen variants	15
2.1	Introduction	16
2.2	Results	20
2.3	Discussion	29
2.4	Methods	33
2.A	Supplementary movies	43
3	Tip cell overtaking occurs as a side effect of sprouting in computational models of angiogenesis	45
3.1	Introduction	46
3.2	Results	48
3.3	Discussion	61
3.4	Conclusions	63
3.5	Methods	64
3.A	Supplementary movies	70
3.B	Supplementary tables	70
3.C	Supplementary figures	72
4	Synergy of cell-cell repulsion and vacuolation in a computational model of lumen formation	79
4.1	Introduction	80
4.2	Results	82
4.3	Discussion	92

4.4	Material and methods	96
4.A	Supplementary movies	100
4.B	Supplementary figures	101
5	A global sensitivity analysis approach for morphogenesis models	105
5.1	Background	106
5.2	Methods	108
5.3	Results	114
5.4	Discussion	124
5.5	Conclusions	127
5.6	Supplementary figures	128
6	Discussion	131
6.1	Interactions between matrix degradation and tip cell selection	132
6.2	Lumen formation and dynamic sprouting	134
6.3	Model sensitivity analysis	135
6.4	Three-dimensional models	137
6.5	Model validation	138
6.6	Relevance of modeling	139
6.7	Model predictions	140
	Bibliography	143
	Summary	155
	Samenvatting	159
	Dankwoord	163
	Curriculum vitae	165
	Publications	167

1

Introduction

This chapter is based on:

- Sonja E. M. Boas, Margriet M. Palm, Pieter Koolwijk and Roeland M.H. Merks, *Computational Modeling of Angiogenesis: Towards a Multi-Scale Understanding of Cell-Cell and Cell-Matrix Interactions*(2013) Mechanical and Chemical Signaling in Angiogenesis, Studies in Mechanobiology, Tissue Engineering and Biomaterials Volume 12, 161-183
- M. G. Dallinga and Sonja E. M. Boas *et al.*, *Tip cells in angiogenesis* (2015) Tip Cells in Angiogenesis. In: eLS. John Wiley & Sons, Ltd: Chichester. DOI: 10.1002/9780470015902.a0025977
- Sonja E.M. Boas, Yi Jiang, Roeland M.H. Merks, Sotiris A. Prokopiou and Elisabeth G. Rens *Cellular Potts model: applications to vasculogenesis and angiogenesis* In: Louis, P.-Y. and Nardi, F.R. (Eds.) Probabilistic Cellular Automata: Theory, Applications and Future Perspectives. Springer. (in press)

1.1 Angiogenesis and vasculogenesis

Blood vessels supply tissues with oxygen and nutrients and carry away waste products. A network of blood vessels is formed during embryogenesis [1, 2]. Vascular networks form *de novo* from endothelial progenitor cells, a process called vasculogenesis [1, 2]. A well studied model system is vasculogenesis in the retina [3, 4], in which circulating progenitor cells organize into early retinal vessels. Angiogenesis, the formation of new blood vessels from existing vessels, then proceeds to extend the retinal vasculature to the periphery [1, 3, 4]. Throughout our lives, angiogenesis is important in many physiological processes, such as the menstrual cycle and wound healing [1, 5].

Angiogenesis is also involved in many pathological conditions [1, 6]. Tumor growth is highly dependent of sufficient blood supply [2]. The core of a growing tumor becomes necrotic and sends out signals to attract new blood vessels. Similarly, blood vessels are attracted towards the inflamed region in rheumatoid arthritis [7]. As a result, the inflammation is sustained by the increased delivery of inflammatory cells, nutrients, and oxygen for the proliferating inflamed tissue [7]. In age-related macular degeneration (AMD), pathological ocular neovascularization can cause severe vision loss [8]. Whereas medical therapies focus on inhibition of angiogenesis in cancer, rheumatoid arthritis and AMD, diabetic patients can suffer from wound healing defects caused by reduced levels of angiogenesis [6, 9]. A better understanding of the mechanisms of angiogenesis aids the development of such medical therapies.

Besides for medical therapies, a true understanding of vasculogenesis and angiogenesis is important for tissue engineering [10–12]. Over the last decades, major steps have been taken in the field of tissue engineering, aiming for the *in vitro* growth of entire organs [13]. Oxygen supply through simple diffusion is insufficient for such large tissues and requires vascularization of the tissue. Creation of a functional vasculature is challenging and would benefit from a better understanding of angiogenesis [10–13].

In this thesis, we use computational modeling to gain insights in the mechanisms of angiogenesis.

1.2 The mechanisms of angiogenesis

Driven by the goal to improve medical therapies and tissue engineering, angiogenesis has been extensively studied. As holds for most biological processes, angiogenesis showed to be a very complex process. Figure 1.1 shows an overview of the major components involved in angiogenesis. A blood vessel wall consists of quiescent endothelial cells, also known as phalanx cells [14]. Phalanx cells can be activated by signals from nearby regions that demand more blood supply, such as wounds, tumors or inflamed tissues. Vascul-

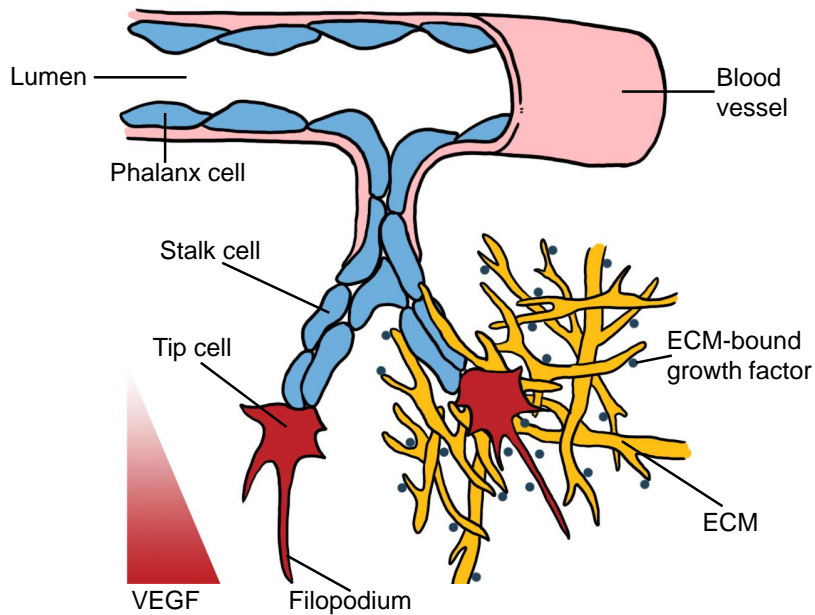


Figure 1.1: Overview of the mechanisms of blood vessel formation. The quiescent endothelial cells that form the capillary blood vessel are called phalanx cells. An external signal, such as the chemoattractant VEGF that is secreted by hypoxic tissue, can activate phalanx cells in a nearby vessel to form a sprout towards higher concentrations of the signal (gradient indicated by red triangle). Upon activation, endothelial cells differentiate into tip cells and stalk cells. Tip cells form long filopodia to sense the environment and lead the sprout. Blood vessels are surrounded by an extracellular matrix, composed out of a web of fibers and matrix-bound growth factors. Endothelial cells invade the matrix by degrading it, which can result in the release of matrix-bound growth factors to stimulate further sprouting. This figure was adapted from [16]

lar endothelial growth factor (VEGF) is a well known growth factor that serves this purpose [3, 15]. VEGF activates phalanx cells in nearby vessels and promotes sprouting of new blood vessels towards higher concentrations of the growth factor, the growth factor gradient is indicated by the red triangle in Figure 1.1. Here, we discuss the major steps of angiogenesis: matrix degradation, tip cell selection and vessel maturation. Each of these steps are the focus of a chapter in this thesis.

1.2.1 Matrix degradation

During sprouting, there is an intensive interaction with the extracellular environment. Blood vessels are surrounded with extracellular matrix (ECM, see yellow fibers in Figure 1.1), the non-cellular component present within all tissues and organs that provides structural support [17]. The extracellular matrix is a web of interlinked fibers, such as collagen, laminin or fibrin fibers [17]. In addition, many proteins such as growth factors bind to the extracellular matrix [18]. Sprouts invade the surrounding matrix by creating a tunnel through it. This tunnel is made by active proteolytic degradation of the matrix fibers [19]. For this purpose, cells secrete proteolytic enzymes that cut the matrix fibers. This can result in the release of growth factors that were bound to the matrix (see blue dots in Figure 1.1), which can modulate sprouting behavior [20]. A new hypothesis for the interactions between proteolytic degradation and invasion of the matrix is introduced in Chapter 2.

1.2.2 Tip cell selection

Upon stimulation of phalanx cells with a growth factor from the extracellular environment, activated endothelial cells differentiate into one of two fates: 'tip cells' or 'stalk cells' [3, 21–23]. In Figure 1.1, tip cells are colored red, whereas phalanx cells and stalk cells are colored blue. Tip cells are the leaders of sprouts and have long filopodia to sense signals from their environment, such as the VEGF gradient [3]. Stalk cells form the base of the sprout and elongate the sprout by proliferation [14]. Selection of tip and stalk cells occurs by lateral inhibition through Dll4-Notch signaling [3, 21–23]. Dll4 is a ligand on a tip cell membrane that interacts with the Notch receptor on a neighboring stalk cell. Activation of Notch result in the cleavage of the Notch-intracellular domain (NICD), which then travels to the nucleus for transcription of Notch target genes [21]. Eventually, cells with low Notch activity (low Notch/high Dll4) become tip cells and cells with high Notch activity (high Notch/low Dll4) become stalk cells [3].

It was long thought that once endothelial cells have differentiated into tip and stalk cells, that the tip cell present at the sprout tip would stay the leader of the sprout [3]. In contrast, more recent experimental studies show that there is a continuous competition between cells for the sprout tip position [24, 25], a process called tip cell overtaking. In Chapter 3, we study the biological function of tip cell overtaking.

1.2.3 Vessel maturation

Newly formed sprouts are not yet fully functional. To close circulation, the sprout needs to connect to a nearby sprout or blood vessel, a process called anastomosis [26]. Perivascular cells, referred to as pericytes, vascular

smooth muscle cells or mural cells, are recruited to sprouts to envelop the surface of the vascular tube and promote stabilization and maturation of the sprout [27].

The cord of cells that forms the sprout needs to hollow such that blood can flow through. The mechanisms of hollowing or lumen formation have been debated for centuries. Experimental research has led to two main hypotheses: vacuolation [28–31] and cell-cell repulsion [32, 33]. During vacuolation, vacuoles are suggested to form by the fusion of pinocytotic vesicles. Initially, lumens were thought to form intracellularly by spanning the cell with a large vacuole that then fuses to the cell membrane on both sides of the cell [28, 29]. Later, lumens were also suggested to form extracellularly by the secretion of vacuoles between cells [30, 31]. During cell-cell repulsion, cell membranes of adjacent cells are suggested to repulse each other to form an extracellular lumen between the cells [32, 33]. Both hypotheses are supported by strong experimental evidence, leaving the debate unresolved. In Chapter 4, we address this debate with a computational model of lumen formation that can represent both hypotheses, separately and in combination.

Each of these steps in angiogenesis are intensively studied in the laboratory as well as with mathematical or computational models. The next section summarizes the experimental assays that have been used for these studies. In the following section, we discuss the usefulness of modeling and introduce computational models of vasculogenesis and angiogenesis. Finally, we give the outline of this thesis.

1.3 Experimental models of angiogenesis and vasculogenesis

Experimental models of angiogenesis and vasculogenesis can roughly be categorized in cell cultures, organ cultures, and *in vivo* models. A good overview of these experimental models is given in [34–37], here we discuss the assays that are most relevant for the validation experiments in this thesis.

1.3.1 Cell cultures

Cell cultures are well-suited to study specific steps in angiogenesis, such as proliferation, matrix invasion, cell migration, and tube formation [34–37]. In two-dimensional cell cultures, cells are placed on a plastic dish that is coated with ECM proteins for adhesion [37]. This assay is often used to study cell proliferation or migration. It is also suitable to study vasculogenesis, since vasculogenesis in the retina is considered a two-dimensional process.

Tube formation assays are developed to investigate angiogenesis in a three-dimensional environment (e.g. the assay by Koolwijk *et al.* [38] in Chapter 2).

1. Introduction

The endothelial cells are seeded on top of a three-dimensional matrix, invade the matrix and form tubular structures [38, 39]. Different substances can form the extracellular matrix. Matrigel is a popular matrix for angiogenesis assays, because it naturally contains pro-angiogenic growth factors. It is secreted by mouse tumor cells and is composed of a mixture of ECM proteins, such as laminin and collagen. Alternatively, cells are cultured on purified matrices, such as collagen matrices [40] or fibrin matrices [38, 39], of which the composition is more controlled.

Instead of seeding a monolayer of endothelial cells on top of a matrix, embryoid bodies of endothelial cells can be placed within an extracellular matrix [37]. Subsequently, sprouts grow out from these embryoid bodies. Jakobsson *et al.* [24] monitored the cell migration trajectories during sprouting in this assay to study tip cell overtaking.

1.3.2 Organ cultures

In comparison to cell cultures, organ cultures contain multiple cell types and there is a larger heterogeneity between the cells [34–36]. Commonly used organ cultures are retinal explants and the rat aortic ring assay [36]. In the former assay, the retina is dissected, covered with a collagen matrix and stimulated with VEGF. In the latter, a segment of the aorta is cultured *in vitro*. This assay was for instance used by Arima *et al.* [25] to study sprouting dynamics and tip cell overtaking.

1.3.3 In vivo models

The environmental conditions of angiogenesis *in vivo* are far more complex than in the isolated cultures. This makes *in vivo* experiments more complicated to interpret, but also essential for an understanding of the complete system. The mouse retina model is extensively used to study angiogenesis [41]. The retinal vasculature is immature in mouse pups and pruning of these easily accessible, developing vessels has been of great value to gain a mechanistic understanding of angiogenesis [41]. The *in vivo* ischemia retina model is commonly used to study retinopathy [36]. Mouse pups are exposed to high-oxygen condition to induce vessel regression, and angiogenesis into avascular regions is studied after elevation hereof. In the hindlimb ischemia model, angiogenesis is triggered in the leg muscle after ligation of the main artery in the thigh. Zebrafish embryos form a particular well model to study embryonic processes due to their transparency in this stage. This allows for live time-lapse imaging of blood vessel formation over long periods, as was e.g. done by Kamei *et al.* [29] and Blum *et al.* [30] to study lumen formation.

1.4 Computational models of angiogenesis and vasculogenesis

Angiogenesis and vasculogenesis research can benefit from computational modeling in three ways. Firstly, computational models help to gain overview in such complex systems by testing which components and interactions are minimally required. These components and interactions can then be examined to understand their function and predict their effects. By modeling mechanisms on a lower level of organization, e.g the cell, predictions can be generated on a higher level of organization, such as the blood vessels in vasculogenesis. This way, computational models are not only useful to gain mechanistic understanding of angiogenesis, but also to propose new therapeutic targets.

Secondly, computational models can discriminate between and select from alternative hypotheses. Often, more than one hypothesis explains a biological observation, such as network formation from dispersed endothelial cells. Computational models can test the sufficiency of each hypothesis to reproduce the biological observations. Predictions that result from these models can be validated experimentally to support or reject the tested hypotheses.

Thirdly, computational models can connect and combine knowledge on single proteins and mechanisms to examine angiogenesis as a system. Experimental research is often limited to a specific step or protein in angiogenesis and does not grasp how this part is integrated in the whole. Ultimately, multi-scale computational models would include processes at multiple scales, such as tissues, cells, and molecules simultaneously.

1.4.1 Modeling techniques

Several modeling techniques can be used to model angiogenic sprouting and vasculogenesis. We categorize them in continuous models, single-particle models and multi-particle models [42].

1.4.2 Continuous models

Continuous models describe variables as continuous in time and space and can be described using ordinary differential equations (ODEs) or partial differential equations (PDEs). ODEs predict the change in concentration of e.g. proteins, without considering the spacial component. Ventrakaman *et al.* [43] used a system of ODEs to represent the concentration of proteins that are completely mixed in solution. They showed a bistability in the concentrations of plasmin, which degrades fibrin. ODEs can also describe the protein reactions within cells. Collier *et al.* [44] used this technique to developed the first mathematical model of pattern formation due to Dll4-Notch dependent lat-

eral inhibition in a static monolayer of cells [44]. A system of ODEs described the level of Notch activation and the level of Delta activity in each cell. They obtained alternating patterns of cells with high and low Delta expression using a simple rule to describe lateral inhibition: "the more intense the inhibition a cell receives, the weaker its ability to deliver inhibition must become" [44]. Sprinzak *et al.* [45, 46] developed a more refined ODE model of Delta-Notch signaling to study the effect of cis-interactions, the mutual inactivation of interacting Delta and Notch of the same cell, on lateral inhibition [45, 46]. They showed that cis-interaction between Delta and Notch speeds up the patterning dynamics and amplifies the feedback in lateral inhibition.

If the spatial aspect is relevant for a question, one can model the system as a continuum or density function using the conservation of mass equation to formulate a PDE. PDEs are often used to model the migration of cells, with cells represented as densities [47–50]. Anderson & Chaplain [47] used a PDE model to explain why endothelial cells in capillary sprouts stop migrating towards a tumor in absence of mitosis. Cell migration depends on diffusion, chemotaxis towards a tumor-derived angiogenic factor, and preferential migration towards higher concentrations of extracellular matrix proteins (haptotaxis). The model suggest that mitosis is required to desensitize endothelial cells for the angiogenic factor when they become saturated in regions near the tumor where there are high concentrations of angiogenic factor. Desensitized cells can reestablish chemotaxis-driven angiogenesis towards the tumor.

Chaplain & Lolas [48] examined the dynamics of the plasminogen-plasmin system during matrix invasion by modeling cancer cells with a PDE. The model includes the density of tumor cells, ECM proteins, the ECM protease plasmin, the plasmin-activator uPA, and the inhibitor PAI-1. Cells secrete uPA and PAI-1. Production of plasmin requires the proximity of uPA and cells, to resemble activation of uPA by binding to cell-bound receptors. The matrix is degraded by plasmin and PAI-1 inhibits matrix degradation by scavenging uPA and plasmin. Cells invade the matrix by random motility, biased with chemotaxis towards uPA, chemotactic repulsion by PAI-1, haptotaxis and proliferation.

Manoussaki [50] studied the role of chemical and mechanical forces in blood vessel formation. In the model, cells exert forces on the extracellular matrix. Cells migrate by passive advection along with the matrix deformation, by a preferential bias along high matrix strain representing aligned fibers, and by chemotaxis towards an exogenously supplied chemical stimuli. Their modeling results suggest that purely mechanical interactions between cells and the matrix can suffice for pattern formation. Besides strain-biased migration due to cell-traction forces, Namy *et al.* [49] also included haptotaxis in their model. This model reproduces experimental observations of the effect of changes in the concentrations of seeded endothelial cells and of matrix

protein concentrations on vasculogenesis.

1.4.3 Single-particle models

In contrast to continuous models, cell-based models represent cells as individual entities and can be categorized in single-particle models and multiple-particle models [42]. Single-particle models represent cells as points or ellipsoids in space. Angiogenesis can be represented at the 'vessel-level', with individual cells modeled as discrete particles. Milde *et al.* [51] combined a discrete particle representation for tip cells with a continuum approximation of VEGF, proteolytic enzymes, matrix and endothelial stalk cells. Tip cells migrate and deposit a track of ECs during migration. Tip cells sense the environment by 'filopodia' and are biased in their direction of migration by the matrix density, haptotaxis and by VEGF. This work shows sprout branching due to the release of VEGF from localized pockets of a matrix-bound VEGF isoform by proteolytic enzymes that are secreted by the tip cell.

In the model by Qutub *et al.* [52], sprouts are composed of connected nodes. The leading node represents the tip cell and the following stalk cells consist of two nodes and can elongate the segment in-between to represent proliferation. Their model setup allows for the integration of modules that describe blood-flow, oxygen transport, VEGF gradients, and tissue geometry to study angiogenesis on a multi-scale level.

In single-particle models, based on Lagrangian dynamics, sprouting occurs when cells follow a random walk biased by attractive and repulsive forces resulting from interactions with nearby cells [53, 54].

1.4.4 Multi-particle models

Single-particle models do not include cell shape or interaction surfaces between cells for signaling. In multiple-particle models, a collection of particles represent a cell and its shape. A cell can for instance be represented by a collection of spheroids that stay in proximity of one other due to higher attractive forces between intracellular particles than between particles of different cells [55].

Alternatively, some multiple-particle models only represent the cell membranes; nodes in the membrane can be connected by vertexes [56, 57] or springs [58]. To study tip cell selection during sprouting, Bentley *et al.* [58, 59] developed a computational model in which the membrane of each endothelial cell is composed of nodes that are interlinked by springs. Filopodia can grow out of nodes and are assumed to extend towards higher concentrations of vascular endothelial growth factor (VEGF) [59]. The model predicted that tip cell patterning will stabilize faster in VEGF gradients than in uniform VEGF environments and that high VEGF levels induce oscillation of the alter-

nating tip-stalk cell pattern. Anastomosis led by filopodia can create new cell-cell junctions with new Dll4-Notch signaling opportunities, which can make tip and stalk cells within the sprout switch fate [58]. Although the cell membrane is composed out of multiple nodes, cells function as single, immobile agents that can switch fate, thus this model might better be categorized as a single-particle model. To study the mechanisms of tip cell overtaking, Bentley *et al.* [60] extended their model with a true multiple-particle representation of cells by using the cellular Potts Model [61, 62] to represent the shape and movement of the cells, thereby explicitly modeling cell-cell adhesion and junctional reshuffling.

The cellular Potts model (CPM) [61, 62] is a commonly used model to study *de novo* sprouting [16, 63–66]. It represents cells as motile patches of lattice sites and includes cell shapes, cell-cell interactions, cell-matrix interactions, and cell motility. The cellular Potts model can easily be coupled to PDEs to describe concentration fields of e.g. proteases, growth factors or matrix proteins [16, 63–66]. In addition, a system of ODEs can be coupled to each cell to model protein interactions within cells and intercellular signaling pathways, such as Delta-Notch signaling [67]. For these reasons, the cellular Potts model is an excellent modeling framework for all questions addressed in this thesis, which involve mechanisms that depend on growth factor gradients, cell-cell signaling pathways and cell-matrix interactions.

1.5 CPM-based models of vasculogenesis and angiogenesis

Since all models of angiogenesis in this thesis are based on the cellular Potts model, we will pay some extra attention to CPM-based models that have already been developed to study which cell behaviors drive sprouting and network formation. This self-organization into sprouts and networks requires communication between the cells. We will discuss three types of communication used for this purpose: chemical signals, cell-cell interactions and cell-matrix interactions.

1.5.1 Chemical signals

Cells can respond to chemical signals, such as VEGF, by migrating towards higher concentrations of it [3], a process called chemotaxis. VEGF is a chemo-attractant known to be secreted by ECs and to attract ECs [70]. Merks *et al.* [64] hypothesized that dispersed ECs form vascular networks when they only chemotact towards EC-secreted VEGF at regions of their membrane that are not adhering to other cells with VE-cadherins, a mechanism called VE-cadherin mediated contact-inhibited chemotaxis. This hypothesis was based

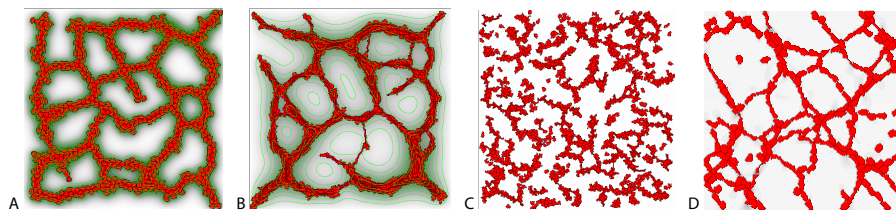


Figure 1.2: Vasculogenesis models. Simulation results of vasculogenesis driven by (A) contact-inhibited chemotaxis [64], (B) cell elongation with chemotaxis [63], (C) preferential adhesion to elongated cells [68], and (D) by mechanical cell-matrix interactions [69].

on the biological findings that cells adhere to each other with VE-cadherins and that VE-cadherins can inhibit VEGF signaling by interacting with the VEGF receptor 2. Indeed, the modeling results showed self-organization of endothelial cells into vascular networks (Figure 1.2A). By the same mechanism of contact-inhibited chemotaxis, sprouts can grow out from spheroids of cells. The latter setup models angiogenesis, rather than vasculogenesis, and for instance represents the *in vitro* assay in which embryoid bodies of endothelial cells are seeded within a matrix.

Another mechanism that can drive network formation is a combination of cell elongation and regular chemotaxis to an auto-secreted chemoattractant [63] (Figure 1.2B). This mechanism also suffices to model angiogenesis from a spheroid of cells.

Although both chemotaxis-based models can reproduce vasculogenesis and angiogenesis, Köhn-Luque *et al.* [71] noted that the diffusion speed assumed for VEGF by Merks *et al.* [64] is much lower than reported for most VEGF isoforms. Köhn-Luque *et al.* [71] proposed an alternative CPM-based model for vascularization in which VEGF, containing ECM-binding domains, is secreted by the underlying endoderm. Endothelial cells scavenge VEGF by the secretion of ECM and subsequently chemotact more strongly to ECM-bound VEGF than to soluble VEGF, resulting in network formation.

1.5.2 Cell-cell interactions

Computational modeling suggests that chemical signals are not always required for sprouting, cell-cell adhesion might suffice [68, 72]. Palm & Merks [72] showed that elongated, adhesive cells can self-organize into vascular structures. Cells aggregate into elongated structures that can only rotate very slowly, while connected in the branch points. If the model would run for infinity, the cells would form a spheroid, but this process is so slow that the cells dynamically arrest in a network-like pattern.

Based on experimental observations of elevated cell motility within the pres-

ence of elongated structures [68], Szabó *et al.* proposed that endothelial cells organize into vascular networks by preferential adhesion to elongated structures [68]. Indeed, this mechanism could drive network formation from initially dispersed cells *in silico* (Figure 1.2C).

1.5.3 Cell-matrix interactions

An interesting form of cell-matrix interactions are cell-derived mechanical signals that are transferred through the matrix [69, 73, 74]. Cells can pull on the matrix to generate strains and respond to strain by preferentially moving towards higher strains [69, 73, 74]. This results in a feedback loop of strain generation and migration that can drive sprouting and vascular network formation [69](Figure 1.2D).

Bauer *et al.* [16] explicitly model matrix fibers and tissue-specific cells and showed that inhomogeneities in the ECM lead to branching and anastomosis of sprouts. Daub & Merks [65] showed that branching can be stimulated by ECM-guided cell migration, or haptotaxis, towards high ECM concentrations. Sprout migration speed, sprout integrity and branching is also affected in this model by haptokinesis, which assumes that cells have an optimal motility at intermediate ECM concentrations. Cells can manipulate these optimal ECM conditions themselves by secreting proteolytic enzymes for matrix degradation.

The effect of proteolytic degradation of the matrix on sprout morphology was extensively studied in one of our computational models [75] that represents an *in vitro* assay of angiogenesis in fibrin matrices [38]. In this assay, sprout morphology ranged from narrow sprouts, to cyst, to the lowering of the complete monolayer. We used computational modeling to study how uPA and MMP secretion by tip and stalk cells affects sprout morphology. MMP degrades the basement membrane and uPA degrades fibrin. A simulation is initiated with a monolayer of endothelial cells, with a single tip cell in the middle, on top of a fibrin matrix with a basement membrane in-between. We assume that the tip cell secretes uPA and MMP at a maximal rate, but that the secretion hereof by stalk cells can be stimulated by the addition of angiogenic factors or inflammatory factors. Figure 1.3 gives an overview of the simulation results as a function of the secretion rates of uPA and MMP by stalk cells relative to the maximal secretion rate by the tip cell. Because the simulations are stochastic, variation is seen between simulations with the same parameter settings; representative simulations were selected for the morphospace in Figure 1.3. Sprout morphology can be grouped in four categories: sprouts, solid round cysts, hollow cysts and monolayers. Sprouts have a cord-like orientation of cells, whereas cysts are more round and multi-cellular. A high secretion of both uPA and MMP (Figure 1.3D) by stalk cells results in lowering of the monolayer. Sprouts are formed for low secretion of uPA (Figure

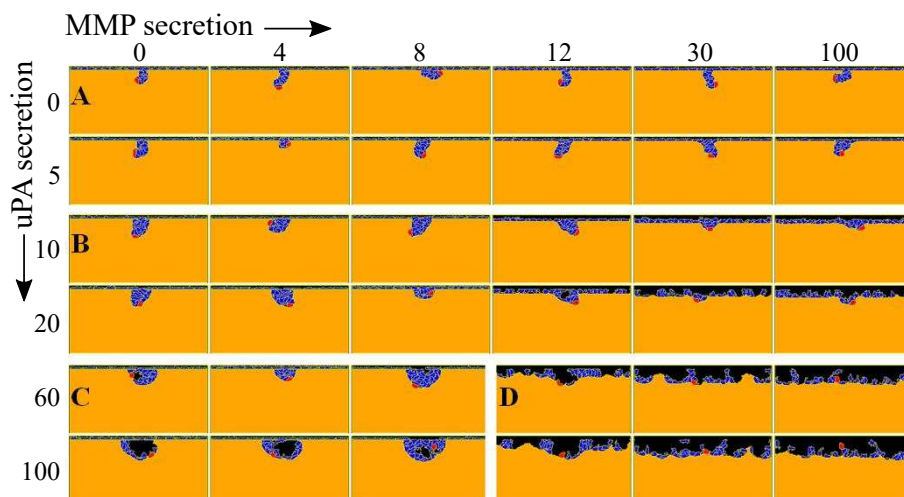


Figure 1.3: Morphospace of proteolytic enzyme secretion by stalk cells. Tip and stalk cells secrete uPA and MMP to degrade fibrin and the basement membrane respectively. The secretion of uPA and MMP by stalk cells is expressed as a percentage of the maximal secretion rate as secreted by the tip cell. This results in different sprout morphologies: (A) sprouts, (B) solid cyst-like structures, (C) hollow cyst-like structures and (D) monolayers.

1.3A), whereas solid cyst-like structures are formed for medium levels of uPA secretion (Figure 1.3B) for all MMP secretion levels by stalk cells. High secretion of uPA and low secretion of MMP (Figure 1.3C) results in hollow-cyst like structures. Occasionally (6 out of 128 simulations), no sprouting occurs for low levels of MMP secretion by stalk cells because stalk cells position themselves between the tip cell and the BM and thereby prevent degradation of the basement membrane. An interesting transition is seen between a hollow cyst-like structure and monolayer lowering for a secretion of MMP between 8% and 12%. The hollow cyst-like structures can be formed since the BM remains intact for attachment of endothelial cells before this transition. These structures are likely to collapse if gravity was included in the model. Experimentally, tubular structures can also disappear due to excessive fibrinolysis [76]. Thus, the intensity and the distribution of proteolytic enzyme secretion over different cell types (tip and stalk cells) seems to be a sufficient explanation for the tissue behavior observed in the laboratory. However, the proteolytic degradation system was strongly simplified in this model and does not include inhibitors of degradation. In Chapter 2, this model is extended with a detailed description of fibrin degradation by the plasminogen-plasmin system.

1.6 Thesis outline

In each chapter of this thesis, there is an overarching question: "How do the behaviors and properties of individual cells affect the collective cell behavior during angiogenesis". With this question in mind, we used CPM-based models to study several aspects of angiogenesis throughout this thesis.

The sprouting process during angiogenesis can be categorized in three themes: extracellular matrix invasion, sprouting dynamics and lumen formation. This thesis highlights each of them:

- In Chapter 2, we study what mechanisms select endothelial cells in a monolayer seeded on an extracellular matrix to form local ingrowth spots and then further invade the matrix to form sprouts. For this purpose, we developed a computational model that represents an *in vitro* model of tube formation [38]. Initial ingrowth and subsequent sprouting is driven in this model by a local, positive feedback loop: cells locally degrade the fibrin matrix and are stimulated in degradation by activators that are released from the matrix by this degradation.
- In Chapter 3, we asked whether the experimentally observed competition of cells for the sprout tip position, called tip cell overtaking, has a biological function or is a side effect of sprouting dynamics. We compared cell trajectories and tip cell overtake rates during sprouting in simulations, with and without regulation by Dll4-Notch signaling, with experimental data.
- In Chapter 4, we used computational modeling to validate two hypotheses of lumen formation. Although there is an ongoing debate on which hypothesis is accurate, our model indicates that both hypotheses might function synergistically and provides a possible explanation for the origin of the debate.
- In Chapter 5, we introduce a workflow for analyzing multi-factorial, non-linear models, such as the CPM-based models in this thesis, with a global sensitivity analysis. So far, such models are mostly studied by changing the parameter values of one or two parameters at the time. This can lead to misinterpretations of the modeling results, because the effect of the other parameters that were kept constant is not taken into account. A global sensitivity analysis studies all parameters simultaneously and determines which parameters or parameter combinations have the largest impact on the model output. A simple model of angiogenesis, based on contact-inhibited chemotaxis, is used as a case study.

Each model in this thesis addresses a biological question that originated from experimental work. Why do only a few cells in a monolayer start to form sprouts? Does tip cell overtaking require regulation by a VEGF-Dll4-Notch pathway? Do lumens form by vacuolation or by cell-cell repulsion? The modeling results give new insights in these questions and generate predictions that can lead further experimental research in this field.

A local uPAR-plasmin-TGF β 1 positive feedback loop in a computational model of angiogenic sprouting explains the *in vitro* effect of fibrinogen variants

This chapter is based on:

Sonja E. M. Boas, Marloes van den Broek, Ester M. Weijers, Pieter Koolwijk and Roeland M.H. Merks, *A local uPAR-plasmin-TGF β 1 positive feedback loop in a computational model of angiogenic sprouting explains the in vitro effect of fibrinogen variants* (in preparation)

Abstract

We developed a computational model of angiogenesis-like invasion of endothelial cells into fibrin matrices. Using an experimental assay of sprouting in three-dimensional fibrin matrices, which is the temporal scaffold formed during wound healing, was found that the composition of fibrin impacts the level of angiogenesis. There was more ingrowth on high molecular weight (HMW) than on low molecular weight (LMW) fibrin. It is unclear which mechanisms regulate where and how many ingrowth spots are formed in the endothelial cell monolayer. To address this question, we studied which mechanisms underlie the reduced angiogenic ingrowth on LMW compared to HMW with a hybrid, cell-based and continuum computational model that represents the experimental setup. Based on the model results, we propose that a local positive feedback mechanism between uPAR, plasmin and TGF β 1 selects cells in the monolayer for matrix invasion and subsequently consolidates sprouting. Plasmin-mediated fibrin degradation by an invading cell releases transforming growth factor β 1 (TGF β 1) from the matrix and TGF β 1 subsequently stimulates locally the ability of that cell to increase fibrin degradation. This model predicts a reduced angiogenic ingrowth on LMW compared to HMW, when we included the experimental observation that LMW binds less TGF β 1 than HMW.

2.1 Introduction

Angiogenesis is the formation of new blood vessels to perfuse hypoxic regions, such as wounds, growing tumors, or tissue-engineered constructs, by the branching or splitting of existing vessels [1, 2, 12, 15]. During angiogenesis, a fibrin matrix is formed as a provisional scaffold by leakage of fibrinogen into the tissue [77]. To (re)establish the blood supply, endothelial cells (ECs) from nearby blood vessels invade this fibrin matrix [77]. Tissue engineering and medical therapies aim to control the level of angiogenesis and could benefit from a mechanistic understanding of angiogenesis in fibrin matrices [6, 12]. It is unclear which mechanisms regulate the onset of capillary formation or 'ingrowth spots' in an endothelial cell monolayer and consolidate further angiogenic sprouting.

The level of ingrowth spots and angiogenesis is strongly affected by the fibrin composition [39, 76, 78, 79]. Weijers *et al.* [39] used an *in vitro* model of capillary-like tube formation in a three-dimensional fibrin matrix, previously introduced by Koolwijk *et al.* [38], to study the effect of the fibrin composition on angiogenesis. A monolayer of human microvascular endothelial cells (HMVECs) is seeded on a fibrin matrix and sprouts grow into the fibrin matrix upon stimulation with an angiogenic factor, vascular endothelial growth factor (VEGF) and/or basic fibroblast growth factor (bFGF), in combination with

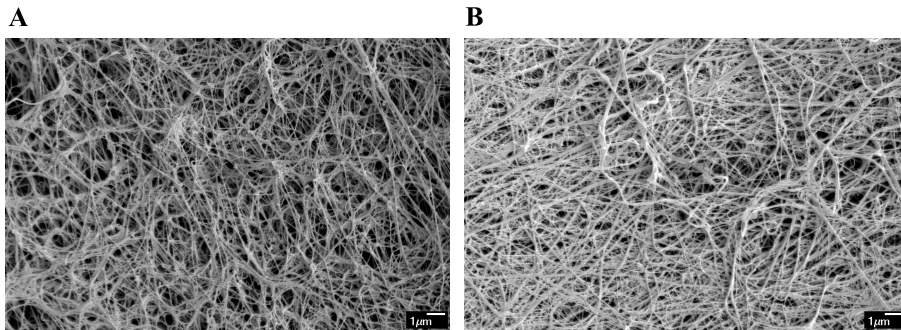


Figure 2.1: Fibrin matrices. Scanning electron microscopic analysis of (A) high molecular weight (HMW) fibrinogen and (B) low molecular weight (LMW) fibrinogen. HMW has thicker fibers and forms more open network structures than LMW. Bars represent 1 μm . The figures are derived from Kaijzel *et al.* [78].

the inflammatory mediator $\text{TNF}\alpha$ (tumor necrosis factor α). From now on we will refer to this *in vitro* model as the ‘HMVEC-fibrin assay’. Fibrinogen naturally occurs in three different variants: HMW (high molecular weight) fibrinogen (Figure 2.1A), LMW (low molecular weight) fibrinogen (Figure 2.1B) and LMW’ fibrinogen [39]. HMVECs proliferate more and show more angiogenic ingrowth on HMW fibrin than on LMW or unfractionated fibrin mixture [39]. In addition, the spacing between ingrowth spots is more wide-spread [80] than what would be expected from selection of tip cells through lateral inhibition by Dll4-Notch signaling [23, 24, 44, 45]. To study which mechanisms regulate the spacing of ingrowth spots and consolidate sprouting, we developed a computational model to evaluate a hypothetical mechanism for sprouting that could also explain a reduced ingrowth on LMW compared to HMW. This mechanism provides an alternative next to Dll4-Notch in leader cell or ‘tip cell’ selection [3, 21–23].

HMW and LMW differ in protein structure and after clotting result in different fibrin matrix structures. Polymerization of intact HMW fibrinogen results in HMW fibrin, whereas LMW fibrinogen, that lacks the C-terminus of one of the two $\text{A}\alpha$ -chains of fibrinogen, forms LMW fibrin [39]. HMW fibrin has a more open matrix structure, with thicker fibers and larger openings between the fibers compared to LMW fibrin (see Figure 2.1). A simple explanation for the increased ingrowth on HMW fibrin compared to LMW fibrin could be that the ECs can invade the open matrix structure of HMW fibrin more easily. Furthermore, the mechanical properties could differ, which was shown to affect two-dimensional sprouting and network formation [69, 73, 74]. Additionally, HMVEC-associated fibrin degradation (fibrinolysis) is higher on HMW compared to LMW fibrin [39]. Finally, LMW fibrin has a reduced number of binding

2. Computational modeling of matrix invasion

sites for growth factors, e.g. TGF β 1 [81], that are located at the C-terminus of the A α -chains. In this chapter we will focus on cell-associated fibrinolysis and protein binding.

Cell-associated fibrinolysis is mostly performed by the trypsin-like protease plasmin [19, 82–84]. Plasmin is the active conversion product of plasminogen, which is mainly produced by the liver and reaches fibrin scaffolds through the blood stream. Conversion of plasminogen into plasmin occurs by plasminogen activators and is highly regulated. Urokinase plasminogen activator (uPA) and tissue-type plasminogen activator (tPA) are secreted by ECs as single-chain proteins. tPA is expressed in quiescent endothelium [85] and is primarily involved in clot dissolution [86], whereas uPA and its cellular receptor (uPAR) are expressed during angiogenesis and control pericellular proteolysis [85, 87]. ECs secrete inactive, single chain pro-uPA. Pro-uPA binds to uPA receptors (uPARs) on the membrane of endothelial cells, and is subsequently converted into an active two-chained form. This active membrane-bound uPA-uPAR complex converts plasminogen into plasmin [19]. To balance fibrin degradation, ECs secrete plasminogen inhibitor type 1 (PAI-1) that binds to tPA and uPA for deactivation and the PAI-1-uPA-uPAR complex is internalized [82, 83]. Besides plasmin, membrane-type 1 metalloproteinase (MT1-MMP) can perform cell-associated fibrinolysis [88], but the MT1-MMP inhibitor TIMP-1 had only minor effects on angiogenesis in an assay similar to the HMVEC-fibrin assay, using a fibrin-10% collagen matrix [89]. In summary, the HMVEC-associated fibrinolysis [39] is due to the plasminogen-plasmin degradation system.

TGF β 1 has a strong pro-angiogenic effect in HMVEC cultured on Matrigel [90]. This pro-angiogenic effect depends on the upregulation of PAI-1 and uPAR by TGF β 1 and was inhibited by TGF β 1 antagonist peptides. TGF β 1 also induces PAI-1 and uPAR expression in hepatic stellate cells [91] and uPA/PAI-1 levels in human tumor tissues [92]. LMW has a reduced number of C-termini of the A α -chain of fibrinogen compared to HMW. LTBP1 (latent transforming growth factor β (TGF β) binding protein 1) potentially binds the C-terminus of this A α -chain: the level of LTBP1 is dramatically reduced in LMW fibrinogen fraction I-9, which lacks major parts of the C-termini of the A α -chain, compared to commercially available fibrinogen and intact fibrinogen fraction I-2 [81]. LTBP1 sequesters latent-TGF β 1 in the plasma to fibrin, resulting in an inactive TGF β 1 reservoir that can locally be activated and released by plasmin [20, 93]. In summary, the reduced number of LTBP1 binding sites in LMW compared to HMW can result in a lower bio-availability of TGF β 1, which could affect angiogenesis.

Based on the experimental data of cell-associated fibrinolysis and TGF β 1, we suggest that a local uPAR-plasmin-TGF β 1 positive feedback loop drives angiogenesis (see Figure 2.2): cell-bound uPAR activates plasmin (Figure 2.2,

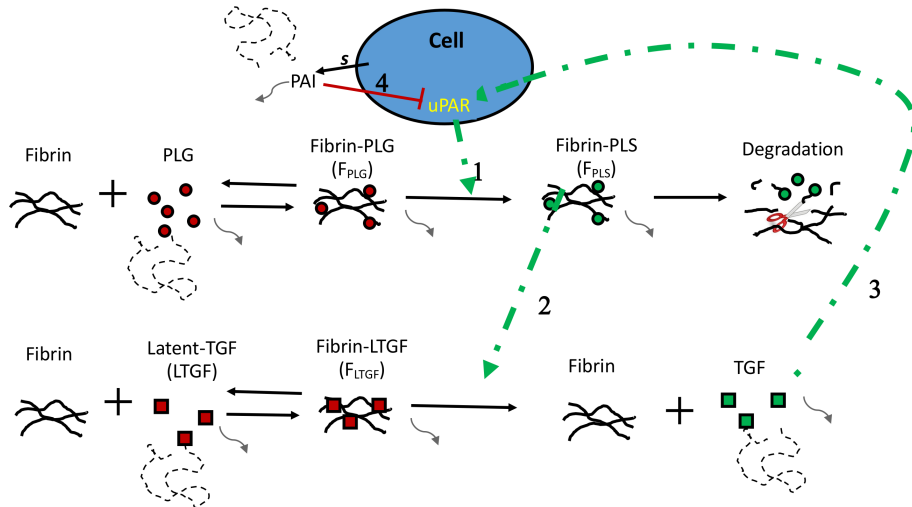


Figure 2.2: Schematic overview of plasmin and $TGF\beta_1$ interactions. Plasminogen (PLG) reversibly binds fibrin, forming fibrin-bound plasminogen (F_{PLG}). F_{PLG} is converted by cell-bound uPAR (arrow 1) to fibrin-bound plasmin (F_{PLS}). F_{PLS} degrades fibrin. Latent- $TGF\beta_1$ ($LTGF$) binds fibrin reversibly. Fibrin-bound latent- $TGF\beta_1$ (F_{LTGF}) is activated and released by F_{PLS} (arrow 2), resulting in active, diffusive $TGF\beta_1$ and free fibrin. Active $TGF\beta_1$ induces production of uPAR (arrow 4). Cells secrete (s) PAI-1 (PAI), which inhibits uPAR activity (arrow 4). The gray, dotted lines indicate diffusion of proteins and curved, gray lines indicate decay.

arrow 1), plasmin locally degrades fibrin and releases active $TGF\beta_1$ (see Figure 2.2, arrow 2), and $TGF\beta_1$ upregulates uPAR production in the protruding cell (see Figure 2.2, arrow 3), whereas nearby cells which experience only mild $TGF\beta_1$ -dependent uPAR stimulation are silenced by self-secreted PAI-1 (see Figure 2.2, arrow 4).

In this hypothesis, cells are activated to degrade the matrix by an external growth factor. This mechanism for capillary sprout formation was first introduced in a mathematical model of Levine *et al.* [94]. This continuum model, which models cells and matrix as densities, shows that cells in a capillary aggregate into a bimodal structure to sprout towards a nearby tumor. The tumor secretes a growth factor and the location of capillary onset depends on the shape of the growth factor gradient. In the HMVEC-fibrin assay, it is unpredictable which cells in the monolayer become sprout leaders. To study what causes such a spontaneous onset of ingrowth, we do not include a growth factor gradient as was done by Levine *et al.* [94] and others [16, 51, 52, 65]. Nor do we bias the location of capillary onset by initializing with a leading cell in the monolayer as we did in a previous model [75] that represented the HMVEC-fibrin assay.

2. Computational modeling of matrix invasion

To study our hypothesis that an uPAR-plasmin-TGF β 1 positive feedback loop could account for spontaneous ingrowth, we model the plasminogen-plasmin degradation system in detail. This system is extensively studied in cell-free models [43, 95, 96]. We based the plasminogen-plasmin system in our model on the cell-free system of Diamond & Anand [95], which was used to predict lysis-fronts across fibrin clots for different administration regimes for tPA and uPA. The continuum model by Chaplain & Lolas [48] studied how the spatiotemporal dynamics of the plasmin system affect tumor invasion, using a fairly detailed description of the plasminogen-plasmin system: endothelial cells secrete uPA and PAI-1, plasmin is activated in proximity of uPA and cells, and PAI-1 scavenge uPA and plasmin. Our question requires a cell-based approach, rather than a continuum approach, because the physical interactions between cells and fibrin are important for locally triggering the positive feedback loop. Previous cell-based models of matrix invasion showed how an interplay of cell behaviors, such as haptotaxis towards higher concentrations of matrix proteins or chemotaxis towards higher concentrations of growth factor, drive sprouting and branching [51, 52, 65, 75]. These models did not focus on the details of matrix degradation, but simplified it to the secretion of proteolytic enzymes to degrade the extracellular matrix. We constructed a hybrid, cell-based and continuum computational model that combines a detailed description of cell-fibrin interactions, the plasminogen-plasmin system and the activation of proteolytic cellular activity by the growth factor TGF β 1.

2.2 Results

To study by what mechanism the level of angiogenesis is reduced on LMW compare to HMW fibrin, we developed a computational model that mimics the HMVEC-fibrin assay. The hybrid, cell-based and continuum computational model represents a cross-section of the *in vitro* model (Figure 2.3). The model is initialized with a monolayer of fifty endothelial cells on top of a fibrin matrix. Fibrin forms a physical obstruction for cells, while at the same time, fibrin offers cells support as cells can adhere to fibrin. Using cell-based modeling, we explicitly model cell shape, cell motility, cell-cell adhesion, and cell-fibrin adhesion. Each cell has a concentration of active uPAR homogeneously spread over its membrane and each cell secretes PAI-1. PAI-1, fibrin, latent-TGF β 1, active TGF β 1, plasminogen and plasmin are modeled as concentration fields and interact with each other, resulting in a local activation of plasminogen by cell-bound uPAR into plasmin (Figure 2.2). This releases and activates latent-TGF β 1 and degrades fibrin. Active TGF β 1 induces the production of uPAR in nearby cells, resulting in a local positive feedback loop that drives fibrin degradation. Cells can invade regions where fibrin is degraded, driven by adhesion of cells to the fibrin and contact-inhibited cell division.

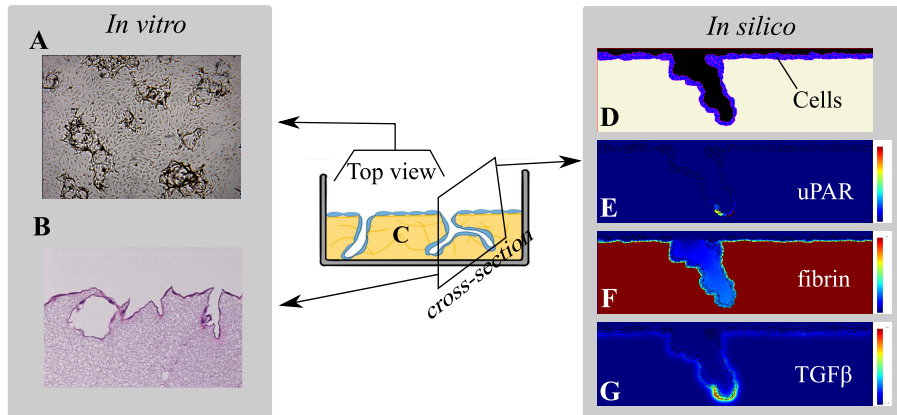


Figure 2.3: *In vitro* and *in silico* model setup. The HMVEC-fibrin assay can be studied with (A) nonphase contrast views of the monolayer or by (B) histological staining of cross-sections of the matrix after fixation. (C) A schematic illustration of the model is shown in the middle, with a monolayer of endothelial cells (blue) that form capillary-like tubes in a fibrin matrix (yellow). Images of an *in silico* simulation that represents a cross-section of the *in vitro* model are shown on the right. (D) Endothelial cells and fibrin are modeled with the CPM, (E) the uPAR concentration of cells is modeled with an ODE equation, and a PDE system calculates the concentration of (F) fibrin, (G) $\text{TGF}\beta_1$, PAI-1, PLG, PLS and all fibrin-bound forms (not shown).

To represent cells and their physical interactions with the fibrin matrix, the cellular Potts model [61, 62] was used. Cells are projected as patches of lattice sites on a lattice and move by copying lattice sites inward or outward, representing the extension and retraction of filopodia. A time step in the model, also called Monte Carlo step (MCS), represent approximately 2.5 minutes and a simulation takes 10 days similar to the HMVEC-fibrin assay [38].

The concentration of uPAR for each cell is modeled by one ordinary differential equation (ODE). A concentration field for uPAR is projected on the CPM grid, with each lattice site that is occupied by a cell having the uPAR concentration of that cell. The concentration of uPAR moves along with the location of the cell after cell movement. A system of coupled partial differential equations (PDEs, see Section 2.4.3) describes the reactions between fibrin, $\text{TGF}\beta_1$, plasminogen, plasmin, PAI-1 and all fibrin-bound forms. The plasminogen-plasmin system in this model is based on the cell-free model by Diamond & Anand [95] that studies the penetration of uPA and tPA in a fibrin clot present in the blood stream. To make it suitable for our question, we include the uPAR-plasmin- $\text{TGF}\beta_1$ positive feedback, simplified the implementation of fibrinolysis, and removed blood flow.

To model the plasminogen-plasmin degradation system and the uPAR-

plasmin-TGF β 1 positive feedback, we made the following assumptions:

1. Cell-bound uPAR carries out active proteolysis. We do not consider the activity of t-PA, because addition of tPA specific antibodies does not have a significant effect on the formation of capillary-like tubular structures in the HMVEC-fibrin assay.
2. Plasminogen binds fibrin reversibly.
3. Fibrin-bound plasminogen is converted to fibrin-bound plasmin by uPAR. Plasminogen is in a closed configuration in circulation, but binding to fibrin induces an open configuration that is much more susceptible for activation [97–99].
4. Plasmin remains fibrin-bound. As a result, plasmin is localized at the cell surface or in immediate proximity of the cell [100].
5. Endothelial cells secrete PAI-1, which diffuses and decays [19, 38]
6. PAI-1 inhibits uPAR activity by internalization of uPAR-PAI-1 complexes [82, 83]
7. Latent-TGF β 1 binds fibrin reversibly [20], we thereby implicitly model binding of LTBP1 to latent-TGF β 1.
8. We assume a non-competitive binding of latent-TGF β 1 and plasminogen for fibrin.
9. Fibrin-bound latent-TGF β 1 is activated and released by plasmin, resulting in diffusive TGF β 1 [20].
10. TGF β 1 induces expression of uPAR [90]
11. Plasminogen and latent-TGF β 1 are bound to fibrin at initialization. We assume that plasminogen and latent-TGF β 1 are readily bound to plasma-derived fibrin or are present in the serum and bind during the preparation of the fibrin matrix.

2.2.1 uPAR-plasmin-TGF β 1 positive feedback selects ‘uPAR-rich’ cells in the monolayer

In the HMVEC-fibrin assay, only a few cells in the monolayer end up with a high uPAR concentration [80] to lead invasion of sprouts. The selection mechanism of the ‘uPAR-rich’ cells in the monolayer is not completely understood. We used the model to test if the uPAR-plasmin-TGF β 1 positive feedback mechanism can select for uPAR-rich cells in the monolayer. For this purpose, we initialized each cell in the monolayer with the same level of uPAR (Figure 2.4A). Random cell movements change the contact-level and contact-duration with fibrin, resulting in local differences of plasmin activation. Fibrin is degraded at sites with a high plasmin activity (Figure 2.4B), and TGF β 1 is released from the matrix (Figure 2.4C). Released TGF β 1 induces the expression of uPAR in nearby cells (Figure 2.4D). The expression of uPAR in more distant cells can also be somewhat induced by the released TGF β 1, but uPAR activity is counterbalanced by self-secreted PAI-1. Due to stochasticity, only a few cells in

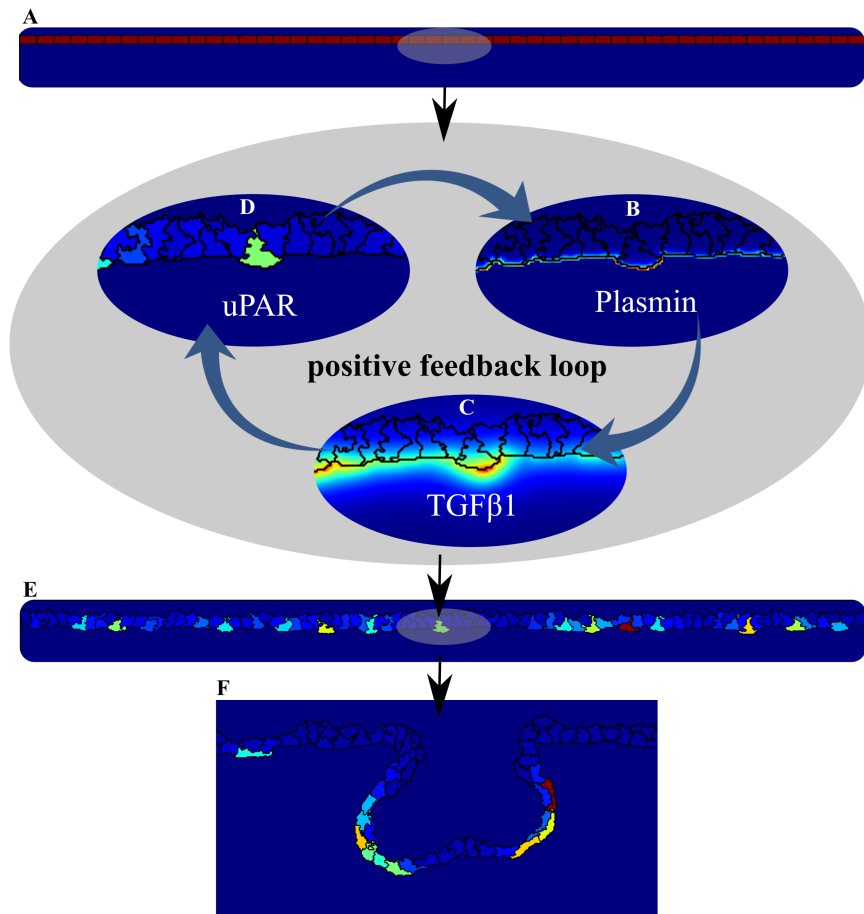


Figure 2.4: Spontaneous 'uPAR-rich' cell selection in the monolayer by a uPAR-plasmin-TGF β 1 positive feedback loop. (A) All cells in the model have the same uPAR concentration (the uPAR concentration in the cells is indicated by the red color) at initialization of a simulation. Local changes in fibrin-cell contact can increase (B) local plasmin concentration, resulting in degradation of fibrin and (C) release of active TGF β 1. (D) TGF β 1 can stimulate uPAR production. (E) The positive feedback loop selects 'uPAR-rich' cells in the monolayer, with a few cells having high level (red color) and most cells having low levels (blue color). (F) The positive feedback loop consolidates sprouting.

the monolayer are able to trigger the positive feedback loop sufficiently to overcome inhibition by PAI-1 and gain high levels of uPAR to start ingrowth (Figure 2.4E). In absence of fibrin-bound latent-TGF β 1, none of the cells in the monolayer, in a hundred stochastic simulations, manage to gain high levels of

uPAR due to the lack of TGF β 1-induced uPAR expression. Thus, our modeling results suggest that the uPAR-plasmin-TGF β 1 positive feedback loop might select for uPAR-rich cells in a monolayer of endothelial cells to form ingrowth spots.

Once uPAR-rich cells are spontaneously selected in the monolayer, the uPAR-plasmin-TGF β 1 positive feedback consolidates sprout progression in the model (see Figure 2.4F and Movie S1). The cell that leads the sprout, which we will refer to as the tip cell, has the highest concentration of uPAR (see Figure 2.4F). This is in agreement with experimental observations [80]. As commonly observed *in vitro*, in the model sprouts can spontaneously branch (see Figure 2.4F and Movie S1). This occurs when a cell neighboring the tip cell also becomes a tip cell and moves into another direction, or when a cell higher up the sprout manages to trigger the feedback loop and starts a branch.

2.2.2 TNF α stimulates sprouting by inducing of uPAR activity

Sprouts are not formed in every simulation; sometimes due to stochasticity none of the cells are able to activate the positive feedback loop sufficiently to overcome the inhibition of PAI-1. Similarly, ingrowth is not seen in every experiment in the *in vitro* HMVEC-fibrin assay, but is highly variable per cell donor and even per assay with cells from the same donor. *In vitro*, TNF α is required to induce sprouting [38] and the mean tube length increases at higher doses of TNF α . TNF α increases uPA production and the level of cell-bound uPA [38]. Thus, addition of TNF α likely increases uPAR activity in all cells in the endothelial cell monolayer. We asked how it is possible that a global induction of uPAR activity by TNF α increases the number of local ingrowth spots, rather than causes excessive fibrinolysis and a subsequent lowering of the complete endothelial cell monolayer?

We used our model to test whether an increase of the production of uPAR in all cells would increase sprout frequency and the angiogenesis level. To mimic the effect of TNF α , we increased the constant production rate of uPAR. We found that the frequency of successful sprouting in a set of simulations increases with higher constant uPAR production rates (Figure 2.5). Figure 2.5A shows a set of simulation results after ten days of sprouting for a constant uPAR production rate of 0.001, 0.002, 0.003, and 0.005 (relative units (RU)/MCS). The quantitative level of the constant uPAR production level is experimentally not known, therefore we express the concentration relative to the concentration of the initial plasminogen concentration in the model. There is a more extensive ingrowth and a higher frequency of successful sprouting in simulations with higher constant uPAR production rates. Each set contains four stochastic simulation results for the same parameter settings and clearly shows the strong diversity in ingrowth frequency and sprout morphology.

To quantify sprouting, we used three measures: the angiogenesis level, the sprouting frequency and the fibrinolysis level. The angiogenesis level simultaneously reflects sprout depth and sprout count (see Section 2.4.2 for the quantification method). The blue curve in Figure 2.5B represents the mean angiogenesis level for all simulations that formed sprouts (angiogenesis level > 0). The sprouting frequency is the number of simulations out of a hundred simulations that formed sprouts (red curve in Figure 2.5B). The fibrinolysis level, quantified as the mean percentage of initial fibrin lattice sites that are invaded by the endothelial cells in all hundred simulations, also increases for higher constant uPAR production rates, as is expressed by the green curve in Figure 2.5B.

In summary, an increase of the basal uPAR activity in all cells increases the chance that a cell in the monolayer can trigger the uPAR-plasmin-TGF β 1 positive feedback loop and gain high levels of uPAR for ingrowth. As a consequence, sprouts form more frequently and more excessively. The feedback loop functions locally, such that sprouts form rather than that the entire endothelial cell monolayer lowers by overall fibrinolysis. Thus, our model gives a mechanistic explanation of how the global stimulation of uPAR activity by TNF α might induce local sprouting.

2.2.3 Validation experiments

As a validation of the model, we tested whether it could reproduce the outcome of three published *in vitro* experiments of the plasminogen-plasmin degradation system.

Firstly, Koolwijk *et al.* [38] reported that there was no angiogenic ingrowth and tubule formation in fibrin matrices that were made using plasminogen-depleted fibrinogen. In agreement, Figure 2.6A shows that there is no ingrowth in our model for low initial levels of fibrin-bound plasminogen. The sprouting percentage, the fibrinolysis percentage, and the angiogenesis level all increase when the initial fibrin-bound plasminogen concentration is increased. Plasminogen was expected to be rate limiting in plasmin-dependent fibrin degradation as plasmin is the conversion product of plasminogen.

Secondly, inhibition of uPAR-bound uPA activity by addition of uPA specific polyclonal antibodies, or prevention of the binding of uPA to uPAR by soluble uPAR or blocking antibodies inhibited capillary-like tube formation dose-dependently [38, 80]. We modeled the inhibition of uPAR activity by an increase of the decay rate of uPAR. Consistent with the experimental results, Figure 2.6B shows that an increase in the decay rate of uPAR decreases the sprouting percentage, the fibrinolysis percentage, and angiogenesis level. Inhibition of uPAR activity was expected to reduce cell-associated fibrinolysis required for angiogenesis, since uPAR converts plasminogen into plasmin.

Thirdly, experiments show that there is an optimum PAI-1 concentration for

2. Computational modeling of matrix invasion

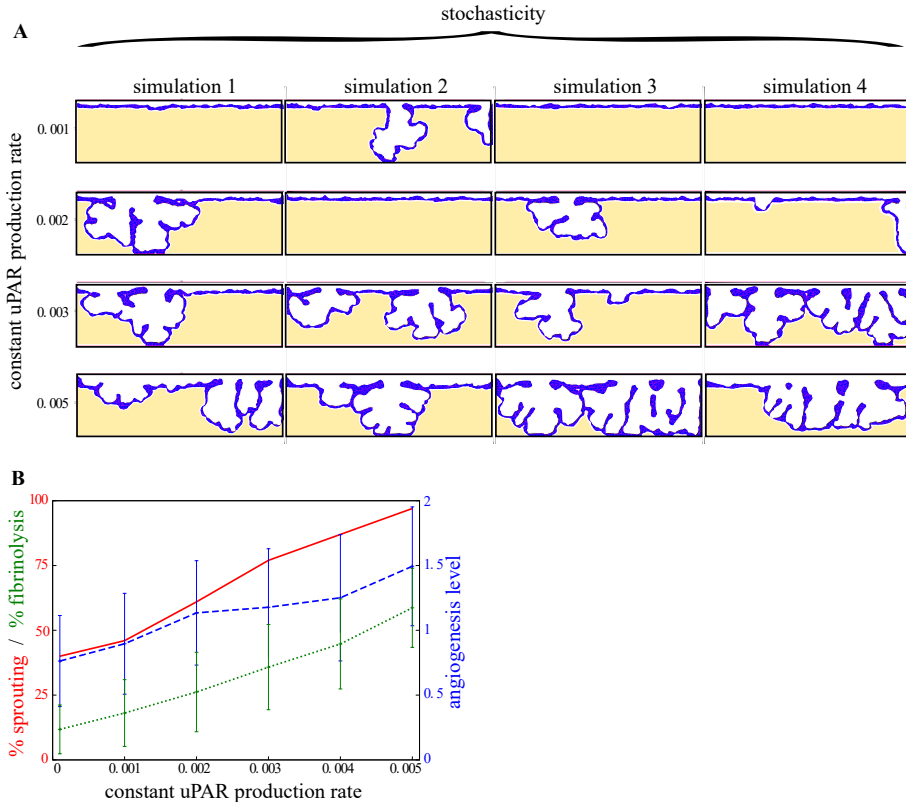


Figure 2.5: The angiogenesis level is sensitive to the constant uPAR production rate. Panel A shows a set of four stochastic simulation results at Monte Carlo step (MCS) 6000 for a constant uPAR production rate of 0.001, 0.002, 0.003, and 0.005 (relative units/MCS). Sprouts form more frequently and more extensively at higher constant uPAR production rates. For all simulations that formed sprouts, the mean angiogenesis level (blue curve) is calculated, representing the sprout count and sprout depth. The red curve in (B) represents the percentage of simulations that formed sprouts at MCS 6000 out of a hundred simulations. The green curve in (B) represents fibrinolysis, it is the mean (out of a hundred simulations) percentage of the initial fibrin lattice sites that are invaded by the endothelial cells at MCS 6000.

angiogenesis [101]: addition of PAI-1 to implants in wild-type mice enhanced angiogenesis up to 3-fold at low concentrations but inhibited angiogenesis nearly completely at high concentrations. Absence of protease inhibitors results in excessive fibrinolysis, which is incompatible with normal capillary formation [102, 103]. As for uPAR, we modeled the manipulation of PAI-1 activity by an increase of the decay rate of PAI-1. Figure 2.6C shows that the fibrinolysis percentage strongly increases when the decay rate of PAI-1 is increased.

High decay rate of PAI results in low PAI-1 activity, and thus in excessive fibrinolysis; no sprouts are formed, but the entire monolayer lowers simultaneously. Low decay rates of PAI-1 result in high PAI-1 activity and sprouting is completely inhibited. Only for intermediate levels of PAI-1 activity, we find sprouting, indicated by the peaks in Figure 2.6C for the sprouting percentage and the angiogenesis level.

In conclusion, the model can reproduce three essential validation experiments for the plasminogen-plasmin system. In absence of fibrin-bound latent-TGF β 1, no sprouts are formed in all hundred simulations with a parameter set for which sprouts formed well in presence of fibrin-bound latent-TGF β 1 in Figure 2.5B and 2.6 (constant uPAR production rate=0.005 RU/MCS , initial fibrin-bound plasminogen concentration=1 RU , PAI-1 decay rate=0.01 MCS^{-1} , and uPAR decay rate=0.0095 MCS^{-1}). This shows that initialization and consolidation of sprouting truly depends on the uPAR-plasmin-TGF β 1 positive feedback in our model.

2.2.4 The bio-availability of TGF β 1 regulates the level of angiogenesis in HMW and LMW

As a next step, we used our model to design new hypotheses about the mechanisms that reduce the level of angiogenic ingrowth on LMW compared to HMW. The level of LTBP1 is dramatically reduced in LMW fibrinogen fraction I-9, which lacks major parts of the C-termini of the A α -chain, compared to commercially available fibrinogen and intact fibrinogen fraction I-2 [81]. As LTBP1 sequesters latent-TGF β 1 to fibrin, this could result in a lower level of fibrin-bound latent-TGF β 1. We hypothesize that this reduced level of fibrin-bound latent TGF β 1, in combination with our suggested local uPAR-plasmin-TGF β 1 positive feedback, could cause the reduced level of angiogenesis on LMW compared to HMW. If the levels of inactive TGF β 1 in the fibrin matrix are too low, cells are not able to induce a strong enough uPAR-plasmin-TGF β 1 positive feedback loop to overcome the inhibition of PAI-1 and thus will not form sprouts.

In line with this hypothesis, Figure 2.7A shows that the sprouting percentage, the fibrinolysis percentage, and the angiogenesis level decrease with lower initial concentrations of fibrin-bound latent TGF β 1 in our model. In conclusion, our simulations results suggest that the angiogenic ingrowth is reduced on LMW compared to HMW due to a reduction in binding sites for LTBP1.

The addition of active TGF β 1 has a biphasic effect on *in vitro* sprouting [40], quantified by measuring the total length of all cellular structures that have penetrated beneath the surface monolayer. Addition of active TGF β 1 to the assay stimulates sprouting at low doses and inhibits sprouting at high doses of TGF β 1 [40]. In previous work, Pepper *et al.* [104] showed that TGF β 1 reduces bFGF-induced extracellular proteolysis and this could explain the re-

2. Computational modeling of matrix invasion

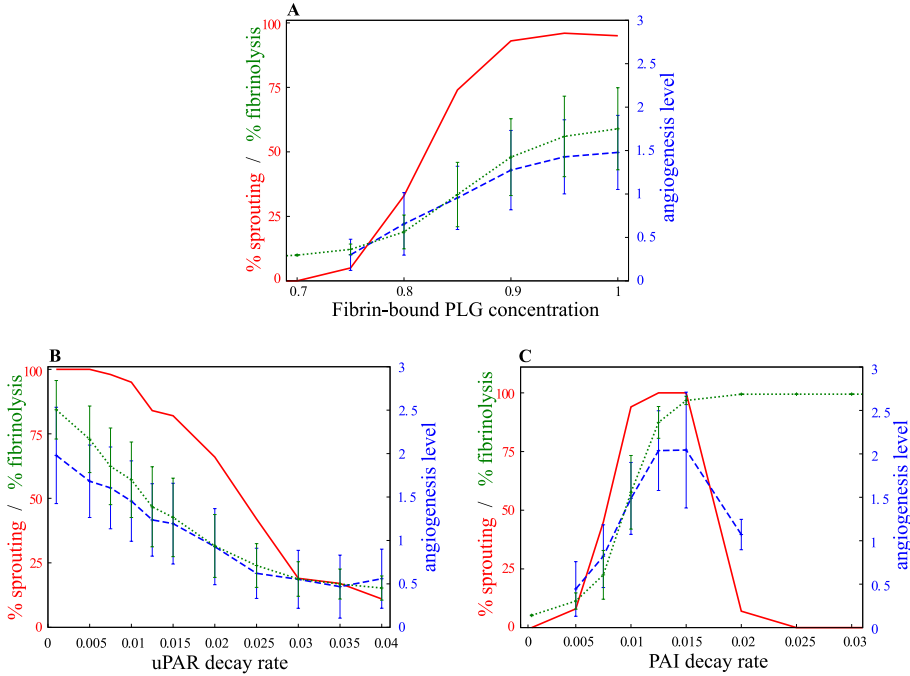


Figure 2.6: Model validation experiments. The sprouting percentage (red curve), the angiogenesis level (blue curve), and the fibrinolysis percentage (green curve), are plotted against changes in (A) the initial concentration of fibrin-bound plasminogen (relative units), (B) the decay rate of uPAR (MCS^{-1}), and (C) the decay rate of PAI-1 (MCS^{-1}). The sprouting percentage is the percentage of simulations (out of a 100 simulations) that have an angiogenesis level larger than zero. The angiogenesis level is a measure that simultaneously reflects sprout depth and sprout count, and the mean angiogenesis level is taken over all simulations that actually formed sprouts. The fibrinolysis percentage is the percentage of the initial fibrin lattice sites that are invaded by the endothelial cells at MCS 6000.

duced invasion at high doses of TGF β 1 [40]. To test this biphasic effect in the model, we initialized the model with a homogeneously spread concentration of active TGF β 1. The medium containing TGF β 1 is refreshed every two days *in vitro*, similarly we reset the TGF β 1 concentration to the initial value after every two days in the model. Figure 2.7B shows that TGF β 1 also has a biphasic effect on angiogenesis in the model. At low concentrations of added TGF β 1 (TGF β 1=0.5 and TGF β 1=10 in Figure 2.7B), more sprouts are formed than without addition of TGF β 1 (TGF β 1=0 in Figure 2.7B). The uPAR activity in all cells increases due to the overall addition of TGF β 1, allowing some cells to get over the inhibitory PAI-1 threshold for triggering the uPAR-plasmin-TGF β 1 positive feedback loop. This is a similar effect as was seen

for the stimulation with $\text{TNF}\alpha$ in Section 2.2.2. However, the upregulation of uPAR activity is too strong at high doses of $\text{TGF}\beta 1$, and consequently all cells degrade the matrix. This results in lowering of the complete endothelial cell monolayer, rather than in local sprouting ($\text{TGF}\beta 1=1000$ in Figure 2.7B) and sprouting is thus reduced. In this case, fibrin is quickly degraded and some cells loose contact with fibrin. Because the model only includes fibrin adhesion and contact-inhibited mitosis, these cells are no longer stimulated to migrate along with the degrading matrix and sometimes form a stack of cells above the monolayer. This is a model artefact, and these stacks of cells are not considered to be sprouts, but are considered to be part of the endothelial cell monolayer.

In conclusion, our model can reproduce the biphasic effect of $\text{TGF}\beta 1$ on angiogenesis, but the cause of the reduction of sprouting at high doses of $\text{TGF}\beta 1$ in our model is inconsistent with the proposed mechanism hereof by Pepper *et al.* [40]. Our model suggests that low doses of $\text{TGF}\beta 1$ increase the probability that cells in the monolayer can trigger the uPAR-plasmin- $\text{TGF}\beta 1$ positive feedback loop and start sprouting, whereas high doses of $\text{TGF}\beta 1$ reduce sprouting due to excessive matrix degradation. Unfortunately, the level of matrix degradation was not measured in the *in vitro* experiment by Pepper *et al.* [40]. Our current model does not include a negative feedback of $\text{TGF}\beta 1$ on bFGF-induced extracellular proteolysis. Future work should verify if a biphasic effect of $\text{TGF}\beta 1$ on angiogenesis, without excessive matrix degradation at high levels of $\text{TGF}\beta 1$, can be found in presence of such a feedback in our model.

2.3 Discussion

We developed a computational model to study what mechanisms cause angiogenic ingrowth and subsequent sprouting in a HMVEC-fibrin assay, in which endothelial cells form angiogenic-like tubule structures in fibrin matrices [38, 39]. For this purpose, we asked what mechanisms cause a reduced level of angiogenesis on LMW compared to HMW matrices [39]. Based on experimental data, we propose that an uPAR-plasmin- $\text{TGF}\beta 1$ positive feedback loop drives angiogenic sprouting. Model simulations that include this feedback loop show a spontaneous selection of ‘uPAR-rich’ cells in a monolayer of cells. Subsequently, the feedback loop allows for the ‘uPAR-rich’ cells to continue matrix invasion and sprouting. The model can reproduce several basic experimental observations of the plasminogen-plasmin degradation system. The model predicts a reduced level of angiogenesis on LMW compared to HMW, when the uPAR-plasmin- $\text{TGF}\beta 1$ positive feedback loop cannot be activated sufficiently for sprouting in LMW. This could be due to an experimentally observed [81] reduced level of $\text{TGF}\beta 1$ bound to LMW, which lacks major parts of the C-termini

2. Computational modeling of matrix invasion

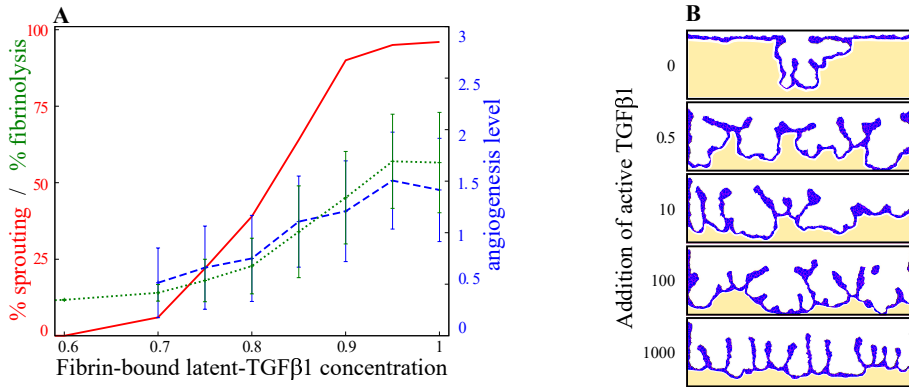


Figure 2.7: TGF β 1 experiments. (A) The sprouting percentage (red curve), the angiogenesis level (blue curve), and the fibrinolysis percentage (green curve), are plotted against changes in the initial concentration of fibrin-bound latent-TGF β 1 (relative units). The sprouting percentage is the percentage of simulations (out of a 100 simulations) that have an angiogenesis level larger than zero. The angiogenesis level is a measure that simultaneously reflects sprout depth and sprout count, and the mean angiogenesis level is taken over all simulations that actually formed sprouts. The fibrinolysis percentage is the percentage of the initial fibrin lattice sites that are invaded by the endothelial cells at MCS 6000. (B) Addition of active TGF β 1 has a biphasic effect on sprout formation in our model. The sprouting frequency increases for the addition of low doses of TGF β 1, but global degradation of the complete endothelial cell monolayer prevents sprout formation at high doses of TGF β 1.

of the A α -chain, compared to HMW. In conclusion, the model gives a new mechanistic hypothesis for the driving mechanisms of angiogenic sprouting in the *in vitro* model.

The uPAR-plasmin-TGF β 1 positive feedback loop in our model causes a spontaneous selection of 'uPAR-rich' cells in the monolayer. Due to random cell movements, the feedback loop is activated more strongly by some cells than by others, resulting in autonomous selection of sprout leader cells in the monolayer. Due to stochasticity, in some simulations there no cells are able to activate the feedback loop sufficiently to overcome PAI-1 inhibition. Similarly, in our hands there is a large variation in the success of sprouting in the HMVEC-fibrin assay. We found that the basic production level of uPAR strongly regulates the probability that 'uPAR-rich' cells are locally selected and sprouts are formed. A possible candidate for the induction of uPAR activity is TNF α [38]. Addition of TNF α is required in the *in vitro* experiment to induce angiogenesis. Thus, our simulations provide an explanation for how a slight upregulation of uPAR activity by TNF α could induce sprouting.

Endothelial cells in the HMVEC-fibrin assay secrete the main inhibitor of the

plasmin system PAI-1 [38], but it is unknown if all cells, only the quiescent cells in the monolayer or perhaps only the invading uPAR-rich cells secrete PAI-1. The classic work by Turing [105] and Gierer & Meinhardt [106] shows that periodic patterns form when an inhibitor and an activator are secreted by the same cell. This requires that the activator stimulates the production of the activator and the inhibitor, and that the inhibitor diffuses faster than the activator. The self-activation locally increases the activator's concentration and overcomes the inhibition, while neighboring areas are silenced by the diffusing inhibitor. Interestingly, our uPAR-plasmin-TGF β 1 positive feedback loop matches this system, as the positive feedback loop drives local activation of uPAR, and the inhibitor PAI-1 diffuses, whereas uPAR only moves small distances by cell movement. We currently assumed that all cells secrete PAI-1, but it is very well possible that the uPAR-rich cells secrete most PAI-1, because TGF β 1 induces production of uPAR as well as PAI-1 in MVEC cultured on Matrigel [90]. In conclusion, to determine whether activator-inhibitor dynamics play a role in pattern formation of ingrowth spots in the monolayer in the HMVEC-fibrin assay, the localization of PAI-1 secretion should be determined.

Besides the activator-inhibitor system, the closely related substrate-depletion model [106] is a well-studied mechanism for pattern formation. In our model, plasminogen is the substrate for plasmin production. Conversion of plasminogen at sites of matrix invasion results in depletion of plasminogen in surrounding regions by diffusion. In agreement, plasminogen is a limiting factor for angiogenesis in the HMVEC-fibrin assay [38]. Plasminogen depletion has low impact in the current model, because we initialize with a high, homogeneously spread concentration of immobile fibrin-bound plasminogen. However, plasminogen binds fibrin reversibly, thus this mechanism might influence the location of ingrowth spots for lower levels of fibrin-bound plasminogen. Interestingly, there is a delay of sprout initiation when the model initializes with unbound PLG. It takes some time to reach sufficiently high concentrations of fibrin-bound plasminogen, which is then converted to plasmin by uPAR for matrix degradation.

Another patterning mechanism that is involved in angiogenesis is lateral inhibition by Delta-Notch signaling [3, 21–23]. Cells that have high levels of Delta ligands on their membrane differentiate into so called 'tip cells', which are the leaders of sprouts, and cells with low levels of Delta become 'stalk cells' [23]. Lateral inhibition occurs by interaction of Delta ligands with the Notch receptor of neighboring cells, resulting in the suppression of Delta production in those neighbors [3, 21–23]. Lateral inhibition creates a pepper-and-salt pattern of tip and stalk cells, with tip cells surrounded by a rosette of stalk cells in monolayers *in silico* [44, 45]. The patterning of bristles in *Drosophila* epithelium becomes more sparse by Dll4-Notch signaling induced by long, dynamic filopodia that reach over several cell diameters in distance

[107]. However, the resulting pattern of bristles is still more fine-mazed and more regular than the observed pattern of uPAR-rich leader cells in the monolayer of the HMVEC-fibrin assay [80]. Thus, Delta-Notch signaling alone cannot account for this more widespread and irregular pattern. Possibly the involvement of another local regulation, such as our proposed uPAR-plasmin-TGF β 1 positive feedback loop, interferes with tip cell selection to make it more wide-spread. Notably, gene expression levels of Dll4 and Notch4 were significantly higher in endothelial cells cultured on LMW matrices than on HMW matrices [39]. The Dll4 and Notch4 expression differences by themselves cannot explain the reduced ingrowth on LMW, as specific inhibition of DLL4-Notch was unable to induce recovery of tube formation in LMW. In conclusion, local activation and lateral inhibition mechanisms might be involved in selection of ingrowth spots in the monolayer.

Furthermore, interference of Dll4-Notch signaling in the local degradation feedback loop could affect sprout morphology. In simulations of our current model, cells neighboring the leading tip cell are also somewhat activated by the released TGF β 1 and contribute to sprouting. This results in fairly wide, sometimes cyst-like sprouts. This is in agreement with results on sprout morphology from our previous model [75], in which we initialize with one predefined tip cell in the monolayer to model sprouting in the HMVEC-fibrin assay. Here, cyst-like sprouts also form when stalk cells contribute to matrix degradation, whereas narrow sprouts form when solely the tip cell secretes proteolytic enzymes for matrix degradation. We propose that one of the functions of lateral inhibition by Delta-Notch signaling could be to repress proteolytic activity of the stalk cells adjacent to the tip cell, such that only the tip cell degrades the matrix and thinner sprouts form.

Our model reproduces angiogenic sprouting by very simple sprouting dynamics, namely cell-fibrin adhesion and cell-division. However, the addition of TNF α in the *in vitro* model strongly inhibits cell division [38]. Many alternative mechanisms of cell migration and angiogenic sprouting have been proposed and are also tested *in silico*, such as haptotaxis towards higher concentrations of binding epitopes in fibrin [65], different forms of chemotaxis towards higher concentrations of growth factor [16, 63–66, 71], mechanotaxis towards higher regions of strains in the matrix [69], and preferential attraction to elongated structures [108]. Our model could be extended with such sprouting and cell migration mechanisms to replace cell division.

A detailed description of the plasminogen-plasmin system is included in our model, but still some simplifications were made. For instance, we did not take into account interactions with matrix metalloproteinases (MMPs). Membrane-type 1 metalloproteinase (MT1-MMP) can perform cell-associated fibrinolysis [88], but only plays a minor role in angiogenesis in the HMVEC-fibrin assay as the inhibitor TIMP-1 had only minor effects [89]. Furthermore, we neglected

the low proteolytic activity of pro-uPA [19], and only modeled active uPAR. Interactions between pro-uPA and plasmin could give some interesting dynamics. Venkatraman *et al.* [43] considered a positive feedback loop in which the initial cleavage of plasminogen into plasmin is more efficient by uPA than pro-uPA, and the conversion of pro-uPA to uPA is driven by plasmin. By the use of a cell-free model, they predict that uPA-plasmin activation is bistable in the presence of this positive feedback loop in combination with substrate competition for plasmin.

Our model predicts that the reduced level of angiogenesis on LMW compared to HMW fibrin could at least in part be explained by a reduced level of fibrin-bound latent-TGF β 1 in LMW. To validate this hypothesis, we propose to check if there is indeed a reduced level of fibrin-bound latent-TGF β 1 in LMW matrices in the *in vitro* HMVEC-fibrin assay. As a second experiment, we propose to validate whether angiogenesis can be reduced on HMW by addition of TGF β 1-antagonists. These validation experiments can bring us closer to a true understanding of the mechanisms that selects leader or 'tip cells' in the monolayer and consolidate sprouting in the HMVEC-fibrin assay.

2.4 Methods

We developed a hybrid, cell-based and continuum computational model of angiogenic sprouting to represent the *in vitro* HMVEC-fibrin assay (Figure 2.3). The model includes a uPAR-plasmin-TGF β 1 positive feedback loop that drives sprouting and is used to explain the reduced ingrowth on LMW compared to HMW. Cells and their physical interaction with fibrin are modeled with the cellular Potts model (CPM). The CPM is coupled to concentration fields to model the uPAR-plasmin-TGF β 1 positive feedback loop. Each cell has a concentration of uPAR, homogeneously spread on its membrane, modeled by an ordinary differential equation (ODE). A system of partial differential equations (PDEs) described the interactions between fibrin, plasminogen, plasmin, PAI-1 and TGF β 1.

2.4.1 Cellular Potts model

The model is initialized with a monolayer of fifty endothelial cells on top of a fibrin matrix and some medium on top (see Figure 2.8). These are enclosed by a border and a small immobile 'cell patch' is present in the border at the level of the monolayer, to mimic a continuous monolayer of cells.

The shape and motility of endothelial cells are modeled with the cellular Potts model (CPM) [61, 62]. The model domain is a two-dimensional, regular lattice $\Lambda \subset \mathbb{Z}^2$, with $\vec{x} \in \Lambda$ the coordinates in the lattice. Cells are projected on the lattice as patches of connected lattice sites. All lattice sites that belong to a cell are marked with the same unique identifier ($\sigma(\vec{x})$). Each identifier

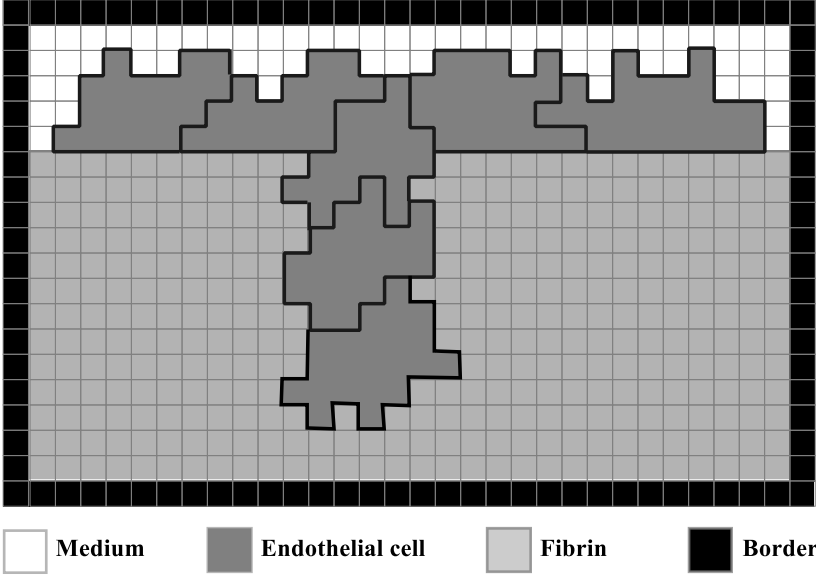


Figure 2.8: Schematic representation of the Cellular Potts model. The different colors depict the types defined in the computational model of the HMVEC-fibrin assay. A monolayer of endothelial cells is seeded on top of a fibrin matrix, with some medium on top. The modeling domain is surrounded with a border. Cells degrade fibrin, invade and form sprouts.

is associated with a type (τ), here $\tau = \{\text{cell, fibrin, cell patch, border, medium}\}$. Cells are motile, while fibrin, the border and the cell patch are static. Cells move by extending or retracting filopodia, modeled by copy attempts of the state (σ) of a randomly selected lattice site \vec{x} into a randomly selected adjacent (second neighbor order) lattice site \vec{x}' (see Figure 2.9). Whether such a copy attempt is accepted depends on the change of energy of the system (Hamiltonian) resulting from this copy. The Hamiltonian (H) of the system describes the forces resulting from cell behaviors and properties in the model. The cell behaviors and properties included in the model are cell adhesion, cell size, cell connectivity and fibrin invasion. A copy attempt is always accepted if it moves along a force and thus decreases the Hamiltonian. If a copy increases the Hamiltonian, the copy will be accepted according the Boltzmann probability function: $P_{\text{Boltzmann}}(H) = e^{-\frac{\Delta H}{\mu}}$, with μ representing active random membrane fluctuations. In one time step, a Monte Carlo step (MCS), as many copy attempts are performed as there are lattice sites in the lattice.

Cell adhesion. The energy resulting from adhesion is described as:

$$H_{\text{contact}} = \sum_{(\vec{x}, \vec{x}')} J(\tau(\sigma(\vec{x})), \tau(\sigma(\vec{x}'))(1 - \delta(\sigma(\vec{x}), \sigma(\vec{x}'))), \quad (2.1)$$

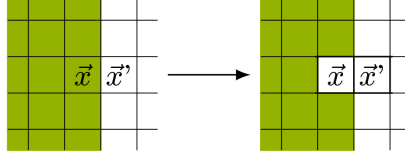


Figure 2.9: Graphical representation of a copy attempt. A random grid site (\vec{x}) is chosen to copy the state of a neighboring grid site (\vec{x}') to simulate pseudopod extensions and retractions.

in which adhesion is restricted to the cell membrane by the Kronecker delta ($\delta(x, y) = 1, x = y, 0, x \neq y$) and (\vec{x}, \vec{x}') represents the set of all neighboring lattice site pairs. Each type combination has an adhesion energy $J_{\tau, \tau'}$, with low values representing strong adhesion and high values weak adhesion or even repulsion.

Cell size. Cells have a preferred size (A) and deviation of their actual size (a) from this preferred size cost energy, following

$$H_{\text{size}} = \lambda_A(\sigma) \sum_{\sigma} (A(\sigma) - a(\sigma))^2, \quad (2.2)$$

with λ_A representing cell elasticity.

Fibrin invasion. To model fibrin invasion, we coupled the CPM to a system of coupled PDEs that describes all kinetic reactions involved in the uPAR-plasmin-TGF β 1 feedback loop that we propose in this chapter. The PDE concentration fields are discretized on the CPM lattice. The probability that a cell invades fibrin, thus performs an extending copy into fibrin, depends on the total concentration of fibrin at the invaded fibrin pixel ($f(\vec{x}')$). The total concentration of fibrin is the sum of all the PDE components that contain fibrin,

$$f(\vec{x}') = F(\vec{x}') + F_{\text{PLG}}(\vec{x}') + F_{\text{PLS}}(\vec{x}') + F_{\text{LTGF}}(\vec{x}') + F_{\text{PLG,LTGF}}(\vec{x}') + F_{\text{PLS,LTGF}}(\vec{x}'). \quad (2.3)$$

To model the physical obstruction of fibrin for cell invasion, a penalty of $H_{\text{invasion}} = \frac{1000}{1 + e^{f(\vec{x}') - 0.5}}$ is added if $f(\vec{x}') > 0.3$.

Mitosis. Every ten time steps, each cell has a probability (P_{mitosis}) to divide over its shortest axis if it is in little contact with other cell. More specifically, a cell may divide if $R_{\sigma} < R_{\text{mitosis}}$, with ($R_{\sigma} = \frac{\text{size membrane with cell-cell contact}}{\text{size total membrane}}$). The concentration of uPAR of the dividing cell is equally distributed over the daughter cells.

Model dimensions. The lattice size is $1000\mu\text{m} \times 300\mu\text{m}$, with each lattice site representing $2\mu\text{m} \times 2\mu\text{m}$. Sprouts fully develop in 6000 MCS in our model. Endothelial cells are cultured for 10 days in the HMVEC-fibrin assay [38], thus

2. Computational modeling of matrix invasion

a MCS is approximately 2.5 minutes. The parameter settings for the CPM are listed in Table 2.1. Except for cell size (A), the parameters of the cellular Potts model can only be quantitatively coupled to experimental data.

Table 2.1: Parameters CPM.

$A = 800 \mu m^2$	$\lambda_A = 100$	$\mu = 100$
$J_{\text{cell,Medium}} = 30$	$J_{\text{cell,cell}} = 15$	$J_{\text{fibrin,Medium}} = 120$
$J_{\text{cell,border}} = 1 \cdot 10^6$	$J_{\text{cell,fibrin}} = 75$	$H_{\text{connectivity}} = 1 \cdot 10^9$
$P_{\text{mitosis}} = 0.6$	$R_{\text{mitosis}} = 0.65$	$\Delta x = 2 \cdot 10^{-6} m$
lattice dimensions = $1000 \mu m \times 300 \mu m$		

2.4.2 Quantification of the angiogenesis level

The angiogenesis level simultaneously reflects sprout depth and sprout count. At the end of each simulation, the angiogenesis level is calculated as follows: 1) Ten equally distributed horizontal lines are drawn between 0 and 90 percent of initial fibrin matrix height. 2) For each line, the number of connected components consisting of cells or medium within fibrin are counted. Only the components larger than one cell size (20 lattice sites) and smaller than the complete line are counted. A component as large as the complete line would resemble lowering of the complete monolayer rather than sprouting. 3) The count of the ten lines is averaged.

2.4.3 Plasminogen-plasmin system and uPAR-plasmin-TGF β 1 positive feedback

The plasminogen-plasmin system in this model is based on the cell-free model by Diamond & Anand [95]. We made some changes to make it suitable for our question, most importantly we include the uPAR-plasmin-TGF β 1 positive feedback, simplified the implementation of fibrinolysis, and removed blood flow. Figure 2.10 shows an overview of the binding and conversion reactions of plasminogen and latent-TGF β 1 in relation to fibrin that are included in our model. In this section we will discuss the reactions in Figure 2.10 to explain the PDE system that describes the plasminogen-plasmin system and the uPAR-plasmin-TGF β 1 positive feedback loop.

2.4.4 Latent-TGF β 1 and plasminogen bind fibrin

Plasminogen (PLG) reversibly binds fibrin (F), forming fibrin-bound plasminogen (F_{PLG}). This reaction (reaction 1A in Figure 2.10) has a forward rate k_{f1} and a reverse rate k_{r1} . Similarly, the reversible binding of latent-TGF β 1 ($LTGF$)

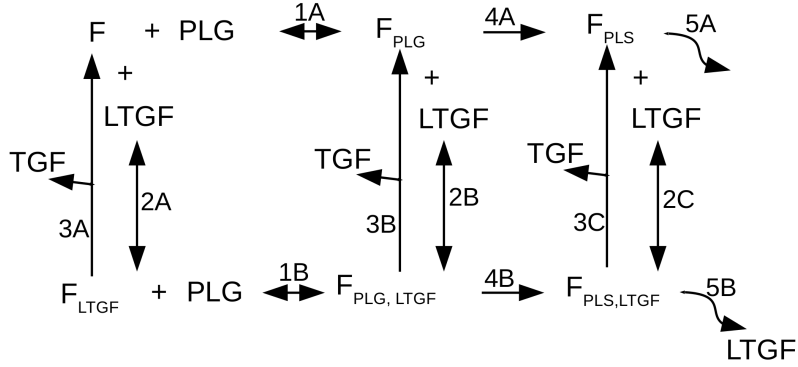


Figure 2.10: Overview of the binding and conversion reactions of plasminogen and latent-TGF β 1 in relation to fibrin. Plasminogen (PLG) and latent-TGF β 1 ($LTGF$) do not compete for binding with fibrin, thus fibrin can be unbound (F), bound solely by plasminogen (F_{PLG}), bound by solely latent-TGF β 1 (F_{LTGF}), or by both ($F_{PLG,LTGF}$). Plasminogen reversible binds fibrin (reactions 1A and 1B). Latent-TGF β 1 also reversible binds fibrin (reactions 2A, 2B, and 2C). Latent-TGF β 1 is released from fibrin by plasmin into the active form (TGF , reactions 3A, 3B, and 3C). Fibrin-bound plasminogen can be converted to fibrin-bound plasmin, either without (F_{PLS} , reaction 4A) or with ($F_{PLS,LTGF}$, reaction 4B) co-binding of latent-TGF β 1. Reactions 5A and 5B represent fibrinolysis, which can result in the release of latent-TGF β 1 (reaction 5B).

to fibrin (reaction 2A) depends on a forward rate k_{f2} and a reverse rate k_{r2} . $LTGF$ that is bound to fibrin (F_{LTGF}) can be released and activated by plasmin-mediated proteolytic activity, resulting in active TGF β 1 and free fibrin (reaction 3A). This reaction follows Michaelis Menten kinetics with constants k_{u2} and k_{m2} . The change in concentration of fibrin depends on $PLG - Fibrin$ binding (1A), $LTGF - Fibrin$ binding (2A) and release of TGF (3A), following:

$$\frac{\partial F}{\partial t} = \underbrace{-PLG * F * k_{f1} + F_{PLG} * k_{r1}}_{PLG-Fibrin binding (1A)} + \underbrace{F_{LTGF} * k_{r2} - LTGF * F * k_{f2}}_{LTGF-Fibrin binding (2A)} + \underbrace{\frac{F_{LTGF} * (F_{PLS} + F_{PLS,LTGF}) * k_{u2}}{k_{m2} + F_{LTGF}}}_{Release TGF (3A)} \quad (2.4)$$

We assume that plasminogen and latent-TGF β 1 do not compete with each other for the binding sites in fibrin. Consequently, the rates of the reversible binding reaction of PLG to fibrin are equal to the rates for PLG binding to fibrin to which $LTGF$ is bound (F_{LTGF}), thus reactions 1A and 1B in Figure

2. Computational modeling of matrix invasion

2.10 have the same rate constants. Plasminogen binding to F_{LTGF} forms $F_{PLG,LTGF}$ (reaction 1B). PLG diffuses with diffusion coefficient D_{PLG} and decays with rate ϵ_{PLG} . The change in concentration of plasminogen depends on $PLG - Fibrin$ binding (1A), $PLG - F_{LTGF}$ binding (1B), and its diffusion and decay, following:

$$\frac{\partial PLG}{\partial t} = \underbrace{D_{PLG} \nabla^2 PLG}_{\text{Diffusion}} - \underbrace{\epsilon_{PLG} PLG}_{\text{Decay}} + \underbrace{F_{PLG} * k_{r1} - PLG * F * k_{f1}}_{\text{PLG-Fibrin binding (1A)}} + \underbrace{F_{PLG,LTGF} * k_{r1} - PLG * F_{LTGF} * k_{f1}}_{\text{PLG-F}_{LTGF} \text{ binding (1B)}} \quad (2.5)$$

Similarly, the reversible binding of $LTGF$ to fibrin has equal rates for fibrin to which plasminogen or plasmin is bound, F_{PLG} and F_{PLS} respectively. Thus, reactions 2A, 2B and 2C in Figure 2.10 have the same rate constants. Unbound $LTGF$ diffuses with diffusion coefficient D_{LTGF} and decays with rate ϵ_{LTGF} . $LTGF$ is released from the matrix upon plasmin-mediated fibrinolysis (reaction 5B), modeled with a Hill equation with constant d . The change in concentration of latent-TGF β 1 depends on $LTGF - Fibrin$ binding (2A), $LTGF - F_{PLG}$ binding (2B), $LTGF - F_{PLS}$ binding (2C), release of $LTGF$ (5B), and its diffusion and decay, following:

$$\begin{aligned} \frac{\partial LTGF}{\partial t} = & \underbrace{D_{LTGF} \nabla^2 LTGF}_{\text{Diffusion}} - \underbrace{\epsilon_{LTGF} LTGF}_{\text{Decay}} + \underbrace{F_{LTGF} * k_{r2} - LTGF * F * k_{f2}}_{\text{LTGF-Fibrin binding (2A)}} + \\ & \underbrace{F_{PLG,LTGF} * k_{r2} - LTGF * F_{PLG} * k_{f2}}_{\text{LTGF-F}_{PLG} \text{ binding (2B)}} + \underbrace{\frac{F_{PLS,LTGF}^2}{d + F_{PLS,LTGF}^2}}_{\text{Release LTGF (5B)}} + \\ & \underbrace{F_{PLS,LTGF} * k_{r2} - LTGF * F_{PLS} * k_{f2}}_{\text{LTGF-F}_{PLS} \text{ binding (2C)}} \end{aligned} \quad (2.6)$$

The change in concentration of fibrin-bound latent-TGF β 1 depends on $PLG - F_{LTGF}$ binding (1B), $LTGF - Fibrin$ binding (2A), release of TGF (3A), and its decay, following:

$$\begin{aligned} \frac{\partial F_{LTGF}}{\partial t} = & - \underbrace{\epsilon_{LTGF} F_{LTGF}}_{\text{Decay}} + \underbrace{F_{PLG,LTGF} * k_{r1} - PLG * F_{LTGF} * k_{f1}}_{\text{PLG-F}_{LTGF} \text{ binding (1B)}} + \\ & \underbrace{LTGF * F * k_{f2} - F_{LTGF} * k_{r2}}_{\text{LTGF-Fibrin binding (2A)}} - \underbrace{\frac{F_{LTGF} * (F_{PLS} + F_{PLS,LTGF}) * k_{\mu 2}}{k_{m2} + F_{LTGF}}}_{\text{Release TGF (3A)}} \end{aligned} \quad (2.7)$$

2.4.5 Plasminogen conversion into plasmin

Fibrin-bound plasminogen (F_{PLG}) can be converted to fibrin-bound plasmin (F_{PLS}). This conversion (reaction 4A) occurs in proximity of uPAR, modeled by Michaelis Menten kinetics with rate constants k_{u1} and k_{m1} . To express the proximity of uPAR, the concentration of uPAR at a certain pixel is calculated by taking the average concentration of uPAR of that pixel and of its second neighboring pixels (together forming the set of pixels $NB(\sigma)$), resulting in $U = \langle uPAR_{\sigma} \rangle_{NB(\sigma)}$. The change in concentration of fibrin-bound plasminogen depends on $PLG - Fibrin$ binding (1A), $LTGF - F_{PLG}$ binding (2B), plasmin activation (4A), release of TGF (3B) and its decay, following:

$$\frac{\partial F_{PLG}}{\partial t} = \underbrace{PLG * F * k_{f1} - F_{PLG} * k_{r1}}_{PLG-Fibrin binding (1A)} - \underbrace{\frac{F_{PLG} * U * k_{u1}}{k_{m1} + F_{PLG}}}_{Plasmin activation (4A)} + \underbrace{F_{PLG,LTGF} * k_{r2} - LTGF * F_{PLG} * k_{f2}}_{LTGF-F_{PLG} binding (2B)} - \underbrace{\epsilon_{F_{PLG}} F_{PLG}}_{Decay} + \underbrace{\frac{F_{PLG,LTGF} * (F_{PLS} + F_{PLS,LTGF}) * k_{u2}}{k_{m2} + F_{PLG,LTGF}}}_{Release TGF (3B)} \quad (2.8)$$

The change in concentration of $F_{PLG,LTGF}$ depends on $PLG - F_{LTGF}$ binding (1B), $LTGF - F_{PLG}$ binding (2B), plasmin activation (4B), release of TGF (3B) and its decay, following:

$$\frac{\partial F_{PLG,LTGF}}{\partial t} = - \underbrace{\epsilon_{F_{PLG,LTGF}} F_{PLG,LTGF}}_{Decay} + \underbrace{PLG * F_{LTGF} * k_{f1} - F_{PLG,LTGF} * k_{r1}}_{PLG-F_{LTGF} binding (1B)} + \underbrace{LTGF * F_{PLG} * k_{f2} - F_{PLG,LTGF} * k_{r2}}_{LTGF-F_{PLG} binding (2B)} - \underbrace{\frac{F_{PLG,LTGF} * U * k_{u1}}{k_{m1} + F_{PLG,LTGF}}}_{Plasmin activation (4B)} - \underbrace{\frac{F_{PLG,LTGF} * (F_{PLS} + F_{PLS,LTGF}) * k_{u2}}{k_{m2} + F_{PLG,LTGF}}}_{Release TGF (3B)} \quad (2.9)$$

2.4.6 Plasmin activity

Fibrin-bound plasminogen is converted to fibrin-bound plasmin by uPAR. F_{PLS} is the conversion product of F_{PLG} (reaction 4A), and $F_{PLS,LTGF}$ is the conversion product of $F_{PLG,LTGF}$ (reaction 4B). To model fibrinolysis, F_{PLS} (reaction 5A) and $F_{PLS,LTGF}$ (reaction 5B) are degraded, modeled with a Hill equation with constant d . The change in concentration of F_{PLS} depends on plasmin activation (4A), fibrinolysis (5A), $LTGF - F_{PLS}$ binding (2C), release of TGF (3C),

2. Computational modeling of matrix invasion

and its decay, following:

$$\begin{aligned}
 \frac{\partial F_{\text{PLS}}}{\partial t} = & \underbrace{-\epsilon_{F_{\text{PLS}}} F_{\text{PLS}}}_{\text{Decay}} + \underbrace{\frac{F_{\text{PLG}} * U * k_{u1}}{k_{m1} + F_{\text{PLG}}}}_{\text{Plasmin activation (4A)}} - \underbrace{\frac{F_{\text{PLS}}^2}{d + F_{\text{PLS}}^2}}_{\text{Fibrinolysis (5A)}} + \quad (2.10) \\
 & \underbrace{F_{\text{PLS,LTGF}} * k_{r2} - LTGF * F_{\text{PLS}} * k_{f2}}_{\text{LTGF-F}_{\text{PLS}} \text{ binding (2C)}} + \\
 & \underbrace{\frac{F_{\text{PLS,LTGF}} * (F_{\text{PLS}} + F_{\text{PLS,LTGF}}) * k_{u2}}{k_{m2} + F_{\text{PLS,LTGF}}}}_{\text{Release TGF (3C)}}
 \end{aligned}$$

The change in concentration of $F_{\text{PLS,LTGF}}$ depends on plasmin activation (4B), fibrinolysis (5B), $LTGF - F_{\text{PLS}}$ binding (2C), release of TGF (3C), and its decay, following:

$$\begin{aligned}
 \frac{\partial F_{\text{PLS,LTGF}}}{\partial t} = & \underbrace{\frac{F_{\text{PLG,LTGF}} * U * k_{u1}}{k_{m1} + F_{\text{PLG,LTGF}}}}_{\text{Plasmin activation (4B)}} + \underbrace{LTGF * F_{\text{PLS}} * k_{f2} - F_{\text{PLS,LTGF}} * k_{r2}}_{\text{LTGF-F}_{\text{PLS}} \text{ binding (2C)}} - \quad (2.11) \\
 & \underbrace{\frac{F_{\text{PLS,LTGF}}^2}{d + F_{\text{PLS,LTGF}}^2}}_{\text{Fibrinolysis (5B)}} - \underbrace{\frac{F_{\text{PLS,LTGF}} * (F_{\text{PLS}} + F_{\text{PLS,LTGF}}) * k_{u2}}{k_{m2} + F_{\text{PLS,LTGF}}}}_{\text{Release TGF (3C)}} - \\
 & \underbrace{\epsilon_{F_{\text{PLS,LTGF}}} F_{\text{PLS,LTGF}}}_{\text{Decay}}
 \end{aligned}$$

2.4.7 TGF β 1 activation

Plasmin can release and activate latent-TGF β 1, resulting in active TGF β 1 (TGF) that diffuses with diffusion coefficient D_{TGF} and decays with rate ϵ_{TGF} . TGF can originate from each form of fibrin-bound latent-TGF β 1 (F_{LTGF} , $F_{\text{PLG,LTGF}}$ and $F_{\text{PLS,LTGF}}$), released by plasmin following Michaelis Menten kinetics with constants k_{u2} and k_{m2} . The change in concentration of TGF depends on release of TGF (3A, 3B, and 3C), and its diffusion and decay, following:

$$\begin{aligned}
\frac{\partial TGF}{\partial t} = & \overbrace{D_{TGF} \nabla^2 TGF}^{\text{Diffusion}} - \overbrace{\epsilon_{TGF} TGF}^{\text{Decay}} + \overbrace{\frac{F_{LTGF} * (F_{PLS} + F_{PLS,LTGF}) * k_{u2}}{k_{m2} + F_{LTGF}}}_{\text{Release TGF (3A)}} + \\
& \overbrace{\frac{F_{PLG,LTGF} * (F_{PLS} + F_{PLS,LTGF}) * k_{u2}}{k_{m2} + F_{PLG,LTGF}}}_{\text{Release TGF (3B)}} + \\
& \overbrace{\frac{F_{PLS,LTGF} * (F_{PLS} + F_{PLS,LTGF}) * k_{u2}}{k_{m2} + F_{PLS,LTGF}}}_{\text{Release TGF (3C)}}
\end{aligned} \tag{2.12}$$

2.4.8 uPAR and PAI-1

Each cell has an individual concentration of uPAR with a constant production rate (c), a decay rate (ϵ_{uPAR}), a $TGF\beta 1$ -dependent production and a PAI-1 dependent internalization. For the $TGF\beta 1$ -dependent production, the total amount of TGF on all membrane pixels of a cell (P_σ) is summed and this total amount of TGF upregulates the uPAR production with Michaelis Menten kinetics, using constants k_{u3} and k_{m3} . Cells secrete PAI-1 (PAI) with rate α . PAI-1 binds uPAR for inactivation, resulting in a depletion of PAI and $uPAR$ with rate k_{f3} . For this purpose the concentration of PAI is calculated over all cell pixels (C_σ). PAI diffuses with diffusion coefficient D_{PAI} and decays with rate ϵ_{PAI} . The change in concentration of PAI depends on its internalization when bound to uPAR, its secretion, and its diffusion and decay, following:

$$\begin{aligned}
\frac{\partial PAI}{\partial t} = & - \sum_{\sigma=1}^n \overbrace{(uPAR_\sigma * PAI * k_{f3})}^{\text{Internalization}} - \overbrace{\epsilon_{PAI} PAI}^{\text{Decay}} + \overbrace{\alpha 1_{\tau(x)=\text{cell}}}_{\text{Secretion}} + \overbrace{D_{PAI} \nabla^2 PAI}^{\text{Diffusion}}
\end{aligned} \tag{2.13}$$

The concentration of $uPAR$ is homogeneously spread over the cell membrane and is continuously updated to the location of the cell. It decays with rate ϵ_{uPAR} . The change in concentration of $uPAR$ depends on its internalization when bound to PAI , a constant production, a TGF -induced production and its

decay, following:

$$\begin{aligned}
 \frac{\partial uPAR_\sigma}{\partial t} = & \underbrace{- \sum_{i \in C_\sigma} (uPAR_\sigma * PAI(i) * k_{f3})}_{\text{Internalization}} - \underbrace{\epsilon_{uPAR} uPAR_\sigma}_{\text{Decay}} + \\
 & \underbrace{c}_{\text{Constant production}} + \underbrace{\frac{k_{u3} (\sum_{j \in P_\sigma} TGF(j))^2}{k_{m3} + (\sum_{j \in P_\sigma} TGF(j))^2}}_{\text{TGF-induced uPAR production}} \forall \sigma \in 1, \dots, 50
 \end{aligned}
 \tag{2.14}$$

2.4.9 Numerical solution

The uPAR concentration per cell is solved numerically once every MCS, with $\Delta x = 2 \cdot 10^{-6} m$ and $\Delta t = 150 s$, and all other concentration fields are solved ten times per MCS, using an explicit finite-difference scheme. The quantitative values of the parameters involved in the plasminogen-plasmin system and uPAR-plasmin-TGF β 1 positive feedback loop are experimentally not known. We manually looked for a set of parameter values for which only a few cells in the monolayer initialized sprouting. We subsequently studied the sensitivity of the model to changes in the parameter values in Sections 2.2.2 and 2.2.3. The parameter settings for the kinetic reactions are listed in Table 2.2.

We initialize the model with a readily fibrin-bound concentration of latent-TGF β 1 and plasminogen, by setting the initial concentration $I_{F_{PLG,LTGF}}=1$ at every lattice site of type fibrin. All other concentrations are relative to this concentration level, expressed in relative units (RU). For the model validation experiments, we either reduced the level of plasminogen or of latent-TGF β 1 in the fibrin matrix and kept the other constant, by reducing the initial concentration of $I_{F_{PLG,LTGF}}$ and increasing the concentration of $I_{F_{LTGF}}$ or $I_{F_{PLG}}$ respectively.

Table 2.2: Parameter settings kinetics. The concentration of all proteins is expressed in relative units (RU) and one MCS represents approximately 2.5 minutes.

$I_{F_{PLG,LTGF}} = 1 \text{ RU}$	$\epsilon_{F_{PLG}} = 1 \cdot 10^{-4} \text{ MCS}^{-1}$
$I_{uPAR} = 1 \text{ RU}$	$\epsilon_{F_{PLS}} = 1 \cdot 10^{-4} \text{ MCS}^{-1}$
$\alpha = 0.01 \text{ RU/MCS}^{-1}$	$\epsilon_{F_{LTGF}} = 1 \cdot 10^{-4} \text{ MCS}^{-1}$
$D_{PLG} = 5 \cdot 10^{-12} \text{ m}^2/\text{MCS}$	$\epsilon_{F_{PLG,LTGF}} = 1 \cdot 10^{-4} \text{ MCS}^{-1}$
$D_{LTGF} = 5 \cdot 10^{-12} \text{ m}^2/\text{MCS}$	$\epsilon_{F_{PLS,LTGF}} = 1 \cdot 10^{-4} \text{ MCS}^{-1}$
$D_{TGF} = 5 \cdot 10^{-12} \text{ m}^2/\text{MCS}$	$\epsilon_{PAI} = 1 \cdot 10^{-2} \text{ MCS}^{-1}$
$k_{m1} = 1 \text{ RU}$	$\epsilon_{uPAR} = 9.5 \cdot 10^{-3} \text{ MCS}^{-1}$
$k_{m2} = 1.1 \text{ RU}$	$\epsilon_{PLG} = 1 \cdot 10^{-3} \text{ MCS}^{-1}$
$k_{m3} = 8 \text{ RU}$	$\epsilon_{LTGF} = 1 \cdot 10^{-3} \text{ MCS}^{-1}$
$c = 5 \cdot 10^{-3} \text{ s}^{-1} \text{ RU/MCS}^{-1}$	$\epsilon_{TGF} = 5 \cdot 10^{-2} \text{ MCS}^{-1}$
$k_f1 = 1 \cdot 10^{-2} \text{ MCS}^{-1} \text{ RU}^{-1}$	$k_u1 = 1 \text{ MCS}^{-1}$
$k_f2 = 1 \cdot 10^{-2} \text{ MCS}^{-1} \text{ RU}^{-1}$	$k_u2 = 0.8 \text{ MCS}^{-1}$
$k_f3 = 1 \cdot 10^{-2} \text{ MCS}^{-1} \text{ RU}^{-1}$	$k_u3 = 0.85 \text{ MCS}^{-1}$
$k_r1 = 1 \cdot 10^{-4} \text{ MCS}^{-1}$	$d = 4 \cdot 10^{-2} \text{ RU}^2$
$k_r2 = 1 \cdot 10^{-8} \text{ MCS}^{-1}$	

2.A Supplementary movies

An archive containing all supplementary movies can be found at

<http://persistent-identifier.org/?identifier=urn:nbn:nl:ui:18-23531>.

Movie S1 Sprouting by the uPAR-plasmin-TGF β 1 positive feedback. This movie shows the selection of ingrowth spots in the endothelial cell monolayer and further sprouting due to the uPAR-plasmin-TGF β 1 positive feedback in a simulation with default parameter settings. The movie is divided in four panels. The top left panel shows the CPM representation of cells (blue) and fibrin (yellow). The top right panel shows the concentration of uPAR in the cells. The bottom left frame shows the concentration of active TGF β 1 and the bottom right panel shows the concentration of PAI-1. Protein concentrations are colored according a color bar, with red indicating the highest concentration in the current field and blue the lowest concentration.

3

Tip cell overtaking occurs as a side effect of sprouting in computational models of angiogenesis

This chapter is based on:

Sonja E. M. Boas and Roeland M.H. Merks, *Tip cell overtaking occurs as a side effect of sprouting in computational models of angiogenesis*. BMC Systems Biology (in press) arXiv:1507.06230

Abstract

During angiogenesis, the formation of new blood vessels from existing ones, endothelial cells differentiate into tip and stalk cells, after which one tip cell leads the sprout. More recently, this picture has changed. It has become clear that endothelial cells compete for the tip position during angiogenesis: a phenomenon named tip cell overtaking. The biological function of tip cell overtaking is not yet known. From experimental observations, it is unclear to what extent tip cell overtaking is a side effect of sprouting or to what extent it is regulated through a VEGF-Dll4-Notch signaling network and thus might have a biological function. To address this question, we studied tip cell overtaking in computational models of angiogenic sprouting in absence and in presence of VEGF-Dll4-Notch signaling.

We looked for tip cell overtaking in two existing cellular Potts models of angiogenesis. In these simulation models angiogenic sprouting-like behavior emerges from a small set of plausible cell behaviors. In the first model, cells aggregate through contact-inhibited chemotaxis. In the second model the endothelial cells assume an elongated shape and aggregate through (non-inhibited) chemotaxis. In both these sprouting models the endothelial cells spontaneously migrate forwards and backwards within sprouts, suggesting that tip cell overtaking might occur as a side effect of sprouting. In accordance with other experimental observations, in our simulations the cells' tendency to occupy the tip position can be regulated when two cell lines with different levels of *Vegfr2* expression are contributing to sprouting (mosaic sprouting assay), where cell behavior is regulated by a simple VEGF-Dll4-Notch signaling network.

Our modeling results suggest that tip cell overtaking can occur spontaneously due to the stochastic motion of cells during sprouting. Thus, tip cell overtaking and sprouting dynamics may be interdependent and should be studied and interpreted in combination. VEGF-Dll4-Notch can regulate the ability of cells to occupy the tip cell position in our simulations. We propose that the function of VEGF-Dll4-Notch signaling might not be to regulate which cell ends up at the tip, but to assure that the cell that randomly ends up at the tip position acquires the tip cell phenotype.

3.1 Introduction

Angiogenesis is a complex process that involves interactions of endothelial cells with their environment as well as interactions between the cells. The previous chapter (Chapter 2) focused on the interactions of cells with the environment, specifically the extracellular matrix, and gave insights in how proteolytic degradation of the matrix by the cells influences sprouting. This chapter focuses on the interactions between the endothelial cells during sprouting.

Oxygen deprived regions, such as wounds and growing tumors, stimulate the sprouting of side branches from nearby vessels by the secretion of growth factors [1]. These growth factors activate quiescent endothelial cells in the nearby vessels, which differentiate into one of two alternative fates: a 'tip cell' or a 'stalk cell' [3, 21, 22]. Tip cells are the initiators and leaders of new sprouts, while stalk cells form the body of the new sprout. Activated endothelial cells compete for the tip cell fate through lateral inhibition by Dll4-Notch signaling, a process called tip cell selection [3, 21, 22]. In this process, tip cells present Dll4 ligands on their membrane to activate Notch receptors of their neighbors. Upon Notch activation, the Notch-intracellular domain (NICD) is cleaved off and travels to the nucleus for transcription of Notch target genes. Eventually, cells with low Notch activity (low Notch/high Dll4) become tip cells and cells with high Notch activity (high Notch/low Dll4) become stalk cells. Previous work assumed that the tip cell at the sprout front maintained its leader position during sprouting [3]. More recently, Jakobsson *et al.* [24] and Arima *et al.* [25] showed independently that cells compete for the tip position of sprouts during angiogenesis, a phenomenon named tip cell overtaking [24, 25]. The biological relevance of tip cell overtaking is not yet clear. In this chapter we use computational modeling to study if tip cell overtaking is merely a side effect of sprouting, or if it is regulated by intercellular signaling and thus likely has a regulatory function in sprouting.

Jakobsson *et al.* [24] and Arima *et al.* [25] both observed tip cell overtaking in sprouting assays, but they interpret their data differently with respect to the driving mechanism of tip cell overtaking. Using genetic mosaic sprouting assays, Jakobsson *et al.* [24] found that cells with relatively high levels of *Vegfr2* expression or relatively low levels of *Vegfr1* expression are more likely to end up at the tip position in a Notch-dependent fashion, suggesting that the competitive potential of cells to take up the tip position is regulated by the signaling networks consisting of VEGF, Dll4 and Notch. VEGF influences tip cell selection by inducing Dll4 production upon VEGFR2 activation [109]. Notch activation in neighboring cells down-regulates *Vegfr2* expression [110]. Using this signaling network, computational modeling by Jakobsson *et al.* [24] suggested that tip cell overtaking is regulated by Notch activity. In a follow-up model, Bentley *et al.* [60] studied the role of cell-cell adhesion and junctional reshuffling, using a variant of the cellular Potts Model, allowing cells to crawl along one another within a preformed cylindrical hollow sprout. By comparing different combinations of mechanisms, their modeling results suggested a more detailed regulatory mechanism for tip cell overtaking: 1) VEGFR2 signaling causes endocytosis of VE-cadherin, which reduces cell-cell adhesion. 2) Notch activity decreases extension of polarized actomyosin protrusions towards the sprout tip. Thus, these results suggest that Dll4-Notch and VEGF signaling strongly regulate tip cell overtaking.

3. Computational modeling of tip cell overtaking

In apparent contradiction with this interpretation, Arima *et al.* [25] found that tip cell overtake rates were not affected by addition of VEGF or by inhibition of Dll4-Notch signaling, although other measures of sprouting kinetics were influenced, e.g. sprout extension rate and cell velocity. Arima *et al.* [25] presented extensive cell tracking data of cell movement and position during angiogenic sprouting and found that individual ECs migrate forwards and backwards within the sprout at different velocities, leading to cell mixing and overtaking of the tip position. Thus, tip cell overtaking might arise spontaneously from collective cell behavior driving angiogenic sprouting.

To help interpret these results, we first studied to what extent tip cell overtaking occurs in existing computational models, without making any additional assumptions (Figure 3.1A). Although the exact cellular mechanisms driving angiogenesis are still incompletely understood, a range of computational models has been proposed each representing an alternative, often related mechanism [111, 112]. In absence of a definitive sprouting model, we compared two previous cellular Potts models [63, 64]. In the first model, the cells secrete a chemical signal that attracts surrounding cells via chemotaxis. Portions of the membrane in contact with adjacent cells become insensitive to the chemoattractant [64]. The model forms sprouts of one or two cell diameters thickness (Figure 3.2A and 3.2C). The second model hypothesizes that non-inhibited chemotaxis suffices to form angiogenesis-like sprouts, if the cells have an elongated shape [63] (Figure 3.2B and 3.2D).

As a second step, we studied how Dll4-Notch and *Vegfr2* expression can bias cells to the tip position in these sprouting models (Figure 3.1B). We introduced a modified existing model of the VEGF-Dll4-Notch signaling network [45] into each simulated cell, and asked to what extent such molecular signaling can fine-regulate tip cell overtaking.

3.2 Results

3.2.1 Spontaneous tip cell overtaking in computational models of angiogenic sprouting

To study if tip cell overtaking can arise spontaneously as a side effect of sprouting, we used two computational models in which sprouts form autonomously, in absence of any type of tip cell selection or regulation. We will briefly introduce both models here, referring to the Method Section 3.5.1 and previous publications [63, 64] for detail. Both models consider a restricted set of cell behaviors to explain the autonomous growth of angiogenic sprouts from an initial spheroid of endothelial cells.

Both models assume that endothelial cells attract one another via a secreted, diffusive, short-lived chemical signal, forming exponential chemoattraction gradients, e.g., via isoforms of VEGF diffusing over one to few cell

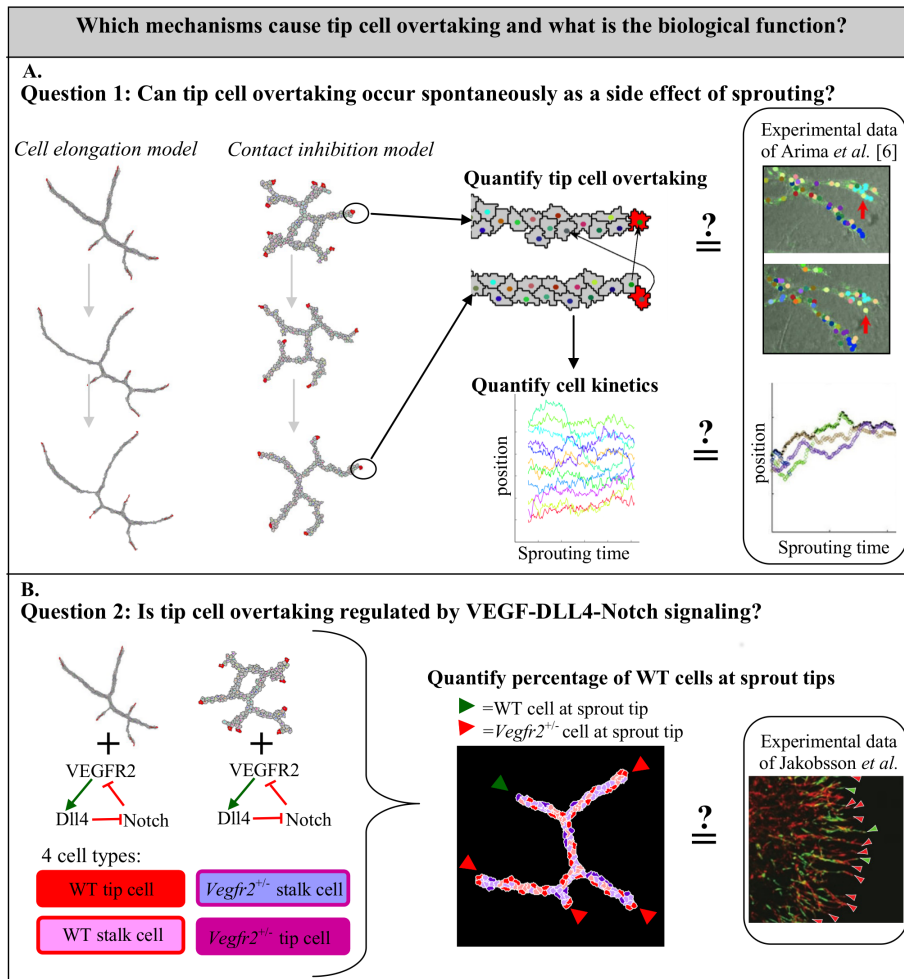


Figure 3.1: Overview of the workflow. We studied the biological relevance and the driving mechanisms of tip cell overtaking. (A) As a first step, we asked whether tip cell overtaking can be a side effect of sprouting. We studied tip cell overtaking in two computational models of angiogenic sprouting (the contact inhibition model and cell the elongation model), with different sprouting dynamics. We quantified tip cell overtaking and cell kinetics during simulations of these models and compared the results with similar *in vitro* experiments of Arima *et al.* [25]. (B) As a next step, we asked if tip cell overtaking can be regulated by VEGF-Dll4-Notch signaling. We added a VEGF-Dll4-Notch signaling network to each cell in the two models of angiogenic sprouting. Simulations are initialized with spheroids that contain a mix of wild type (WT) cells and *Vegfr2*^{+/-} cells. Due to signaling, cells can switch between four phenotypes during sprouting: WT tip cell, WT stalk cell, *Vegfr2*^{+/-} tip cell, and *Vegfr2*^{+/-} stalk cell. At the end of the simulations we quantified the percentage of sprout tips that were occupied by WT cells and compared the simulation results to experimental results of Jakobsson *et al.* [24].

3. Computational modeling of tip cell overtaking

diameters. This assumption produces aggregates of endothelial cells [63, 64, 113], but it will form networks of cells with an additional assumption. The 'contact inhibition model' [64] (Figure 3.2A), additionally proposes that chemotaxis is inhibited at cell-cell interfaces, i.e., they only chemotact at cell-extracellular matrix interfaces. The effect might be due to VE-cadherin-signaling, with VE-cadherins interacting locally with VEGFR2 [114]. The 'cell elongation model' [63] (Figure 3.2B) showed that the elongated shape of endothelial cells suffices for network formation. In variants of this model cells attract one another via weak cell-cell adhesion [72] or via a longer range potential [54].

In order for VEGF to serve as an attraction signal, its diffusion coefficient must be sufficiently low or the degradation rate sufficiently high so it can form gradients with a diffusion length of one to a couple of cell diameters. This contradicts with VEGF's role as a long-range cue guiding blood vessels over longer distances; e.g., hypoxic tumors can attract over distances up to 2-3 mm [115]. A recent model [71, 116] and experimental observations [116] suggest that secreted VEGF accumulates close to the endothelial cells and colocalizes with fibronectin and heparin sulfate proteoglycan. Thus although the diffusion length of soluble VEGF is longer than what was assumed in these computational models, binding to the extracellular matrix may strongly reduce the diffusion rate of VEGF and create much shorter gradients of ECM-bound VEGF near the endothelial cells. This role of VEGF as a short-range attractive signal differs from the role of VEGF as a long range guidance cue. For the purpose of this paper, chemo-attraction is considered representative for other potential attraction mechanisms including cell-cell adhesion [72, 108] or mechanotransduction via the extracellular matrix [69, 117]. The insights do not depend on the precise mechanism of the attractive forces between endothelial cells.

Spontaneous tip cell overtaking occurs in both models as a side effect of sprouting. Figure 3.2C shows an example of tip cell overtaking in the contact inhibition model. The cell labeled with a green dot overtakes the cell labeled with a gray dot. Figure 3.2D shows an example of a tip cell overtake in the cell elongation model, where the cell labeled with a purple dot overtakes the cell labeled with a pink dot. In our recent model of mechanical cell-cell communication via the extracellular matrix [69], tip cell overtaking rarely occurred; we therefore did not study tip cell overtaking in this model.

3.2.2 Quantification of tip cell overtaking

To quantify tip cell overtaking during sprouting in the contact inhibition model and in the cell elongation model, we first identified the cell on the sprouting tip, 'the leader cell'. The leader cell of each sprout is identified at each time step (Monte Carlo Step, MCS) of the simulations, using an automated method

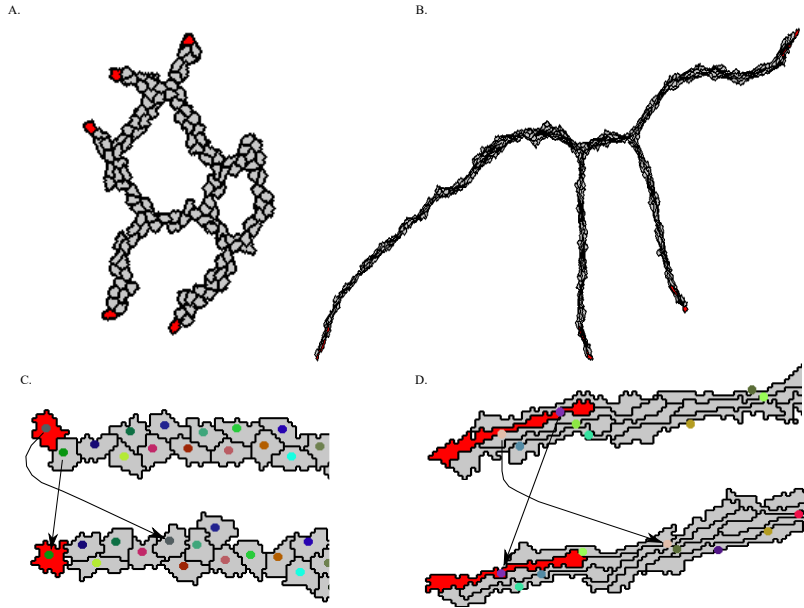


Figure 3.2: Leader identification and tip cell overtaking in the contact inhibition and cell elongation model. Sprouts formed from a spheroid in 30000 MCS by (A) the contact inhibition model and by (B) the cell elongation model. Red cells at the sprout tips indicate the identified leader cells. Tip cell overtaking occurs in the (C) contact inhibition model as well as in (D) the cell elongation model. Two images of the same sprouts are shown for each model, with the lower sprout being at a later time point than the upper sprout. The center of mass is depicted with a colored dot for each cell and the displacement of the leader cells in time is visualized with the arrows. The mean tip cell overtake rate per sprout, calculated over 15 independent stochastic simulations, is $0.67 (\pm 1.32)$ overtakes per 20000 MCS for the contact inhibition model and $4.59 (\pm 5.24)$ overtakes per 20000 MCS for the cell elongation model.

(see Method Section 3.5.2). Figure 3.2A and 3.2B show a vascular network formed by the contact inhibition model and the cell elongation model with the leader cells colored in red. Tracking of the leader cells allowed us to identify overtaking events. We define a tip cell overtake as the replacement of a leader cell by a neighboring cell. To prevent overestimates of tip cell overtake events due to the short-lived, random cell protrusions that the Cellular Potts describes, an overtake is counted only if both the leader cell and the overtaking neighboring cell have been present at the tip position for at least 80 consecutive MCS. Assuming that 1 MCS corresponds to thirty seconds, we thus count overtake events lasting for longer than forty minutes.

To quantify the frequency of tip cell overtaking, the mean overtake rate per

3. Computational modeling of tip cell overtaking

sprout of a simulation was calculated by dividing the number of overtakes within each sprout by the total number of sprouts present in the simulation between MCS 10000 and 30000; i.e. over a period of 7 days with the assumed time scaling of 1 MCS = 30 s. The calculation started from MCS 10000, since sprouts are then well formed from the initial spheroid and the overtake rate was averaged over fifteen independent simulations with the reference parameter settings. Within the time period of 7 days we identified on average 0.67 ± 1.32 overtake events in the contact inhibition model. Within the same simulated interval, we identified on average 4.59 ± 5.24 overtakes in the cell elongation model. Thus, the average tip cell overtake rate for the cell elongation model is significantly higher than for the contact inhibition model ($p=0.0089$ using an unpaired t-test). There are two explanations for the higher tip cell overtake rate in the cell elongation model compared to the contact inhibition model. First, in the cell elongation model, aligned elongated cells in a multi-cellular sprout tip can easily slide past another to overtake the tip position, whereas in the contact-inhibition model cells must pass one another completely to establish a tip cell overtake. Second, sprouts in the cell elongation model have longer life-times. In the contact inhibition model sprouts often fuse by anastomosis, resulting in sprouts with short life-times and often lacking a tip cell overtake.

In addition to the tip cell overtake frequency per sprout, we measured the average life-time of tip cells in sprouts for both models. In the contact inhibition model tip cells persist on average for 442 ± 361 minutes and in the cell elongation model on average for 1372 ± 1417 minutes. Interestingly, the cell elongation model has a higher tip cell overtake frequency in combination with a higher tip cell duration compared to the contact inhibition model. This can be explained by the shorter life-time of sprouts in the contact inhibition model due to frequent anastomosis, thereby often producing short-lived sprouts (and tip cells) not associated with tip cell overtake events. The tip cell overtake rates found in our models of around one per 7 hours to one per 23 hours are of the same order as those observed in experiments [24, 25]. Arima *et al.* [25] measured an interval of approximately 6 to 15 hours for the overtaking of tip cells and Jakobsson *et al.* [24] measured an interval of 3.7 hours, but note that this similarity between model and experiment depends on our choice of the time scaling of the cellular Potts model (CPM).

The mean tip cell overtake rate in both models is robust to changes in parameter values of most of the main parameters of the models (Figure S1 and S2). In the contact inhibition model however, the tip cell overtake rate is sensitive to the level of cell-cell adhesion. In summary, these results show that tip cell overtake events can occur in both models based on intrinsic cell behaviors as a side effect of sprouting, in absence of Dll4-Notch signaling or other molecular regulation.

3.2.3 Simulations suggest that sprouting drives cell mixing and tip cell overtaking

Jakobsson *et al.* [24] and Arima *et al.* [25] have both tracked cell movement during sprouting and showed that individual cells migrate forwards and backwards in sprouts, resulting in shuffling of cells within the sprout, called cell mixing. In this light, tip cell overtaking could be seen as cell mixing specifically at the tip of the sprout. We therefore studied if cell mixing occurred spontaneously in the sprouts formed in the contact inhibition model and in the cell elongation model. Figure 3.2C and 3.2D already showed that cell mixing occurs in both models, as the leader cells in the first time frame are both overtaken and subsequently migrate backwards in the sprout. Supplementary movies **Movie S1** and **Movie S2** show tip cell overtakes in time for the contact inhibition model and for the elongation model, respectively. To study cell mixing in more detail, Arima *et al.* [25] used time-lapse microscopy to track the position of each cell in a sprout over time and quantified their movements. They proposed a range of measures, including: *coordination* (angle between the direction of cell movement and the direction of sprout elongation) and *directional motility* (percentage of cells moving anterograde or retrograde).

We performed an identical analysis for the contact inhibition model and the cell elongation model. A sprout is defined as the leading cell together with its ten nearest neighbors in the same sprout (see Methods Section 3.5.3). Figure 3.3A-C show the position of cells relative to the axis of elongation (see Methods Section 3.5.3) of a sprout in time, for an experiment by Arima *et al.* [25] (Figure 3.3A), for the contact inhibition model (Figure 3.3B) and for the cell elongation model (Figure 3.3C). The cell with the highest positional index represents the tip cell. Overtakes of tip cells can be seen in figures 3.3A-C, as each figure contains at least one intersection of a line representing the position of a competing cell with the line that represents the position of the overtaken tip cell. Additionally, each figure shows cells migrating forwards and backwards (cell mixing) within the sprout. For example, the leader cell in the contact inhibition model at 400 minutes of sprouting time migrates backwards in the sprout as indicated by the decrease in position of this cell in Figure 3.3B, with five cells in front of it at 1600 minutes.

Forward and backward movement is expressed by *coordination*, defined as the average angle (θ) of cell movement with the sprout elongation axis measured each 20 MCS. Figure 3.3D shows the standard deviation of the pooled time series of $\frac{\theta}{\pi}$ for anterograde moving cells and Figure 3.3E for retrograde moving cells, showing similar values for experimental and computational results. Similar to *directional motility* in the experimental observations, the majority of the cells is moving forwards ($\frac{\theta}{\pi}$) or backwards in both models (Figure 3.3F). Only a small portion of the cells is not moving, this 'stopped' cell

3. Computational modeling of tip cell overtaking

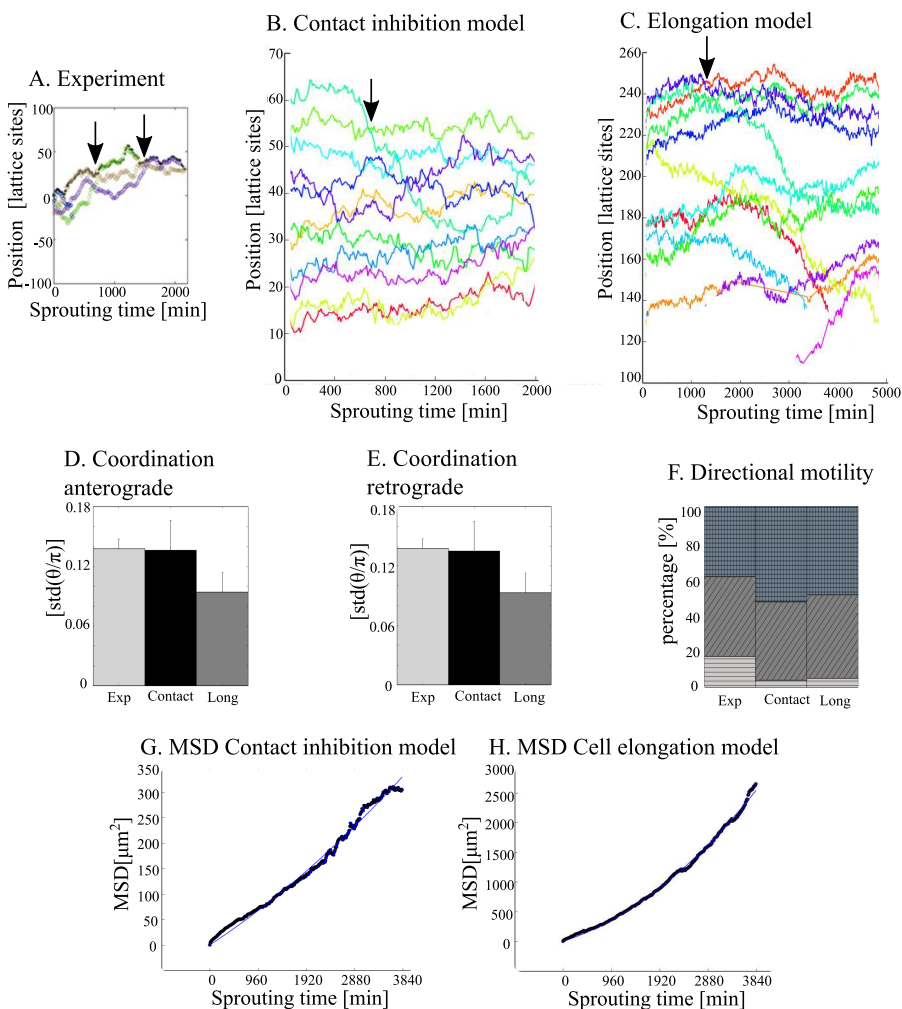


Figure 3.3: Analysis of cell migration within sprouts. The position of each cell is orthogonally projected onto the sprout elongation axis and plotted against sprouting time in minutes for (A) a sprout in a murine aortic ring assay (Figure A is adapted from [25]), (B) in the contact inhibition model and (C) in the cell elongation model; arrows indicate tip cell overtake events. The standard deviation $\text{std}(\frac{\theta}{\pi})$ is given for (D) anterograde moving cells ($\theta < \frac{\pi}{2}$) and (E) retrograde moving cells ($\theta > \frac{\pi}{2}$) for the experimental observations by Arima *et al.* [25] (exp), for the contact inhibition model (contact) and for the cell elongation model (long). (F) Directional motility represents the percentage of cells moving anterograde (blocked pattern), retrograde (diagonal striped pattern) or stopped (horizontally striped pattern). Mean square displacement (MSD) of cells, calculated by the projection of the center of mass on the sprout elongation axis, plotted against sprouting time for (G) the contact inhibition model and for (H) the cell elongation model. The fluent blue line represents the fitted curve following: $MSD = 2Dt + (\nu t)^2$, with D the dispersion coefficient and ν the sprout elongation velocity.

fraction is smaller in the models than in the experiments, indicating that cells in the model are a bit more motile than in the experiments.

Inspired by the notion of cell mixing, we asked whether cell movement during sprouting follows a random walk along the sprouting axis. For this purpose, the centers of mass of the cells were tracked during sprouting and projected on the sprout elongation axis (see Methods Section 3.5.3). Figure 3.3G and Figure 3.3H show the one-dimensional mean square displacement of cells during sprouting in the contact inhibition model and in the cell elongation model, respectively. From the MSD over sprouting time, one can derive that cells move by a biased random walk during sprouting, with a dispersion coefficient of $0.0021 \pm 1.2 * 10^{-5} \mu\text{m}^2/\text{s}$ in the contact inhibition model and of $0.0086 \pm 5.1 * 10^{-5} \mu\text{m}^2/\text{s}$ in the cell elongation model (see Methods Section 3.5.3). The dispersion coefficient for cells in the cell elongation model is slightly overestimated since small protrusions by an elongated cell can cause a large position change for its center of mass.

In summary, these results show that all cells in the sprouts behave as random walkers, moving forwards and backwards along the sprout, resulting in cell mixing. Cell mixing also occurs at the tip of the sprout, leading to tip cell overtaking. This passive cell mixing is in line with the experimental observations of Arima *et al.* [25] and Jakobsson *et al.* [24], and arises spontaneously in our models as a side effect of sprouting, without any regulation by Dll4-Notch and VEGF signaling.

We next set out to investigate if Dll4-Notch and VEGF signaling can fine-tune tip cell overtaking in our models when cells have different levels of *Vegfr2* expression. As a first step, we will include Dll4-Notch signaling in our models and study how collective cell behavior during sprouting affects Dll4-Notch patterning (Section 3.2.4). Subsequently, VEGF signaling is incorporated in the models and simulations will be performed for spheroids that contain a mix of cells with differential levels of *Vegfr2* expression (Section 3.2.5).

3.2.4 Branching, anastomosis and tip cell overtaking affect Dll4-Notch expression

To study if Dll4-Notch signaling can influence the random tip cell overtaking that we observed in our models, we incorporated a model of the Dll4-Notch signaling network into each of the endothelial cells into both the contact-inhibition and cell elongation models. In this section, we examined how patterning of Dll4 (determining the tip cell phenotype) changes during sprouting, more specifically during branching, anastomosis and tip cell overtaking. To focus on the effect that the local sprout morphology might have on Dll4 patterning, in the simulations presented in this section tip and stalk cells have the same cell behavior, independent of Dll4-Notch activity. In the next section, we will consider differential behavior between tip and stalk cells.

3. Computational modeling of tip cell overtaking

The Dll4-Notch model was based on an ordinary-differential equation (ODE) model proposed by Sprinzak *et al.* [45]. Endothelial cells present Notch receptors and Dll4 ligands on their membranes [3, 21, 22]. Upon cell-cell contact, Dll4 ligands activate Notch receptors of neighboring cells through trans-signaling. This activation results in cleavage of Notch and the release of its intracellular domain (NICD). NICD subsequently inhibits the production of Dll4. Notch receptors and Dll4 ligands can also interact and deactivate one another on the same cell, a mechanism that is known as cis-inhibition [45]. To model Dll4-Notch signaling in each cell, each endothelial cell in the model has its own set of ODEs describing the concentration of Dll4, Notch and NICD. To make the level of trans-signaling dependent of the amount of cell-cell contact, the fraction of Dll4 and Notch that a cell presents to an adjacent cell is proportional to the fraction of the cell's membrane that is in contact with it. Cells are assumed to switch between the tip and stalk phenotype when passing a NICD activity threshold: if the NICD level is below the threshold, cells differentiate into tip cells, otherwise they differentiate into stalk cells. The NICD threshold is unknown experimentally; we therefore estimated it such that a salt-and-pepper pattern of alternating tip and stalk cells was formed in agreement with experimental observations [23, 24]. For details on the implementation of tip cell selection, see section 3.5.4.

Figures 3.4A and 3.4B show that, in agreement with experiments [23, 24], in our models Dll4-Notch signaling generates a checkerboard-like patterning of Dll4. In Figure 3.4, cells are colored according to a color map, with red representing high levels of Dll4 (tip cells) and blue low levels (stalk cells and extracellular matrix). Also in line with experimental observations [23, 24], cells at the tip position frequently show high concentrations of Dll4. This phenomenon is due to the tip cells' low levels of cell-cell contact with adjacent cells, resulting in a low stimulation of their Notch receptors and, consequently Dll4 production is not inhibited.

Figures 3.4C-K visualize Dll4-patterning during branching, anastomosis and tip cell overtaking in a simulation of the contact inhibition model, and similar patterns can be seen for the cell elongation model in Figure S3. During branching, new buds are formed and develop over time into growing sprouts, and the leading cell acquires the tip cell phenotype (Figures 3.4C-E). Figures 3.4F-H show anastomosis of two sprouts that are led by tip cells. Once the two sprouts meet, they fuse and the two tip cells compete for survival of their tip cell phenotype. Tip cell overtaking is visualized in Figures 3.4I-K, in which the cell annotated with a star overtakes the cell annotated with a square and subsequently acquires the tip cell phenotype itself. In summary, branching, anastomosis and tip cell overtaking induce switching of tip and stalk fates in our models, depending on the relative position, shape and cell-cell contact of the cells in the sprouts.

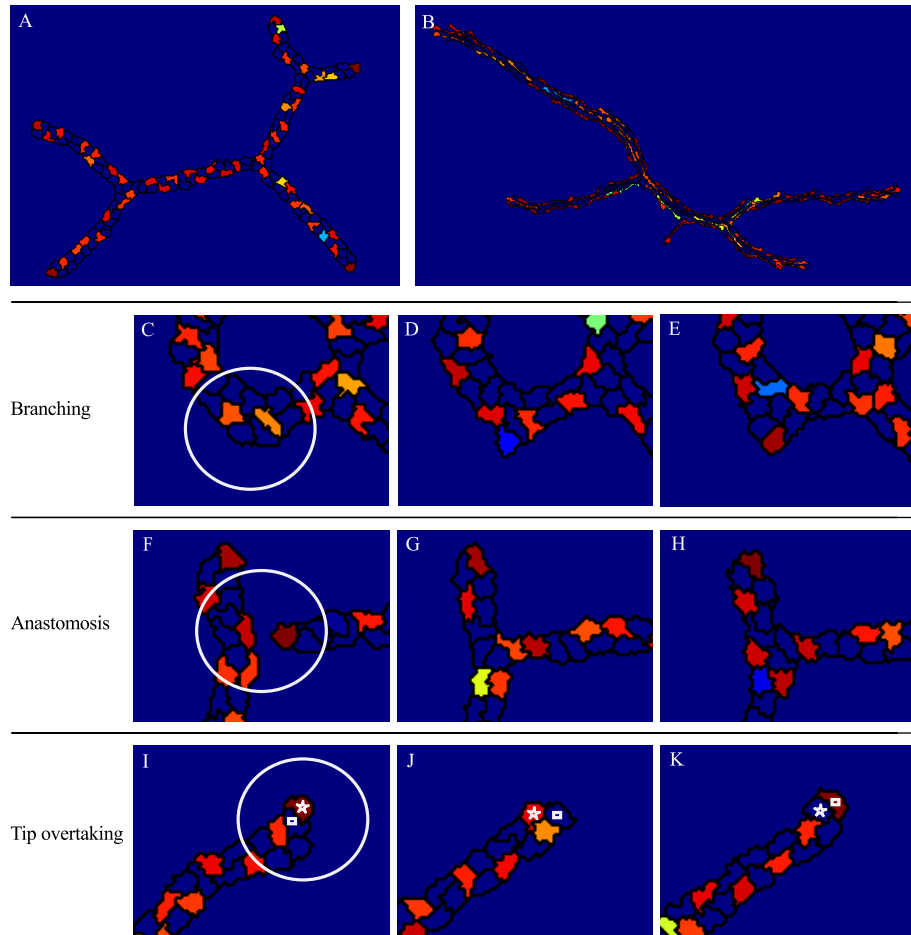


Figure 3.4: Dll4 patterning by tip cell selection. (A) Checkerboard-like patterning of tip and stalk cells in a simulation of the contact inhibition model. The red color indicates high levels of Dll4 (tip cells) and blue indicates low levels of Dll4. (B) Checkerboard-like patterning of tip and stalk cells in a simulation of the cell elongation model. Figures C-J are images from a simulation of the contact inhibition model. (C-E) Enlarged view of a sprout in which branching occurs over time, at the location of the white circle in panel C. (F-H) Enlarged view of two fusing sprouts (anastomosis) in time, indicated by the white circle in panel F. (I-K) Enlarged view of a sprout in which tip cell overtaking occurs in time at the location of the white circle in panel I. The cell annotated with a square overtakes the tip cell position from the cell annotated with a star.

3.2.5 Effect of VEGF and Dll4-Notch on tip cell overtaking

Our modeling results suggest that tip cell overtaking can occur spontaneously and in absence of Dll4-Notch and VEGF signaling. We next asked how, in our models, Dll4-Notch and VEGF signaling could regulate tip cell overtaking. Jakobsson *et al.* [24] showed in a mosaic sprouting assay using mouse embryonic stem cells that VEGF sensitive cells (wild type, WT) have a higher probability to occupy the tip position than relatively insensitive cells (*Vegfr2* haploid cells, *Vegfr2*^{+/-}). After ten days of sprouting, the WT cells occupied 87%, 60% and 40% of the sprout tips when mixed in a 1:1, 1:4 and 1:9 ratio of WT:*Vegfr2*^{+/-} cells, respectively. Which mechanisms underlie the increased probability of VEGF sensitive cells to occupy the tip position? We asked whether regulation of cell behavior by VEGF-Dll4-Notch signaling can make VEGF sensitive cells move to the leading position of the sprout.

To address this question, we included a simple model of VEGF signaling into our models: VEGFR2 activation up-regulates Dll4 production, and NICD down-regulates VEGFR2 production [60, 109, 110] (see Section 3.5.5). *Vegfr2* haploids have half of the VEGFR2 production capacity and therefore have a lower VEGFR2 activity than WT cells. In the *in vitro* experiments of Arima *et al.* [25] and Jakobsson *et al.* [24], VEGF was added uniformly to the growth medium. In our simulation we therefore assumed a uniform field of external VEGF. For simplicity, we will assume in this section that the secreted chemical in the model does not interfere with the external VEGF concentration; i.e. the attractive force is mediated by another chemoattractant (e.g., CXCL12 [118]), by another VEGF-isoform, or even by another means than by chemotaxis (e.g., mechanotaxis [69]).

Tip and stalk cells differ in their behavior, regardless of their genotype. For example, tip cells are more motile than stalk cells and have more VEGF-A-sensitive filopodia, whereas stalk cells proliferate in response to VEGF-A [3]. Tip and stalk cells differentially express genes involved in cell signaling, cell motility and proliferation [119]. We therefore asked which set of differential tip and stalk cell behaviors could cause WT cells to occupy the tip position more often than *Vegfr2* haploids. We first tested if a reduced cell adhesion capacity of tip cells compared to stalk cells can cause VEGF sensitive cells to become sprout leaders, as VEGFR2 activity can cause endocytosis of VE-cadherins and thereby reduce the cell adhesion capacity [120]. To reduce cell adhesion of tip cells in our models, we set the adhesion parameters (J) as follows (with higher values of J giving lower adhesion): $J_{\text{stalk,stalk}}=0.2$, $J_{\text{tip,tip}}=0.8$, $J_{\text{stalk,tip}}=0.8$, $J_{\text{ECM,stalk}}=1$, $J_{\text{ECM,tip}}=1$. In the contact inhibition model, 93% of the sprout tips in thirty independent simulations were occupied by WT cells for a WT:*Vegfr2*^{+/-} ratio of 1:1, 49% for a ratio of 1:4 and 27% for a ratio of 1:9 (Table 3.1). The results of the 1:1 ratio match the experimental results by Jakobsson *et al.* [24]. WT cells that are located near a sprout tip prefer to be-

come the sprout leader, as the leader cell position has relatively few cell-cell contacts (Figure 3.5A). The percentages for the lower ratios differ more from the experimental results, because the probability that a WT cell is located near the sprout tip is lower when there are less WT cells in the mix. In this case, WT tip cells manage to go to the outer surface of the sprout, but do not always reach the sprout tip position. In the cell elongation model, the number of WT cells at the sprout tip positions was not significantly different from the number of WT cells at the sprout tips in case of random cell mixing (Table 3.1). In the cell elongation model, sprout tips often have multiple elongated cells next to each other and a large part of the membrane of the leader cell is in contact with neighboring cells (Figure 3.5B). The leader cell has much more cell-cell contacts than cells at the sides of the sprout, making it unfavorable for WT tip cells with reduced cell-cell adhesion strengths to become the leader cell in such multi-cellular sprout tips.

Next, we asked if WT cells would more frequently occupy the tip position if the chemoattractant sensitivity differs between tip and stalk cells. Palm *et al.* [67] showed that reduced sensitivity to the chemoattractant increased the potential of a cell to reach the tip position in the contact inhibition model. To further test this hypothesis in our system, we made tip cells less sensitive to the chemoattractant than stalk cells ($\lambda_c=5$ for tip cells and $\lambda_c=10$ for stalk cells), whereas the adhesion energies of tip and stalk cells were set to the same values ($J_{\text{stalk,stalk}}=0.4$, $J_{\text{tip,tip}}=0.4$, $J_{\text{stalk,tip}}=0.4$, $J_{\text{ECM,stalk}}=0.6$, $J_{\text{tip,ECM}}=0.6$). Indeed, a reduced sensitivity of tip cells to the chemoattractant compared to stalk cells allowed WT cells to occupy the sprout tip more often than *Vegfr2* haploid cells in the contact inhibition model (ratio WT:*Vegfr2*^{+/-} 1:1 gives a WT tip occupancy of 87%, ratio 1:4 gives 53% and 1:9 gives 34%; Table 3.1). WT cells are more prone to reach the sprout tip position than *Vegfr2* haploids in the contact inhibition model, because WT cells are less sensitive to the chemoattractant of which the concentration is higher in the sprout center than at the sprout tip as it is secreted by the cells themselves. WT cells do not dominate the tip position in the cell elongation model as strongly as in the contact inhibition model (Table 3.1). However, the percentage of WT cells at the sprout tips in the cell elongation model is significantly higher than the percentage that would be expected from random cell-mixing. The reduced dominance of WT cells at the sprout tips in the cell elongation model can be explained by the multi-cellular composition of the sprout tips (Figure 3.5B), as WT cells with a high sensitivity to the chemoattractant are only weakly stimulated to migrate to the tip position in this configuration due to a small difference in concentration of the chemoattractant at the sprout center compared to at the sprout tip.

Thus in our models differential cell behavior of tip and stalk cells can make WT cells occupy the tip position more frequently than *Vegfr2* haploids. In our

3. Computational modeling of tip cell overtaking

Table 3.1: Sprout tip occupancy by WT cells. Overview of the percentile sprout tip occupancy by WT cells. WT occupancy was quantified for different initial WT:*Vegfr2*^{+/-} mixing ratios in experiments [24] (Experiment), in the contact inhibition model (Contact) and in the cell elongation model (Long). The WT:*Vegfr2*^{+/-} mixing ratios were 1:1, 1:4 and 1:9, resulting in a WT percentage of 50, 20 and 10 respectively. Two different mechanisms are tested in the models: differential adhesion between tip and stalk cells and differential sensitivity to an auto-secreted chemoattractant between tip and stalk cells. The p-values represent the probability that the total number of simulated sprouts were occupied by at least the indicated percentage of WT cells when assuming only random motion (calculated with a binomial distribution, with n the number of sprouts, k the number of sprouts occupied by WT cells, and p the mixing ratio).

WT percentage	Exp	Differential adhesion		Differential sensitivity to chemoattractant	
		Contact	Long	Contact	Long
50	87	93 ($p=6.7 \cdot 10^{-16}$)	48 ($p=0.73$)	87 ($p < 1 \cdot 10^{-16}$)	64 ($p=6.2 \cdot 10^{-4}$)
20	60	49 ($p=7.7 \cdot 10^{-16}$)	18 ($p=0.75$)	53 ($p < 1 \cdot 10^{-16}$)	25 ($p=3.6 \cdot 10^{-2}$)
10	40	27 ($p=6.9 \cdot 10^{-9}$)	11 ($p=0.33$)	34 ($p < 1 \cdot 10^{-16}$)	22 ($p=7.2 \cdot 10^{-8}$)

model, the behavior of *Vegfr2* haploid tip and stalk cells was assumed identical to the behavior of WT tip and stalk cells. What then causes WT tip cells to be overrepresented at the sprout tip relative to *Vegfr2* haploid tip cells? A potential explanation is that WT more easily differentiate to tip cells than *Vegfr2* haploid, due to the higher levels of VEGFR2 and Dll4 in WT cells [24]. To test this possibility, we quantified the number of WT cells and *Vegfr2* haploid cells in the entire cell population (not only at sprout tips) that differentiated into tip cells. Indeed, in our models WT cells are more likely to become tip cell than *Vegfr2* haploids when mixed in a 1:1 ratio and in presence of VEGF. At the end of a simulation of the contact inhibition model, 59 percent of all the WT cells in the population had differentiated into tip cells compared to only 20 percent of the *Vegfr2* haploid cells (percentages measured over n=30 simulations). In the cell elongation model, 49 percent of all the WT cells differentiated into tip cells compared to 29 percent of all the *Vegfr2* haploid cells. In conclusion, in our model WT cells have a higher probability to differentiate into the tip cell phenotype than *Vegfr2* haploids as a result of the interactions between VEGFR2 signaling and Dll4-Notch signaling. As a consequence, the tip cells that end up at the tip were more likely to derive from WT cells than from *Vegfr2* haploids.

To study if an external gradient of VEGF can affect tip cell overtaking differently than a homogeneous VEGF field, we also performed simulations with the contact inhibition model with differential cell-cell adhesion for tip and stalk cells in the presence of an external VEGF gradient. We only let tip cells chemo-

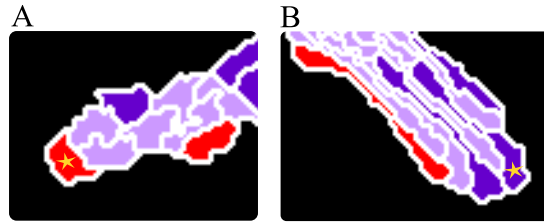


Figure 3.5: Relative cell positions at sprout tips. Enlarged view of a sprout tip in a simulation of (A) the contact inhibition model and of (B) the cell elongation model. WT tip cells are colored red, *Vegfr2* haploid tip cells dark purple and *Vegfr2* stalk cells light purple. The leader cells of the sprouts are marked with yellow stars. The leader cell in the contact inhibition model has relatively little cell-cell contact compared to other cells in the sprout, while the leader cell in the cell elongation model is in contact with other cells for a large part of its membrane due to the multi-cellular composition of the sprout tip.

tact towards VEGF to simulate the most extreme advantage for tip cells. The presence of a VEGF gradient rather than a uniform VEGF field did not significantly change the mean tip cell overtake frequency in sprouts (Figure S2), the sprout tip occupancy by WT versus *Vegfr2*^{+/-} cells (Table S1) or the cell trajectory analysis results (Table S2). Once VEGFR2 is stimulated by VEGF, lateral inhibition by Dll4-Notch signaling quickly generates a comparable alternating tip-stalk pattern as in the presence of a uniform VEGF field.

In conclusion, simulation results of the contact inhibition model suggest that VEGF-Dll4-Notch signaling might tune which cells end up at the sprout tip position when cells have different levels of *Vegfr2* expression. To make this possible tip and stalk cells must behave differently, such as differential cell-cell adhesion or differential sensitivity to an attractant. Interestingly, in the cell elongation model *Vegfr2* expression did not significantly affect the ability of cells to reach the tip cells position. The multi-cellular sprout tip environment is unfavorable for cells with such cell behaviors, suggesting that sprout morphology can affect the regulation by VEGF and Dll4-Notch signaling in tip cell overtaking.

3.3 Discussion

Our simulation results show that the collective cell behavior responsible for *in silico* angiogenesis-like sprouting produces cell mixing and tip cell overtaking dynamics in accordance with published measurements [25]. The contact inhibition model as well as the cell elongation model reproduced the experimental results of Arima *et al.* [25], who found that tip and stalk cells mix at sprout tips. Our modeling results thus show that tip cell overtaking can occur

3. Computational modeling of tip cell overtaking

as a *side effect* of sprouting and might not be necessarily functional.

In disagreement with this conclusion but in agreement with Jakobsson *et al.* [24], in the contact inhibition model the activity of the VEGF-Dll4-Notch signaling network affected the competitiveness of cells for the tip cell position. A possible interpretation is that tip cell overtaking is genetically regulated, implying that tip cell overtaking must be functional. Jakobsson *et al.* [24] proposed that tip cell overtaking allowed for the most VEGF sensitive cell to become the leader cell at all times to optimally respond to VEGF in the environment. Alternatively, based on our modeling results that suggest that tip cell overtaking occurs as a side effect of sprouting, we propose that the VEGF-Dll4-Notch signaling network makes the cell in the tip position cross-differentiate into a tip cell. Here the VEGF-Dll4-Notch signaling network would act to protect the growing sprout against the loss of a tip cell at the sprout front due to random cell mixing. In this interpretation tip cell overtaking would be a purely random side effect of sprouting and be non-functional in itself.

Our simulations also suggest that the morphology of the sprout tip might be important to tip cell overtaking. The sprout tip position was less favorable for tip cells with reduced cell-cell adhesion or reduced sensitivity to the chemoattractant in the cell elongation model: sprouts in the cell elongation model consist of multiple cells parallel to one another, whereas in the contact inhibition model (and in many actual angiogenic sprouts) only one cell leads the sprouts.

Bentley *et al.* [60] assume in their model that long-range cell movements during cell mixing are driven by Notch/VEGFR-regulated differential dynamics of VE-cadherin junctions. Their simulations suggest that the observations by Jakobsson *et al.* [24] are best reproduced when tip cells have a reduced cell-cell adhesion compared to stalk cells, and are more polarized than stalk cells, preferentially extending protrusions towards the sprout tip. In contrast to the results by Bentley *et al.*, in our simulations, cell mixing occurs spontaneously without any assumptions on differential adhesion or polarization. This discrepancy could be caused by a difference in the models. Whereas in the model of Bentley *et al.* [60] cells can only migrate relative to a static sprout, in our models sprout formation emerges from the assumptions on cell behavior. In simulations with the contact inhibition model, differential cell-cell adhesion between tip and stalk suffices to reproduce the results by Jakobsson *et al.* [24]. Because sprout extension biases cell movement towards the tip, we do not require explicit tip-directed cell polarization.

Although the contact inhibition variant of our model best reproduced the experimental observations on tip cell overtaking, our previous motivation for assuming contact inhibition of chemotaxis is inconsistent with the present model. We previously assumed that contact-dependent phosphorylation of VEGFR2 by VE-cadherin mediates contact inhibition of chemotaxis [64, 114].

Recent work showed that VEGFR2 activity internalizes VE-cadherins [120]. If this mechanism were implemented in our model, high VEGFR2 activity in the tip cells would internalize VE-cadherins and reduce the strength of VE-cadherin-mediated contact inhibition. The chemotactic sensitivity to VEGF in these tip cells would thus increase and tip cells would move towards the center of the sprouts, inconsistent with biological observations. Potential fixes for this experimental discrepancy include (a) the possibility that cells do not aggregate via VEGF, but via another chemoattractant or attractive forces, or (b) to consider matrix-bound VEGF [71, 116] in our models, which would only be available at the periphery of the spheroids.

By what mechanisms are cells driven forwards and backwards along sprouts? Apart from the random cell motility the Cellular Potts model describes, the chemoattractant gradients seem to play a key role in our model. The models predict that the concentration of chemoattractant will be higher in the center of the sprout than at the flanks, and higher in concave regions of the sprout surface than at convex regions. Cells in the center of the sprout are, therefore, constrained by the gradient, whereas a compressive force towards the center of the sprout pushes the cells forwards. Cells on the flank of the sprout sense a shallower gradient and are therefore more motile, allowing them to walk backwards along the sprout towards the high concentration of the chemoattractant at concave branch points. Experimentally, it will be interesting to validate this hypothesis by comparing the relative position of cells in the sprout to the migration direction within the sprout. Besides by a chemoattractant, the attractive force could be caused by other biological mechanisms, such as mechanical strains in the extracellular matrix [69] or signaling through long filopodia [107]. In our ongoing research we are investigating whether forward and backward motion indeed requires a chemotactic gradient or if it can also be driven by other mechanisms such as cell-cell adhesion [72] or mechanotransduction via the ECM [69].

3.4 Conclusions

Tip cell overtaking has been studied in different experimental setups [24, 25], but the biological function is still unknown. We asked whether tip cell overtaking is merely a side effect of sprouting or whether it is regulated through a VEGF-Dll4-Notch signaling network, and thus might be functional. For this purpose, we studied two existing computational models of angiogenic sprouting, allowing us to study the effect of sprouting dynamics on tip cell overtaking. In our models, cells spontaneously move back and forth along the sprout as a side effect of the sprouting mechanisms, as was seen in experiments of Arima *et al.* [25]. This suggests that tip cell overtaking and sprouting dynamics may be interdependent and, therefore, should be studied and interpreted in com-

ination.

In experiments with mosaic endothelial spheroids [24], it was found that wild type cells have a competitive advantage over *Vegfr2* haploid cells for the tip cell position, suggesting that VEGF-Dll4-Notch signaling regulates tip cell overtaking. In agreement with these experiments, in one of our models the wild type cells also end up at the tip position more frequently than *Vegfr2* haploids, simply because the wild type cells more often differentiate into tip cells. This would suggest that VEGF-Dll4-Notch signaling can regulate tip cell overtaking. Based on the model results that tip cell overtaking is a *non-functional side effect* of sprouting, we suggest an alternative function for VEGF-Dll4-Notch signaling: Rather than regulating which cell ends up at the tip, it might assure that the cell that randomly ends up at the tip position acquires the tip cell phenotype.

3.5 Methods

3.5.1 The contact inhibition model and the cell elongation model

The contact inhibition model [64] and the cell elongation model [63] are both based on the cellular Potts method (CPM) [61, 62]. See Section 2.4.1 for a detailed description of the basic CPM. Cells can be differentiated into tip and stalk cells, represented by $\tau(\sigma) = \{\text{tip, stalk}\}$. The following cell properties and behaviors are represented in the Hamiltonian (H) of the contact inhibition model and the cell elongation model: cell shape (cell size and cell length) and adhesion. See Section 2.4.1 for a mathematical description of cell size and adhesion.

Cell elongation. To constrain the cell length (l) in the cell elongation model, an additional constraint is used as previously described [63]. Briefly, $H_{\text{length}} = \lambda_{\text{length}}(\sigma) \sum_{\sigma} (L(\sigma) - l(\sigma))^2$, with $\lambda_{\text{length}}(0) = 0$ and $\lambda_{\text{length}}(\sigma) > 0$ for all $\sigma > 0$, i.e., the length constraint holds for the cells only. $L(\sigma)$ and $l(\sigma)$ are the target cell length and current cell length. The current cell length can be efficiently estimated from the cell's inertia tensor, as described previously. To prevent cells from splitting up in an attempt to optimize the moments of inertia, A large penalty ($H_{\text{connectivity}}$) is added to the Hamiltonian in case a copy would split up a cell locally.

Chemoattractant secretion. We assume that the endothelial cells secrete a chemical signal, $c(\vec{x})$, which diffuses and degrades according to a partial-differential equation (PDE) coupled to the CPM,

$$\frac{\partial c}{\partial t} = \alpha(1 - \delta(\sigma(\vec{x}), 0)) - \epsilon\delta(\sigma(\vec{x}), 0)c + D\nabla^2 c. \quad (3.1)$$

The cells secrete the signal at rate α per second, it is degraded at a rate ϵ per second, and it diffuses in the ECM at rate $D \text{ m}^2/\text{s}$. The Kronecker-delta

constructions indicate that the cells secrete the chemoattractant, which is degraded in the ECM ($\delta(\sigma(\vec{x}), 0) = 0$ inside cells and $\delta(\sigma(\vec{x}), 0) = 1$ in the ECM). After each MCS, this partial differential equation is solved numerically using a finite-difference scheme on a lattice that matches the CPM lattice, using 15 diffusion steps per MCS with $\Delta t = 2s$ and $\Delta x = 2\mu m$.

Chemotaxis. To model chemotaxis, we bias the update probabilities such that membrane fluctuations up gradients of the chemoattractant are [121] favored. To this end, we modify the Hamiltonian during each copy attempt, $\Delta H_{\text{chemotaxis}} = \Delta H + \lambda_c (c(\vec{x}) - c(\vec{x}'))$, with λ_c a parameter giving the sensitivity to the chemoattractant. The contact inhibition model assumes that cell-cell contact inhibits chemotaxis: i.e., λ_c becomes zero for copies at cell-ECM interfaces.

Model set up The contact inhibition model [64] and the elongation model [63] make use of the standard cellular Potts model, and the chemoattractant diffusion and chemotaxis models, where the contact inhibition model restricts chemotaxis to cell-matrix interfaces as described above. The cell elongation model additionally includes a cell length constraint. The simulations are initialized with a spheroid of cells, of a radius of 45 lattice sites containing square cells of 7 lattice sites wide, surrounded by extracellular matrix. The simulations are initiated with cell spheroids. In these models, sprout form after 30000 MCS, corresponding to approximately 10 days of sprouting as required for sprouting of embryoid bodies [24]. A MCS corresponds to 30 seconds. At 10000 MCS we start to monitor tip cell overtakes and cell mixing in the models. The parameter values for both models, obtained from [63, 64], are listed in Table S3. The models were implemented with the modeling environment CompuCell3D, scripts are available on request.

3.5.2 Leader cell identification

To identify leader cells in a network of endothelial cells, sprouts are detected by converting the network of cells into a graph of edges, branch nodes and end nodes as in [64]. To this end, the irregularities of the network are closed with a morphological closing operation using a disk of radius (r), the network is thinned by a radius (t) and subsequently the branches are pruned with a distance (p) [122]. Nodes within a range of m lattice sites are merged. The settings to create graphs from simulated networks in the contact inhibition model are $r=4$, $t=4$, $p=10$, and $m=10$, and for the cell elongation model $r=2$, $t=5$, $p=25$, and $m=15$. A sprout is defined as a connection between a branch point B and an endnote E.

The leader cell of a sprout is found in a few steps. The first guess (G) for the leader cell is the cell in which the endnote E is located. If E happens to be located in the ECM, the cell belonging to the most frequently occurring cell identifier in the set of neighboring lattice sites of E is selected as G. Next, a

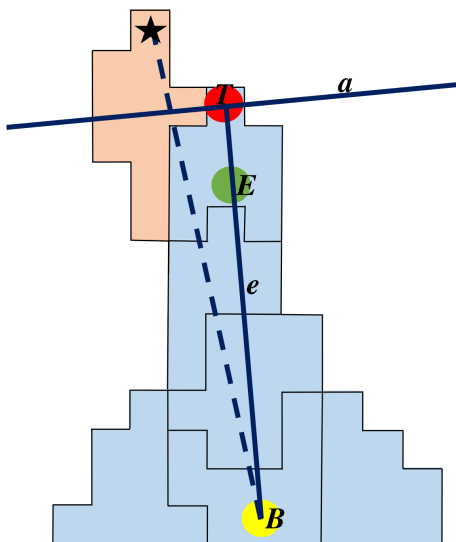


Figure 3.6: Leader cell identification. Schematic representation of a sprout to illustrate the identification of the leader cell. Line e is drawn through nodes B and E to find T , the furthest lattice site in the sprout on line e . Line a is perpendicular to line e and through T . The cell in which E is located and its neighbors that are on line a , are candidates to become the leader cell. The cell with the lattice site farthest from B (indicated with a star) and is connected to B through at least an equal amount of cells, will become the leader cell (indicated in red).

straight line (e) is drawn from B through E in the direction of the sprout tip. The furthest lattice site belonging to a cell in the sprout on this line, after which at least five consecutive ECM lattice sites follow, is identified as T . Subsequently, a line (a) perpendicular to the line e and through T , is constructed (Figure 3.66). All cells on line a that are neighbors of cell G become additional candidates for leader cell. Each of these cells that are connected to node B through at least an equal amount of cells as G is, taking the shortest path according the Dijkstra algorithm through a graph in which each cell is a node and shares an edge with the node belonging to a neighboring cell, remain candidate together with cell G . The cell that has the lattice site with the largest distance to B (indicated with a star in Figure 3.6) becomes the leader cell of the sprout.

3.5.3 Cell trajectory analysis

Cells are tracked during a simulation by storing the position of their center of mass every 20 MCSs. This cell trajectory data is used to calculate cell coordination and directional motility by the methods described by Arima et

al. in [25]. Two adaptations have been made compared to the methods used by Arima *et al.* [25] to automate the analysis: defining a sprout and defining the elongation axis of a sprout. We define a sprout as the leading cell (see Methods Section 3.5.2) together with its ten nearest neighbors in the same sprout. The ten nearest neighbors are found by listing the cells that contact the leader cell and subsequently listing the cells they contact that are not listed yet and so on, until ten cells are listed. We defined the elongation axis as the edge between the start and end position of a sprout. The start position is the average of the position of the branch node at the first and last time frame of the existence of a sprout. The end position is the average of the tip position for these two time frames. This was required since sprouts often shift and curve. Cell coordination and directional motility are calculated according to the methods in Arima *et al.* [25]. We have averaged the results over the sprouts (or the cells in the sprouts) formed during 15 simulations with different random seeds. In the calculation for the directional motility, cells that traveled a smaller distance than 0.5 lattice sites [25] are considered to be stopped. The dispersion coefficient of cells during sprouting can be derived from the mean square displacement ($MSD = \langle \bar{x}^2 \rangle$) of the centers of mass of all cells within sprouts measured each 20 MCS during sprouting time, with the data of all 15 simulations grouped. For this purpose, we measured the one-dimensional displacement of the projection of the centers of mass of cells on the sprouting elongation axis. The dispersion coefficient (D) and the sprout elongation velocity (ν) are derived by fitting the MSD curve with $\langle \bar{x}^2 \rangle = 2Dt + (\nu t)^2$.

3.5.4 Dll4-Notch signaling model

A model of lateral inhibition by Dll4-Notch signaling is included in each cell of the CPM. The model is based on an ordinary-differential equation (ODE) model previously proposed by Sprinzak *et al.* [46]. In this model, Notch binds Dll4 ligands in adjacent cells (trans-interaction) leading to the production of NICD; Notch and Dll4 also bind intracellularly leading to inhibition of NICD production. Such *cis*-inhibition makes the Dll4 and Notch lateral inhibition mechanism more robust to noise [46] and has been observed, e.g., in the *Drosophila* wing [123] and eye [124]. *Cis*-inhibition of Dll4 and Notch remains to be confirmed in endothelial cells; recent modeling work [125] suggests, however, that it has little effect on the robustness of tip cells.

The model is described by the following set of ODEs:

$$\frac{dD_i}{dt} = \beta_{Dc} + \frac{\beta_D}{1 + S_i^{m_D}} - \gamma_D D_i - \frac{D_i N_i}{k_c} - \frac{1}{k_t d^2} \sum_{j \in NB(\sigma)} D_i N_j \frac{|P_{i,j}|^2}{|P_i| |P_j|} \quad (3.2)$$

$$\frac{dN_i}{dt} = \beta_N - \gamma_N N_i - \frac{N_i D_i}{k_c} - \frac{1}{k_t d^2} \sum_{j \in NB(\sigma)} N_i D_j \frac{|P_{i,j}|^2}{|P_i| |P_j|} \quad (3.3)$$

$$\frac{dS_i}{dt} = \alpha_S \frac{\left(\frac{1}{d^2} \sum_{j \in NB(\sigma)} N_i D_j \frac{|P_{i,j}|^2}{|P_i| |P_j|} \right)^{ns}}{k_S + \left(\frac{1}{d^2} \sum_{j \in NB(\sigma)} N_i D_j \frac{|P_{i,j}|^2}{|P_i| |P_j|} \right)^{ns}} - \gamma_S S_i \quad (3.4)$$

Each cell i has an individual concentration of Dll4 (D_i), Notch (N_i) and activated Notch signal (S_i). The ODE model contains constants for constitutive production of Notch and Dll4 (β_N and β_{Dc}), decay constants for Notch (γ_N), Dll4 (γ_D) and NICD (γ_S), a cis-interaction coefficient (k_c), a trans-signaling coefficient (k_t) and a scaling factor (d). Trans-signaling results in NICD production following a Hill equation, with a production rate (α_S). The variable Dll4 production (β_D) is inhibited by NICD using a repressive Hill function (m_D). In contrast to the Sprinzak model, our model considers the size of cell-cell contacts for trans-signaling. Dll4 and Notch are assumed to be spread homogeneously over all lattice sites in the membrane of the cell (P_i). Cell i and neighboring cell j contact each other at region of the cell membrane. Cell i will present a fraction of its Dll4 receptors to its neighbor, proportional to the length of the contacting cell membrane region ($|P_{i,j}|$) divided by the total length of the membrane ($|P_i|$). This results in contact-surface dependent trans-signaling obeying: $D_i \left(\frac{|P_{i,j}|}{|P_i|} \right) N_j \left(\frac{|P_{i,j}|}{|P_j|} \right)$. The collection of cells that are in contact with cell i are represented by the set $NB(\sigma)$. We solve these equations ten times per MCS with $\Delta t = 3s$. The reference parameter values of the model by Sprinzak *et al.* [46] were rescaled after the extension of the contact-surface dependent trans-signaling to obtain the experimentally observed tip and stalk patterns as discussed in Section 3.2.4. The parameter values of the Dll4-Notch signaling network are listed in Table S4.

3.5.5 Modeling of Dll4-Notch signaling in presence of VEGF

VEGF signaling was added to the tip cell selection model described in section 3.5.4. A non-diffusive, constant, homogeneous, external VEGF (V) field with a value of one was added to the model. The equations that are altered or added due to the presence of VEGF relative to the Dll4-Notch signaling equations (method section 3.5.4) are:

$$\frac{dR_i}{dt} = \beta_{Rc} + \frac{\beta_R}{1 + S_i^{mR}} - \gamma_R R_i \quad (3.5)$$

$$\frac{dA_i}{dt} = \alpha_A \frac{\left(\sum_{j \in P_i} \frac{R_j V_j}{|P_i|} \right)^{n_A}}{k_A + \left(\sum_{j \in P_i} \frac{R_j V_j}{|P_i|} \right)^{n_A}} - \gamma_A A_i \quad (3.6)$$

$$\frac{dD_i}{dt} = \beta_{Dc} + \frac{\beta_D}{1 + S_i^{mD}} - \gamma_D D_i - \frac{D_i N_i}{k_c} - \frac{1}{k_t d^2} \sum_{j \in NB(\sigma)} D_i N_j \frac{|P_{i,j}|^2}{|P_i| |P_j|} + \dots \quad (3.7)$$

$$\alpha_D \frac{A_i^{n_D}}{k_D + A_i^{n_D}}.$$

The equations for solving N_i and S_i remain the same, and two equations are added that describe the VEGFR2 concentration (R_i) and the VEGF signaling activity (A_i) of cell i . The total VEGF concentration a cell perceives at its membrane ($\left(\sum_{j \in P_i} \frac{R_j V_j}{|P_i|} \right)$) upregulates its VEGF signaling activity with production rate α_A , following a Hill equation ((n_A, k_A)). VEGF signaling activity has a decay constant (γ_A) and VEGFR2 has a decay constant (γ_R). An additional term is present for Dll4 that expresses the positive feedback of VEGF activity on the Dll4 production, modeled with a Hill equation ((n_D, k_D)) and a production rate (α_D). *Vegfr2*^{+/-} cells are modeled by multiplying the constant production of VEGFR2 (β_{Rc}) and the variable production (β_R), which is inhibited by NICD (S_i) using a repressive Hill equation, by a half. The parameter values of the VEGF-Dll4-Notch signaling network are listed in Table S4. We manually fitted the parameters for VEGF-Dll4-Notch signaling, such that the experimentally observed tip and stalk patterns (as discussed in Section 3.2.4) are maintained, and in addition, that Dll4 and VEGFR2 levels are correlated with one another as shown by Jakobsson *et al.* [24].

3.A Supplementary movies

An archive containing all supplementary movies can be found at <http://persistent-identifier.org/?identifier=urn:nbn:nl:ui:18-23531>.

Movie S1 Tip cell overtaking in the contact inhibition model. Tip cell overtakes are visible during sprouting in a simulation of the contact inhibition model. The center of mass of each cell is depicted with a colored dot to allow tracking of individual cells.

Movie S2 Tip cell overtaking in the cell elongation model. Tip cell overtakes are visible during sprouting in a selected sprout in a simulation of the cell elongation model. The center of mass of each cell is depicted with a colored dot to allow tracking of individual cells.

3.B Supplementary tables

Table S1: Effect of VEGF gradients on the sprout tip occupancy by WT cells. The mean (out of 10 simulations) occupancy of sprout tips by WT cells at the end of a simulation with the contact inhibition model with differential adhesion between tip and stalk cells, in which only tip cells have a chemotactic sensitivity ($\lambda_c, \text{VEGF}=0.1$) to an external VEGF field, is listed for different VEGF gradient shapes (columns) and for different ratios of WT and *Vegfr2* haploids in the spheroid (rows). The columns represent different shapes of the gradients of the external VEGF field ranging from concentration 0 to 1, which was uniformly spread over the grid, or increased from left to right over the grid in a linear, exponential or sigmoidal fashion. The p-values represent the probability that the total number of simulated sprouts were occupied by at least the indicated percentage of WT cells when assuming only random motion (calculated with a binomial distribution, with n the number of sprouts, k the number of sprouts occupied by WT cells, and p the mixing ratio).

Ratio	Uniform	Linear	Sigmoidal	Exponential
1:1	86 ($p=1.1 * 10^{-7}$)	71 ($p=1.9 * 10^{-3}$)	78 ($p=7.8 * 10^{-5}$)	75 ($p=3.6 * 10^{-4}$)
1:4	36 ($p=8.7 * 10^{-3}$)	57 ($p=1.2 * 10^{-8}$)	53 ($p=4.6 * 10^{-7}$)	49 ($p=3.3 * 10^{-6}$)
1:9	17 ($p=9.3 * 10^{-2}$)	13 ($p=3.3 * 10^{-1}$)	19 ($p=4.1 * 10^{-2}$)	25 ($p=1.2 * 10^{-3}$)

Table S2: Effect of VEGF gradient on cell trajectory data. Anterograde coordination, retrograde coordination, and the directional motility is listed for cells in the contact inhibition model (average of ten simulations), in which only tip cells have a chemotactic sensitivity ($\lambda_c, \text{VEGF}=0.1$) to an external VEGF field. The simulations were initialized with a mix of WT cells and *Vegfr2* haploids in a 1:1 ratio. The columns represent different shapes of gradients of the external VEGF field ranging from concentration 0 to 1, which was uniformly spread over the grid, or increased from left to right over the grid in a linear, exponential or sigmoidal fashion.

	Uniform	Linear	Sigmoidal	Exponential
Coordination anterograde	0.14 (± 0.03)	0.14 (± 0.03)	0.14 (± 0.02)	0.14 (± 0.02)
Coordination retrograde	0.14 (± 0.03)	0.14 (± 0.03)	0.14 (± 0.02)	0.14 (± 0.02)
Directional motility				
- percentage anterograde	48	29	35	22
- percentage retrograde	48	67	63	75
- percentage stopped	4	3	2	3

Table S3: Parameter values of the contact inhibition model and the cell elongation model.

Parameter	Description	Contact	Long	Unit
μ	Cellular temperature	1	1	-
A	Target cell size	50	100	lattice sites
λ_A	Cell elasticity	0.5	1	-
$J_{\text{cell,ECM}}$	Cell-ECM adhesion	0.4	0.35	-
$J_{\text{cell,cell}}$	Cell-cell adhesion	0.8	0.5	-
λ_c	Chemotaxis sensitivity	10	10	-
α	Secretion rate	$1 \cdot 10^{-3}$	$1.8 \cdot 10^{-4}$	s^{-1}
ϵ	Decay rate	$1 \cdot 10^{-3}$	$1.8 \cdot 10^{-4}$	s^{-1}
D	Diffusion coefficient	$1 \cdot 10^{-13}$	$1 \cdot 10^{-13}$	m^2/s
$H_{\text{connectivity}}$	Connectivity	$1 \cdot 10^8$	$1 \cdot 10^8$	-
λ_L	Cell length elasticity	-	0.1	-
L	Target cell length	-	60	lattice sites

3. Computational modeling of tip cell overtaking

Table S4: Parameter values VEGF-Dll4-Notch signaling model Dimensional units: decay rates, $\gamma_N, \gamma_D, \gamma_S, \gamma_R$, and γ_A are per 30 seconds (30s=1MCS), production rates $\beta_N, \beta_D, \beta_{Dc}, \beta_R$, and β_{Rc} in RU/30 seconds and affinities k_S, k_D , and k_A in RU·30 seconds. Here Relative Units (RU) replace concentrations which are unknown.

Parameter	Description	Value
β_N	Production rate Notch	1
γ_N	Decay rate Notch	0.1
β_D	Variable production rate Dll4	5
γ_D	Decay rate Dll4	0.1
β_{Dc}	Constitutive production rate Dll4	0.1
γ_S	Decay rate NICD	0.1
α_S	Production rate NICD	100
k_S	Hill constant that relates Dll4-Notch signaling to NICD production	3000
n_S	Hill constant that relates Dll4-Notch signaling to NICD production	2
m_D	Hill constant that relates NICD no Dll4 production	1
k_t	Trans-signaling coefficient	80
k_c	Cis-signaling coefficient	10
d	Scaling constant	2
k_D	Hill constant that relates VEGF signaling activity to Dll4 production	130000
α_D	Production rate of Dll4 depending on VEGF signaling activity	15
β_R	Variable VEGFR2 production rate	2
β_{Rc}	constant VEGFR2 production rate	0.01
γ_R	VEGFR2 decay rate	0.3
m_R	VEGF signaling activity	2
n_D	Hill constant that relates VEGF signaling activity to Dll4 production	2
α_A	Production rate of VEGF signaling activity	100
n_A	Hill constant that relates VEGF-FEGVR2 binding to VEGF signaling activity	2
k_A	Hill constant that relates VEGF-VEGFR2 binding to VEGF signaling activity	30
γ_A	Decay rate of VEGF signaling activity	0.1

3.C Supplementary figures

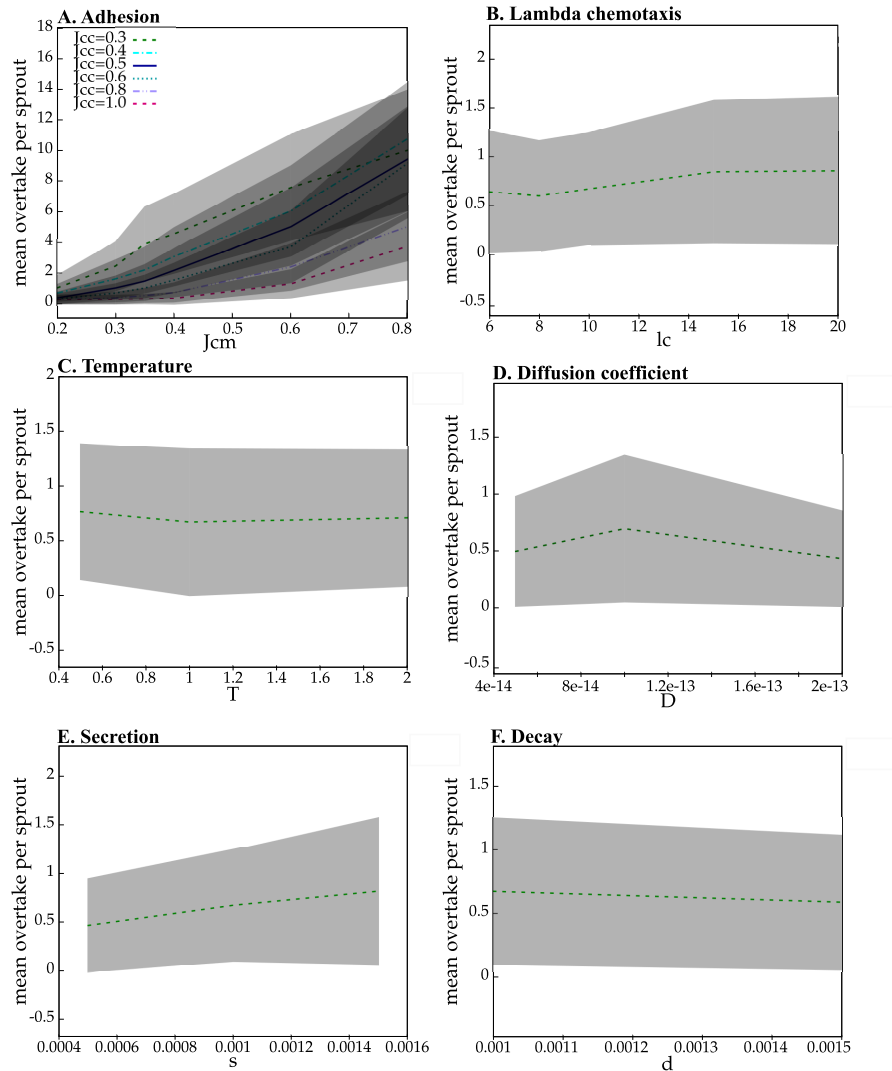


Figure S1: Sensitivity of tip cell overtaking in contact inhibition model. The mean overtake rate per sprout, based on 15 independent simulations, is plotted against cell-cell adhesion ($J_{cell,cell}$) and cell-ECM adhesion ($J_{cell,ECM}$), sensitivity to the auto-secreted chemoattractant (λ_c), the cellular temperature (μ), the diffusion constant of the chemoattractant (D), the chemoattractant's decay rate (ϵ), and secretion rate (s) by the cells for the contact inhibition model. The gray regions represent the 95% confidence intervals. None of the parameters, except for adhesion, affected the mean tip cell overtake rate per sprout significantly. As a rough estimate, all 95% confidence intervals overlap for the tip cell overtake rates. To quantitatively illustrate this, the mean tip cell overtake rate for $T=0.5$ compared to $T=2$ are not significantly different with a p-value of 0.901 for the contact inhibition model based on a Welch's t-test.

3. Computational modeling of tip cell overtaking

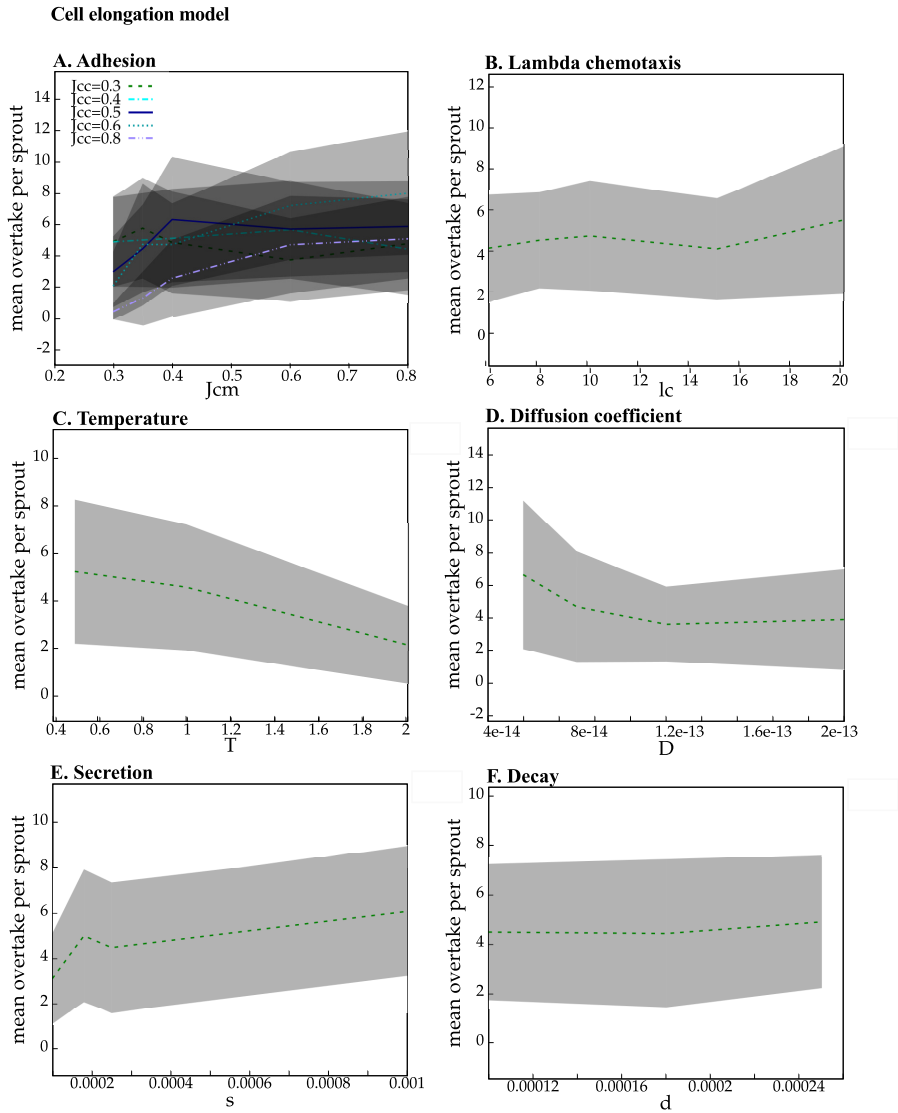


Figure S2: Sensitivity of tip cell overtaking in cell elongation model. See next page for caption.

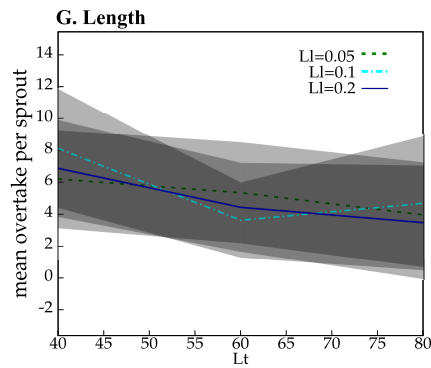


Figure S2: Sensitivity of tip cell overtaking in cell elongation model. The mean overtake rate per sprout, based on 15 independent simulations, is plotted against cell-cell adhesion ($J_{\text{cell,cell}}$) and cell-ECM adhesion ($J_{\text{cell,ECM}}$), sensitivity to the auto-secreted chemoattractant (λ_c), the cellular temperature (μ), the diffusion constant of the chemoattractant (D), the chemoattractant's decay rate (ϵ), secretion rate (s), and the length of the cell (target length L and cell elasticity λ_L) for the cell elongation model. The gray regions represent the 95% confidence intervals. None of the parameters affected the mean tip cell overtake rate per sprout significantly. As a rough estimate, all 95% confidence intervals overlap for the tip cell overtake rates. To quantitatively illustrate this, the mean tip cell overtake rate for $T=0.5$ compared to $T=2$ are not significantly different with a p-value of 0.093 for the cell elongation model based on a Welch's t-test.

3. Computational modeling of tip cell overtaking

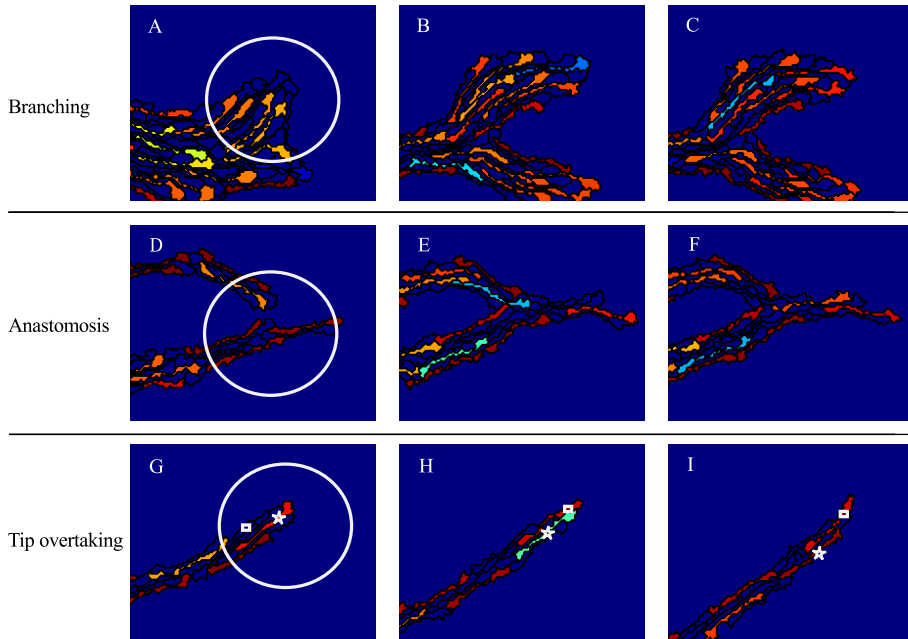


Figure S3: Dll4 patterning by tip cell selection in a simulation of the cell elongation model. Patterning of tip and stalk cells in the cell elongation model. (A-C) Enlarged view of a sprout in which branching occurs in time, at the location of the white circle in panel A. (D-F) Enlarged view of two fusing sprouts (anastomosis) in time, indicated by the white circle in panel D. (G-I) Enlarged view of a sprout in which tip cell competition occurs in time at the location of the white circle in the panel G. The cell annotated with a square overtakes the tip cell position from the cell annotated with a star.

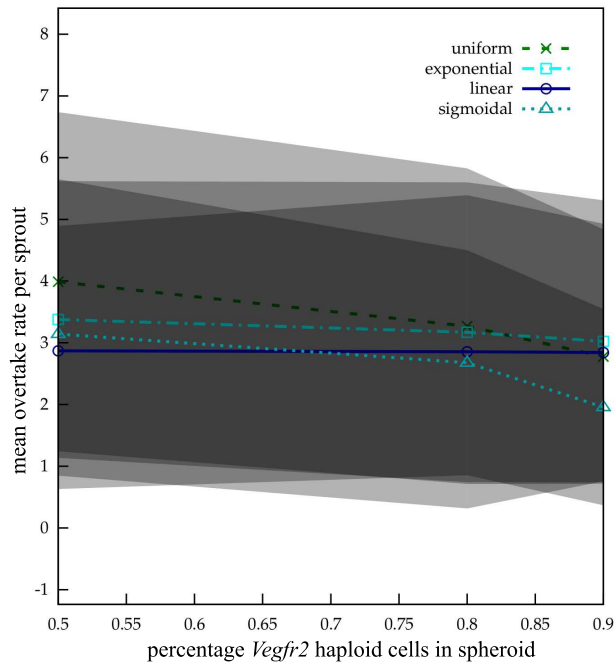


Figure S4: Effect of VEGF gradients on the mean overtake rate per sprout. The mean overtake rate per sprout was calculated from ten simulations with the contact inhibition model in which only tip cells have a chemotactic sensitivity ($\lambda_{c,VEGF} = 0.1$) to an external VEGF field. The different lines represent different shapes of the gradients of the external VEGF field ranging from concentration 0 to 1, which was uniformly spread over the grid, or increased from left to right over the grid in a linear, exponential or sigmoidal fashion. The mean overtake rate per sprout is plotted against the percentage of *Vegfr2* haploid cells in a mixed spheroid of WT cells and *Vegfr2* haploids. The gray regions represent the 95% confidence intervals. The mean overtake rate per sprout is not significantly different for distinct gradients of VEGF.

Synergy of cell-cell repulsion and vacuolation in a computational model of lumen formation

This chapter is based on:

Sonja E. M. Boas and Roeland M.H. Merks, *Synergy of Cell-Cell Repulsion and Vacuolation in a Computational Model of Lumen Formation* (2014). J. R. Soc. Interface 11: 20131049.

Abstract

A key step in blood vessel development (angiogenesis) is lumen formation: the hollowing of vessels for blood perfusion. Two alternative lumen formation mechanisms are suggested to function in different types of blood vessels. The *vacuolation* mechanism is suggested for lumen formation in small vessels by coalescence of intracellular vacuoles, a view that was extended to extracellular lumen formation by exocytosis of vacuoles. The *cell-cell repulsion* mechanism is suggested to initiate extracellular lumen formation in large vessels by active repulsion of adjacent cells, and active cell shape changes extend the lumen. We used an agent-based computer model, based on the cellular Potts Model, to compare and study both mechanisms separately and combined. An extensive sensitivity analysis shows that each of the mechanisms on its own can produce lumens in a narrow region of parameter space. However, combining both mechanisms makes lumen formation much more robust to the values of the parameters, suggesting that the mechanisms may work synergistically and operate in parallel, rather than in different vessel types.

4.1 Introduction

In the previous chapters, we studied how local cell-matrix (Chapter 2) and cell-cell interactions (Chapter 3) affect sprouting dynamics. In Chapter 2, we examined how local degradation of the extracellular matrix by endothelial cells affects the morphology of sprouts. Chapter 3 focused on the interplay of intercellular signaling and collective cell behavior in tip cell overtaking, the competition of cells for the leading sprout tip position. Once a sprout is formed, the new sprout hollows to allow blood to perfuse [29, 126]. This hollowing is called lumen formation, and can occur in absence of blood pressure, such as *in vitro* [28, 29, 31, 33] and also *in vivo* in intersegmental vessels of zebrafish [31]. Which mechanisms are responsible for lumen formation is heavily debated [22, 36, 127–130].

Lumen formation is extensively studied in epithelial tissues, which has resulted in a range of potential mechanisms [131]. Three of these can form lumens in cords of cells: cavitation, cell hollowing and cord hollowing. Cavitation is unlikely to play a role in lumen formation of endothelial tubes, where apoptosis is rarely observed [29]. The two remaining mechanisms assume intracellular lumen formation within cells in uni-cellular tubes (cell hollowing), versus extracellular lumen formation between cells in multi-cellular tubes (cord hollowing). The debate whether lumens form intracellularly [132] or extracellularly [133] in blood vessels originates from the 19th century [134]. This led to two opposing views on the molecular mechanisms of lumen formation in endothelium: the vacuolation mechanism [28, 29] and the cell-cell repulsion mechanism [32, 33]. The vacuolation mechanism (Figure 4.1a

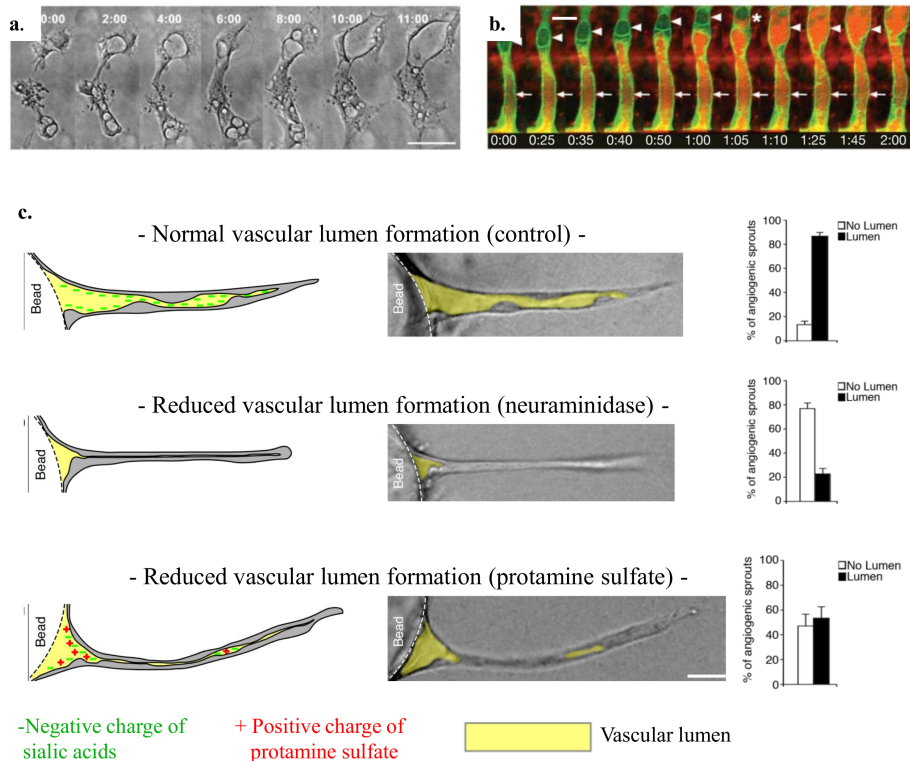


Figure 4.1: Experimental observations in lumen formation. a. Adapted from Kamei *et al.* 2006, time-lapse images of ECs in 3D collagen gel, showing formation of vacuoles into larger intracellular compartments. b. Adapted from Kamei *et al.* 2006, two-photon time lapse imaging of an ISV in which membranes are labeled with EGFP-cdc42wt and intravascular injected red quantum dots are serially transferred by vacuole fusion. c. Adapted from Strilić *et al.* 2010, lumens form during *in vitro* 3D angiogenic sprouting assays by cell-cell repulsion facilitated by negatively charged CD34-sialomucins (control panel). Cleavage (neuraminidase panel) or neutralization (protamine sulfate panel) hereof reduces lumen formation.

and 4.1b) originally suggests that an intracellular lumen is formed by coalescence of vacuoles [29, 135] and this view was extended with extracellular lumen formation by exocytosis of vacuoles [30, 31]. The cell-cell repulsion mechanism (Figure 4.1c) assumes that extracellular lumens initiate by active repulsion of adjacent cells and are expanded by active cell shape changes [32, 33]. As vacuoles are often observed in intersegmental vessels (ISVs), but not in aortae, the vacuolation mechanism is suggested to function in small vessels and cell-cell repulsion in large vessels [22, 31, 36, 129, 130].

It is difficult to distinguish the two proposed lumen formation mechanisms experimentally, because they use similar proteins and pathways; everything

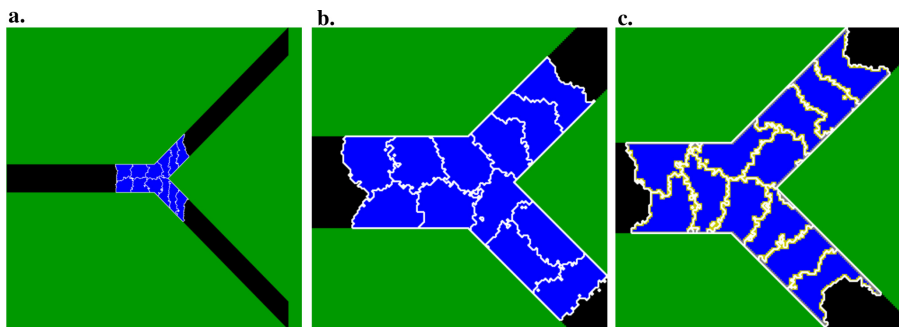


Figure 4.2: Model initialization. a. The configuration of the model at initialization. b. Final outcome of a simulation without cell surface polarization. c. Final outcome of a simulation with cell surface polarization.

is intertwined. Therefore, we used a computational model, which allows us to isolate, modify, and study single mechanisms and selected components [136–138], and compared the efficiency of both lumen formation mechanisms separately and combined. An extensive parameter sensitivity analysis of the model suggest that lumen formation is most robust to inhibitions of either mechanism when the two mechanisms are combined, indicating that they function synergistically in lumen formation. Thus our model challenges the idea that each of the mechanisms operates on its own in different types of blood vessels [22, 31, 36, 129, 130], and supports the idea that the different mechanisms operate in parallel [127].

4.2 Results

We developed a two-dimensional, multi-scale, agent-based computational model in which lumen formation emerges from predefined behavior of components at the cellular and subcellular scale. During angiogenesis, lumens form shortly after new sprouts have originated [29, 126]. Thus we can assume that sprouting and lumen formation are separated in time, such that we can model lumen formation in a preformed sprout. The sprout is represented as a branched cord of twelve cells within an extracellular matrix (ECM; Figure 4.2a and 4.2b). The bifurcating geometry contains narrow, single cell wide regions at the tips of the branch and two cell wide regions at the trunk of the branch. The model currently neglects degradation or secretion of ECM by the cells that we considered in previous work [75] and in Chapter 2. ECM fluid is present at each end of the branch to allow stretching rather than widening (as seen in experiments Figure 4.1a and 4.1c) of the vessel during lumen formation.

The model represents a two-dimensional cross-section of the vessel. In a

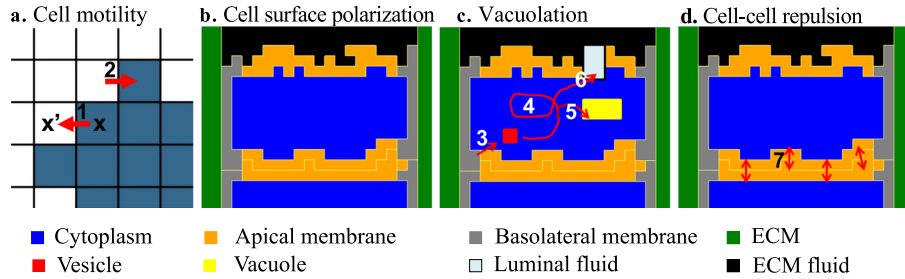


Figure 4.3: Modules of computational model. a. Cell motility by a copy of the membrane outward (1) and inward (2). b. Cell surface polarization, resulting in cytoplasm (blue) surrounded by a basolateral membrane (gray) and an apical membrane (orange). c. Vesicles (red) can be created by pinocytosis (3), move in the cell by a biased random walk (4), fuse into vacuoles (yellow) (5) and be secreted (6) into luminal fluid (light blue). d. The apical membranes of different cells repulse each other (7) due to the negative charges on the extracellular domains of the CD34-sialomucins herein.

cross-section, a cell with an intracellular lumen will be split up, while it could be donut-shaped in three dimensions. Despite this obvious disadvantage of using a two-dimensional simulation, it still gives us useful insights in the local mechanisms driving lumen formation. Furthermore, the computational efficiency of the two-dimensional model allows us to evaluate the behavior of the model for a large number of parameter settings.

The model consists of four modules (Figure 4.3) that we combine in different combinations to represent each of the mechanisms. *Cell motility* is regulated by the cellular Potts Model (CPM) [61, 62] that considers the shape of cells and their adhesive properties. Agent-based extensions of the CPM represent subcellular structures, including membrane proteins, vesicles, and vacuoles. *Cell surface polarization* results in a basolateral membrane that lines the vessel and connects the cells, and an apical membrane where the lumen will form. During *vacuolation*, pinocytotic vesicles are formed within the cells, coalesce into vacuoles and are secreted at the apical membrane. *Cell-cell repulsion* occurs by active repulsion of apical membranes from opposing cells. We briefly describe each module here, for details and reference settings (Table 4.1-4.3) see Section 4.4.

4.2.1 Cell motility module

The cellular Potts Model [61, 62] is a convenient model to deal with structural and spatial aspects in lumen formation, since it considers the shape of cells and their physical interactions with their surroundings. Cells are represented as patches on a lattice. The diameter of a cell is approximately 5-10 μm (1 lat-

4. Computational modeling of lumen formation

tice site=250 nm) and a cell is initialized with 625 lattice sites ($\pm 25 \times 25$). We represent the subcellular scale using a compartmentalized CPM [139–141]. Each lattice site \vec{x} in a compartment is associated with the same unique compartment identifier ($\sigma(\vec{x})$). Depending on the mechanism that is tested, compartments with the type ($\tau(\sigma(\vec{x}))$) *cytoplasm*, *apical membrane*, *basolateral membrane*, *vesicle*, and *vacuole* can exist within a cell. ECM, ECM fluid and cells have an additional unique cell identifier $\xi(\sigma(\vec{x}))$, with the set of compartments σ that belong to the same cell having the same cell identifier. The ECM is immobile, but cells and compartments move by copying lattice sites at the membrane inward or outward (Figure 4.3a). The source lattice site (\vec{x}) together with a random, adjacent target lattice site (\vec{x}') is randomly selected for each copy attempt, resulting in a stochastic simulation. Acceptance of these copies depends on properties of the cells and compartments, such as adhesion/repulsion strength (contact) and size (area). Adhesion or repulsion strength can result from protein interactions and from surface tensions on membranes and is modeled by contact energy. A distinction is made between internal contact energy between compartments of the same cell ($J_I(\tau, \tau)$) and external contact energy between compartments of different cells ($J_E(\tau, \tau)$). As a reference contact energy we use a value of $J = 10$: a lower contact energy leads to adhesion, while a higher contact energy leads to repulsion. Lattice sites that are not occupied by ECM or cells are of type *ECM fluid* or *luminal fluid*. ECM fluid is already present at initialization next to the branch and is in contact with the ECM. Luminal fluid is secreted by vesicles and vacuoles inbetween cells. Luminal fluid will fuse to the ECM fluid when surrounded by ECM fluid or when in contact with ECM. Cells, vesicles, vacuoles and subvolumes of fluid have a preferred size (A), which is conserved on average, with the elasticity parameter λ_{type} (see section 4.4 for details) regulating the allowed deviation from the preferred size [61]. For cells, vesicles and vacuoles, this reflects the semi-permeability of membranes for water. For subvolumes of fluids, this results in near-incompressibility which could resemble a hydrostatic pressure in the sublumens.

4.2.2 Cell surface polarization module

Cell surface polarization into a basolateral and an apical domain is the first step in lumen formation and is regulated by integrin-signaling from the ECM [32, 129, 142–146]. In the computational model, the membrane (re)polarizes every other time step into an apical and a basolateral compartment based on the relative position to the ECM (Figure 4.2c and Figure 4.3b). During repolarization, each ‘mispolarized’ lattice site in the membrane is assigned to the correct compartment. A lattice site of the membrane becomes part of the basolateral compartment when it is in direct contact with the ECM. To form the lateral junctional regions of the cells, lattice sites of the membrane that have

at least two neighboring lattice sites that are in direct contact with ECM, also become part of the basolateral compartment. The rest of the membrane lattice sites become part of the apical compartment. Contact energy is used to mimic adherens junctions ($J_I(\text{apical}, \text{basolateral})$) and to set the surface tension of the apical membrane ($J_E(\text{media}, \text{apical})$).

4.2.3 Vacuolation module

The vacuolation mechanism is one of the two proposed mechanisms for lumen formation in blood vessels [29, 135]. Vacuoles are often observed *in vitro* and *in vivo* during lumen formation as summarized by Davis & Bayless [28]. Vacuoles were visualized with electron microscopy (Figure 4.1a) and by expression of the green fluorescent protein (GFP) fusion proteins GFP-Rac1, GFP-Cdc42, and Moesin1-EGFP, which co-localize with the vacuoles [28, 147–149]. Vacuoles show highly dynamic behavior, as they continuously fuse together, grow, shrink and disappear [29, 31]. Kamei *et al.* [29] showed that a label (carboxyrhodamine) added to the medium is taken up into the vesicles by pinocytosis and is transferred to vacuoles by fusion of vesicles into vacuoles. Fusion might be facilitated by caveolin-1, since it concentrates at vacuole-vacuole contact areas [28]. Pinocytotic vesicles are likely trafficked along microtubules and actin filaments [150]. Targeting to the apical membrane might involve Cdc42 and Moesin1 [28, 31], which both co-localize with vesicles and have high affinity for phospholipids specific for the apical membrane. Eventually, vesicles and vacuoles bridge the entire cell [29] and are exported at the apical membrane through exocytosis to create fluid-filled space for a lumen [30]. Each of these steps is explicitly modeled in this module.

To mimic pinocytosis, we assumed that if a lattice site of the membrane becomes internalized in the cell due to cell movements it has a probability (P_{pin}) to become a new compartment of type vesicle (Figure 4.3c; step 3) or to become part of the cytosol. Vesicle diameter is approximated at 250 nm [151], which is equal to one lattice site length in the model. This size is achieved by means of a target area of 1 and a high inelasticity ($\lambda_{vesicle}$). Vesicle transport is precisely regulated with vesicle-associated motor proteins that walk along microtubules and actin filaments [150], which gives rise to stochastic motion of vesicles if the cytoskeleton is randomly oriented [150–152]. Random binding and unbinding of vesicles and associated motor proteins to a randomly oriented cytoskeleton leads to diffusive transport behaviour [152]. In our model we therefore model vesicle transport by a random walk with stepping probability P_A (see section 4.4), biased by preferential adhesion to the apical membrane and fusion into vacuoles (Figure 4.3c; step 4). Vesicles preferentially adhere to the apical membranes, vesicles, and vacuoles by considering their contact energy in their stepping. Fusion of neighboring vesicles, vacuoles or a combination of the two happens with probability P_{fuse}

4. Computational modeling of lumen formation

(Figure 4.3c, step 5) and generates a single vacuole compartment for which the target areas are combined. A vacuole moves by means of the usual CPM rules (see section 4.4) and is only restricted by its contact energy and size constraint. When a single lattice site of type vacuole is no longer in contact with vesicles or vacuoles, it becomes a vesicle. Secretion occurs when a vesicle or vacuole lattice site is in the apical membrane (Figure 4.3c; step 6). This lattice site, together with all connected lattice sites of type vesicle or vacuole, is secreted to form a fluid-filled luminal space of type *luminal fluid*. The cell membrane is subsequently repolarized, which also leads to an increase in size of the apical membrane.

4.2.4 Cell-cell repulsion module

The alternative cell-cell repulsion mechanism [32, 33] assumes active, electrostatic repulsion of the apical membranes of adjacent cells, followed by active cell shape changes to extend the lumen. Previously, it was suggested that lumens can form by relocalization of junctional complexes over the cell membrane, leading to local differences in cell adhesion at the future luminal and basolateral sides of cells [153–155]. In addition to such differential adhesion driven lumen formation, Strilić *et al.* [32, 33] showed in the developing mouse aorta and in a 3D angiogenic sprouting assay that apical membranes actively repulse each other during lumen formation by expression of CD34-sialomucin glycoproteins, like PODXL. These transmembrane glycoproteins have negatively charged extracellular domains and are transported to the apical membrane in preformed vesicles.

This active repulsion is modeled with high contact energy between apical membranes of adjacent cells ($J_E(\text{apical}, \text{apical})$); see Figure 4.3d; step 7). Lattice sites of type cytoplasm can be at the membrane, since cell surface polarization is only performed every other time step in the model to allow some freedom of movement for the membranes and for internalization of membrane lattice sites for pinocytosis. Therefore $J_E(\text{cytoplasm}, \text{apical})$ is set to the same value. $J_E(\text{apical}, \text{apical})$ and $J_E(\text{cytoplasm}, \text{apical})$ together will now be referred to as J_{rep} . Note that this module of cell-cell repulsion only includes short-range, electrostatic membrane repulsion due to CD34-sialomucin glycoproteins. The additional mechanisms in our model, including cell shape changes and invasion of luminal fluid may act to further separate the membranes from each other.

4.2.5 Reconstruction of the mechanisms

Each lumen formation mechanism can be reconstructed from the four modules: cell motility, cell surface polarization, vacuolation, and cell-cell repulsion. The first three modules are combined to study the vacuolation mech-

anism, the first two and last for the cell-cell repulsion mechanism and all four modules together to study them combined, 'the combined mechanism'. A simulation is run for 10000 time steps to allow the creation of continuous lumens. During one time step, the Monte Carlo Step (MCS), as many copy attempts as there are lattice sites in the grid are attempted. Continuous lumens are formed in approximately 24 hours [28, 33]; a time step in the model thus corresponds with a few seconds in real time.

Since the model has a strong stochastic component, we run each simulation thirty times. Efficiency of lumen formation is expressed as the fraction of simulations that have formed a continuous lumen at the end of a simulation (continuity fraction). The lumen is continuous when the fluid in the three tips of the branch is part of one single connected component. Figure 4.4 shows a time-lapse for each mechanism at reference settings (corresponding to Video S1-3). During cell-cell repulsion (e.g. Figure 4.4a. MCS 10000), the cells stretch and flatten along the ECM, very similar to the experimental pictures in Figure 4.1c. The shape and size of the sublumens that are formed during vacuolation (e.g. Figure 4.4b, MCS 500) visually resemble the experimental observations of Kamei *et al.* [29] (Figure 4.1a). Although lumens do not form by vacuolation at reference settings, they do form for higher pinocytosis rates. The model is robust to practically all changes in parameters that describe the transport and fusion of vesicles and vacuoles (Figure S1 and supplementary text S1).

Ideally, all parameters in the model would have a quantitative value derived from experiments to allow comparison. However, most values are not known experimentally. Notably, Klann *et al.* [156] point out that they could not quantify time constants of reactions and transport processes in vesicle dynamics, because present experimental results focus on the functional and qualitative identification of molecular interactions and pathways rather than on the dynamics of the system. Fortunately our computational model can still be validated in a qualitative manner. Most parameters in the lumen formation model correspond to a protein or molecular process in lumen formation. As a result, qualitatively reducing the value of a parameter corresponds to a molecular knock-out or inhibition of the molecular mechanism it represents and should produce similar effects.

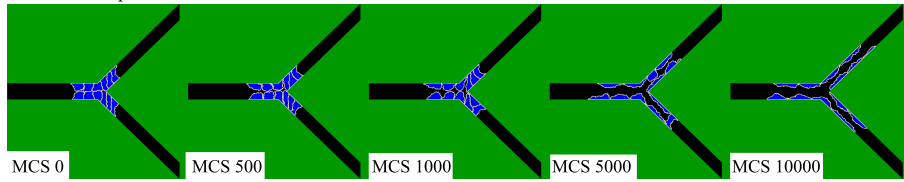
4.2.6 Vacuolation requires a high pinocytosis rate

In experiments, inhibition of pinocytosis prevents lumen formation and vacuole formation. Pinocytosis is an integrin-dependent process and is inhibited during these experiments by blockage of these sites ($\alpha2\beta1$ in collagen matrices [135] or $\alpha v\beta3$ and $\alpha5\beta1$ in fibrin-fibronectin matrices [157]).

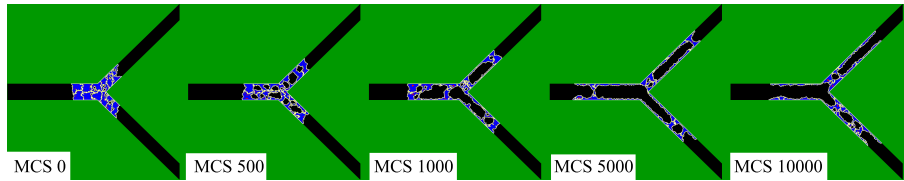
To mimic this blockage we reduced the rate of pinocytosis (P_{pin}) in our model. In agreement with the experiments, continuous lumens formed by vacuola-

4. Computational modeling of lumen formation

a. Cell-cell repulsion



b. Vacuolation



c. Combination of cell-cell repulsion and vacuolation

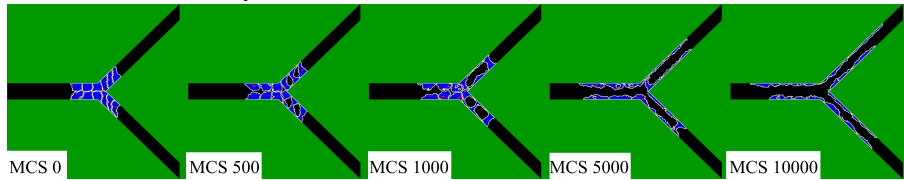


Figure 4.4: Time-lapses of lumen formation by each mechanism. a-c. A time-lapse of lumen formation by cell-cell repulsion, vacuolation, and the combined mechanism for reference setting, respectively.

tion for high pinocytosis rates, but not for low rates (Figure 4.5a and 4.5b).

4.2.7 Cell-cell repulsion requires a high cell-cell repulsion strength

Reduction of the cell-cell repulsion strength by cleavage or neutralization of the negative extracellular charged domains of CD34-sialomucins also inhibits lumen formation [33]. Lumen formation is rescued by subsequent addition of negatively charged dextran sulfate that binds to cell surfaces.

To mimic the cleavage/neutralization in our model, we reduced the repulsion strength (J_{rep}). As seen in the experiment, continuous lumens formed by cell-cell repulsion for high repulsion strengths, but not for low values of this parameter (Figure 4.5c and 4.5e).

4.2.8 Vacuolation and cell-cell repulsion combined produce lumens most robustly

Figure 4.5b and 4.5c show that lumen formation by the combined mechanism (green curve) is more robust to changes in the pinocytosis rate than the vac-

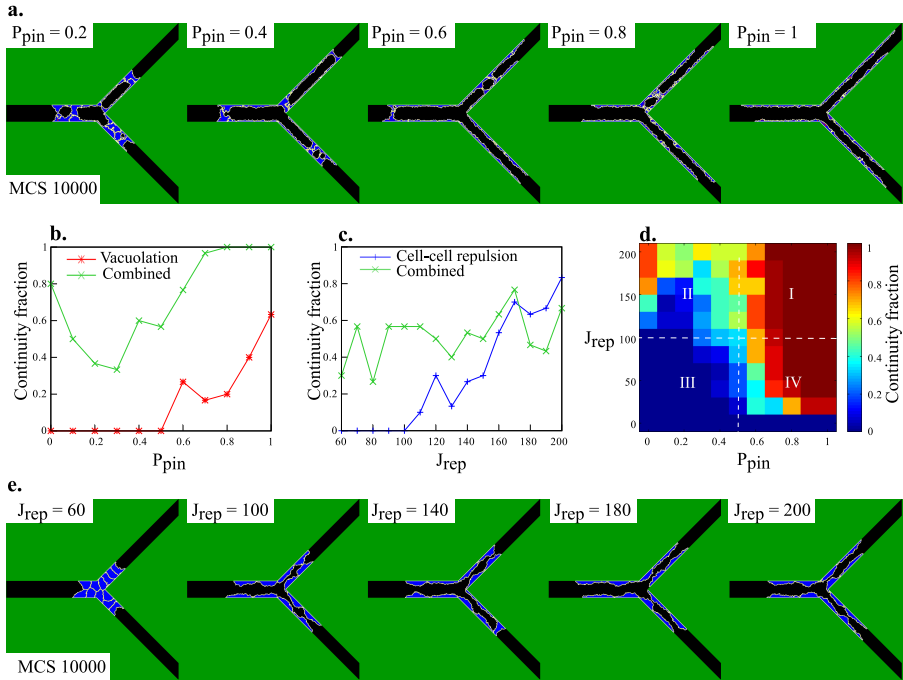


Figure 4.5: Robustness and synergy. a. Lumen formation by vacuolation at Monte Carlo Step (MCS) 10000 for different values of the pinocytosis rate (P_{pin}). b. Continuity fraction of the combined mechanism and the vacuolation mechanism as a function of P_{pin} . c. Continuity fraction of the combined mechanism and the cell-cell repulsion mechanism as a function of the repulsion strength (J_{rep}). d. The continuity fraction of the combined mechanism expressed in a heat map as a function of P_{pin} and J_{rep} . e. Lumen formation by cell-cell repulsion at MCS 10000 for different values of J_{rep} .

uolation mechanism (red curve) and that the combined mechanism is more robust to changes in the repulsion strength than the cell-cell repulsion mechanism (blue curve), respectively. The combined mechanism already has a continuity fraction of 0.8 in absence of pinocytosis (Figure 4.5b). The continuity fraction of the combined mechanism is 0.3 at $J_{rep} = 60$ compared to a continuity fraction of zero for the cell-cell repulsion mechanism (Figure 4.5c, p -value=1.1E-3).

The robustness of the combined mechanism to inhibition of the pinocytosis rate and to inhibition of the cell-cell repulsion strength disagrees with the experiments discussed above, in which inhibition of either mechanism reduced lumen formation. This discrepancy between our model and the experimental observations could be caused by the fact that the mechanisms of vacuolation and cell-cell repulsion are likely intertwined, while they are completely

separated in the model. Firstly, blockage of integrins to inhibit pinocytosis could also affect cell surface polarization, which is a crucial step for cell-cell repulsion. Secondly, cleavage or neutralization of the negative extracellular charged domains of CD34-sialomucins can affect the cytoskeleton and thereby might also affect the transport and exocytosis of vesicles and vacuole at the apical membrane. The intracellular domains of CD34-sialomucins are linked to the cytoskeleton, which disengages upon neutralization of the extracellular domains [158]. Thus the discrepancy of the combined mechanism with experiments does not necessarily mean that the combined mechanism is incorrect, but could reflect the high level of cross-talk between the mechanism that drive vacuolation and cell-cell repulsion.

4.2.9 Synergy of vacuolation and cell-cell repulsion

We next asked if the robustness of the combined mechanism is due to synergy of vacuolation and cell-cell repulsion. Figure 4.5d shows the combined effect of the pinocytosis rate P_{pin} and the repulsion strength J_{rep} on the continuity fraction of the combined mechanism. Lumens are practically never continuous for low values of P_{pin} and J_{rep} (quadrant III), and practically always continuous for high values of both (quadrant I). The high continuity fractions in quadrant IV indicate that vacuolation (dependent of P_{pin}) reinforces cell-cell repulsion (dependent of J_{rep}) in lumen formation. Similarly, the high continuity fractions in quadrant II indicate that cell-cell repulsion reinforces vacuolation in lumen formation.

How does this synergy arise in the model? The cell-cell repulsion mechanism assists the vacuolation mechanism by breaking barriers, formed by adhering cells, between the sublumens. Additionally cell-cell repulsion enlarges and stabilizes small sublumens that are created by secretion of vacuoles between cells. The vacuolation mechanism also reinforces the cell-cell repulsion mechanism. In absence of vacuolation and for low cell-cell repulsion strength, cells do not detach and the vessel thus remains solid. An increase of the pinocytosis rate (quadrant IV) results in the formation of sublumens, which drive cells to reposition into a multi-cellular, overlapping configuration. Cells that become overlapping can now detach by cell-cell repulsion in combination with secretion of vacuoles between the overlapping cells. Single cells that span the vessel can become pierced by vacuolation to create a continuous lumen. However, cell-cell repulsion for high repulsion strengths (Figure 4.5d, $J_{rep} > 140$) is more efficient in absence of pinocytosis than for low pinocytosis rates. For the latter, cells do not get the chance to overlap, as will be explained in the next section.

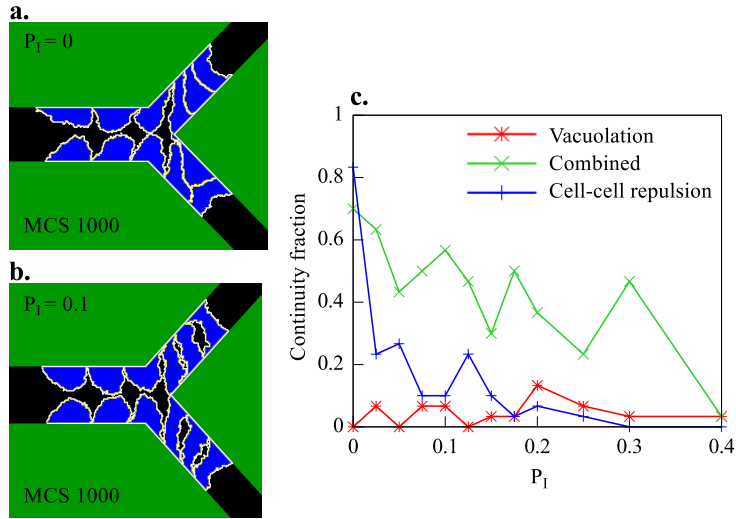


Figure 4.6: Effect of cell overlap. a. Enlarged view of overlapping cells for $P_I = 0$. b. Enlarged view of reduced overlapping capacity for $P_I = 0.1$. c. Continuity fraction of all three mechanisms as a function of P_I .

4.2.10 Cells in uni-cellular sprouts need to reposition for cell-cell repulsion

A priori, we had expected that cell-cell repulsion could only generate a continuous lumen in multi-cellular tubes and not in tubes with linearly, head-to-tail arranged cells such as in the tips of the branch. However, the cells in the branch tips repositioned to an overlapping (brick-like), multi-cellular configuration, in line with experimental observations [30, 159], and this overlap allows lumen formation by cell-cell repulsion. We found that this repositioning is driven by two counteracting forces between cells: strong attachment and active cell-cell repulsion. Cells do not immediately detach from each other upon active cell-cell repulsion as the standard CPM model treats the attachment of adjacent cell membranes as a vacuum. The membranes must zipper apart to let the fluid seep in. In presence of vacuolation (Figure 4.5d, $J_{rep} > 140$), fluid is created between cells, and cells use cell-cell repulsion to instantly detach rather than overlap.

To check if this zipping affects the efficiency of lumen formation by the cell-cell repulsion mechanism, we adapted the CPM to allow *de novo* insertion of ECM fluid [160]. With probability P_I , we consider the change in effective energy (ΔE) resulting from ECM fluid insertion $\xi_{ECMfluid}(\vec{x} \rightarrow \vec{x}')$, rather than the extension of the cell membrane $\xi_{cell}(\vec{x} \rightarrow \vec{x}')$. In this extended CPM the original CPM is recovered for $P_I = 0$. Higher values of P_I allow cells to insert

ECM fluid in between the repulsive apical membranes. Figure 4.6a and 4.6b are magnifications of MCS 1000 in the simulation for $P_I = 0$ (Figure 4.4a, Video S2) and in a simulation for $P_I = 0.1$ (Video S4), respectively. These magnifications show that cells overlap in the tips of the branch for $P_I = 0$ and not for $P_I = 0.1$. Fluid insertion between cells thus seems to reduce overlap of cells and thereby prevents lumen formation in the tips of the branch (see Figure S2 for quantified results).

We next studied the robustness of each mechanism to changes in the value of P_I . Figure 4.6c shows that the combined mechanism (green curve) is more robust to changes in P_I than the cell-cell repulsion mechanism (blue curve). The vacuolation mechanism (red curve) was not continuous for reference settings and this does not significantly change for higher values of P_I . Notably, the continuity fraction of the combined mechanism is often higher than the continuity fraction of the cell-cell repulsion mechanism and the vacuolation mechanism combined (e.g. for $P_I = 0.3$, p-value=1.1E-4), another indication of reinforcement.

4.2.11 Vacuolation requires impermeable vessel walls

The vacuolation mechanism and the cell-cell repulsion mechanism assume a different permeability of cells for fluid. Kamei *et al.* [29] showed that red quantum dots in lumens, formed by vacuolation, do not mix with the extracellular environment. The red quantum dots serially transferred from the dorsal aorta to previous unlabeled vacuolar compartments of ISVs in zebrafish. In contrast, the cell-cell repulsion mechanism assumes open connections through paracellular openings and fluid can flow into the lumen from the extracellular matrix [32]. To mimic the effect of permeable vessel walls, we tested the behavior of the model for $\lambda_{fluids} = 0$. In this case the fluids become completely compressible. Only the vacuolation mechanism requires fluid incompressibility for generating continuous lumens (Figure S3), since the lumens otherwise continuously collapse. Thus our simulations suggest that vessel walls must be impermeable to water (or lumen fluid must be actively replenished e.g. hydrostatic pressure) in order to generate continuous lumens by the vacuolation mechanism, but this is not required for the cell-cell repulsion mechanism or for the combined mechanism.

4.3 Discussion

Extensive experimental research has resulted in two alternative proposed mechanisms of lumen formation: vacuolation [28, 29] and cell-cell repulsion [32, 33]. Our computational model suggests that the two mechanisms may act synergistically in lumen formation. Cell-cell repulsion can reinforce vacuolation by stabilizing sublumens and by separating cells to connect sublu-

mens with the ECM fluid. Vacuolation can reinforce cell-cell repulsion by creating sublumens, which repositions cells into an overlapping configuration, and by piercing single cells in the tips of the branch. Additionally, vacuolation could assist in the expansion of the lumen, which was so far suggested in the cell-cell repulsion mechanism to occur by cell shape changes.

We validated our model assumptions and simulation results based on published experimental evidence. As previously discussed, for lack of quantitative values of the model parameters, the model can only make qualitative predictions. First, without apical-basolateral cell surface polarization, no lumens are formed in our model (see Figure 4.2b). This agrees with experiments in which polarization was prohibited in absence of functional vascular endothelial (VE)-cadherin or Phosphatase and Tensin homolog (PTEN) [31, 32]. Second, in our simulations of the vacuolation mechanism, lumens cannot form for low pinocytosis rates (Figure 4.5b). Experimentally, lumen formation is indeed prevented by blockage of integrin-signaling for pinocytosis [135, 157]. Third, in our simulations of the cell-cell repulsion mechanism, continuous lumens cannot form at low repulsion strengths (see Figure 4.5c). In agreement with this model prediction, neutralization or cleavage of the extracellular negative domains of CD34-sialomucins reduces lumen formation [33].

Although the model simulations suggest that the vacuolation and repulsion mechanisms act synergistically, one may ask if both mechanisms indeed co-occur *in vivo*. It is possible that vacuolation and cell-cell repulsion function in different types of vessels; vacuolation for single cell capillaries (e.g. ISV of zebrafish) and cell-cell repulsion for multi-cellular tubes (e.g. dorsal aortae of mice) [22, 29, 31, 36, 129, 130]. Therefore, we tested how the vacuolation, cell-cell repulsion and combined mechanisms would act in different types of vessels, which we represent in our model by initial configurations of one, two and three layers of cells (Figure 4.7). Cell-cell repulsion is not functional in a one-cell thick vessel with aligned cells (Figure 4.7a). Cells do start to overlap, but not sufficiently. Vacuolation does create a lumen, but it continuously collapses again (Figure 4.7b). The combined mechanism forms stable lumens (Figure 4.7c). In two-cell thick vessels, cell-cell repulsion is much more efficient than vacuolation (Figure 4.7d-f) and stable lumens form by cell-cell repulsion and by the combined mechanism, but not by vacuolation. In three cell-thick vessels, the cell-cell repulsion and combined mechanisms can reproduce cavitation, the apoptosis of cells in the middle of the vessel that detached from the vessel wall (Figure 4.7g and Figure 4.7i), which is often seen in epithelium [131]. Interestingly, the combined mechanism produces phenomena that optically resemble aspects of vacuolation or of cell-cell repulsion, depending on whether it acts in one-cell thick vessels or in two-cell thick vessels. The optical resemblance of vacuolation is illustrated in Fig-

4. Computational modeling of lumen formation

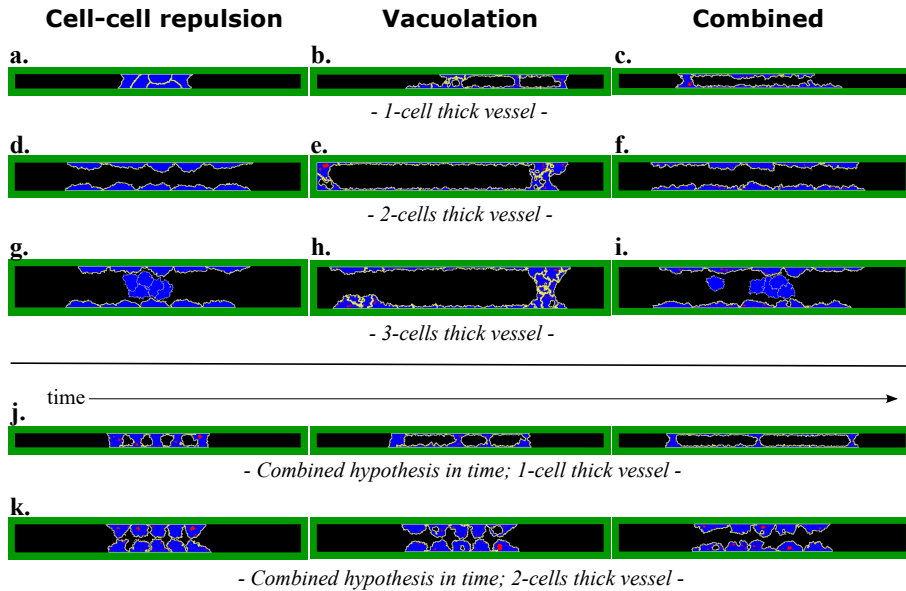


Figure 4.7: Lumen formation by each mechanism in different vessel types. a-i. Lumen formation by cell-cell repulsion, vacuolation, or the combined mechanism from left to right for an initial vessel thickness of one cell (top row), two cells (second row), or three cells (third row) at MCS 10000. j-k. Time-lapse (MCS 500, 1000, and 2000) of lumen formation by the combined mechanism in a one-cell thick vessel and in a two-cells thick vessel.

ure 4.7j) and of cell-cell repulsion in Figure 4.7k, which show the temporal development of lumen formation by the combined mechanisms in a one-cell thick vessel and a two-cells thick vessel, respectively. Thus, although vacuolation is observed in capillaries and cell-cell repulsion in multi-cellular tubes, the combined mechanism could be the underlying mechanism in both vessel types.

To validate if the combined mechanism is actually functional *in vivo*, we propose the following experiments. Based on our modeling results in Figure 4.7, we expect that inhibition of vacuolation by reducing pinocytosis should prevent lumen formation in capillaries (as in Figure 4.7a), but not in larger vessels (as in Figure 4.7d and Figure 4.7g) and inhibition of cell-cell repulsion by cleavage of negatively charged extracellular proteins should destabilize lumen formation in all vessel types (as in Figure 4.7b, Figure 4.7e, and Figure 4.7h). Here simply visualizing vacuoles microscopically will not suffice for validating the combined mechanism: Lumens also form with cell-cell repulsion in combination with secretion of pinocytotic vesicles, without fusion of vesicles into vacuoles, depending on the amount of vesicles (Figure S4).

Besides synergy of the vacuolation and cell-cell repulsion mechanisms, our

model also predicts that lumen formation by cell-cell repulsion in uni-cellular tubes requires cells to reposition into a (brick-like) overlapping, multi-cellular configuration. Our model results suggest that cell-cell adhesion along with strong cell-cell repulsion strengths facilitate the formation of such overlapping cellular configurations. To validate this mechanism, it should be established experimentally if cells immediately detach once CD34-sialomucins are in the apical membrane, or that strong adhesion keeps them attached for time spans sufficiently long to allow overlap of cells.

These validation experiments all result from qualitative model predictions, as the quantitative values for most parameters are not known. Dose-dependent experiments for cell adhesion strengths, pinocytosis rates and cell-cell repulsion strengths can help to tune the representing qualitative parameters in the model. Additionally, various parameters could be quantified experimentally to allow for quantitative model predictions. The adhesion strength of cells can be quantified by the force that is required to pull them apart [161]. This method might also be useful to find quantitative values, or at least the relative ordering, of the contact energy parameters that describe adhesions between polarized cells, non-polarized cells and possibly also the ECM. Other contact energy parameters of our model describe adhesions of subcellular compartments such as vesicles, which cannot be quantified in this way. Instead, vesicles and vacuoles can be visualized microscopically and their speed and type of movement (e.g. diffusive) could thus be quantified.

Our model can become a useful tool for designing new experiments and new insights into lumen formation. We propose three new research questions in which we believe a cooperation of computational and experimental research is important. Firstly, what is the exact function of several key proteins in lumen formation? Cdc42 and Moesin1 are for instance suggested to be involved in polarization of the cell, in targeting of vesicles to the apical membrane and in structural changes of the cytoskeleton for cell shape changes [31, 32, 142]. It is difficult to pinpoint their exact function by experiments only, since lumen formation fails all together in absence of these proteins. Secondly, how is lumen formation regulated in dynamically growing sprouts? To focus on lumen formation, we started our model with a preformed sprout. To gain insight in the regulation of angiogenesis as a whole, the model could be extended with ECM remodeling and dynamic sprouting. Thirdly, if the combined mechanism indeed drives lumen formation, then how are the two mechanisms regulated and balanced to locally optimize lumen formation? For each question, the model can be used to test consistency of hypotheses, which can provide new insights and help to guide new experiments. In conclusion, in cooperation with experimentalist, our simulation model can contribute to a better understanding of the mechanisms of lumen formation during blood vessel development.

1	1	1	2	2	2
1	1	1	2	2	2
1	1	1	1	3	2
1	4	5	3	3	3
4	4	5	5	5	3
4	4	4	4	4	3

Figure 4.8: Representation of cells in the extended CPM. The extended CPM projects cells on a regular lattice and cells can consist of multiple compartments. All lattice sites, \vec{x} , of the same cell are outlined by a bold black line, representing that they share the same unique cell identifier $\xi(\sigma(\vec{x}))$. Each lattice site has a number that represents its compartment identifier $\sigma(\vec{x})$ and its type $\tau(\sigma(\vec{x}))$ is indicated by its color.

4.4 Material and methods

We developed an agent-based, computational model of lumen formation that connects the subcellular, cellular and the ‘vessel’ scales. The cellular Potts Model (CPM) [61, 62] describes the motility, shape and physical interactions of cells. The basic CPM is explained in Section 2.4.1. To model polarization of the cell surface and the creation of fluid-filled vesicles and vacuoles, we use an extension of the CPM in which cells can compartmentalize [140]. In this section, we first explain the extended version of the CPM. Next we outline the modeling of pinocytosis, vesicle and vacuole movement and secretion.

4.4.1 Extended CPM

The CPM projects cells on a regular lattice (Figure 4.8). Each lattice site, \vec{x} , is associated with a unique compartment identifier $\sigma(\vec{x})$ and has a type $\tau(\sigma(\vec{x}))$, which can be *cytoplasm*, *apical*, *basolateral*, *vesicle*, *vacuole*, *ECM*, *ECM fluid* or *luminal fluid* (Figure 4.3). Initially cells, ECM and ECM fluid consist of a single compartment with a unique cell identifier $\xi(\sigma(\vec{x}))$. Additional compartments, that are formed in a cell upon membrane polarization and vacuolation, obtain the same cell identifier $\xi(\sigma(\vec{x}))$. New cell identifiers with type *luminal fluid* are created upon secretion of vesicles and vacuoles. To model random motility, fluids and subcellular compartments (except for vesicles) move by copies from \vec{x} to a randomly selected second neighboring lattice site \vec{x}' (Figure 4.3a), as explained in Section 2.4.1.

The effective energy of the system (H) depends on the areas and contacts

(adhesive properties) of cells, compartments and fluids: $H = H_{area} + H_{contact}$. H_{area} is the costs in energy for deviation of the actual area (a) from the preferred target area (A), with an elasticity lambda, and is given by:

$$H_{area} = \lambda_{area}(\xi) \sum_{\xi} (A(\xi) - a(\xi))^2 + \lambda_{area}(\sigma) \sum_{\sigma} (A(\sigma) - a(\sigma))^2. \quad (4.1)$$

We model fluids as near-incompressible fluids; fluids are cell identifiers of type *ECM fluid* or *luminal fluid* with $\lambda_{area}(\xi) \neq 0$ and $\lambda_{area}(\sigma) \neq 0$.

Contact energy ($H_{contact}$) mimics adhesion and repulsion at interfaces of compartments. There are two types of contact energy: internal (J_I) and external (J_E). Internal contact energy is defined between compartments of the same cell and external contact energy between compartments of different cells. The total contact energy is defined as:

$$H_{contact} = \sum_{(\vec{x}, \vec{x}')} J_E(\tau(\sigma(\vec{x})), \tau(\sigma(\vec{x}')))(1 - \delta(\xi(\sigma(\vec{x})), \xi(\sigma(\vec{x}')))) + \quad (4.2)$$

$$\sum_{(\vec{x}, \vec{x}')} J_I(\tau(\sigma(\vec{x})), \tau(\sigma(\vec{x}')))(1 - \delta(\sigma(\vec{x}), \sigma(\vec{x}')))\delta(\xi(\sigma(\vec{x})), \xi(\sigma(\vec{x}')))$$

, with the Kronecker delta $\delta(x, y) = 1, x = y; 0, x \neq y$. All J-values are listed in Table 4.2 and 4.3. Cells (non-polarized or polarized) remain a solid vessel in absence of lumen formation mechanisms (Figure 4.2b and 4.2c) for reference J-values.

4.4.2 Pinocytosis

During each Monte Carlo Step (MCS), as many copy attempts as there are lattice sites in the lattice are performed (550x550). Extra mechanisms (m) of lumen formation are performed after every n_m Monte Carlo Steps (Figure 4.9). Cell surfaces polarize every other MCS (Figure 4.9; mechanism 5; $n_5 = 2$) to allow these polarized membrane lattice sites to internalize by usual CPM copies, representing invagination of ECM fluid at the membrane as seen during pinocytosis. Such internalized polarized membrane lattice sites become compartments of type *vesicle* with probability P_{pin} or otherwise part of the cytoplasm (Figure 4.9; function 6; $n_6 = 2$). A vesicle is kept one lattice site in size by a target area of one and a high lambda. As ECM fluid is taken up into the vesicle during pinocytosis, the target area of ECM fluid decreases, while the target area of the pinocytosing cell increases by one.

4.4.3 Vesicle and vacuole movement

Vesicles swap position with a randomly selected neighbor once per MCS (Figure 4.9; function 1; $n_1 = 1$). This swapping is performed with a preset accep-

4. Computational modeling of lumen formation

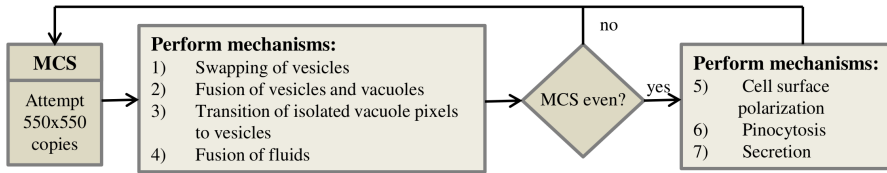


Figure 4.9: Flowchart of the model. During each time step, also called Monte Carlo Step (MCS), as many copy attempts as there are lattice sites in the lattice (550x550) are attempted. After each time step, or after every other time step, additional functions for lumen formation are performed.

tance probability P_A multiplied by $P_{Boltzmann}(E)$, with E the resulting effective energy of the swap. P_A tunes the velocity of the vesicle.

Fusion events of vesicles and vacuoles can occur every MCS (Figure 4.9; function 2; $n_2= 1$) and during a copy of a vacuole over a vesicle. Every MCS, neighboring compartments of type *vesicle* or *vacuole* fuse with probability P_{fuse} into a single compartment with type *vacuole*. The target area of the formed vacuole is the sum of the target areas of the fused compartments. Similarly, when a vacuole copies over a vesicle of the same cell, the target area of the vacuole is increased by the target area of the vesicle.

As vesicles can become vacuoles by fusion, small vacuoles can also become vesicles. First, single lattice sites of type *vacuole* that are split off from a vacuole, called the donor vacuole, and are surrounded by cytoplasm become vesicles each MCS (Figure 4.9; function 3; $n_3= 1$). Second, a donor vacuole that became a single lattice site in size by a copy becomes a vesicle. In both cases, the created vesicle gets a target area of one, unless the donor vacuole in question had a target area of zero. Then the vesicle is assigned with a target area of zero and will soon be deleted by regular CPM movements. If a donor vacuole remains, the target area of the created vesicle is subtracted from the target area of the donor vacuole. If a donor vacuole becomes one lattice site in size by a copy event and has a target area larger than one, its residual target area must be redistributed to remain a target area of one for the created vesicle. If the donor vacuole was copied over by luminal fluid or a vacuole, the residual target area is added to that compartment. Otherwise, the residual target area is added to ECM fluid to keep the total target area of the system constant.

4.4.4 Secretion

Secretion can occur every other MCS (Figure 4.9; function 7; $n_7= 2$) and by a copy of a fluid over a vesicle or vacuole. Every other MCS, a lattice site at the membrane of type *vesicle* or *vacuole*, together with all first order connected

lattice sites of type *vesicle* or *vacuole*, become a compartment of type *luminal fluid*. The combined target area of the simultaneously secreted vesicles and vacuoles is assigned to the luminal compartment and is subtracted from target area of the secreting cell. If only a part of the vacuole is secreted, then the size of the secreted part is subtracted from the target area of the vacuole, leaving a vacuole with a minimal target area of zero. Secretion can also occur by a copy \vec{x} to \vec{x}' , for which $\tau(\sigma(\vec{x}'))$ is *vesicle* and $\tau(\sigma(\vec{x}))$ is *luminal fluid* or *ECM fluid*, resulting in a decrease of one of the target area of the secreting cell and an increase of one of the fluid. Similarly, the target area of the secreting cell decreases by one when its vesicle is copied over by a compartment of the same cell of type *apical*, *basolateral* or *cytoplasm* or by a compartment of another cell. To conserve the total target area of the system, the target area of ECM fluid is then increased by one.

ECM fluid and luminal fluids can fuse every MCS (Figure 4.9; function 4; $n_4=1$) and by some copy events. Neighboring cells of type *luminal fluid* are fused every MCS and can fuse to ECM fluid when the luminal fluid is in contact with the surrounding ECM or when it is completely surrounded by ECM fluid. When luminal fluid copies over luminal fluid of a different cell identifier and thereby deletes it, the target area of the latter is added to the first. If luminal fluid is deleted by another cell type than *luminal fluid*, its target area is added to ECM fluid.

Table 4.1: Reference values of external contact energy. The external contact energy (J_E) is listed for each type combination.

	cytoplasm	basolateral	apical	vesicle	vacuole	ECM	ECM fluid	luminal fluid
cytoplasm	10							
basolateral	10	30						
apical	200	50	200					
vesicle	10	10	10	10				
vacuole	10	10	10	10	10			
ECM	130	10	10	10	10	10		
ECM fluid	10	200	50	10	10	130	0	
luminal fluid	10	200	50	10	10	130	0	0

4. Computational modeling of lumen formation

Table 4.2: Reference values of internal contact energy. The external contact energy (J_l) is listed for each type combination.

	cytoplasm	basolateral	apical	vesicle	vacuole	ECM	ECM fluid	luminal fluid
cytoplasm	10	5	5	10	20	-	-	-
basolateral		10	70	100	100	-	-	-
apical			10	1	1	-	-	-
vesicle				10	5	-	-	-
vacuole					5	-	-	-
ECM						-	-	-
ECM fluid							-	-
luminal fluid								-

Table 4.3: Reference parameter values. The reference value is listed for parameters that regard probabilities, the motility μ and the elasticity for certain types.

$P_A = 1.0$	$P_{fuse} = 1.0$	$P_{pin} = 1.0$	$\mu = 50$
$\lambda_{cell} = 7$	$\lambda_{fluids} = 6$	$\lambda_{vacuole} = 50$	$\lambda_{vesicle} = 1000$

4.A Supplementary movies

An archive containing all supplementary movies can be found at <http://persistent-identifier.org/?identifier=urn:nbn:nl:ui:18-23531>.

Movie S1 Cell-cell repulsion mechanism. Video of lumen formation by the cell-cell repulsion mechanism that corresponds to Figure 4.4a ($P_{pin} = 0$, $J_{rep} = 200$, $P_l = 0$); continuous lumens are formed.

Movie S2 Vacuolation mechanism. Video of lumen formation by the vacuolation mechanism that corresponds to Figure 4.4b ($P_{pin} = 0.5$, $J_{rep} = 0$, $P_l = 0$); no continuous lumens are formed.

Movie S3 Combined mechanism. Video of lumen formation by the combined mechanism that corresponds to Figure 4.4c ($P_{pin} = 0.5$, $J_{rep} = 200$, $P_l = 0$); continuous lumens are formed.

Movie S4 Cell-cell repulsion mechanism with *de novo* fluid creation between membranes. Video of lumen formation by the cell-cell repulsion mechanism, during which fluid can be created *de novo* between adhering cells, that corresponds to Figure 4.6b ($P_{pin} = 0$, $J_{rep} = 200$, $P_l = 0.1$); no continuous lumens are formed.

4.B Supplementary figures

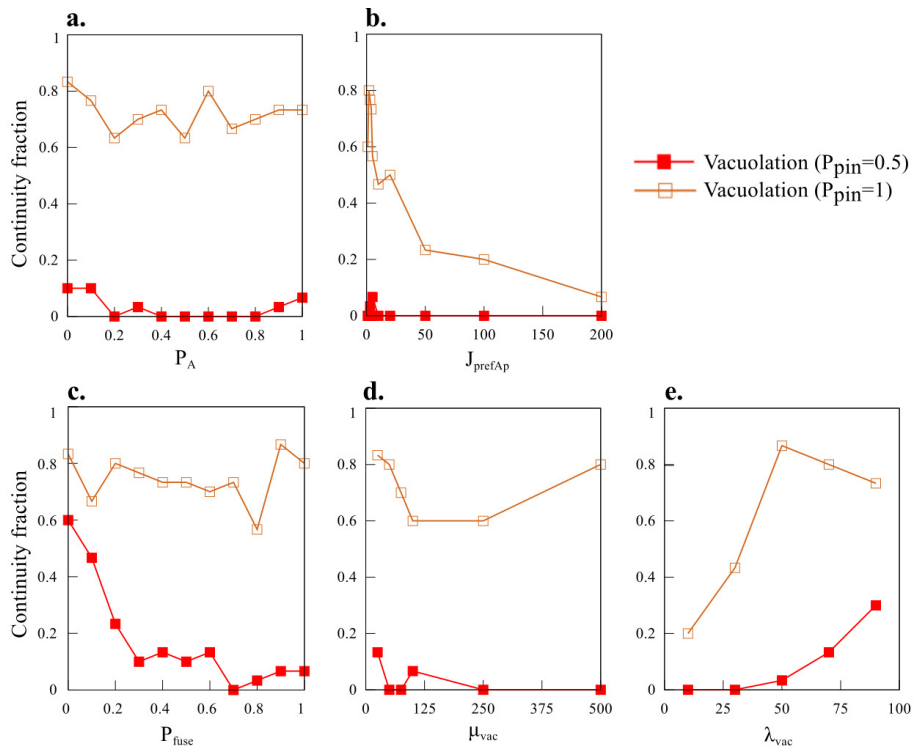


Figure S1: Sensitivity to vesicle and vacuole transport and fusion. a-e. Effect of vesicle movement (J_{prefAp} , P_A) or vacuole dynamics (P_{fuse} and λ_{vac}) on the continuity fraction of lumen formation. The effect on the continuity fraction is plotted for vacuolation with $P_{pin} = 0.5$ (filled squares) to examine if this parameter can stimulate lumen formation and for vacuolation with $P_{pin} = 1.0$ (unfilled squares) to examine if this parameter can break down lumen formation.

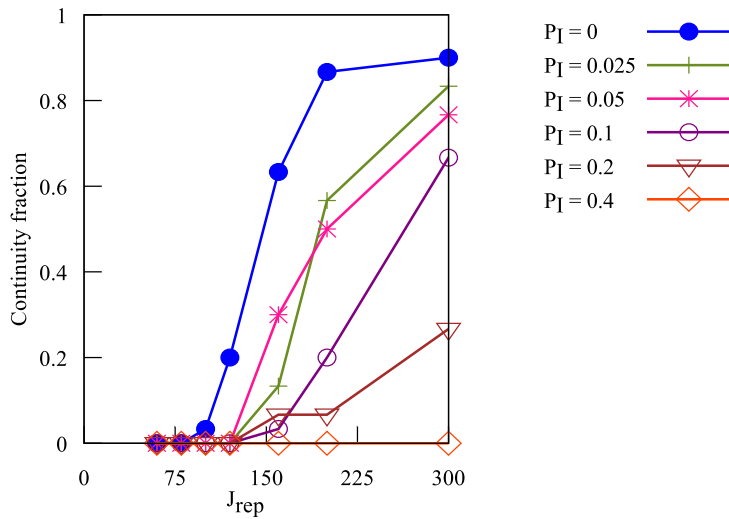


Figure S2: Effects of fluid insertion between cells on cell overlap. Continuity fraction for the cell-cell repulsion mechanism for different P_I values as a function of J_{rep} .

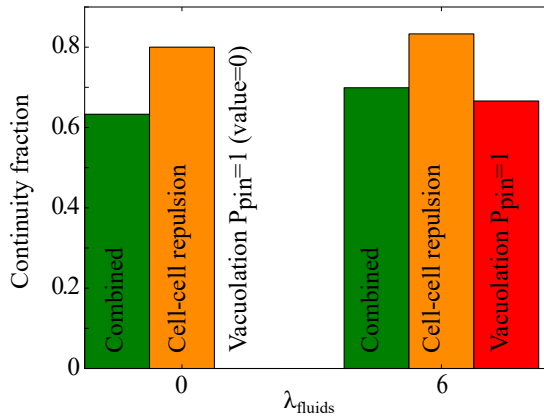


Figure S3: Cell permeability. Effect of fluid compressibility (λ_{fluids}) on the continuity fraction of lumen formation by the cell-cell repulsion mechanism, by the vacuolation mechanism with a high pinocytosis rate ($P_{pin} = 1.0$) and by the combined mechanism ($P_{pin} = 0.5$).

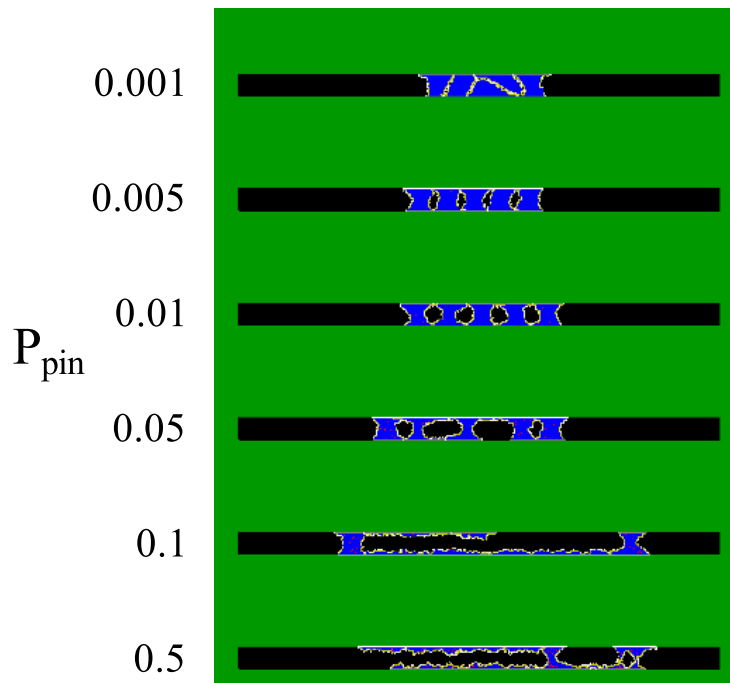


Figure S4: Lumen formation by the combined mechanism without vacuoles. The effect of the pinocytosis rate (P_{pin}) on the combined mechanism without fusion of vesicles into vacuoles ($P_{fuse} = 0$) at MCS 10000.

5

A global sensitivity analysis approach for morphogenesis models

This chapter is based on:

Sonja E. M. Boas, Maria I. Navarro Jimenez, Roeland M.H. Merks and Joke G. Blom, *A global sensitivity analysis approach for morphogenesis models*. BMC Systems Biology (in press) arXiv: 1507.08504

Abstract

Morphogenesis is a developmental process in which cells organize into shapes and patterns. Complex, non-linear and multi-factorial models with images as output are commonly used to study morphogenesis. It is difficult to understand the relation between the uncertainty in the input and the output of such 'black-box' models, giving rise to the need for sensitivity analysis tools. In this chapter, we introduce a workflow for a global sensitivity analysis approach to study the impact of single parameters and the interactions between them on the output of morphogenesis models.

To demonstrate the workflow, we used a published, well-studied model of vascular morphogenesis. The parameters of this cellular Potts model (CPM) represent cell properties and behaviors that drive the mechanisms of angiogenic sprouting. The global sensitivity analysis correctly identified the dominant parameters in the model, consistent with previous studies. Additionally, the analysis provided information on the relative impact of single parameters and of interactions between them. This is very relevant because interactions of parameters impede the experimental verification of the predicted effect of single parameters. The parameter interactions, although of low impact, provided also new insights in the mechanisms of *in silico* sprouting. Finally, the analysis indicated that the model could be reduced by one parameter.

We propose global sensitivity analysis as an alternative approach to study the mechanisms of morphogenesis. Comparison of the ranking of the impact of the model parameters to knowledge derived from experimental data and from manipulation experiments can help to falsify models and to find the operand mechanisms in morphogenesis. The workflow is applicable to all 'black-box' models, including high-throughput *in vitro* models in which output measures are affected by a set of experimental perturbations.

5.1 Background

In this thesis, we have introduced several computational models of vascular morphogenesis. Morphogenesis is a key process in biological development that describes the organization of multiple cells into shapes and patterns, such as vascular networks. Computational modeling is commonly used to study mechanistic hypotheses on morphogenesis [111, 162–167] as they allow for simplification and isolation of the process. As for the models in this thesis, these computational studies typically involve multi-scale, non-linear and multi-factorial models. So far, the behavior of these computational models is studied for one or occasionally two parameters at a time, which can lead to a wrong interpretation for non-linear models, because the effects of changes in the fixed parameters are not linear and thus often unpredictable.

Studying all parameters collectively with global sensitivity analysis resolves this problem.

In this chapter, we introduce a workflow that uses global sensitivity analysis to find the relevant single parameters and parameter interactions in ‘black-box’ models of morphogenesis, which are strongly non-linear and multifactorial. Sensitivity analyses of computational models enable us to identify the effects of uncertainties in parameter values on the model output. Local sensitivity analysis investigates the behavior of the model in a small region around the nominal parameter values and is most often used to study model robustness. Global sensitivity analysis (GSA) covers the entire input parameter space, or a specifically selected region hereof. In its most powerful form, it gives information on the impact of individual parameters and combinations thereof on a nonlinear model for arbitrary parameter distributions. This is what e.g. variance-based methods like FAST [168] and the Sobol’ method [169, 170] do. This, of course, is computationally expensive, therefore many methods have been proposed with simplifying assumptions like linearity of the model (MLR [171]); methods that produce less sophisticated results, e.g. partial or no information on interactions (Morris method [172]; [173, 174]); are less robust like DGSM ([175, 176]); or that use prior knowledge of the model, like Bayesian DGSM [177]). In this paper we use the Sobol’ method [170], where we have modified the original method for efficiency reasons (for more details see Section 5.2.2). Moreover, we introduce an approach to determine the sampling size *a priori* with an *a posteriori* error check. Thus, it is not likely that the proposed GSA will excel in computational efficiency, but it will excel in predictability of the costs and reliability of the results. In the biological field GSA is mostly applied to ODE-type models, e.g., in pharmacology [178, 179], neurodynamics [180], or gene expression [181] and biochemical pathways [177] in cells.

GSA can give interesting new insights into models of morphogenesis. Firstly, GSA predicts which parameters can best be tuned to affect the model output. When the model parameters can be associated with biological cell properties, extracellular matrix properties, or gene expression, knowledge of their influence on morphogenesis can give predictions for *in vitro* perturbation experiments, e.g. genetic knock-outs. Secondly, apart from identifying the impact of single parameters, GSA notably identifies parameter interactions. These can give new mechanistic insights in the functioning of the model. Thirdly, GSA is a tool to reduce the number of parameters in the model. When the analysis indicates that parameter variation does not impact the model output, the parameter value can be fixed. Fourthly, GSA can be used to make a selection of models that support biologically plausible hypotheses in a set of contradicting mechanistic hypotheses.

As a case study, we performed GSA on a previously published [64], well-

studied computational model of vascular morphogenesis. In the model, a spheroid of cells develops into a vascular network. Cells secrete a compound to which cells chemotact by migrating towards higher concentrations of the compound. Vascular networks form when chemotaxis is inhibited at cell-cell interfaces. Vascular endothelial growth factor (VEGF) is a candidate for the secreted compound and extensions of pseudopods in the direction of cell-cell contacts might be locally inhibited by interference of vascular endothelial cadherins with VEGF receptor 2 signaling. Because of the key role of such ‘contact-inhibited chemotaxis’ in this model, we will henceforth refer to it as the ‘contact inhibition model’. Numerous alternative hypotheses for vascular morphogenesis have been proposed [16, 63, 64, 66, 69, 71, 108, 111, 182], and it is unsure which of these - if any - is correct. Thus the contact inhibition model is here used as an example model for morphogenesis, while the proposed GSA approach can assist in falsifying mechanisms in the future.

Figure 5.1 shows the workflow of the GSA analysis proposed in this chapter. The input (Figure 5.1A), a list of parameter sets, is fed into the cellular Potts-based contact inhibition model (Figure 5.1B). This model generates images (Figure 5.1C) of the resulting cell configuration as raw output, ranging from spheroids, to networks, to dispersed cells. Subsequently, two quantitative output measures (compactness and lacuna count) are derived from these images (Figure 5.1D). Two types of GSA are performed on the output measures (Figure 5.1E). Firstly, intensity plots show the impact of parameter combinations on the variation in the output measures (Figure 5.1F). This analysis only allows for a two-dimensional GSA, in which the value of two parameters are varied simultaneously while keeping all other parameter values fixed. Secondly, a truly multivariate GSA ranks the impact of individual parameters and of parameter combinations on the variance of the output measures (Figure 5.1G). Important aspects we address in this chapter are the reliability and the pitfalls of GSA.

5.2 Methods

5.2.1 Vascular morphogenesis model

The contact inhibition model [64] is based on the cellular Potts Model (CPM) [61, 62], for details on the CPM see Section 2.4.1. The nominal parameters settings are conform the settings in our previous work [64].

Each cell identifier is associated with a type: $\tau(\sigma) \in \{\text{ECM, cell, border}\}$. Cells have cell properties and behaviors, such as adhesion, cell size, and chemotaxis. There are three non-zero types of adhesion: $J_{\text{cell,cell}}$, $J_{\text{cell,border}}$ and $J_{\text{cell,ECM}}$. $J_{\text{cell,cell}}$ represents the adhesion strength between cells, and $J_{\text{cell,ECM}}$ the adhesion strength of cells to the ECM. The lattice is surrounded with a border by which cells are repulsed, by setting $J_{\text{cell,border}} = 100$.

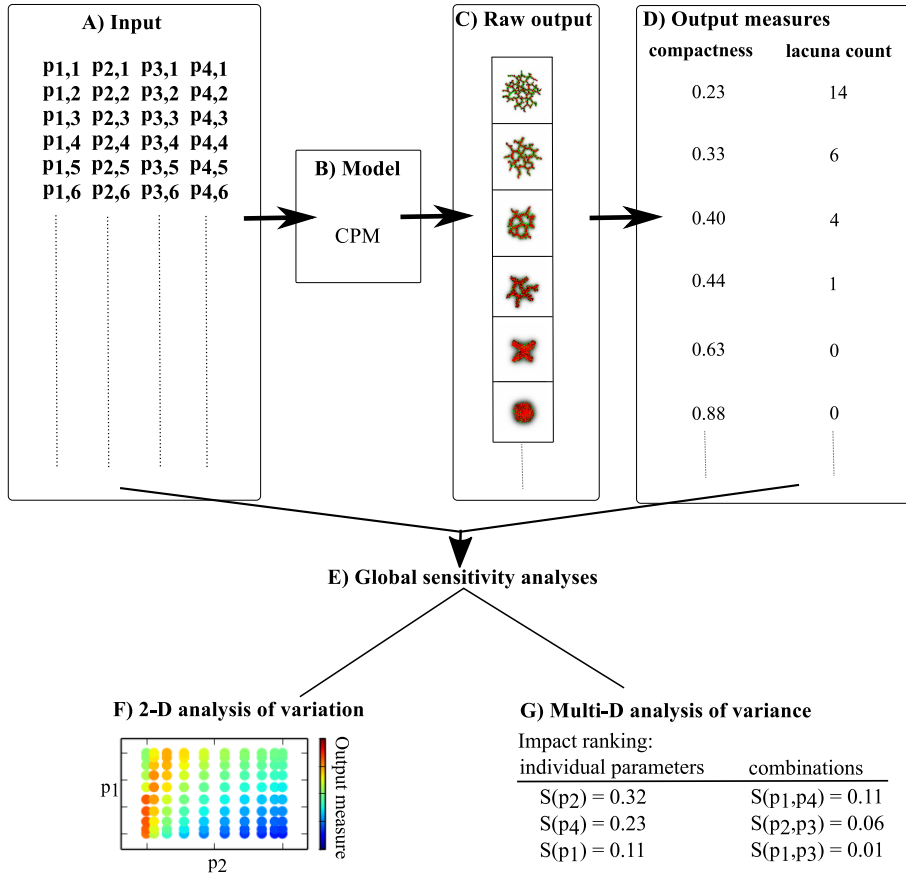


Figure 5.1: Overview of the global sensitivity analysis. (A) The input of the model is a list of parameter sets. Each parameter set contains uniformly randomly selected values of parameters p_1 to p_4 . This input is then fed into (B) the cellular Potts Model (CPM)-based contact inhibition model. (C) The raw output of these models are images of the cell configuration at the end of the simulations. (D) Two output measures, compactness and lacuna count, are derived from these images. Two types of global sensitivity analysis are performed on these output measures (E). Firstly, intensity plots are used to study the impact of two-parameter combinations on the variation in the output measures (F). Secondly, Sobol' indices are used to rank the impact of individual parameters and of parameter combinations on the variance of the output measures (G).

Chemotaxis. We assume that cells secrete a chemoattractant at rate α (s^{-1}), producing a concentration field $c(\vec{x})$. The chemoattractant diffuses with a diffusion coefficient D (m^2/s) and decays with rate ϵ (s^{-1}) in the ECM,

resulting in the following PDE:

$$\frac{\partial c}{\partial t} = \alpha(1 - \delta(\sigma(\vec{x}), 0)) - \epsilon\delta(\sigma(\vec{x}), 0)c + D\nabla^2 c, \quad (5.1)$$

such that secretion is located at the cells, where $\delta(\sigma(\vec{x}), 0) = 0$, and decay in the ECM. The field of the chemoattractant is initialized as $c(\vec{x}) = 0$ and fixed boundary conditions are imposed. Cells can respond to this chemoattractant by migrating towards higher concentrations (chemotaxis). To this end, the change in the Hamiltonian by that copy, ΔH , is augmented with $\Delta H_{\text{chemotaxis}} = \lambda_c(c(\vec{x}) - c(\vec{x}'))$ [121], and contact-inhibition is implemented by setting $\lambda_c = 0$ at cell-cell interfaces such that chemotaxis only occurs at the cell-ECM interface.

The PDE for chemoattractant diffusion and degradation (Equation 5.1) is discretized on the CPM lattice and we solve it numerically using a finite-difference scheme. We use 15 diffusion steps per MCS. The model is initialized with a centralized spheroid of 256 cells within a lattice of 400×400 sites (lattice spacing $2\mu\text{m}$). We run the model for 5000 MCS, each representing 30 seconds, as networks are well formed in this time in the model as well as *in vitro* [63].

5.2.2 Global sensitivity analysis

The variation in a solution or a measure thereof, like compactness, over the complete parameter space can only be visually inspected by looking at one or at most two parameters at a time while keeping the others fixed (cf. Figure 5.2, 5.4, and 5.5). Since different measures will produce different multivariate output distributions and therefore also might result in a different outcome of the GSA, it is important to choose a measure or, more likely a number of measures that are significant for the study at hand. If one wants to take the influence of all parameters simultaneously into account some form of a global measure of the multivariate output distribution is required. One such a measure is the variance of the distribution, which will be used in this paper.

We are specifically interested whether parameter *interactions* have a large impact on the output of this specific CPM-based model. Interactions of the parameters are unpredictable in non-linear models such as the CPM, but their impact is significant, since a large combined effect of parameters on the output impedes the experimental testing of a predicted effect of a single parameter.

Sobol' [169, 170] introduced so-called global sensitivity indices that describe the impact of specific parameters or combinations thereof on the uncertainty in the model output and more in particular on the variance of the output distribution, hence the term 'variance-based' GSA. In the original method the necessary integrals are computed with Monte Carlo. However, the

Sobol' indices can be computed very efficiently when the distribution of the output measure or response surface is expanded into a series of orthogonal polynomials, the Polynomial Chaos Expansion (PCE) [183, 184]. An overview of this method, using the same notation as in the following, can be found in [185]; here we summarize only the most important definitions for the case that the stochastic input consists of independently uniformly distributed random variables. Note, however, that the method can also be applied for arbitrary, even non-parametric, distributions, allowing for data-driven GSA (see also [186]). The strength of the method described below is that it (i) can efficiently study multiple output measures derived from the output images, (ii) can robustly identify parameter interactions, and (iii) checks the reliability of the result.

Let ξ be the n -dimensional vector of the independently uniformly distributed input parameters and $\varrho(\xi)$ its joint probability density function (pdf). The output measure $u(\xi)$, e.g., of the (black-box) cellular Potts Model, is expanded into a truncated series of polynomials that are orthogonal with respect to the pdf ϱ , separating the output into a deterministic and a stochastic part

$$u(\xi) \approx \sum_{i=0}^N u_i \Phi_i(\xi), \quad (5.2)$$

where the n -variate polynomials $\Phi_i(\xi)$ are products of n univariate Legendre polynomials. The number of expansion terms N is given by $N + 1 = \frac{(n+\hat{p})!}{n! \hat{p}!}$, with n the number of parameters and the *approximation order* \hat{p} the highest order of Φ_i .

To compute the expansion coefficients u_i of Equation (5.2) we apply *Spectral Projection* which has the advantage that it can be used for black-box models since it projects the solution - and not the model - onto the polynomial space

$$u_i = \frac{\langle u(\xi), \Phi_i(\xi) \rangle}{\langle \Phi_i(\xi), \Phi_i(\xi) \rangle} = \frac{1}{\|\Phi_i\|^2} \int_{\Xi} u(\xi) \Phi_i(\xi) \varrho(\xi) d\xi, \quad i = 0, 1, \dots, N, \quad (5.3)$$

where Ξ is the support of the joint pdf $\varrho(\xi)$. As the parameter inputs are independent, both Φ_i and ϱ can be written in product form; for the multivariate polynomial Φ_i this results in a product of univariate polynomials

$$\Phi_i(\xi) = \prod_{k=1}^n \Phi_{\text{index}(i,k)}(\xi_k), \quad \text{with } \text{index}(i, k) = \{0, \dots, \hat{p}\} \text{ and } \Phi_0(\xi_k) = 1. \quad (5.4)$$

The integrals in Equation (5.3) can then be computed by a repeated one-dimensional Gauss-Legendre quadrature rule

$$u_i \approx \frac{1}{\|\Phi_i\|^2} \sum_{l_1=1}^{N_g} \cdots \sum_{l_n=1}^{N_g} u(\xi_{l_1}, \dots, \xi_{l_n}) \prod_{k=1}^n w_{l_k} \Phi_{\text{index}(i,k)}(\xi_{l_k}), \quad (5.5)$$

5. Sensitivity analysis of network formation

with N_q the number of quadrature points and w the associated weights. Note, that for integrals with a known weight function, like e.g. a pdf, Gauss quadrature has the optimal convergence order of $2N_q - 1$ for N_q quadrature points, where the points and the weights of the quadrature rule are dependent on the weight function.

How to choose N_q and \hat{p} to obtain reliable Sobol' indices will be the subject of Section 5.2.3.

Statistics and Polynomial Chaos Expansion

Using a PC expansion, the only input needed to compute the moments and the Sobol' indices of the output distribution are the expansion coefficients. E.g., the mean $\mu = u_0$ and the variance is given by

$$\int_{\Xi} (u(\xi) - \mu)^2 \varrho(\xi) d\xi \approx \sum_{i=1}^N u_i^2 \|\Phi_i\|^2 =: \text{Var}_{\text{PCE}}. \quad (5.6)$$

Note, that the approximation, Var_{PCE} , is a monotonously increasing function of N and thus of \hat{p} . The sum in the variance formula can be directly split into contributions from the various parameters or combinations thereof, the Sobol' indices (cf. [187]). E.g., for the first-order Sobol' index for parameter j only terms contribute if $\Phi_i(\xi)$ equals a univariate polynomial in ξ_j

$$S_j \approx \frac{\sum_{i=1}^N \text{bool}(i, j) u_i^2 \|\Phi_i\|^2}{\text{Var}_{\text{PCE}}}, \quad (5.7)$$

where $\text{bool}(i, j) = (\text{index}(i, j) > 0 \wedge \text{index}(i, k) = 0, \forall k \neq j)$. For a combined influence of more than one parameter like S_{13} the Sobol' index can be computed analogously. The sum of all Sobol' indices equals one.

5.2.3 Reliable GSA in practice

At first sight the accuracy of the PCE approximation of the response surface - and thus of the statistics - seems to be determined by the *number* of expansion terms, N , in Equation (5.2). But the *accuracy* of the expansion coefficients u_i also plays an important role. This accuracy is determined by the approximation (Equation 5.5) of the integral in Equation (5.3), which is determined by the number of quadrature points, N_q . Moreover, the higher PCE order \hat{p} needed to obtain sufficient accuracy, the higher the polynomial order of $\Phi_i(\xi)$ becomes, which increases the complexity of the integrand. If one computes the integral of a high order polynomial with a small amount of points, the resulting expansion coefficients are merely noise instead of being informative.

The question we want to answer in this section is how to determine the number of quadrature points, N_q , and the expansion order, \hat{p} , to obtain a suffi-

ciently high accuracy for the coefficients to allow us to trust the Sobol' indices and more specifically the ranking of the parameters that follows from it. Here, we sketch a method to determine the number of quadrature points. It relies on the fact that the Sobol' indices are variance-based, i.e., one can not expect to compute Sobol' indices accurately from a PCE expansion for which the variance (Equation 5.6) is not a sufficiently accurate approximation of the true value or at least comparable to the Gauss-Legendre quadrature approximation of the integral. So, let us define

$$err_{\text{Var}} := \text{Var}_{\text{data}} - \text{Var}_{\text{PCE}}, \quad (5.8)$$

with

$$\begin{aligned} \text{Var}_{\text{data}} &= \sum_{l_1=1}^{N_q} \cdots \sum_{l_n=1}^{N_q} w_{l_1} \cdots w_{l_n} u(\xi_{l_1}, \dots, \xi_{l_n})^2 - \mu_{\text{data}}^2, \\ \mu_{\text{data}} &= \sum_{l_1=1}^{N_q} \cdots \sum_{l_n=1}^{N_q} w_{l_1} \cdots w_{l_n} u(\xi_{l_1}, \dots, \xi_{l_n}). \end{aligned}$$

For a given choice of N_q one can easily compute PC expansions for various orders \hat{p} . If err_{Var} is small and the required Sobol' indices have converged, the result can be trusted.

We illustrate this approach with a function for which the values of the statistics are analytically known, viz., the Ishigami function [188, 189]

$$f(\boldsymbol{\xi}) = \sin(\xi_1) + a \sin^2(\xi_2) + b \xi_3^4 \sin(\xi_1), \quad (5.9)$$

with $\xi_i \sim \mathcal{U}[-\pi, \pi]$, $i = \{1, 2, 3\}$, and $a = 7$ and $b = 0.1$. We compute the PCE approximation of Equation (5.9) for an increasing number of PCE terms and an increasing number of quadrature points. Table 5.1 illustrates the result of using not enough quadrature points ($N_q = 2$ and $N_q = 5$): there is no convergence in the statistics of the PCE approximation and for $\hat{p} = 3$ and 6 , respectively, the noise takes over and the results are meaningless. Table 5.2 shows that, using sufficient quadrature points, for an increasing number of expansion terms the PCE variance converges to the data variance. If both variances are alike also the Sobol' indices have converged to the true values. Still the number of expansion terms should not be taken too large as can be seen for $\hat{p} > 9$ and $\hat{p} > 13$ where again the noise gradually takes over.

Finally, we also used the original Sobol' method [170] for this problem. To reach a similar accuracy approximately 100 times as many sampling points are required, thus showing the gain in efficiency using the PCE-Gauss method to compute the Sobol' indices.

5. Sensitivity analysis of network formation

Table 5.1: Statistics computed with insufficient quadrature points. The resulting PCE approximation and thus the statistics can not be trusted.

N_q	$\hat{\rho}$	Var_{data}	Var_{PCE}	S_1	S_2	S_{13}	S_3	S_{12}	S_{23}
2	1	4.09	4.09	1.00	0.00	0.00	0.00	0.00	0.00
	2	4.09	4.09	1.00	0.00	0.00	0.00	0.00	0.00
	3	4.09	8.32	1.00	0.00	0.00	0.00	0.00	0.00
	4	4.09	185.91	0.36	0.32	0.00	0.32	0.00	0.00
	5	4.09	197.44	0.34	0.30	0.03	0.30	0.03	0.00
5	1	18.60	2.64	1.00	0.00	0.00	0.00	0.00	0.00
	2	18.60	2.70	0.98	0.02	0.00	0.00	0.00	0.00
	3	18.60	6.22	0.69	0.01	0.30	0.00	0.00	0.00
	4	18.60	17.17	0.25	0.64	0.11	0.00	0.00	0.00
	5	18.60	18.50	0.23	0.60	0.17	0.00	0.00	0.00
	6	18.60	29.49	0.14	0.75	0.11	0.00	0.00	0.00
	7	18.60	31.41	0.19	0.70	0.11	0.00	0.00	0.00
	8	18.60	31.50	0.19	0.70	0.11	0.00	0.00	0.00
	9	18.60	37.51	0.23	0.59	0.18	0.00	0.00	0.00
	10	18.60	88.82	0.29	0.43	0.08	0.20	0.00	0.00
Exact		13.84	0.31	0.44	0.24	0	0	0	0

5.2.4 Software and dataset

All software used in this chapter is publicly available. The contact inhibition model resides at <http://sourceforge.net/projects/tst/>. For GSA we provide a repository containing the dataset and the analysis software at <http://www.cwi.nl/~gollum/GSAMorphogenesis/>.

5.3 Results

As a case study for the global sensitivity analysis (GSA) approach, we used a well-studied computational model of vascular morphogenesis: the contact inhibition model [64]. We studied what single parameters and parameter interactions are important in the development of a spheroid of cells into vascular networks. For this purpose, we used the procedure outlined in Figure 5.1: 1) select output measures, 2) select input parameters, 3) select a relevant subset of the global parameter space, 4) analyze the raw output, 5) perform GSA.

Table 5.2: Statistics computed with sufficient quadrature points. The PCE approximation and the statistics show convergence (bold lines).

N_q	$\hat{\rho}$	Var_{data}	Var_{PCE}	S_1	S_2	S_{13}	S_3	S_{12}	S_{23}
8	1	13.59	2.64	1.00	0.00	0.00	0.00	0.00	0.00
	2	13.59	3.00	0.88	0.12	0.00	0.00	0.00	0.00
	3	13.59	6.55	0.66	0.05	0.29	0.00	0.00	0.00
	4	13.59	10.34	0.42	0.40	0.18	0.00	0.00	0.00
	5	13.59	11.73	0.37	0.35	0.28	0.00	0.00	0.00
	6	13.59	13.45	0.32	0.44	0.24	0.00	0.00	0.00
	7	13.59	13.59	0.32	0.43	0.25	0.00	0.00	0.00
	8	13.59	13.59	0.32	0.43	0.25	0.00	0.00	0.00
	9	13.59	13.59	0.32	0.43	0.25	0.00	0.00	0.00
	10	13.59	15.32	0.28	0.50	0.22	0.00	0.00	0.00
	11	13.59	15.35	0.29	0.49	0.22	0.00	0.00	0.00
	12	13.59	19.17	0.23	0.60	0.18	0.00	0.00	0.00
	13	13.59	21.08	0.29	0.54	0.17	0.00	0.00	0.00
	14	13.59	21.51	0.28	0.55	0.17	0.00	0.00	0.00
	15	13.59	27.62	0.32	0.43	0.25	0.00	0.00	0.00
10	1	13.84	2.64	1.00	0.00	0.00	0.00	0.00	0.00
	2	13.84	3.00	0.88	0.12	0.00	0.00	0.00	0.00
	3	13.84	6.54	0.66	0.05	0.29	0.00	0.00	0.00
	4	13.84	10.36	0.42	0.40	0.18	0.00	0.00	0.00
	5	13.84	11.75	0.37	0.35	0.28	0.00	0.00	0.00
	6	13.84	13.59	0.32	0.44	0.24	0.00	0.00	0.00
	7	13.84	13.72	0.32	0.44	0.25	0.00	0.00	0.00
	8	13.84	13.84	0.31	0.44	0.24	0.00	0.00	0.00
	9	13.84	13.84	0.31	0.44	0.24	0.00	0.00	0.00
	10	13.84	13.84	0.31	0.44	0.24	0.00	0.00	0.00
	11	13.84	13.84	0.31	0.44	0.24	0.00	0.00	0.00
	12	13.84	13.95	0.31	0.45	0.24	0.00	0.00	0.00
	13	13.84	13.95	0.31	0.45	0.24	0.00	0.00	0.00
	14	13.84	15.81	0.27	0.51	0.21	0.00	0.00	0.00
	15	13.84	15.84	0.28	0.51	0.21	0.00	0.00	0.00
Exact		13.84		0.31	0.44	0.24	0	0	0

5.3.1 Selection of output measures

The contact inhibition model [64] produces images of cell configurations as raw output. We chose two measures to quantify the raw output: compactness and lacuna count. Compactness of the network is a suitable measure of network development [64] and is defined as the ratio $A_{\text{cells}}/A_{\text{hull}}$, with A_{cells} the number of lattice sites occupied by cells within a convex hull around all cells and A_{hull} the total number of lattice sites within the convex hull. A solid spheroid and a confluent monolayer of cells have a compactness close to one, while networks that contain lacunae have low values for compactness. Lacuna count is the number of lacunae in a network. Lacunae are defined as patches of medium (connected components of $\sigma = 0$) enclosed by cells and are only counted when they have at least the size of a cell (50 lattice sites $\approx 200 \mu\text{m}^2$).

5.3.2 Selection of input parameters

The contact inhibition model [64] is a stochastic, multi-factorial model. We refer to Section 5.2.1 for a detailed description of the model. The contact inhibition model has nine parameters: the number of cells (N), the target size of a cell (A), the rigidity of the cell (λ_A), cell-cell adhesion ($J_{\text{cell,cell}}$), adhesion between cells and the extracellular matrix ($J_{\text{cell,ECM}}$), the secretion rate of a chemoattractant by cells (α), a diffusion coefficient of the chemoattractant (D), the decay rate of the chemoattractant (ϵ), and a sensitivity of cells to the chemoattractant at cell-matrix interfaces (λ_c).

In total, there are four model components or mechanisms in the contact inhibition model, namely cell size, adhesion, contact-inhibited chemotaxis and the gradient of the chemoattractant. In order to study the impact of each mechanism in the model extensively, we selected one parameter for each, ensuring that it is computationally feasible to generate enough data points for reliable GSA results. We thus selected four parameters: the cell rigidity (λ_A), cell-cell adhesion ($J_{\text{cell,cell}}$), the diffusion coefficient of the chemoattractant (D), and a sensitivity of cells to the chemoattractant at cell-matrix interfaces (λ_c). The other parameters that regulate cell size (A), adhesion ($J_{\text{cell,ECM}}$), or the gradient of the chemoattractant (ϵ and α) will be fixed at the reference values corresponding to the values in [64]. We kept the number of cells (N) in the spheroid constant, because we know from experience that it does not influence sprouting of spheroids in our model.

A GSA with four parameters can give new insights as four parameters are too many to obtain the relative impact of the parameters and their interactions with visual plots or to know their effect solely by logic or intuition, while the number of simulations required for a GSA with four input parameters is computationally very feasible. A GSA with all parameters of the model is

not expected to give additional information on the relative balance of the mechanisms and would be very time-consuming for a computationally intense model like the contact inhibition model. It would require roughly 10^9 simulations (c.f., Section 5.2.3) to obtain reliable GSA results with all model parameters.

5.3.3 Selection of a relevant subset of the global parameter space

To select the parameter ranges for which spheroids of cells develop into networks, we studied one-dimensional parameter sweeps of the four selected input parameters for the compactness and lacuna count (Figure 5.2). The red lines in Figure 5.2 represent the compactness and the blue lines the lacuna count. We selected the region in which the morphology of the network, and thus the value of the output measures, is changing and where no model artefacts arise. It is well studied for which parameter ranges artefacts arise in the CPM [166], such as lattice anisotropy and ‘frozen’ motility of cells. The regions shaded in gray indicate the deleted regions from the parameter space. For λ_A the region 0 to 5 is deleted: cells cannot retain their volume here and disappear. This is a model artefact and does not represent a biological plausible situation. The region $\lambda_A > 300$ is deleted, because cells are so rigid here that they hardly move. In the region $\lambda_c < 10$ only spheroids form and for $\lambda_c > 3000$ similar networks are always formed, thus these regions are deleted because the network morphology does not change. The parameters and their selected value ranges are listed in Table 5.3.

Based on the reliability study for the Ishigami test model (see Section 5.2.3), we expected that we required 10000 data points to perform a reliable GSA on our model. The points were chosen according to the Gauss-Legendre quadrature rule (see Section 5.2.2), resulting in ten values for each parameter. To correct for the stochasticity of the contact inhibition model, each parameter set is replicated twenty times with a different random seed and the output is averaged over them. The size of the standard deviations in Figure 5.2 indicate that the variation over different random seeds is very small for compactness, whereas the stochasticity in the model has a larger affect on the lacuna count. Nevertheless, this lacuna count is a reasonable measure for the network morphology.

5.3.4 Analysis of the raw output

The raw output of a model simulation is an image of the cell configuration at the end of a simulation. Figure 5.3 gives an overview of the raw output for the selected parameter space. Examples of possible morphologies are shown in Figure 5.3, ranging from spheroids to small networks with one lacuna, to fine-

5. Sensitivity analysis of network formation

Table 5.3: Overview of the parameter selection for the GSA. The names of the parameters are listed in the first column, a parameter description in the second column, and the selected parameter value ranges in the last column.

Name	Description	Range
λ_c	Chemotaxis	10 to 3000
D	Diffusion coefficient	$1 \cdot 10^{-14}$ to $5 \cdot 10^{-13} \text{ m}^2\text{s}^{-1}$
λ_A	λ Area	5 to 300
$J_{\text{cell,cell}}$	Cell-cell adhesion	0 to 120

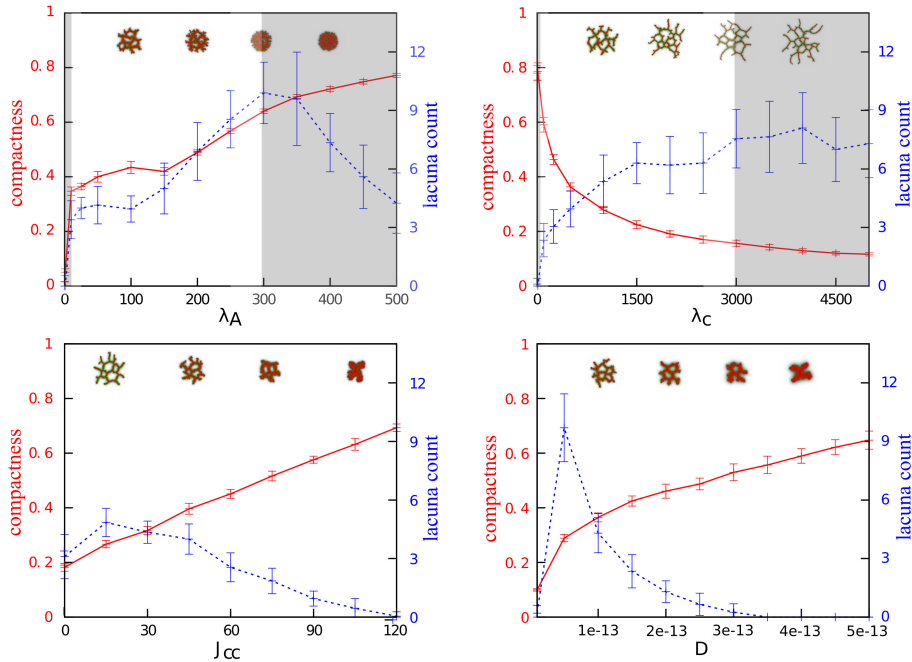


Figure 5.2: One-dimensional parameter sweeps for compactness and lacuna count. Plots of one-dimensional parameter sweeps for each of the four selected parameters: cell rigidity (λ_A), cell-cell adhesion ($J_{\text{cell,cell}}$), diffusion coefficient of the chemoattractant (D in m^2/s), and sensitivity of cells to the chemoattractant at cell-matrix interfaces (λ_c). The red lines indicate compactness and the blue lines lacuna count (mean and standard deviation of 20 simulations).

mazed networks with many lacunae. This is a visual reassurance that the input parameter space is well chosen. However, it is very difficult to predict from the raw output which parameters have a strong impact on the development of networks from spheroids. A GSA can give us insights into this, as we

will show in the next section.

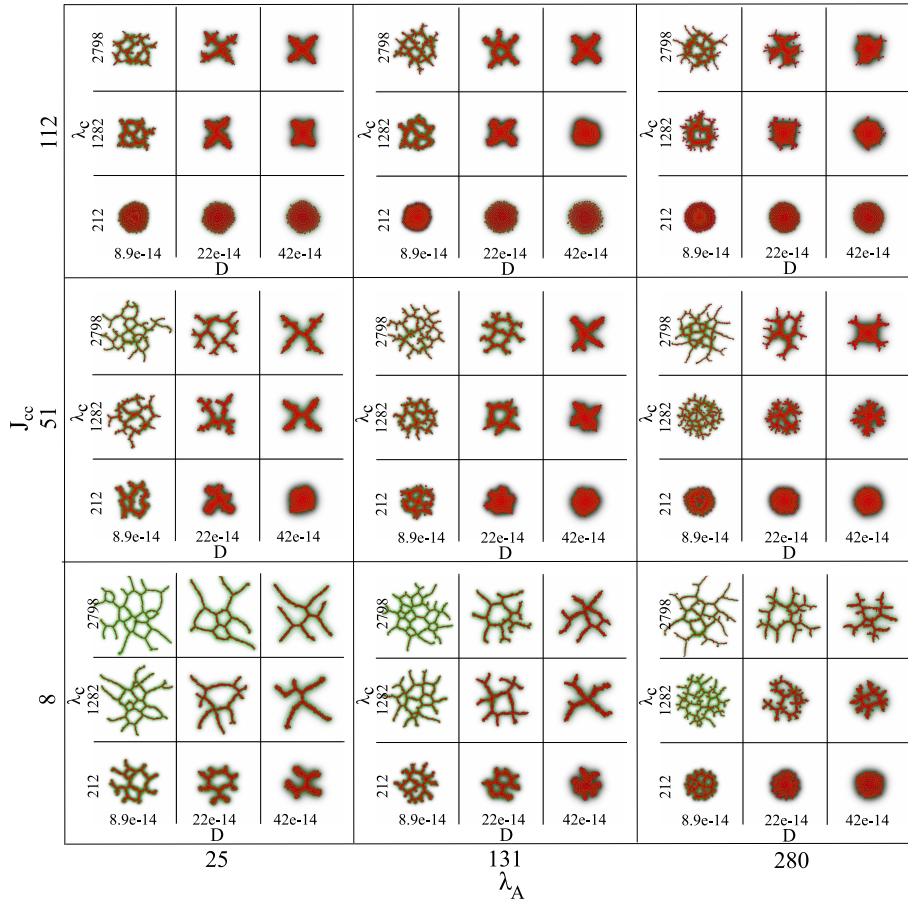


Figure 5.3: Overview of the raw output. An overview of the raw output of the contact inhibition model, the cell configurations at the end of a simulation, is shown in a collage of images. The cell rigidity (λ_A) is varied over the horizontal axis and cell-cell adhesion ($J_{\text{cell,cell}}$) over the vertical axis. For each selected combination hereof, a subcollage is shown in which the diffusion coefficient of the chemoattractant (D in m^2/s) is plotted against the sensitivity of cells to the chemoattractant at cell-matrix interfaces (λ_c).

5.3.5 GSA of network development from spheroids

We performed two types of GSA on the distribution of the output measures, compactness and lacuna count, to study the impact of the parameters on vascular network development. The first type of GSA studies the variation of the output measures and the second type studies the decomposition of the

variance of the distribution of the output measures.

GSA of the variation of the output measures

The variation in the output measures can be visualized by plotting the intensity of the output measures over two-dimensional slices of the parameter space. Figure 5.4 and 5.5 show the intensity plots of the lacuna count and compactness, respectively, for each possible pairing of parameters. The parameter values are selected according to the Gauss-Legendre quadrature rule.

Figure 5.4 shows that the diffusion coefficient is the main source of variation for the lacuna count: the lacuna count is high for low values of D and low for high values of D , independent of the other parameters. That the lacuna count does not vary significantly over the entire perpendicular axis indicates that the parameter of the perpendicular axis does not have much impact. The dominance of the diffusion coefficient masks the impact of the other parameters. To reveal the impact of the other parameters, Figure S1 caps the intensity values at a lacuna count of five.

Figure 5.5 shows a high variation of the compactness in each plot. As a consequence, it is difficult to determine which parameters have a dominant impact on compactness. Interactions between parameters are difficult to deduce from these two-dimensional intensity plots. A variance-based GSA is well suited to derive parameter interactions and the ranking of individual parameter effects, as will be outlined in the following subsection.

Variance-based GSA of the output measures

To study the impact of single parameters and of parameter combinations on the development of networks from spheroids, we performed a GSA of the output distribution of compactness and lacunae count using the Sobol' indices. We refer to Section 5.2.2 for a detailed description of how to obtain the Sobol' indices that represent the impact of the parameters. The GSA results of both measures are reliable, since the Sobol' indices have converged for values of \hat{p} for which err_{var} (Equation 5.8) is small (see Table S1 and S2).

The second column of Table 5.4 lists the impact of the individual parameters and their combinations on compactness. The sensitivity for the chemoattractant at cell-matrix interfaces (λ_c) has the highest impact on network development ($S(\lambda_c)=0.3188$), followed by the diffusion coefficient with $S(D)=0.2969$, and cell-cell adhesion with $S(J_{cell,cell})=0.2048$. Elasticity of cells has a low impact of ($S(\lambda_A)=0.0266$). Seventeen percent of the variance is caused by interactions of parameters. λ_c and $J_{cell,cell}$ have a combined impact of 0.0559. The impact of all other interactions was lower than $S(\lambda_A)$, which we will consider as a threshold for relevant impact.

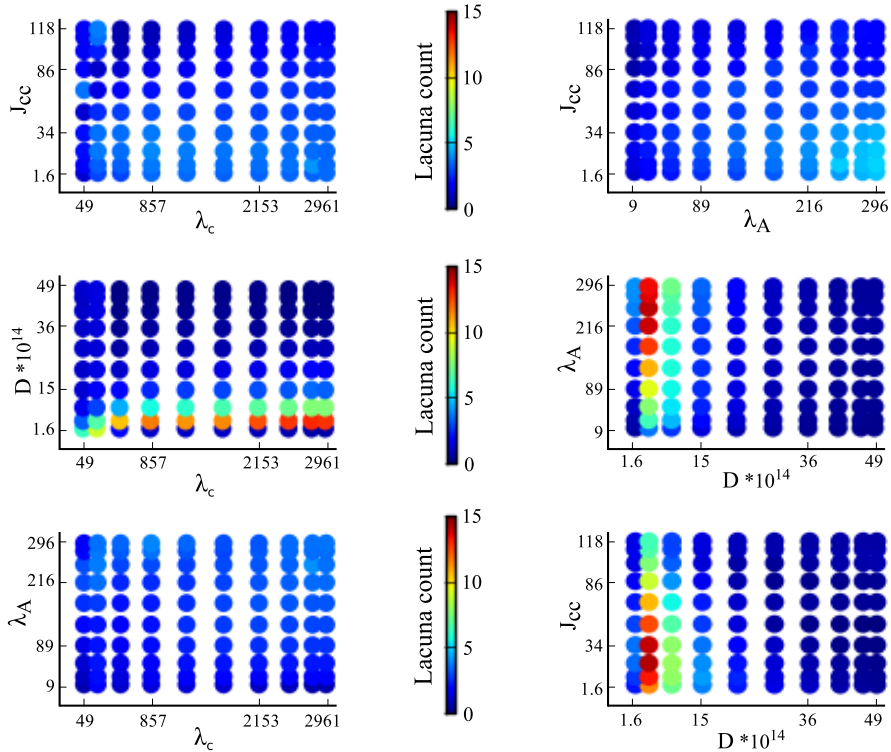


Figure 5.4: Two-dimensional intensity plots of lacuna count. The intensity of the output measure lacuna count, mapped to an interval of 0 to 15 as indicated by the color bars, is plotted for each two-parameter combination of the parameters cell rigidity (λ_A), cell-cell adhesion ($J_{cell,cell}$), diffusion coefficient of the chemoattractant (D in m^2/s), and sensitivity of cells to the chemoattractant at cell-matrix interfaces (λ_c).

The third column of Table 5.4 lists the impact of the individual parameters and their combinations on lacuna count. The individual impact of the diffusion coefficient is dominant, with $S(D)=0.7130$. Cell adhesion also has a small individual impact ($S(J_{cell,cell})=0.0407$). In total, twenty four percent of the variance is induced by combinations of parameters. There are five parameter combinations, which all include the diffusion coefficient, with a higher impact than the threshold: $S(\lambda_c, D)=0.0570$, $S(D, \lambda_A)=0.0347$, $S(D, J_{cell,cell})=0.0521$, $S(\lambda_c, D, J_{cell,cell})=0.0476$, and $S(\lambda_c, D, \lambda_A)=0.0315$. The total impact of the diffusion coefficient is 90 percent. When we focus on low values of the lacuna count, by capping the lacuna count at a maximum of five lacunae, the dominance of the diffusion coefficient is slightly reduced and an extra interaction of λ_c and $J_{cell,cell}$ is found ($\lambda_c, J_{cell,cell})=0.0409$ (Table S3).

5. Sensitivity analysis of network formation

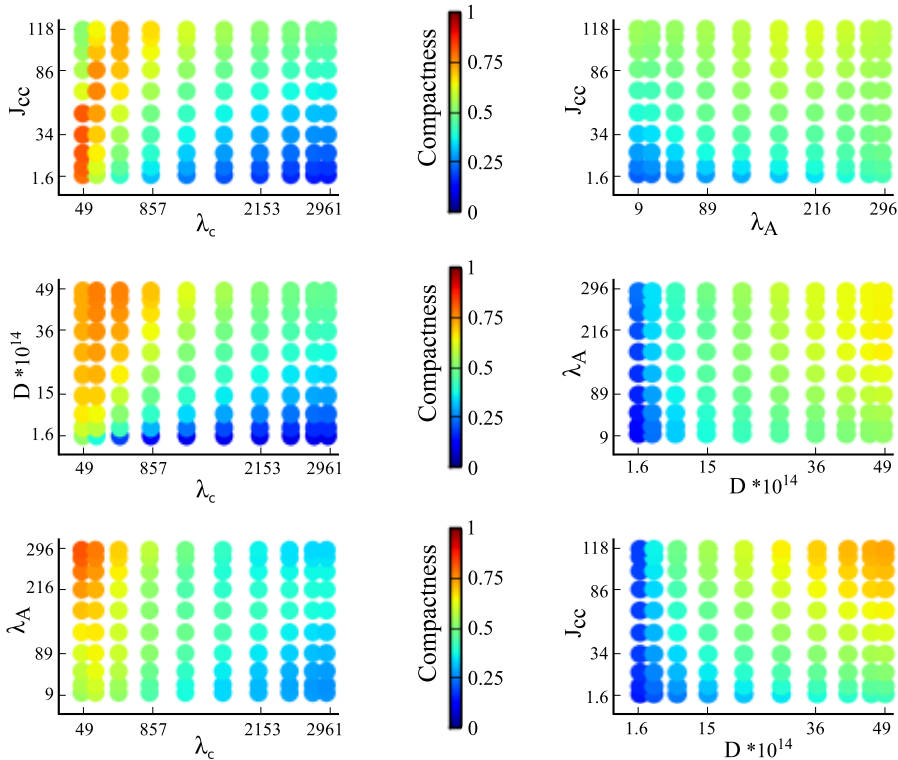


Figure 5.5: Two-dimensional intensity plots of compactness. The intensity of the output measure compactness, mapped to an interval of 0 to 1 as indicated by the color bars, is plotted for each two-parameter combination of the parameters cell rigidity (λ_A), cell-cell adhesion ($J_{cell,cell}$), diffusion coefficient of the chemoattractant (D in m^2/s), and sensitivity of cells to the chemoattractant at cell-matrix interfaces (λ_c).

Interpretation of the GSA results

The GSA results show that three parameters account for over 80 percent of the variance of the compactness distribution. Consistent with previous studies of the contact inhibition model [64], these three parameters are the diffusion coefficient, sensitivity to the chemoattractant at cell-matrix interfaces and cell-cell adhesion. For the lacuna count, the GSA identified solely the diffusion coefficient as the dominant parameter. This dominant effect is apparent in a collage of output images (Figure 5.6): the number of lacunae varies over the horizontal axis that represents the diffusion coefficient D , whereas there is little variation along the vertical axis that represents the sensitivity to the chemoattractant at cell-matrix interfaces λ_c . The number of lacunae is the largest for small values of the diffusion coefficient (around

Table 5.4: Global sensitivity analysis results. The Sobol' indices for the individual parameters (indices above mid-line) and for their combinations (indices below mid-line) are listed for the GSA of compactness and lacuna count.

	compactness	lacuna count
$S(\lambda_c)$	0.3188	0.0074
$S(D)$	0.2969	0.7130
$S(\lambda_A)$	0.0266	0.0125
$S(J_{\text{cell,cell}})$	0.2048	0.0407
$S(\lambda_c, D)$	0.0125	0.0570
$S(\lambda_c, \lambda_A)$	0.0107	0.0043
$S(\lambda_c, J_{\text{cell,cell}})$	0.0559	0.0145
$S(D, \lambda_A)$	0.0017	0.0347
$S(D, J_{\text{cell,cell}})$	0.0127	0.0521
$S(\lambda_A, J_{\text{cell,cell}})$	0.0102	0.0048
$S(\lambda_c, D, \lambda_A)$	0.0102	0.0315
$S(\lambda_c, D, J_{\text{cell,cell}})$	0.0257	0.0232
$S(\lambda_c, \lambda_A, J_{\text{cell,cell}})$	0.0217	0.0131
$S(D, \lambda_A, J_{\text{cell,cell}})$	0.0075	0.0094

$D = 4.3 \cdot 10^{-14} \text{ m}^2/\text{s}$), whereas no lacunae are formed for large values of the diffusion coefficient. A similar trend is seen when the diffusion coefficient is plotted against cell-cell adhesion or cell rigidity (not shown). The distance over which adjacent branches can attract one another is given by the length of the chemoattractant gradient (Equation 5.1), which is characterized by the diffusion length, $L_D = \sqrt{\epsilon/D}$, the distance over which the secreted chemoattractant drops to $1/e$ of the concentration at the cells (see, e.g., the discussion in Ref. [64]). If L_D becomes shorter, branches that would fuse for larger values of L_D will not fuse. Hence the pattern will be more fine-grained. Also a shorter value of L_D will create sharper gradients and hence increase the inward chemotactic force (as $\Delta H = \lambda_c \cdot \text{gradient}$) hence "squeezing" the branches more and making them thinner.

In conclusion, the GSA is able to identify the dominant single parameters for compactness and lacuna count. In addition, it gives new information on the relative ranking of the impact of these single parameters.

In contrast to the one-dimensional parameter studies performed in [64], GSA provides information on interactions of parameters. Combinations of parameters account for 17% of the variance in the compactness distribution, and for 24% of the lacuna count distribution. This indicates that most parameters impact the model output independently. Interestingly, the parameter combination of λ_c and $J_{\text{cell,cell}}$ impacted the lacuna count (as seen in Figure S1, which is capped at a maximum of five lacunae) as well as compactness.

5. Sensitivity analysis of network formation

How can we explain this interaction? Sprout formation requires a balance between λ_c -dependent chemotaxis, creating an inward force perpendicular to the sprout surface, and $J_{\text{cell,cell}}$ -dependent cell-cell adhesion, which is responsible for the surface tension of individual cells. In the limit of zero-surface tension, the cells would behave as a zero-viscosity fluid and the chemotaxis would compress sprouts until they become infinitely thin [190]. The cellular surface tensions resist such compression, thus determining the thickness of sprouts. Altogether, this parameter interdependence highlights a new insight in the mechanisms driving sprouting in our model.

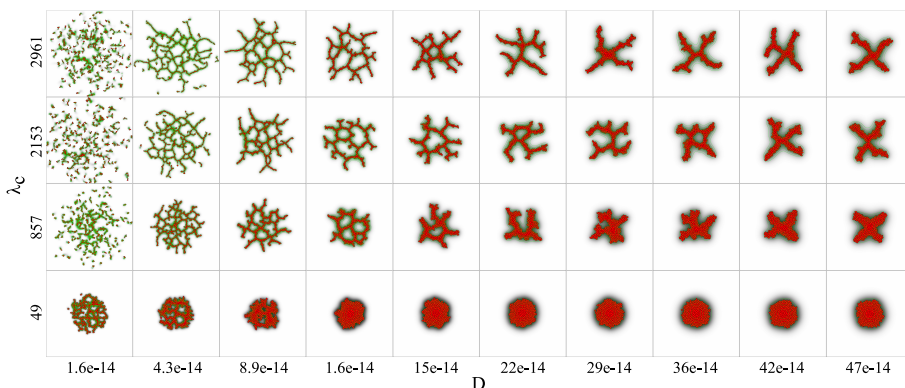


Figure 5.6: Dominant effect of the diffusion coefficient on lacuna count. A collage of the cell configurations at the end of simulations in the contact inhibition model, in which the diffusion coefficient of the chemoattractant (D in m^2/s) is varied over the horizontal axis and the sensitivity of cells to the chemoattractant at cell-matrix interfaces (λ_c) over the vertical axis.

5.4 Discussion

Biological morphogenesis is a highly complicated process, involving genetic regulation, pattern formation, the biophysics of collective cell migration, mechanical cell-cell interactions, and so forth. As such multiscale mechanisms are practically impossible to understand intuitively, in recent years modeling and simulation has become a key tool in developmental biology (see, e.g., refs. [191–194]). These efforts have led to highly complicated models, where traditional analysis tools in dynamical systems theory, such as bifurcation analysis and phase plane analysis, fall short. The models must then be treated as ‘black-box’ systems: one- or two-dimensional parameter sweeps are performed, creating images and movies as output, which can be used to obtain various quantitative output measures. These parameter sweeps must be started from one or a few nominal parameter sets around which

n-dimensional cross-shaped sweeps through the parameter space are performed. However insightful such studies are, a danger is that the impact of some parameters is overlooked: the conclusions may depend on what sets of nominal parameter values were selected. Using a simple, published simulation model of vascular morphogenesis, we have shown in this work how a multivariate GSA helps to get more insight in the relative impact of single parameters and of their interactions. We introduced a workflow for GSA of ‘black-box’ models of morphogenesis.

We applied the workflow to a vascular morphogenesis model which we refer to as the ‘contact inhibition model’. The output of the contact inhibition model consists of images of the cell configuration in a simulation. To quantify network development, we measured the compactness and the lacuna count of the cell configuration at the end of the simulation. A GSA with four input parameter distributions, that each described one of the four general model components, was performed for both measures. The GSA results of compactness and lacuna count both indicated that variation of the rigidity of the cells (λ_A) has very little impact on the model output. As a result, the model can be reduced by fixing this parameter. For compactness, the sensitivity for the chemoattractant at cell-matrix interfaces (λ_c) has the highest impact on network development, followed by the diffusion coefficient (D) and cell-cell adhesion ($J_{\text{cell,cell}}$). In contrast, the GSA showed that the diffusion coefficient alone is dominant for lacuna count. The results for both measures are in line with what has been previously reported [64]. New information from the GSA results is the relative impact of the single parameters. In addition, GSA identified interactions between parameters, which have led to new insights in the mechanism of sprouting in the model. Most notably, the parameter interactions in this specific CPM-based model have very low impact. Since GSA has not been performed for CPM-based models before, it is an important new insight for the CPM community that the most basic mechanisms of the CPM, such as cell size and adhesion here function independently.

Besides the contact inhibition model, there are multiple other computational models of vascular network development [16, 63, 66, 69, 71, 108]. These models often share common mechanisms that drive sprouting, but differ by one or a few mechanisms. It is still not known which mechanisms drive sprouting *in vivo*, or whether a different set of mechanisms is used under different conditions. We propose GSA as an approach to help falsify these models. Firstly, the ranking of the relevance of the mechanisms in the models can be compared with knowledge of the impact of these mechanisms from experimental data to falsify models. A second model falsification method is the validation of the experimental predictions of each model based on the GSA results.

The workflow is designed to take into account some pitfalls of GSA. These

arise from the dependency of the outcome on the choices one makes for the output measure, input parameters and their distributions. Different output measures can give different results, as was the case for compactness and lacuna count. This indicates that it is essential to consider carefully whether the selected measure truly describes your goal and if there are other measures for it. A selection of input parameters might be necessary when it is not computationally feasible or methodologically desirable to use all parameters of the model. The importance of the selection of the correct parameter distributions has also been discussed elsewhere [177]. Intuitively, a large range for the parameter values will allow for the largest variation in the output and thus the most interesting result. However, since the analysis is global over the entire parameter space, local though important features might become unnoticed if the distribution is too widespread. For instance, for the contact inhibition model we were interested in the region where the networks developed and where the measures were changing accordingly, and variation in these regions could become unnoticed if we included large regions where for instance spheroids do not sprout. Ideally, the parameter distribution comes from experimental measurements, but in absence hereof we propose to study the variation of the output measures for each parameter individually.

It is crucial to have an estimate of the accuracy of the sensitivity results. One option is to compare the results with the outcome of an analysis with a higher accuracy computed with more quadrature points and a higher PCE order, like advocated in [177]. In this chapter we proposed a simpler and cheaper rule: given the number of quadrature points the Sobol' indices should show convergence for those values of \hat{p} for which the variance computed with the Gauss-Legendre quadrature rule is more or less equal to the variance computed from the PCE approximation. If a higher PCE order is required, more model simulations are needed. Since the computation of the PCE statistics is 'for free' compared to model simulations this is an efficient way of judging whether the accuracy of the statistics is sufficient for one's aim. Although Gauss quadrature is optimal, it has the disadvantage that it is not a nested quadrature rule, i.e., if more quadrature points are required, the old model results cannot be re-used. An alternative for Gauss quadrature is Monte Carlo (MC) integration. Sampling the PCE integrals by MC is less optimal, so more simulations are needed to obtain reliable GSA results. For the Ishigami test model, MC needs a 100 times more simulations to get comparable results. The benefit of MC is that you can check 'on the fly' if there are enough data points generated to get reliable results. Adding simulations on the fly is particular useful when the estimated number of simulations based on the Gauss quadrature rule is computationally unfeasible, but one expects or hopes that the output distribution is relatively smooth and thus can be described by a low order PCE approximation.

Some studies require GSA of a subspace of the output distribution. For instance in our case study, to study not the conditions for network formation per se, but the details of the network morphology (e.g. branch length, branch thickness, and so forth), we must preselect a region of the parameter space where networks actually form. Unfortunately, such a subspace would no longer guarantee that the input distribution is independently random uniform. For such cases, a more complicated method to compute the Sobol' indices [185] is required.

Besides in computational models, the impact of biological factors on morphogenesis is also studied *in vitro*. High-throughput image-based screenings systematically analyze the impact of genes or potential drugs on cell behavior, such as cell migration [195]. This 'systems microscopy' approach is well suited for parallel screening of cellular responses to numerous experimental perturbations [196]. Such high-throughput screens can be performed for the genes, growth factors or ECM concentrations affecting morphogenesis. This is conceptually very similar to parameter studies of *in silico* 'black-box' models. The perturbed biological factors represent the input parameters and the output is an image from which quantitative data can be derived. Therefore, the GSA workflow proposed in this chapter is directly applicable to high-throughput *in vitro* studies.

5.5 Conclusions

Morphogenesis is a complex biological process in which cells organize into shapes and patterns. Computational modeling is used to get insights in the mechanisms of morphogenesis. These models are often multi-scale, non-linear and multi-factorial, making it difficult to relate their input to their output. The behavior of such 'black-box' models is mostly studied by visual inspection and analyses of the individual output (e.g. images and movies) and with one- or two-dimensional parameter sweeps of output measures. However, this does not provide insight in the relative impact of single parameters and of their interactions on the outcome of the model. GSA fulfills this task. GSA results can give insights in the dynamics of the model and help to generate experimental predictions to manipulate morphogenesis. In this chapter, we introduced a workflow for GSA of such models and addressed pitfalls and reliability of the analysis. The workflow is applied to the contact inhibition model, a cell-based model of vascular morphogenesis. GSA was able to correctly identify dominant parameters and gave new insights on the magnitude and ranking of their individual impact and importantly, on their interactions. In summary, we propose GSA of 'black-box' models, such as complex computational models or high-throughput *in vitro* models, as an alternative approach to get insights in the mechanisms of morphogenesis.

5.6 Supplementary figures

Table S1: Global sensitivity analysis results for compactness.

\hat{p}	12	13	14	15
Variance data	0.0453	0.0453	0.0453	0.0453
Variance PCE	0.0452	0.0453	0.0454	0.0456
$S(\lambda_c)$	0.3190	0.3188	0.3186	0.3183
$S(D)$	0.2971	0.2969	0.2965	0.2958
$S(\lambda_A)$	0.0267	0.0266	0.0266	0.0265
$S(J_{\text{cell,cell}})$	0.2052	0.2048	0.2043	0.2032
$S(\lambda_c, D)$	0.0124	0.0125	0.0126	0.0127
$S(\lambda_c, \lambda_A)$	0.0107	0.0107	0.0109	0.0110
$S(\lambda_c, J_{\text{cell,cell}})$	0.0558	0.0559	0.0561	0.0570
$S(D, \lambda_A)$	0.0016	0.0017	0.0017	0.0017
$S(D, J_{\text{cell,cell}})$	0.0127	0.0127	0.0127	0.0126
$S(\lambda_A, J_{\text{cell,cell}})$	0.0102	0.0102	0.0102	0.0101
$S(\lambda_c, D, \lambda_A)$	0.0098	0.0102	0.0104	0.0107
$S(\lambda_c, D, J_{\text{cell,cell}})$	0.0253	0.0257	0.0262	0.0268
$S(\lambda_c, \lambda_A, J_{\text{cell,cell}})$	0.0214	0.0217	0.0220	0.0225
$S(D, \lambda_A, J_{\text{cell,cell}})$	0.0073	0.0075	0.0076	0.0078

Table S2: Global sensitivity analysis results for lacuna count.

\hat{p}	11	12	13
Variance data	15.8651	15.8651	15.8651
Variance PCE	15.5295	15.9661	16.7974
$S(\lambda_c)$	0.0075	0.0074	0.0070
$S(D)$	0.7120	0.7130	0.7187
$S(\lambda_A)$	0.0129	0.0125	0.0119
$S(J_{\text{cell,cell}})$	0.0418	0.0407	0.0387
$S(\lambda_c, D)$	0.0579	0.0570	0.0552
$S(\lambda_c, \lambda_A)$	0.0043	0.0043	0.0041
$S(\lambda_c, J_{\text{cell,cell}})$	0.0144	0.0145	0.0143
$S(D, \lambda_A)$	0.0350	0.0347	0.0348
$S(D, J_{\text{cell,cell}})$	0.0533	0.0521	0.0501
$S(\lambda_A, J_{\text{cell,cell}})$	0.0050	0.0048	0.0046
$S(\lambda_c, D, \lambda_A)$	0.0289	0.0315	0.0331
$S(\lambda_c, D, J_{\text{cell,cell}})$	0.0222	0.0232	0.0236
$S(\lambda_c, \lambda_A, J_{\text{cell,cell}})$	0.0118	0.0131	0.0142
$S(D, \lambda_A, J_{\text{cell,cell}})$	0.0086	0.0094	0.0100

Table S3: Global sensitivity analysis results for lacuna count capped at maximum of 5 lacunae.

\hat{p}	12	13	14
Variance data	3.4870	3.4870	3.4870
Variance PCE	3.4346	3.4821	3.5668
$S(\lambda_c)$	0.0081	0.0081	0.0079
$S(D)$	0.6893	0.6861	0.6847
$S(\lambda_A)$	0.0078	0.0077	0.0077
$S(J_{\text{cell,cell}})$	0.0578	0.0571	0.0557
$S(\lambda_c, D)$	0.0561	0.0557	0.0547
$S(\lambda_c, \lambda_A)$	0.0084	0.0085	0.0086
$S(\lambda_c, J_{\text{cell,cell}})$	0.0394	0.0409	0.0429
$S(D, \lambda_A)$	0.0048	0.0048	0.0048
$S(D, J_{\text{cell,cell}})$	0.0489	0.0485	0.0476
$S(\lambda_A, J_{\text{cell,cell}})$	0.0035	0.0035	0.0035
$S(\lambda_c, D, \lambda_A)$	0.0147	0.0160	0.0169
$S(\lambda_c, D, J_{\text{cell,cell}})$	0.0458	0.0476	0.0490
$S(\lambda_c, \lambda_A, J_{\text{cell,cell}})$	0.0239	0.0258	0.0274
$S(D, \lambda_A, J_{\text{cell,cell}})$	0.0121	0.0132	0.0140

5. Sensitivity analysis of network formation

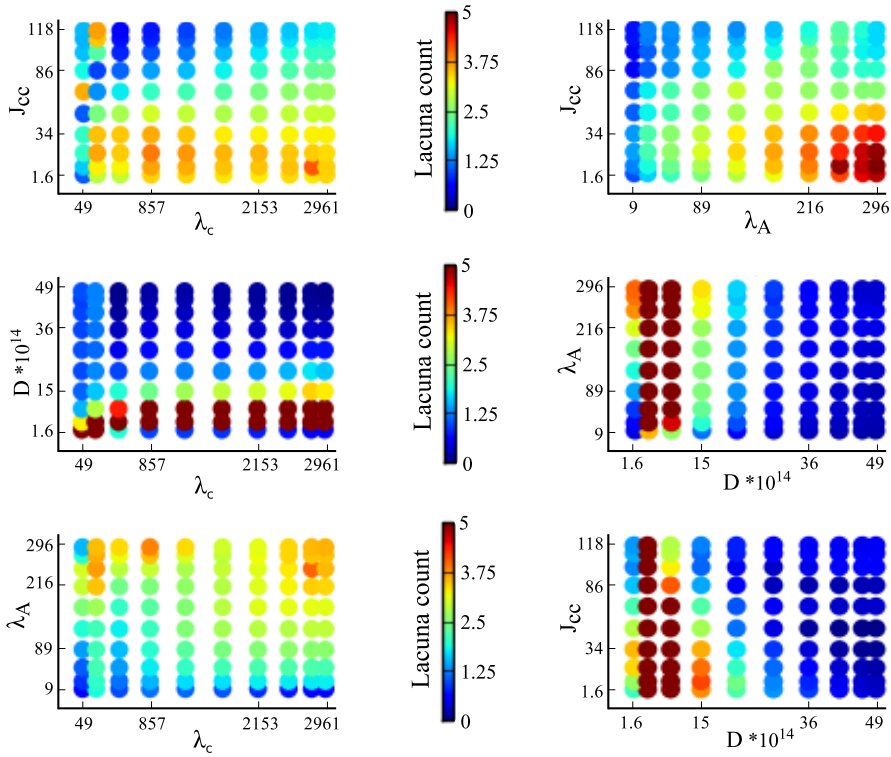


Figure S1: Two-dimensional intensity plots of lacuna count with maximum intensity of 5. The intensity of the output measure lacuna count, mapped to an interval of 0 to 5 as indicated by the color bars, is plotted for each two-parameter combination of the parameters the cell rigidity (λ_A), cell-cell adhesion ($J_{\text{cell,cell}}$), the diffusion coefficient of the chemoattractant (D in m^2/s), and sensitivity of cells to the chemoattractant at cell-matrix interfaces (λ_c).

6

Discussion

In this thesis, we have developed cell-based models to get a mechanistic understanding of the processes involved in angiogenesis. We have captured a number of key steps of angiogenesis. During angiogenesis, endothelial cells degrade the surrounding matrix (Chapter 2), while collective cell behavior in combination with intercellular signaling (Chapter 3) drives sprouting into the matrix. Once a sprout is formed, the sprout lumenizes to allow blood perfusion (Chapter 4). Each of these steps of angiogenesis are studied separately in this thesis and are compared to *in vitro* studies that focus on these steps. The steps were studied in isolation: such reduction of the biological complexity is required for a mechanistic understanding of the process. We believe that a model must be simple enough to explain the results, while complicated enough to generate results that initially surprise us. However, biology is more complex than we even dare to imagine; *in vivo*, all steps of angiogenesis are linked and intertwined. Therefore an important questions to ask is, can we link the isolated models of each step to get a better representation of the *in vivo* situation?

6.1 Interactions between matrix degradation and tip cell selection

In Chapter 2, we studied matrix degradation and invasion. For this purpose, we developed a cell-based computational model that represents an *in vitro* HMVEC-fibrin assay [38, 39] in which endothelial cells are seeded on a fibrin matrix and invade the matrix to form capillary-like tubule structures. It is unclear what mechanisms select the cells in the monolayer that initialize angiogenic ingrowth. The level of angiogenic ingrowth varies for different compositions of the fibrin matrix, it is higher on high molecular weight (HMW) fibrin than on low molecular weight (LMW) fibrin [39]. To ultimately understand what mechanisms cause angiogenic ingrowth, we used a computational model to study why ingrowth differs between HMW and LMW. Our model suggests that sprouting is driven by a feedback loop in which cells stimulate fibrinolysis, fibrinolysis releases $TGF\beta 1$ and $TGF\beta 1$ promotes cells to perform fibrinolysis. LMW has less binding sites than HMW [81] for proteins that link $TGF\beta 1$ to the matrix and keep $TGF\beta 1$ inactive. This results in a reduced availability of $TGF\beta 1$, consequently a lower activation of the feedback loop and in the end less ingrowth on LMW. Simulations show that due to the feedback loop, cells in the monolayer are naturally selected for ingrowth to lead sprouting. From experimental studies it is clear that intercellular signaling by Dll4-Notch, a process called tip cell selection, plays an important role in such a selection of leader cells [3]. In Chapter 3, we explicitly model Dll4-Notch signaling between cells. An interesting follow-up study would be to combine the local degradation feedback and lateral inhibition by Delta-Notch. Their

combination might affect the distances between ingrowth spots in the monolayer. Additionally, their combination might regulate sprout width. Sprouts produced in the fibrinolysis model are often wider than observed in experiments. Simulated sprouts are often spheroid shaped as cells neighboring the leading cell also sense the $TGF\beta 1$ feedback and then start to contribute to the invasion. Inclusion of tip cell selection in the plasmin-mediated fibrinolysis model might inhibit neighboring cells to react on the releases $TGF\beta 1$ by the leader cell, to allow formation of narrow sprouts. However, it is not know how the plasmin-mediated fibrinolysis, the $TGF\beta 1$ system and the Dll4-Notch signaling pathway interlink. Our models plasmin-mediated fibrin degradation and the tip cell selection can be coupled to study these interactions. This combined model could test different options for cross-regulation, e.g. the downregulation of uPAR by Notch signaling. By studying the effect of a variety of regulation pathways on the pattern of ingrowth spots in the monolayer and on sprout morphology, the model could give insights on the functionality of such cross-regulations.

In Chapter 3, we studied sprouting dynamics driven by collective cell behavior and intercellular signaling through Dll4-Notch. Initially it was thought that once a tip cell in a sprout was selected by the Dll4-Notch mechanism, that this cell remains the leader cell [3]. More recent experimental observations show competition of cells for the leading position [24, 25], a process called tip cell overtaking. We studied tip cell overtaking in two of our models of angiogenic sprouting [63, 64], in which sprouting is driven by contact-inhibited chemotaxis towards higher concentrations of a self-secreted growth factor [64] or by regular chemotaxis in combination with cell elongation [63]. We found that tip cell overtaking can result spontaneously from collective sprouting behavior in both models. Intercellular Dll4-Notch signaling can tune tip cell overtaking in simulations with a large difference in *Vegfr2* levels between cells. However, how realistic are such large differences in *Vegfr2* levels between cells *in vivo*? We propose that tip cell overtaking is a non-functional side effect of sprouting and that the function of VEGF-Dll4-Notch signaling might not be to regulate which cell ends up at the tip, but to assure that the cell that randomly ends up at the tip position acquires the tip cell phenotype. In the two models that we used to study tip cell overtaking, sprouts can freely invade the extracellular matrix without proteolytic degradation. It is likely that inclusion of degradation of the extracellular matrix and adhesion of cells to the matrix will affect the dynamics of collective cell behavior. For instance, cells at the flanks of sprouts might travel more efficiently past the sprout when aided by adhesion to the surrounding matrix. In addition, cells at the tip are slowed down because they first need to degrade the matrix for invasion. This delay of cell movement at the tip will likely affect the chemotaxis-driven sprouting mechanisms in the current tip cell overtaking models of Chapter 3.

For chemotaxis-driven sprouting, it is important that cells can quickly respond to changes in the curvature of the growth factor gradient. Thus, a delay of cell movement due to proteolysis of the matrix could affect the response to the growth factor and consequently the sprouting dynamics in these models. Since the matrix is present in *in vivo* sprouting, it is important to consider it in our models to bring them closer to the real situation. Simultaneously, this gives new opportunities for the validation of the sprouting mechanisms in our model. We should first validate if a combination of the fibrinolysis model and the tip cell selection model can still match the experimental data of tip cell overtaking. If not, this is an indication that sprouting might be driven by other mechanisms than that we assumed in our models and we can test if we can reproduce the experimental data by the use of different hypotheses for the mechanisms of sprouting. Mechanical cell-ECM interactions form such an alternative mechanism of sprouting [73, 74]. Cells are sensible to strains in collagen matrices and can also generate strains in the matrix themselves by pulling on it [73, 74]. Computational modeling by van Oers *et al.* [69] showed that cells form sprouts and organize into networks when they generate strain in the matrix and preferentially migrate towards higher strains in the matrix. A model by Santos-Oliveira *et al.* [197] shows the relation between sprout morphology and cell proliferation triggered by endothelial cell strain. In this model, a tip cell generate strain in the matrix and this tension produces strain and/or empty spaces, triggering cell proliferation in the following stalk cells to drive sprouting. The stress-stiffening response of fibrin matrices is extensively studied [198], as a next step it is interesting to study if mechanical-ECM interactions might also play a role in angiogenic fibrin invasion.

6.2 Lumen formation and dynamic sprouting

Once sprouts are formed, lumens form as a next step for the purpose of blood perfusion. In Chapter 4, we addressed the mechanisms of lumen formation. After decades of experimental research, two main hypotheses were formed to explain lumen formation. The first hypothesis is vacuolation [28, 29], in which fluid filled vesicles fuse into vacuoles that finally form a bridging tube through the cell or are secreted between cells to form extracellular lumens. The second hypothesis is cell-cell repulsion [32, 33] that suggests that negatively charged ions on adjacent cell membranes repulse one other to initiate lumen formation and cell shape changes further open the lumen. Our model of Chapter 4 shows that lumens can form for both hypotheses for small parameter ranges, but their combination is far more robust to changes in the parameter settings, suggesting synergy of the two hypotheses. The contradicting experimental observations might be explained by the vessel sizes in different studies; lumen formation looks like vacuolation in simulations with

one-cell thick vessels, whereas it looks like cell-cell repulsion in multi-cellular vessels. A combination of the two hypotheses might make lumen formation more robust to changes in the environmental settings, such as different vessel sizes. In line with our modeling results, recent experimental work indicates that both hypotheses contribute to lumen formation in intersegmental vessels (ISV) of zebrafish [199]. Single cell analysis, by fluorescently labeling the cell nuclei and cell membranes simultaneously, demonstrated the coexistence of intercellular lumens within single cells and extracellular, multicellular enclosed lumens [199].

Robustness of lumen formation to changes in the environment due to synergy of vacuolation and cell-cell repulsion could especially be relevant when lumen formation is already initiated during sprouting, rather than after the sprout is formed. To study this, we made a preliminary model of cells seeded on a bead from which sprouts dynamically form by contact-mediated inhibition of chemotaxis [64]. Lumens form during sprouting by a combination of the vacuolation and the cell-cell repulsion hypotheses (Figure 6.1). In this simulation, lumens form robustly, but they keep on growing by the transfer of fluid by the vacuoles from the extracellular environment towards the interior lumen. Interestingly the vacuolation hypothesis assumes that the vessels are sealed through strong cell-cell interactions and cannot leak fluid [29], whereas the cell-cell repulsion hypothesis assumes vessels are leaky with paracellular openings [32]. This could experimentally be tested by the injection of a dye in the luminal space. The vessel is sealed if the dye remains within the lumen, and is leaky if it diffuses to the extracellular medium. The vessels are sealed in the current model, and we could use the model to hypothesize how the volume of the lumen is controlled in this case. A possible mechanism would be a negative feedback of luminal pressure on the uptake of extracellular fluid from the extracellular matrix. Alternatively, we could adapt our model to include leaky cells. In that case, it is interesting to study what mechanism prevent lumens to collapse in absence of the luminal pressure. Possibly, adhesion of cells to the surrounding matrix suffices. In this case, proteolytic degradation of the surrounding matrix is likely to affect the size of the lumen, indicating that this research question might also require the modeling of matrix degradation. Thus, combining computational models leads us to new research questions that allow for further study and comparison of the two lumen formation hypotheses.

6.3 Model sensitivity analysis

Altogether, it seems that to combine the well-studied isolated models is a good method to generate new research questions and to represent the *in vivo* situation more closely. However, caution should be taken when combining

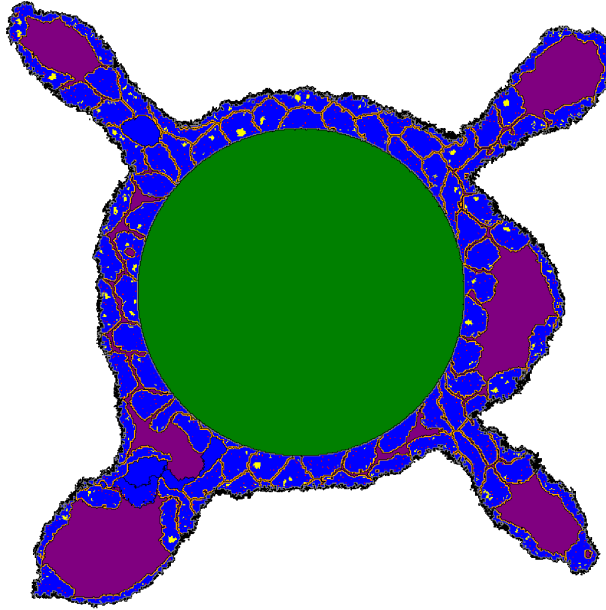


Figure 6.1: Dynamic lumen formation during sprouting. Endothelial cells (blue) are seeded on a bead (green) and polarize their membranes into apical (orange) and basolateral (gray) membranes. Subsequently, sprouts form through contact-mediated inhibition of chemotaxis. During sprouting, luminal fluid (purple) is created by the secretion of vacuoles (yellow) and, in addition, lumens are created through cell-cell repulsion.

models. It results in large and complicated models with many parameters. As a result, analyzing the influence of these parameters in the model becomes more challenging. One- or two-dimensional parameter sweeps can still give insights, but it is important to realize that this is a reflection of a local space in the output distribution as the other parameters are fixed at a nominal value. A global sensitivity analysis can rank the impact of multiple parameters at the same time on the variance of the output. Importantly, it can also identify the impact of parameter interactions. In Chapter 5, we discussed how one can apply a global sensitivity analysis on stochastic, multi-factorial models, such as the cellular Potts models in this thesis. A simple model of vascular morphogenesis, using contact-mediated inhibition of chemotaxis for sprouting [64] (contact inhibition model), is used as a case study. The chapter introduces a flowchart to perform a global sensitivity analysis and focuses on the pitfalls and on the reliability of the results. We developed a rule to predict *a priori* how many simulations are required to get reliable results. One of the pitfalls to consider in a global sensitivity analysis is that the results might not represent the answer to the question at hand. This is strongly de-

pendent of the parameter ranges and output measures one chooses to study the problem. For example, a parameter could have a very large influence, but solely on an interval of, say, 1 to 10. A global sensitivity analysis would identify this parameter as important for a chosen interval of 1 to 10, but not for an chosen interval of 1 to 1000, thus it is crucial to carefully match the choice of the parameter intervals to the regions of interest for the question. Additionally, different output measures can give different global sensitivity analysis results. For instance, the analysis in Chapter 5 for the contact inhibition model showed that compactness of networks depends on a combination of model parameters, whereas the diffusion coefficient of the self-secreted chemoattractant has a dominant impact on the lacuna count.

6.4 Three-dimensional models

In some conditions, angiogenesis can be considered as a quasi-two-dimensional process, such as angiogenesis in the retina *in vivo* and endothelial network formation on cover slips *in vitro*. For this reason, it is reasonable to model angiogenesis as a two-dimensional process. In addition, two-dimensional simulations are faster to compute and easier to analyze than three-dimensional simulations. However, even in quasi-two-dimensional angiogenesis, the third dimension could be of some influence. For instance, the interaction surface between neighboring cells for intercellular signaling can still locally change by the third dimension. Another clear example in which the third dimension could be important is lumen formation. Lumen formation by the vacuolation hypothesis suggests that fluid filled vacuoles fuse in the interior of the cell and finally form a tube through the entire cell that fuses to the to the luminal tubes in the cell in front and behind it in the sprout. The cell becomes a hollow cylinder in three-dimensions, but a cell will appear to be split up in two pieces by the lumen in a two-dimensional cross-section along the long axis. Fortunately, all of our models are scalable to three-dimensions, because all the cells obey local rules. We believe that cells are not pre-programmed during angiogenesis, but are guided by the information from their local surroundings, e.g. by the pericellular gradient of chemoattractant or by the local concentration of fibrin. Therefore, each rule for the cells in our models depends only on the local environment of cells and can consequently be extrapolated from two-dimensions to three-dimensions. As an illustration, Figure 6.2 shows a preliminary three-dimensional model of a sprout that invades fibrin and forms a lumen inside. In summary, future steps can be taken to represent *in vivo* models more closely by combining models as well as by extending them to three-dimensions. The better a model matches reality, the more likely that the insight that are gained from it are directly interpretable and useful for the *in vivo* situation. In addition, a more detailed model can

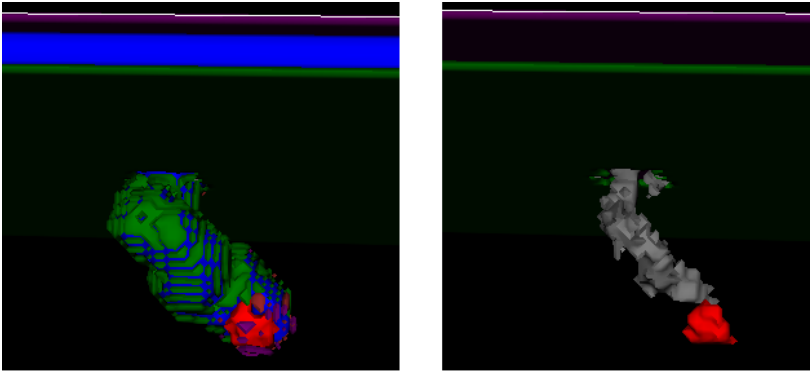


Figure 6.2: Sprouting and lumen formation in three-dimensions. Endothelial cells (blue) are seeded on an extracellular matrix (green). One cell in the monolayer is selected as a tip cell (red). The tip cell secretes proteolytic enzymes to form a tunnel into the matrix for sprouting. On the left, an image is shown in which a sprout is formed inside the matrix and the matrix is made transparent for visualization. A lumen is formed inside the sprout (gray material in image on the right), simply by creating vacuoles that migrate to the center of the sprout and then fuse into one single lumen.

benefit the validation of the model, because it does not suffer from layers of abstraction that could make it difficult to link the effects of parameter changes in the model to the *in vivo* effects. However, it is important to keep in mind that the goal of modeling is to understand a biological process, not to mimic it, thus caution should be taken that the model does not become too complex to mechanistically understand its results.

6.5 Model validation

Validation of our models to experiments performed in the laboratory is crucial. We mostly compare results to *in vitro* models as these are more controlled and isolated, similar to our *in silico* studies. The control of e.g. the composition of the extracellular matrix, the addition of growth factors, and the inhibition of protein activity or gene expression allows for manipulation of the cell behaviors and properties. As a validation of *in silico* models, we try to reproduce such *in vitro* manipulation experiments. For this purpose, ideally, all model parameters are directly coupled to such controllable experimental factors, e.g. a specific protein. Unfortunately, this is not always true in practice. Fortunately, some parameters can be coupled in a qualitative matter. For instance, protein concentrations can be tuned relative to each other. Dose-dependent experiments for manipulation of cell adhesion strengths, rates (e.g. pinocytosis rate) and signaling pathways can help to

tune the representing qualitative parameters in the model. Additionally, various parameters could be quantified experimentally to allow for quantitative model predictions. The adhesion strength of cells can be quantified by the force that is required to pull them apart [161]. This method might be useful to find quantitative values, or at least the relative ordering, of the contact energy parameters that describe adhesions between polarized cells, non-polarized cells and the extracellular matrix.

6.6 Relevance of modeling

What can the Life Sciences community learn from modeling? In the first place, computational models are very useful to test hypotheses. In comparison with experimental assays, a large benefit of computational models is that you can define the level of complexity. Often, we like to study a specific mechanism or regulation system in isolation, such as matrix degradation (Chapter 2), tip cell overtaking (Chapter 3) or lumen formation (Chapter 4). In a computational model, one can focus on the main components and interactions of the system of interest and is not hindered by all the proteins, pathways and environmental conditions that interfere with the system *in vivo*. Sometimes, models show that what was hypothesized to be enough to drive a system is not sufficient to reproduce experimental data. This indicates that the assumptions and mechanisms of the model should be reevaluated. Alternatively, abstraction of a complex mechanisms to a simple model can show that biological phenomena can be much simpler than initially thought. For instance, organization of the axial body segments in vertebrates involves many genes (HOX genes) and regulating pathways [200, 201]. However, patterning might be driven by a far more simple mechanism in some other cases. Mathematical modeling showed that patterns, such as stripes and spots, can emerge through self-organization by a simple reaction-diffusion system [105], in which an activator activates itself and activates an inhibitor that diffuses slower than the activator. Experimental and mathematical modeling results indicate that such a mechanism possibly controls digit patterning, in which the dose of *Hox* genes modulates the digit period or wavelength [202]. In addition, a reaction-diffusion mechanism involving WNT and its inhibitor DKK might regulate spacing of epidermal hair follicles [203].

When we feel that we understand the isolated process, we can start to combine model components to closer match the experimental settings. Some examples of model combinations are discussed in the previous sections, e.g. a combination of matrix degradation and tip cell overtaking. Extending the complexity of models can lead to new research questions and interesting new insights. The greatest strength of modeling is that it allows us to test many different hypotheses in a cheap and efficient manner. Each hypothesis could

result in a different outcome of the model. Predictions on the model outcome emerge on a higher level from modeling hypotheses on a lower level. For instance, lumen formation or tip cell overtaking on a tissue scale arise from assumptions on cellular and intercellular interactions. By testing the model predictions from different hypotheses with experiments, hypotheses can be validated or falsified. As a first validation, we test our model results with readily published data. In this thesis, we for instance compared the tip cell overtaking rates with published experimental data [24, 25]. The next step is to experimentally verify new, experimentally unexplored model predictions that give new biological insights. As an example, the lumen formation model predicted that vacuolation and cell-cell repulsion function synergistically and this hypothesis was recently validated experimentally by Yu *et al.* [199]. In addition, we have a close cooperation with a laboratory specialized in fibrin invasion with whom we plan to test the hypothesis from Chapter 2 that a uPAR-plasmin-TGF β 1 positive feedback loop drives sprouting in their experimental setup. Validation of model predictions is essential for the acceptance of new hypotheses. A model can merely make a strong case that a hypothesis is likely correct. Only by experimental validation, one can be confident that a hypothesis actually describes what is happening *in vivo*. This is why we cannot stress enough how important a close cooperation between computational and experimental biologists is to make steps in the Life Science field.

6.7 Model predictions

By studying the computational models in this thesis, we were able to suggest some experiments to test our model predictions. Here we sum the four most important predictions from the models in this thesis that require experimental validation:

1. The probability of angiogenic ingrowth in a monolayer of endothelial cells in the *in vitro* HMVEC-fibrin assay [38] depends on a TGF β 1-fibrinolysis feedback loop. There is a reduced angiogenic ingrowth on LMW compared to HMW as a result of lower levels of latent-TGF β 1 bound to LMW. Our model predict that addition of TGF β 1 antibodies to cells cultured on HMW should reduce sprouting.
2. Tip cell overtaking occurs spontaneously during sprouting by the cell mixing induced by the collective cell behaviors driving sprouting in our models. In the contact inhibition model, cells are pushed forward in the center of the sprout by the sprouting force and move backward along the sides of the sprouts driven by the gradient of the chemoattractant towards the spheroid center. This suggests that tracking of the position of cells in the sprout in experiments can give information on the driving

mechanisms of cell-mixing in sprouting. This experiment has already been done [25], but the experimental data is not publicly available.

3. Lumen formation is most efficient and robust for changes in the parameters and in the environment when vacuolation and cell-cell repulsion function synergistically. Our model results predict that inhibition of vacuolation by reducing pinocytosis should prevent lumen formation in capillaries, but not in larger vessels, whereas inhibition of cell-cell repulsion by cleavage of negatively charged extracellular proteins should destabilize lumen formation in all vessel types. Recent experimental work in ISV of zebrafish [199] supports our hypothesis that vacuolation and cell-cell repulsion both contribute to lumen formation.
4. A global sensitivity analysis for the contact inhibition model showed that the diffusion coefficient alone is dominant for variation in the lacuna count of vascular networks. The number of lacuna is large for small values of the diffusion coefficient, whereas no lacunae are formed for large values of the diffusion coefficient. To reach such small diffusion coefficients, the chemical in question needs to have a strong binding interaction with the extracellular matrix. Our model suggests VEGF as a possible candidate for the chemoattractant, but the attractive force might be mediated by another chemoattractant (e.g. CXCL12 [64]). Therefore, we suggest to experiment with different matrix types and different binding-epitope blockers, to see if it effects the lacuna count, and if so, to trace back the responsible chemoattractant by checking which chemical corresponds to the most influencing set of changes in binding-epitopes.

In summary, we developed computational models to address key steps in the complex process of angiogenesis. Each model gave new insights in the mechanisms of the isolated steps. Future work can combine and intertwine these models to come to a closer representation of *in vivo* angiogenesis. Experimental validation of the model predictions is essential to test the validity of our model assumptions and hypotheses. Thus, by a combination of computational modeling and experimental assays we are unraveling the mechanisms of angiogenesis, step by step.

Bibliography

- [1] W. Risau. "Mechanisms of angiogenesis". In: *Nature* 386 (1997), pp. 671–674.
- [2] P Carmeliet and R. K. Jain. "Angiogenesis in cancer and other diseases." In: *Nature* 407 (2000), pp. 249–257.
- [3] H. Gerhardt, M. Golding, M. Fruttiger, C. Ruhrberg, A. Lundkvist, A. Abramsson, M. Jeltsch, C. Mitchell, K. Alitalo, D. Shima, and C. Betsholtz. "VEGF guides angiogenic sprouting utilizing endothelial tip cell filopodia". In: *Journal of Cell Biology* 161.6 (2003), pp. 1163–1177.
- [4] K. Friddle. "Pathogenesis of retinopathy of prematurity: Does inflammation play a role?" In: *Newborn and Infant Nursing Reviews* 13 (2013), pp. 161–165.
- [5] A. Hoeben, B. Landuyt, M. S. Highley, H. Wildiers, A. T. Van Oosterom, and E. A. De Bruijn. "Vascular endothelial growth factor and angiogenesis." In: *Pharmacological reviews* 56 (2004), pp. 549–580.
- [6] P. Carmeliet and R. K. Jain. "Molecular mechanisms and clinical applications of angiogenesis." In: *Nature* 473.7347 (2011), pp. 298–307.
- [7] A. Marrelli, P. Cipriani, V. Liakouli, F. Carubbi, C. Perricone, R. Perricone, and R. Giacomelli. "Angiogenesis in rheumatoid arthritis: A disease specific process or a common response to chronic inflammation?" In: *Autoimmunity Reviews* 10 (2011), pp. 595–598.
- [8] E. W. M. Ng and A. P. Adamis. "Targeting angiogenesis, the underlying disorder in neovascular age-related macular degeneration." In: *Canadian journal of ophthalmology. Journal canadien d'ophtalmologie* 40 (2005), pp. 352–368.
- [9] G. K. Kolluru, S. C. Bir, and C. G. Kevil. "Endothelial dysfunction and diabetes: Effects on angiogenesis, vascular remodeling, and wound healing". In: *International Journal of Vascular Medicine* 2012 (2012).
- [10] T. A. E. Ahmed, E. V. Dare, and M. Hincke. "Fibrin: a versatile scaffold for tissue engineering applications." In: *Tissue engineering. Part B, Reviews* 14 (2008), pp. 199–215.
- [11] M. W. Laschke and M. D. Menger. "Vascularization in tissue engineering: Angiogenesis versus inosculation". In: *European Surgical Research* 48 (2012), pp. 85–92.
- [12] H Bramfeldt, G Sabra, V Centis, and P Vermette. "Scaffold vascularization: a challenge for three-dimensional tissue engineering." In: *Current medicinal chemistry* 17 (2010), pp. 3944–3967.
- [13] V. Marx. "Tissue engineering: Organs from the lab." In: *Nature* 522 (2015), pp. 373–377.
- [14] F. De Smet, I. Segura, K. De Bock, P. J. Hohensinner, and P. Carmeliet. "Mechanisms of vessel branching: Filopodia on endothelial tip cells lead the way". In: *Arteriosclerosis, Thrombosis, and Vascular Biology* 29 (2009), pp. 639–649.
- [15] H. Gerhardt. "VEGF and endothelial guidance in angiogenic sprouting". In: *Organogenesis* 4 (2008), pp. 241–246.
- [16] A. L. Bauer, T. L. Jackson, and Y. Jiang. "A cell-based model exhibiting branching and anastomosis during tumor-induced angiogenesis." In: *Biophysical journal* 92.9 (2007), pp. 3105–3121.
- [17] C Frantz, K. M. Stewart, and V. M. Weaver. "The extracellular matrix at a glance." In: *J Cell Sci* (), pp. 4195–4200.

- [18] M. M. Martino, P. S. Briquez, A Ranga, M. P. Lutolf, and J. A. Hubbell. "Heparin-binding domain of fibrin(ogen) binds growth factors and promotes tissue repair when incorporated within a synthetic matrix." In: *PNAS* 110.12 (2013), pp. 4563–4568.
- [19] J. P. Irigoyen, P. Muñoz Cánoves, L. Montero, M. Koziczak, and Y. Nagamine. "The plasminogen activator system: biology and regulation." In: *Cellular and molecular life sciences : CMLS* 56.1-2 (1999), pp. 104–132.
- [20] P. ten Dijke and H. M. Arthur. "Extracellular control of TGFbeta signalling in vascular development and disease." In: *Nature reviews. Molecular cell biology* 8.11 (2007), pp. 857–869.
- [21] C. Roca and R. H. Adams. "Regulation of vascular morphogenesis by Notch signaling". In: *Genes and Development* 21.20 (2007), pp. 2511–2524.
- [22] S. P. Herbert and D. Y. R. Stainier. "Molecular control of endothelial cell behaviour during blood vessel morphogenesis". In: *Nature Reviews Molecular Cell Biology* 12.9 (2011), pp. 551–564.
- [23] M. Hellström, L.-K. Phng, J. J. Hofmann, E. Wallgard, L. Coultas, P. Lindblom, J. Alva, A.-K. Nilsson, L. Karlsson, N. Gaiano, K. Yoon, J. Rossant, M. L. Iruela-Arispe, M. Kalén, H. Gerhardt, and C. Betsholtz. "Dll4 signalling through Notch1 regulates formation of tip cells during angiogenesis." In: *Nature* 445.7129 (2007), pp. 776–780.
- [24] L. Jakobsson, C. a. Franco, K. Bentley, R. T. Collins, B. Ponsioen, I. M. Aspalter, I. Rosewell, M. Busse, G. Thurston, A. Medvinsky, S. Schulte-Merker, and H. Gerhardt. "Endothelial cells dynamically compete for the tip cell position during angiogenic sprouting." In: *Nature cell biology* 12.10 (2010), pp. 943–953.
- [25] S. Arima, K. Nishiyama, T. Ko, Y. Arima, Y. Hakozaki, K. Sugihara, H. Koseki, Y. Uchijima, Y. Kurihara, and H. Kurihara. "Angiogenic morphogenesis driven by dynamic and heterogeneous collective endothelial cell movement". In: *Development* 138.21 (2011), pp. 4763–4776.
- [26] G. Cheng, S. Liao, H. K. Wong, D. A. Lacorre, E. Di Tomaso, P. Au, D. Fukumura, R. K. Jain, and L. L. Munn. "Engineered blood vessel networks connect to host vasculature via wrapping-and-tapping anastomosis". In: *Blood* 118 (2011), pp. 4740–4749.
- [27] G Bergers and S Song. "The role of pericytes in blood-vessel formation and maintenance." In: *Neuro Oncol* (), pp. 452–464.
- [28] G. E. Davis and K. J. Bayless. "An integrin and Rho GTPase-dependent pinocytic vacuole mechanism controls capillary lumen formation in collagen and fibrin matrices." In: *Microcirculation (New York, N.Y. : 1994)* 10.1 (2003), pp. 27–44.
- [29] M. Kamei, W. B. Saunders, K. J. Bayless, L. Dye, G. E. Davis, and B. M. Weinstein. "Endothelial tubes assemble from intracellular vacuoles in vivo." In: *Nature* 442.7101 (2006), pp. 453–456.
- [30] Y. Blum, H. G. Belting, E. Ellertsdottir, L. Herwig, F. Lüders, and M. Affolter. "Complex cell rearrangements during intersegmental vessel sprouting and vessel fusion in the zebrafish embryo". In: *Developmental Biology* 316.2 (2008), pp. 312–322.
- [31] Y. Wang, M. S. Kaiser, J. D. Larson, A. Nasevicius, K. J. Clark, S. A. Wadman, S. E. Roberg-Perez, S. C. Ekker, P. B. Hackett, M. McGrail, and J. J. Essner. "Moesin1 and Ve-cadherin are required in endothelial cells during in vivo tubulogenesis." In: *Development (Cambridge, England)* 137.18 (2010), pp. 3119–3128.
- [32] B. Strilić, T. Kučera, J. Eglinger, M. R. Hughes, K. M. McNagny, S. Tsukita, E. Dejana, N. Ferrara, and E. Lammert. "The Molecular Basis of Vascular Lumen Formation in the Developing Mouse Aorta". In: *Developmental Cell* 17.4 (2009), pp. 505–515.
- [33] B. Strilić, J. Eglinger, M. Krieg, M. Zeeb, J. Axnick, P. Babál, D. J. Müller, and E. Lammert. "Electrostatic cell-surface repulsion initiates lumen formation in developing blood vessels". In: *Current Biology* 20.22 (2010), pp. 2003–2009.
- [34] R. Auerbach, N. Akhtar, R. L. Lewis, and B. L. Shinnars. *Angiogenesis assays: Problems and pitfalls*. 2000.

- [35] R. Auerbach, R. Lewis, B. Shinnars, L. Kubai, and N. Akhtar. *Angiogenesis assays: A critical overview*. 2003.
- [36] I. Geudens and H. Gerhardt. "Coordinating cell behaviour during blood vessel formation". In: *Development* 138.21 (2011), pp. 4569–4583.
- [37] B. Vailhé, D. Vittet, and J. J. Feige. "In vitro models of vasculogenesis and angiogenesis." In: *Laboratory investigation; a journal of technical methods and pathology* 81 (2001), pp. 439–452.
- [38] P. Koolwijk, M. G. M. Van Erck, W. J. A. De Vree, M. A. Vermeer, H. A. Weich, R. Hanemaaijer, and V. W. M. Van Hinsbergh. "Cooperative effect of $\text{TNF}\alpha$, bFGF, and VEGF on the formation of tubular structures of human microvascular endothelial cells in a fibrin matrix. Role of urokinase activity". In: *Journal of Cell Biology* 132.6 (1996), pp. 1177–1188.
- [39] E. M. Weijers, M. H. Van Wijhe, L. Joosten, A. J. G. Horrevoets, M. P. M. De Maat, V. W. M. Van Hinsbergh, and P. Koolwijk. "Molecular weight fibrinogen variants alter gene expression and functional characteristics of human endothelial cells". In: *Journal of Thrombosis and Haemostasis* 8.12 (2010), pp. 2800–2809.
- [40] M. S. Pepper, J. D. Vassalli, L. Orci, and R. Montesano. "Biphasic effect of transforming growth factor-beta 1 on in vitro angiogenesis." In: *Experimental cell research* 204 (1993), pp. 356–363.
- [41] A. Stahl, K. M. Connor, P. Sapieha, J. Chen, R. J. Dennison, N. M. Krahe, M. R. Seaward, K. L. Willett, C. M. Aderman, K. I. Guerin, J. Hua, C. Löfqvist, A. Hellström, and L. E. H. Smith. "The mouse retina as an angiogenesis model". In: *Investigative Ophthalmology and Visual Science* 51 (2010), pp. 2813–2826.
- [42] R. M. H. "'Cell-based modeling" In: *Encyclopedia of Applied and Computational Mathematics*". In: ed. by B. Enquist. Springer, 2013.
- [43] L. Venkatraman, H. Li, C. F. Dewey, J. K. White, S. S. Bhowmick, H. Yu, and L. Tucker-Kellogg. "Steady states and dynamics of urokinase-mediated plasmin activation in silico and in vitro". In: *Biophysical Journal* 101 (2011), pp. 1825–1834.
- [44] J. R. Collier, N. A. Monk, P. K. Maini, and J. H. Lewis. "Pattern formation by lateral inhibition with feedback: a mathematical model of delta-notch intercellular signalling." In: *Journal of theoretical biology* 183.4 (1996), pp. 429–446.
- [45] D. Sprinzak, A. Lakhanpal, L. Lebon, L. a. Santat, M. E. Fontes, G. a. Anderson, J. Garcia-Ojalvo, and M. B. Elowitz. "Cis-interactions between Notch and Delta generate mutually exclusive signalling states." In: *Nature* 465.7294 (2010), pp. 86–90.
- [46] D. Sprinzak, A. Lakhanpal, L. LeBon, J. Garcia-Ojalvo, and M. B. Elowitz. "Mutual inactivation of Notch receptors and ligands facilitates developmental patterning". In: *PLoS Computational Biology* 7.6 (2011).
- [47] A. Anderson and M. Chaplain. "A mathematical model for capillary network formation in the absence of endothelial cell proliferation." In: *Appl. Math. Lett.* 11.3 (1998), pp. 109–114.
- [48] M. A. J. Chaplain and G. Lolas. "Mathematical modelling of cancer cell invasion of tissue: the role of the urokinase plasminogen activation system". In: *Mathematical Models and Methods in Applied Sciences* 15.11 (2005), pp. 1685–1734.
- [49] P. Namy, J. Ohayon, and P. Tracqui. "Critical conditions for pattern formation and in vitro tubulogenesis driven by cellular traction fields". In: *Journal of Theoretical Biology* 227.1 (2004), pp. 103–120.
- [50] D. Manoussaki. "A mechanochemical model of angiogenesis and vasculogenesis". In: *ESAIM: Mathematical Modelling and Numerical Analysis* 37 (2003), pp. 581–599.
- [51] F. Milde, M. Bergdorf, and P. Koumoutsakos. "A hybrid model for three-dimensional simulations of sprouting angiogenesis." In: *Biophysical journal* 95.7 (2008), pp. 3146–3160.
- [52] A. Qutub, G. Liu, P. Vempati, and P. A.S. "Integration of angiogenesis modules at multiple scales: from molecular to tissue". In: *Pac Symp Biocomput.* (2009), pp. 316–327.

- [53] A. Szabó, D. P. Erica, and A. Czirók. “Network formation of tissue cells via preferential attraction to elongated structures”. In: *Physical Review Letters* 98.3 (2007), p. 038102.
- [54] D Palachanis, S. A, and M. R. M. H. “Particle-based simulation of ellipsoid particle aggregation as a model for vascular network formation”. In: *Computational Particle Mechanics* (2015), pp. 1–9. arXiv: 1507.00298.
- [55] T. J. Newman. “Modeling multicellular systems using subcellular elements.” In: *Mathematical biosciences and engineering : MBE* 2 (2005), pp. 613–624. arXiv: 0504028 [q-bio].
- [56] R. Farhadifar, J. C. Röper, B. Aigouy, S. Eaton, and F. Jülicher. “The Influence of Cell Mechanics, Cell-Cell Interactions, and Proliferation on Epithelial Packing”. In: *Current Biology* 17 (2007), pp. 2095–2104.
- [57] R. M. H. Merks, M. Guravage, D. Inzé, and G. T. S. Beemster. “VirtualLeaf: an open-source framework for cell-based modeling of plant tissue growth and development.” In: *Plant physiology* 155 (2011), pp. 656–666.
- [58] K. Bentley, G. Mariggi, H. Gerhardt, and P. a. Bates. “Tipping the balance: Robustness of tip cell selection, migration and fusion in angiogenesis”. In: *PLoS Computational Biology* 5.10 (2009).
- [59] K. Bentley, H. Gerhardt, and P. a. Bates. “Agent-based simulation of notch-mediated tip cell selection in angiogenic sprout initialisation”. In: *Journal of Theoretical Biology* 250.1 (2008), pp. 25–36.
- [60] K. Bentley, C. A. Franco, A. Philippides, R. Blanco, M. Dierkes, V. Gebala, F. Stanchi, M. Jones, I. M. Aspalter, G. Cagna, S. Weström, L. Claesson-Welsh, D. Vestweber, and H. Gerhardt. “The role of differential VE-cadherin dynamics in cell rearrangement during angiogenesis.” In: *Nature cell biology* 16.4 (2014), pp. 309–21.
- [61] J. A. Glazier and F. Graner. “Simulation of the differential adhesion driven rearrangement of biological cells”. In: *Phys. Rev. E* 47.3 (1993), pp. 2128–2154.
- [62] F. Graner and J. A. Glazier. “Simulation of biological cell sorting using a two-dimensional extended Potts model”. In: *Phys. Rev. Lett.* 69 (13 1992), pp. 2013–2016.
- [63] R. M. H. Merks, S. Brodsky, M. Goligorsky, S. Newman, and J. A. Glazier. “Cell elongation is key to in silico replication of in vitro vasculogenesis and subsequent remodeling”. In: *Devel. Biol.* 289 (2006), pp. 44–54.
- [64] R. M. H. Merks, E. D. Perryn, A. Shirinifard, and J. A. Glazier. “Contact-Inhibited Chemotaxis in De Novo and Sprouting Blood-Vessel Growth”. In: *PLoS Comput. Biol.* 4.9 (2008), e1000163.
- [65] J. T. Daub and R. M. H. Merks. “A Cell-Based Model of Extracellular-Matrix-Guided Endothelial Cell Migration During Angiogenesis”. In: *Bulletin of Mathematical Biology* 75.8 (2013), pp. 1377–1399.
- [66] A. Shirinifard, J. S. Gens, B. L. Zaitlen, N. J. Poptawski, M. Swat, and J. A. Glazier. “3D multi-cell simulation of tumor growth and angiogenesis”. In: *PLoS ONE* 4.10 (2009).
- [67] M. M. Palm, M. G. Dallinga, E. van Dijk, I. Klaassen, R. O. Schlingemann, and R. Merks. “Computational Screening of Angiogenesis Model Variants Predicts that Differential Chemotaxis Helps Tip Cells Move to the Sprout Tip and Accelerates Sprouting”. In: *arXiv: 1409.5895* (2014).
- [68] A. Szabó, E. Mehes, E. Kosa, and A. Czirók. “Multicellular sprouting in vitro”. In: *Biophysical Journal* 95.6 (2008), pp. 2702–2710.
- [69] R. F. M. van Oers, E. G. Rens, D. J. LaValley, C. A. Reinhart-King, and R. M. H. Merks. “Mechanical Cell-Matrix Feedback Explains Pairwise and Collective Endothelial Cell Behavior In Vitro.” In: *PLoS computational biology* 10.8 (2014), e1003774. arXiv: 1308.3721.
- [70] L. Coultas, K. Chawengsaksophak, and J. Rossant. “Endothelial cells and VEGF in vascular development”. In: *Nature* 438 (2005), pp. 937–945.

- [71] A. Köhn-Luque, W. de Back, J. Starruß, A. Mattiotti, A. Deutsch, J. M. Pérez-Pomares, and M. a. Herrero. "Early embryonic vascular patterning by matrix-mediated paracrine signalling: A mathematical model study". In: *PLoS ONE* 6.9 (2011), pp. 1–12.
- [72] M. M. Palm and R. M. H. Merks. "Vascular networks due to dynamically arrested crystalline ordering of elongated cells". In: *Physical Review E - Statistical, Nonlinear, and Soft Matter Physics* 87.1 (2013), pp. 1–5. arXiv: 1210.7164.
- [73] C. A. Reinhart-King, M Dembo, and D. A. Hammer. "Cell-cell mechanical communication through compliant substrates". In: *Biophysical Journal* 95.12 (2008), pp. 6044–6051.
- [74] J. Califano and C. Reinhart-King. "A Balance of Substrate Mechanics and Matrix Chemistry Regulates Endothelial Cell Network Assembly". In: *Cell Mol. Bioeng.* 1.2 (2008), pp. 122–132.
- [75] S. E. M. Boas, M. M. Palm, P. Koolwijk, and R. M. Merks. "Computational Modeling of Angiogenesis: Towards a Multi-Scale Understanding of Cell-Cell and Cell-Matrix Interactions". In: *Mechanical and Chemical Signaling in Angiogenesis*. Vol. 12. 2013, pp. 161–183.
- [76] A. Collen, P. Koolwijk, M. Kroon, and V. W. van Hinsbergh. "Influence of fibrin structure on the formation and maintenance of capillary-like tubules by human microvascular endothelial cells." In: *Angiogenesis* 2.2 (1998), pp. 153–165.
- [77] N. Laurens, P. Koolwijk, and M. P. de Maat. "Fibrin structure and wound healing." In: *Journal of thrombosis and haemostasis : JTH* 4 (2006), pp. 932–939.
- [78] E. L. Kaijzel, P. Koolwijk, M. G. M. Van Erck, V. W. M. Van Hinsbergh, and M. P. M. De Maat. "Molecular weight fibrinogen variants determine angiogenesis rate in a fibrin matrix in vitro and in vivo". In: *Journal of Thrombosis and Haemostasis* 4.9 (2006), pp. 1975–1981.
- [79] A. Collen, S. M. Smorenburg, E. Peters, F. Lupu, P. Koolwijk, C. V. Noorden, and V. W. M. V. Hinsbergh. "Unfractionated and Low Molecular Weight Heparin Affect Fibrin Structure and Angiogenesis in Vitro Unfractionated and Low Molecular Weight Heparin Affect Fibrin Structure and Angiogenesis in vitro". In: *Cancer research* (2000), pp. 6196–6200.
- [80] M. E. Kroon, P. Koolwijk, H. van Goor, U. H. Weidle, A. Collen, G. van der Pluijm, and V. W. van Hinsbergh. "Role and localization of urokinase receptor in the formation of new microvascular structures in fibrin matrices." In: *The American journal of pathology* 154.6 (1999), pp. 1731–1742.
- [81] C. Schachtrup, J. K. Ryu, M. J. Helmrick, E. Vagena, D. K. Galanakis, J. L. Degen, R. U. Margolis, and K. Kassoglou. "Fibrinogen triggers astrocyte scar formation by promoting the availability of active TGF- β after vascular damage." In: *The Journal of neuroscience : the official journal of the Society for Neuroscience* 30.17 (2010), pp. 5843–5854.
- [82] M. J. Duffy and C. Duggan. "The urokinase plasminogen activator system: A rich source of tumour markers for the individualised management of patients with cancer". In: *Clinical Biochemistry* 37.7 (2004), pp. 541–548.
- [83] W. Y. Li, S. S. N. Chong, E. Y. Huang, and T. L. Tuan. "Plasminogen activator/plasmin system: A major player in wound healing?" In: *Wound Repair and Regeneration* 11.4 (2003), pp. 239–247.
- [84] A. Bobik and V. Tkachuk. "Metalloproteinases and plasminogen activators in vessel remodeling." In: *Current hypertension reports* 5.6 (2003), pp. 466–472.
- [85] M. S. Pepper. "Role of the matrix metalloproteinase and plasminogen activator-plasmin systems in angiogenesis." In: *Arteriosclerosis, thrombosis, and vascular biology* 21.7 (2001), pp. 1104–1117.
- [86] D. Collen and H. Lijnen. "Basic and clinical aspects of fibrinolysis and thrombolysis". In: *Blood* 78 (1991), pp. 3114–3124.
- [87] J. M. Rakic, C. Maillard, M. Jost, K. Bajou, V. Masson, L. Devy, V. Lambert, J. M. Foidart, and a. Noël. "Role of plasminogen activator-plasmin system in tumor angiogenesis". In: *Cellular and Molecular Life Sciences* 60.3 (2003), pp. 463–473.
- [88] N. Hiraoka, E. Allen, I. J. Apel, M. R. Gyetko, and S. J. Weiss. "Matrix metalloproteinases regulate neovascularization by acting as pericellular fibrinolysins". In: *Cell* 95 (1998), pp. 365–377.

- [89] A. Collen, R. Hanemaaijer, F. Lupu, P. H. A. Quax, N. Van Lent, J. Grimbergen, E. Peters, P. Koolwijk, and V. W. M. Van Hinsbergh. "Membrane-type matrix metalloproteinase-mediated angiogenesis in a fibrin-collagen matrix". In: *Blood* 101 (2003), pp. 1810–1817.
- [90] S. Serrati, F. Margheri, M. Pucci, A. R. Cantelmo, R. Cammarota, J. Dotor, F. Borràs-Cuesta, G. Fibbi, A. Albini, and M. Del Rosso. "TGF β 1 antagonistic peptides inhibit TGF β 1-dependent angiogenesis". In: *Biochemical Pharmacology* 77.5 (2009), pp. 813–825.
- [91] G. Fibbi, M. Pucci, S. D'Alessio, C. Grappone, G. Pellegrini, R. Salzano, A. Casini, S. Milani, and M. Del Rosso. "Transforming growth factor beta-1 stimulates invasivity of hepatic stellate cells by engagement of the cell-associated fibrinolytic system." In: *Growth factors (Chur, Switzerland)* 19 (2001), pp. 87–100.
- [92] D. S. Lang, S. Marwitz, U. Heilenkötter, W. Schumm, O. Behrens, R. Simon, M. Reck, E. Vollmer, and T. Goldmann. "Transforming growth factor-beta signaling leads to uPA/PAI-1 activation and metastasis: A study on human breast cancer tissues". In: *Pathology and Oncology Research* 20 (2014), pp. 727–732.
- [93] L. E. Odekon, F. Blasi, and D. B. Rifkin. "Requirement for receptor-bound urokinase in plasmin-dependent cellular conversion of latent TGF-beta to TGF-beta." In: *Journal of cellular physiology* 158.3 (1994), pp. 398–407.
- [94] H. A. Levine, B. D. Sleeman, and M. Nilsen-Hamilton. "Mathematical modeling of the onset of capillary formation initiating angiogenesis." In: *Journal of mathematical biology* 42 (2001), pp. 195–238.
- [95] S. L. Diamond and S. Anand. "Inner clot diffusion and permeation during fibrinolysis." In: *Biophysical journal* 65.6 (1993), pp. 2622–2643.
- [96] B. E. Bannish, J. P. Keener, and A. L. Fogelson. "Modelling fibrinolysis: A 3D stochastic multiscale model". In: *Mathematical Medicine and Biology* 31 (2014), pp. 17–44.
- [97] G. Cesarman-Maus and K. A. Hajjar. "Molecular mechanisms of fibrinolysis". In: *British Journal of Haematology* 129.3 (2005), pp. 307–321.
- [98] R. W. Colman, V. J. Marder, A. W. Clowes, J. N. George, and S. Z. Goldhaber. "Basic Principles and Clinical Practice". In: *Hemostasis and Thrombosis*. 2006.
- [99] T. Dejouvencel, L. Doeuve, R. Lacroix, L. Plawinski, F. Dignat-George, H. R. Lijnen, and E. Anglés-Cano. "Fibrinolytic cross-talk: A new mechanism for plasmin formation". In: *Blood* 115.10 (2010), pp. 2048–2056.
- [100] E. I. Deryugina and J. P. Quigley. "Cell Surface Remodeling by Plasmin: A New Function for an Old Enzyme". In: *Journal of Biomedicine and Biotechnology* 2012 (2012).
- [101] G. A. McMahon, E. Petitclerc, S. Stefansson, E. Smith, M. K. K. Wong, R. J. Westrick, D. Ginsburg, P. C. Brooks, and D. A. Lawrence. "Plasminogen Activator Inhibitor-1 Regulates Tumor Growth and Angiogenesis". In: *Journal of Biological Chemistry* 276.36 (2001), pp. 33964–33968.
- [102] M. S. Pepper and R. Montesano. "Proteolytic balance and capillary morphogenesis." In: *Cell differentiation and development: the official journal of the International Society of Developmental Biologists* 32 (1990), pp. 319–327.
- [103] R. Montesano, M. S. Pepper, J. D. Vassalli, and L. Orci. "Phorbol ester induces cultured endothelial cells to invade a fibrin matrix in the presence of fibrinolytic inhibitors." In: *Journal of cellular physiology* 132 (2005), pp. 509–516.
- [104] M. Pepper, D. Belin, R. Montesano, R. Orci, and J. Vassalli. "Transforming growth factor-beta 1 modulates basic fibroblast growth factor-induced proteolytic and angiogenic properties of endothelial cells in vitro". In: *J. Cell. Biol.* 111 (1990), pp. 743–755.
- [105] a. M. Turing. "The Chemical Basis of Morphogenesis." In: *Society* 237 (1952), pp. 37–72.
- [106] A. Gierer and H. Meinhardt. "A Theory of Biological Pattern Formation." In: *Kybernetik* 12 (1972), pp. 30–39.
- [107] M. Cohen, M. Georgiou, N. L. Stevenson, M. Miodownik, and B. Baum. "Dynamic Filopodia Transmit Intermittent Delta-Notch Signaling to Drive Pattern Refinement during Lateral Inhibition". In: *Developmental Cell* 19.1 (2010), pp. 78–89.

- [108] A. Szabó and A. Czirók. "The role of cell-cell adhesion in the formation of multicellular sprouts". In: *Math Model Nat Phenom* 5.1 (2010), pp. 106–122.
- [109] Z.-J. Liu, T. Shirakawa, Y. Li, A. Soma, M. Oka, G. P. Dotto, R. M. Fairman, O. C. Velazquez, and M. Herlyn. "Regulation of Notch1 and Dll4 by vascular endothelial growth factor in arterial endothelial cells: implications for modulating arteriogenesis and angiogenesis." In: *Molecular and cellular biology* 23.1 (2003), pp. 14–25.
- [110] C. K. Williams, J. L. Li, M. Murga, A. L. Harris, and G. Tosato. "Up-regulation of the Notch ligand Delta-like 4 inhibits VEGF-induced endothelial cell function". In: *Blood* 107.3 (2006), pp. 931–939.
- [111] R. M. H. Merks and P. Koolwijk. "Modeling Morphogenesis *in silico* and *in vitro*: Towards Quantitative, Predictive, Cell-based Modeling". In: *Math. Model. Nat. Phenom.* 4.4 (2009), pp. 149–171.
- [112] A. Czirók. "Endothelial cell motility, coordination and pattern formation during vasculogenesis". In: *Wiley Interdisciplinary Reviews: Systems Biology and Medicine* 5 (2013), pp. 587–602.
- [113] E. F. Keller and L. A. Segel. "Initiation of slime mold aggregation viewed as an instability". In: *Journal of Theoretical Biology* 26.3 (1970), pp. 399–415.
- [114] E. Dejana. "Endothelial cell-cell junctions: happy together." In: *Nature reviews. Molecular cell biology* 5 (2004), pp. 261–270.
- [115] S. Yoo and S. Kwon. "Angiogenesis and its therapeutic opportunities". In: *Mediators Inflamm* 2013 (2013).
- [116] A. Köhn-Luque, W. de Back, Y. Yamaguchi, K. Yoshimura, M. A. Herrero, and T. Miura. "Dynamics of VEGF matrix-retention in vascular network patterning." In: *Physical biology* 10.6 (2013), p. 066007.
- [117] D. Manoussaki, S. R. Lubkin, R. B. Vernon, and J. D. Murray. "A mechanical model for the formation of vascular networks *in vitro*." In: *Acta biotheoretica* 44.3-4 (1996), pp. 271–282.
- [118] F. Lin and E. C. Butcher. "T cell chemotaxis in a simple microfluidic device." In: *Lab on a chip* 6 (2006), pp. 1462–1469.
- [119] M. J. Siemerink, I. Klaassen, I. M. C. Vogels, A. W. Griffioen, C. J. F. Noorden, and R. O. Schlingemann. "CD34 marks angiogenic tip cells in human vascular endothelial cell cultures". In: *Angiogenesis* 15.1 (2012), pp. 151–163.
- [120] J. Gavard and J. S. Gutkind. "VEGF controls endothelial-cell permeability by promoting the beta-arrestin-dependent endocytosis of VE-cadherin." In: *Nature cell biology* 8.11 (2006), pp. 1223–1234.
- [121] N. J. Savill and P. Hogeweg. "Modelling morphogenesis: from single cells to crawling slugs". In: *J. Theor. Biol.* 184 (1997), pp. 229–235.
- [122] E. Dougherty and R. Lotufo. "Hands-on morphological image processing". In: *SPIE Press* (2003).
- [123] A. C. Miller, E. L. Lyons, and T. G. Herman. "cis-Inhibition of Notch by Endogenous Delta Biases the Outcome of Lateral Inhibition". In: *Current Biology* 19.16 (2009), pp. 1378–1383.
- [124] J. F. de Celis and S. Bray. "Feed-back mechanisms affecting Notch activation at the dorso-ventral boundary in the *Drosophila* wing". In: *Development* 124.17 (1997), pp. 3241–3251.
- [125] M. Boareto, M. K. Jolly, E. Ben-Jacob, and J. N. Onuchic. "Jagged mediates differences in normal and tumor angiogenesis by affecting tip-stalk fate decision". In: *P. Natl. Acad. Sci. USA* 112.29 (2015), pp. 3836–3844.
- [126] A. Czirók, E. A. Zamir, A. Szabó, and C. D. Little. *Multicellular Sprouting during Vasculogenesis*. 2008.
- [127] M. L. Iruela-Arispe and G. E. Davis. *Cellular and Molecular Mechanisms of Vascular Lumen Formation*. 2009.

- [128] K. S. Nelson and G. J. Beitel. "More Than a Pipe Dream: Uncovering Mechanisms of Vascular Lumen Formation". In: *Developmental Cell* 17.4 (2009), pp. 435–437.
- [129] M. Zeeb, B. Strilic, and E. Lammert. *Resolving cell-cell junctions: Lumen formation in blood vessels*. 2010.
- [130] K. Xu and O. Cleaver. "Tubulogenesis during blood vessel formation". In: *Seminars in Cell & Developmental Biology* 22.9 (2011), pp. 993–1004.
- [131] B. Lubarsky and M. A. Krasnow. *Tube morphogenesis: Making and shaping biological tubes*. 2003.
- [132] S. Stricker. "Studien über den Bau und das Leben der capillaren Blutgefäße. [Study on the structure and life of capillary blood vessels.]" In: *Sitz.-Ber. d. kais. Akad. d. Wissensch. f. Math.-Naturw.* 74 (1866-1870), 3. Abt. 1876.
- [133] T. Billroth. "Untersuchungen über die Entwicklung der Blutgefäße, nebst Beobachtungen aus der königlichen chirurgischen Universitäts-Klinik zu Berlin." In: *Berlin, Germany: Georg Reimer*. (1856).
- [134] K. M. Downs. "Florence Sabin and the mechanism of blood vessel lumenization during vasculogenesis." In: *Microcirculation (New York, N.Y. : 1994)* 10.1 (2003), pp. 5–25.
- [135] G. E. Davis and C. W. Camarillo. "An alpha 2 beta 1 integrin-dependent pinocytic mechanism involving intracellular vacuole formation and coalescence regulates capillary lumen and tube formation in three-dimensional collagen matrix." In: *Experimental cell research* 224.1 (1996), pp. 39–51.
- [136] B. B. Aldridge, J. M. Burke, D. A. Lauffenburger, and P. K. Sorger. "Physicochemical modelling of cell signalling pathways." In: *Nature cell biology* 8.11 (2006), pp. 1195–1203.
- [137] R. M. H. Merks and J. A. Glazier. "A cell-centered approach to developmental biology". In: *Physica A: Statistical Mechanics and its Applications* 352.1 (2005), pp. 113–130.
- [138] K. Bentley, M. Jones, and B. Cruys. *Predicting the future: Towards symbiotic computational and experimental angiogenesis research*. 2013.
- [139] M. H. Swat, G. L. Thomas, J. M. Belmonte, A. Shirinifard, D. Hmeljak, and J. A. Glazier. *Multi-Scale Modeling of Tissues Using CompuCell3D*. Vol. 110. 2012, pp. 325–366.
- [140] M. Scianna, L. Preziosi, and K. Wolf. "A Cellular Potts model simulating cell migration on and in matrix environments". In: *Mathematical Biosciences and Engineering* 10.1 (2013), pp. 235–261.
- [141] J. Starruß, T. Bley, L. Søgaard Andersen, and A. Deutsch. "A new mechanism for collective migration in myxococcus xanthus". In: *Journal of Statistical Physics* 128.1-2 (2007), pp. 269–286.
- [142] W. Koh, R. D. Mahan, and G. E. Davis. "Cdc42- and Rac1-mediated endothelial lumen formation requires Pak2, Pak4 and Par3, and PKC-dependent signaling." In: *Journal of cell science* 121.Pt 7 (2008), pp. 989–1001.
- [143] F. Martin-Belmonte and K. Mostov. "Regulation of cell polarity during epithelial morphogenesis". In: *Current Opinion in Cell Biology* 20.2 (2008), pp. 227–234.
- [144] N. R. Leslie, I. H. Batty, H. Maccario, L. Davidson, and C. P. Downes. "Understanding PTEN regulation: PIP2, polarity and protein stability." In: *Oncogene* 27.41 (2008), pp. 5464–5476.
- [145] A. C. Zovein, A. Luque, K. A. Turlo, J. J. Hofmann, K. M. Yee, M. S. Becker, R. Fassler, I. Mellman, T. F. Lane, and M. L. Iruela-Arispe. " β 1 Integrin Establishes Endothelial Cell Polarity and Arteriolar Lumen Formation via a Par3-Dependent Mechanism". In: *Developmental Cell* 18.1 (2010), pp. 39–51.
- [146] E. Denker, I. Bocina, and D. Jiang. "Tubulogenesis in a simple cell cord requires the formation of bi-apical cells through two discrete Par domains." In: *Development* 140.14 (2013), pp. 2985–2996.
- [147] K. J. Bayless and G. E. Davis. "The Cdc42 and Rac1 GTPases are required for capillary lumen formation in three-dimensional extracellular matrices." In: *Journal of cell science* 115.Pt 6 (2002), pp. 1123–1136.

- [148] G. E. Davis, K. J. Bayless, and A. Mavila. "Molecular basis of endothelial cell morphogenesis in three-dimensional extracellular matrices." In: *The Anatomical record* 268.3 (2002), pp. 252–275.
- [149] G. E. Davis, S. M. Black, and K. J. Bayless. "Capillary morphogenesis during human endothelial cell invasion of three-dimensional collagen matrices". In: *In Vitro Cell Dev Biol Anim* 36.8 (2000), pp. 513–9.
- [150] J.-B. Manneville, S. Etienne-Manneville, P. Skehel, T. Carter, D. Ogden, and M. Ferenczi. "Interaction of the actin cytoskeleton with microtubules regulates secretory organelle movement near the plasma membrane in human endothelial cells." In: *Journal of cell science* 116.Pt 19 (2003), pp. 3927–3938.
- [151] S. M. A. Tabei, S. Burov, H. Y. Kim, A. Kuznetsov, T. Huynh, J. Jureller, L. H. Philipson, A. R. Dinner, and N. F. Scherer. "Intracellular transport of insulin granules is a subordinated random walk." In: *Proceedings of the National Academy of Sciences of the United States of America* 110.13 (2013), pp. 4911–6.
- [152] A. Spiro, K. Fahmy, M. Schneider, E. Frei, M. Noll, and S. Baumgartner. "Formation of the bicoid morphogen gradient: an mRNA gradient dictates the protein gradient." In: *Development (Cambridge, England)* 136.4 (2009), pp. 605–614.
- [153] I. Tsarfaty, S. Rong, J. H. Resau, S. Rulong, P. P. da Silva, and G. F. Vande Woude. "The Met proto-oncogene mesenchymal to epithelial cell conversion." In: *Science (New York, N.Y.)* 263.5143 (1994), pp. 98–101.
- [154] G. Forgacs and S. Newman. "Biological physica of the developing embryo". In: *Cambridge, UK: Cambridge University Press* (2005).
- [155] I Tsarfaty, J. H. Resau, S Rulong, I Keydar, D. L. Faletto, and G. F. Vande Woude. "The met proto-oncogene receptor and lumen formation." In: *Science (New York, N.Y.)* 257.5074 (1992), pp. 1258–1261.
- [156] M. Klann, H. Koeppl, and M. Reuss. "Spatial modeling of vesicle transport and the cytoskeleton: The challenge of hitting the right road". In: *PLoS ONE* 7.1 (2012), pp. 1–40.
- [157] K. J. Bayless, R. Salazar, and G. E. Davis. "RGD-dependent vacuolation and lumen formation observed during endothelial cell morphogenesis in three-dimensional fibrin matrices involves the $\alpha(v)\beta(3)$ and $\alpha(5)\beta(1)$ integrins." In: *The American journal of pathology* 156.5 (2000), pp. 1673–1683.
- [158] J. S. Nielsen and K. M. McNagny. "The role of podocalyxin in health and disease." In: *Journal of the American Society of Nephrology : JASN* 20.8 (2009), pp. 1669–1676.
- [159] L. Herwig, Y. Blum, A. Krudewig, E. Ellertsdottir, A. Lenard, H. G. Belting, and M. Affolter. "Distinct cellular mechanisms of blood vessel fusion in the zebrafish embryo". In: *Current Biology* 21.22 (2011), pp. 1942–1948.
- [160] A. Szabó, K. Varga, T. Garay, B. HegedÁss, and A. Czirók. "Invasion from a cell aggregate—the roles of active cell motion and mechanical equilibrium". In: *Physical Biology* 9.1 (2012), p. 016010.
- [161] M. Krieg, Y. Arboleda-Estudillo, P.-H. Puech, J. Käfer, F. Graner, D. J. Müller, and C.-P. Heisenberg. "Tensile forces govern germ-layer organization in zebrafish." In: *Nature cell biology* 10.4 (2008), pp. 429–436. arXiv: 43149088966.
- [162] S Tanaka. "Simulation Frameworks for Morphogenetic Problems". In: *Computation* 3 (2015), pp. 197–221.
- [163] D. Iber, S. Tanaka, P. Fried, P. Germann, and D. Menshykau. "Simulating Tissue Morphogenesis and Signaling". English. In: *Tissue Morphogenesis*. Ed. by C. M. Nelson. Vol. 1189. Methods in Molecular Biology. New York: Springer, 2015, pp. 323–338.
- [164] D. Iber and D. Menshykau. "The control of branching morphogenesis." In: *Open biology* 3.9 (2013), p. 130088.
- [165] B. Boehm, H. Westerberg, G. Lesnicar-Pucko, S. Raja, M. Rautschka, J. Cotterell, J. Swoger, and J. Sharpe. "The role of spatially controlled cell proliferation in limb bud morphogenesis". In: *PLoS Biology* 8.7 (2010).

- [166] A. R. A. Anderson, M. A. J. Chaplain, and K. A. Rejniak, eds. *Single-cell-based models in biology and medicine*. Switzerland: Birkhäuser Verlag Basel, 2007.
- [167] M. A. Herrero, A. Köhn-Luque, and J. M. Pérez-Pomares. *Modelling vascular morphogenesis: current views on blood vessel development*. Vol. 19. supp01. 2009, pp. 1483–1537.
- [168] A. Saltelli, S. Tarantola, and K. P.-S. Chan. “A Quantitative Model-Independent Method for Global Sensitivity Analysis of Model Output”. English. In: *Technometrics* 41.1 (1999), pp. 39–56.
- [169] I. Sobol’. “Sensitivity estimates for nonlinear mathematical models”. In: *Mathematical Modeling and Computational Experiment* 1.4 (1993), pp. 407–414.
- [170] I. Sobol’. “Global sensitivity indices for nonlinear mathematical models and their Monte Carlo estimates”. In: *Mathematics and Computers in Simulation* 55 (2001), pp. 271–280.
- [171] C. Ostrom Jr. *Time Series Analysis, Regression Techniques, 2nd edition*. Newbury Park: Sage Publications, 1990.
- [172] M. Morris. “Factorial sampling plans for preliminary computational experiments”. In: *Technometrics* 33.2 (1991), pp. 161–174.
- [173] Y. Zheng and A. Rundell. “Comparative study of parameter sensitivity analyses of the TCR-activated erk-MAPK signalling pathway”. In: *Systems Biology, IEE Proceedings* 153.4 (2006), pp. 201–211.
- [174] K.-H. Cho, S.-Y. Shin, W. Kolch, and O. Wolkenhauer. “Experimental Design in Systems Biology, Based on Parameter Sensitivity Analysis Using a Monte Carlo Method: A Case Study for the TNF α -Mediated NF- κ B Signal Transduction Pathway”. In: *SIMULATION* 79.12 (2003), pp. 726–739.
- [175] S. Kucherenko, M. Rodriguez-Fernandez, C. Pantelides, and N. Shah. “Monte Carlo evaluation of derivative-based global sensitivity measures”. In: *Reliability Engineering & System Safety* 94 (2009), pp. 1135–1148.
- [176] I. Sobol’ and S. Kucherenko. “Derivative based global sensitivity measures and their link with global sensitivity indices”. In: *Mathematics and Computers in Simulation* 79 (2009), pp. 3009–3017.
- [177] M. Rodriguez-Fernandez, J. Banga, and F. Doyle III. “Novel global sensitivity analysis methodology accounting for the crucial role of the distribution of input parameters: application to system biology models”. In: *International Journal of Robust and Nonlinear Control* 22 (2012), pp. 1082–1102.
- [178] A. Lumen, K. McNally, N. George, J. Fisher, and G. Loizou. “Quantitative global sensitivity analysis of a biologically based dose-response pregnancy model for the thyroid endocrine system”. In: *Frontiers in Pharmacology* 6.107 (2015).
- [179] Y.-Y. Zhang, M. Trame, L. Lesko, and S. Schmidt. “Sobol Sensitivity Analysis: A Tool to Guide the Development and Evaluation of Systems Pharmacology Models”. In: *CPT: Pharmacometrics & Systems Pharmacology* 4.2 (2015), pp. 69–79.
- [180] A. Torres Valderrama, J. Witteveen, M. Navarro, and J. Blom. “Uncertainty Propagation in Nerve Impulses Through the Action Potential Mechanism”. In: *Journal of Mathematical Neuroscience* 5.3 (2015).
- [181] J. Dresch, X. Liu, D. Arnosti, and A. Ay. “Thermodynamic modeling of transcription: sensitivity analysis differentiates biological mechanism from mathematical model-induced effects”. In: *BMC Systems Biology* 4.142 (2010).
- [182] A. Czirok and D. G. Isai. “Cell resolved, multiparticle model of plastic tissue deformations and morphogenesis”. In: *Physical Biology* 12.1 (2015), p. 016005.
- [183] N. Wiener. “The homogeneous chaos”. In: *American Journal of Mathematics* 60 (1938), pp. 897–936.
- [184] D. Xiu. “Fast Numerical Methods for Stochastic Computations: A Review”. In: *Communications in Computational Physics* 5.2–4 (2009), pp. 242–272.

- [185] M. Navarro, J. Witteveen, and J. Blom. "Polynomial Chaos Expansion for general multivariate distributions with correlated variables". In: (2014). eprint: arXiv:1406.5483[math.NA].
- [186] S. Oladyshkin and W. Nowak. "Data-driven uncertainty quantification using the arbitrary polynomial chaos expansion". In: *Reliability Engineering & System Safety* 106 (2012), pp. 179–190.
- [187] B. Sudret. "Global sensitivity analysis using polynomial chaos expansions". In: *Reliability Engineering & System Safety* 93.7 (2008), pp. 964–979.
- [188] T. Ishigami and T. Homma. "An importance quantification technique in uncertainty analysis for computer models". In: *First International Symposium on Uncertainty Modeling and Analysis (ISUMA'90)*. 1990, pp. 398–403.
- [189] I. Sobol' and Y. Levitan. "On the use of variance reducing multipliers in Monte Carlo computations of a global sensitivity index". In: *Computer Physics Communications* 117 (1999), pp. 52–61.
- [190] A. Shirinifard. "Vascular Patterning and Its Application in Cancer and Choroidal Neovascularization". PhD thesis. Indiana University, Department of Physics, 2012.
- [191] R. Sheth, L. Marcon, M. F. Bastida, M. Junco, L. Quintana, R. Dahn, M. Kmita, J. Sharpe, and M. A. Ros. "Hox genes regulate digit patterning by controlling the wavelength of a Turing-type mechanism". In: *Science (New York, NY)* 338.6113 (2012), pp. 1476–1480.
- [192] B. De Rybel, M. Adibi, A. S. Breda, J. R. Wendrich, M. E. Smit, O. Novák, N. Yamaguchi, S. Yoshida, G. Van Isterdael, J. Palovaara, B. Nijse, M. V. Boekschoten, G. Hooiveld, T. Beeckman, D. Wagner, K. Ljung, C. Fleck, and D. Weijers. "Integration of growth and patterning during vascular tissue formation in Arabidopsis." In: *Science (New York, NY)* 345.6197 (2014), pp. 1255215–1255215.
- [193] F. Besnard, Y. Refahi, V. Morin, B. Marteaux, G. Brunoud, P. Chambrier, F. Rozier, V. Mirabet, J. Legrand, S. Lainé, E. Thévenon, E. Farcot, C. Cellier, P. Das, A. Bishopp, R. Dumas, F. Parcy, Y. Helariutta, A. Boudaoud, C. Godin, J. Traas, Y. Guédon, and T. Vernoux. "Cytokinin signalling inhibitory fields provide robustness to phyllotaxis". In: *Nature* 505.7483 (2015), pp. 417–421.
- [194] P. Buske, J. Przybilla, M. Loeffler, N. Sachs, T. Sato, H. Clevers, and J. Galle. "On the biomechanics of stem cell niche formation in the gut - modelling growing organoids". In: *FEBS Journal* 279.18 (2012), pp. 3475–3487.
- [195] S. E. Le Dévédec, K. Yan, H. de Bont, V. Ghotra, H. Truong, E. H. Danen, F. Verbeek, and B. van de Water. "Systems microscopy: An emerging strategy for the life sciences". In: *Cell. Mol. Life Sci.* 67.19 (2010), pp. 219–3240.
- [196] J. G. Lock and S. Strömblad. "Systems microscopy: An emerging strategy for the life sciences". In: *Experimental Cell Research* 316.8 (2010). Special Issue Celebrating the 60-Year Anniversary of ECR and the 200-Year Anniversary of the Karolinska Institute, pp. 1438–1444.
- [197] P. Santos-Oliveira, A. Correia, T. Rodrigues, T. M. Ribeiro-Rodrigues, P. Matafome, J. C. Rodríguez-Manzanaque, R. Seiça, H. Girão, and R. D. M. Travasso. "The Force at the Tip - Modelling Tension and Proliferation in Sprouting Angiogenesis". In: *PLoS Comput Biol* 11.8 (2015), e1004436.
- [198] I. K. Piechocka, R. G. Bacabac, M. Potters, F. C. Mackintosh, and G. H. Koenderink. "Structural hierarchy governs fibrin gel mechanics." In: *Biophysical journal* 98 (2010), pp. 2281–2289.
- [199] J. Yu, D. Castranova, V. Pham, and B. Weinstein. "Single cell analysis of endothelial morphogenesis in vivo". In: *Development* (2015).
- [200] D. M. Wellik. "Hox patterning of the vertebrate axial skeleton". In: *Developmental Dynamics* 236 (2007), pp. 2454–2463.
- [201] J. C. Pearson, D. Lemons, and W. McGinnis. "Modulating Hox gene functions during animal body patterning." In: *Nature reviews. Genetics* 6 (2005), pp. 893–904.

Bibliography

- [202] R. Sheth, L. Marcon, M. F. Bastida, M. Junco, L. Quintana, R. Dahn, M. Kmita, J. Sharpe, and M. a. Ros. "Hox genes regulate digit patterning by controlling the wavelength of a Turing-type mechanism." In: *Science (New York, N.Y.)* 338 (2012), pp. 1476–80.
- [203] S. Sick, S. Reinker, J. Timmer, and T. Schlake. "WNT and DKK determine hair follicle spacing through a reaction-diffusion mechanism." In: *Science (New York, N.Y.)* 314 (2006), pp. 1447–1450.

Summary

A network of blood vessels is formed throughout our bodies during embryogenesis. Postnatally, blood vessels grow new sprouts towards oxygen deprived regions, such as wounds or growing tumors, a process called angiogenesis. A better understanding of angiogenesis and vascular network formation can aid the development of medical therapies and improve the engineering of vascularized tissues. Computational modeling helps to find and understand the mechanisms that drive blood vessel formation. In this thesis, we propose computational models for several steps in the complex process of angiogenesis: matrix invasion, sprouting dynamics, and lumen formation. Chapter 1 describes the biology of angiogenesis and introduces the main computational modeling approaches that are used in the field.

Chapter 2 introduces a computational model of angiogenic-like invasion of endothelial cells into fibrin matrices. Koolwijk *et al.* (1996) have developed an experimental assay of sprouting in fibrin matrices, which is the temporal matrix scaffold formed during wound healing. Weijers *et al.* (2010) showed that the composition of fibrin in this assay impacts the level of angiogenesis; there is more ingrowth on high molecular weight (HMW) than on low molecular weight (LMW) fibrinogen. In Chapter 2, we studied which mechanisms underlie the reduced angiogenic ingrowth on LMW compared to HMW with a cell-based computational model that represents the *in vitro* setup. Based on the model results, we propose that a local feedback mechanism selects cells in the monolayer for matrix invasion and subsequently continues sprouting: plasmin-mediated fibrinolysis by an invading cell releases transforming growth factor $\beta 1$ (TGF $\beta 1$) from the fibrin matrix and TGF $\beta 1$ subsequently stimulates the ability of that cell to perform fibrinolysis. This model also reproduces a reduced ingrowth on LMW compared to HMW, when we included the experimental observation that LMW contains less fibrin-bound TGF $\beta 1$ than HMW.

Chapter 3 develops a model of dynamic sprouting and intercellular signaling to study tip cell overtaking. During angiogenesis, endothelial cells differentiate into tip cells and stalk cells through lateral inhibition mediated by Delta-Notch signaling. Tip cells are equipped with long filopodia to sense the local environment and guide the stalk cells along the sprout. It has long

been thought that once a differentiation pattern was established, the tip cell situated at the sprout tip will stay the leader of the sprout for the entire sprouting process. However, more recently it was shown that cells continuously compete for the sprout tip position, a process called tip cell overtaking. The biological function of tip cell overtaking is unclear. We asked whether tip cell overtaking is merely a side effect of sprouting or whether it is regulated through a vascular endothelial growth factor (VEGF)-Dll4-Notch signaling network, and thus might be functional. For this purpose, we studied two existing computational models of angiogenic sprouting, allowing us to study the effect of different sprouting dynamics on tip cell overtaking. In our models, cells spontaneously move back and forth along the sprout as a side effect of the sprouting mechanisms, as was also experimentally observed. This suggests that tip cell overtaking and sprouting dynamics may be interdependent and, therefore, should be studied and interpreted in combination. However, in experiments with mosaic endothelial spheroids, it was found that wild type cells have a competitive advantage over *Vegfr2* haploid cells for the tip cell position, suggesting that VEGF-Dll4-Notch signaling might regulate tip cell overtaking. In agreement with these experiments, in one of the two models the wild type cells also end up at the tip position more frequently than *Vegfr2* haploids due to VEGF-Dll4-Notch signaling, simply because the wild type cells more often differentiate into tip cells do to the large differences in *Vegfr2* levels. Combining these results, we propose that tip cell overtaking is a non-functional side effect of sprouting and that the function of VEGF-Dll4-Notch signaling might not be to regulate which cell ends up at the tip, but to assure that the cell that randomly ends up at the tip position acquires the tip cell phenotype.

Chapter 4 introduces a model of a next step in blood vessel formation: lumen formation. Once new blood vessels are formed, they hollow to allow blood perfusion. The mechanisms of lumen formation have been debated for centuries. Experimental research has led to two main hypotheses: vacuolation and cell-cell repulsion. During vacuolation, vacuoles are suggested to form by the fusion of pinocytotic vesicles that fuse into large vacuoles. These vacuoles form lumens intracellularly by spanning the entire cell and fusing to the cell membrane on both sides of the cell, or extracellularly by the secretion of vacuoles between cells. During cell-cell repulsion, cell membranes of adjacent cells are suggested to repulse each other to form an extracellular lumen between the cells. Both hypotheses are funded with strong experimental evidence, leaving the debate unresolved. In Chapter 4, we address this debate with a computational model of lumen formation that can represent both hypotheses. Continuous lumens can be formed in the model through a branched blood vessel by vacuolation as well as by cell-cell repulsion. However, lumen formation is far more robust for the values of the parameters

of the model when the two hypotheses are combined, suggesting that the two hypotheses work synergistically. One may question synergy of the two hypotheses as experimentalists mostly found evidence for one or the other hypothesis. It is important to realize that lumen formation by vacuolation is mostly studied in small intersegmental vessels (ISV) of zebra fish, whereas cell-cell repulsion is mostly studied in aortae of mice. In the model, when lumen formation by synergy of the two hypotheses is performed in a one-cell thick vessel, the resulting lumen formation visually resembles vacuolation, whereas it visually resembles cell-cell repulsion when it is performed in a multi-cell thick vessel. In conclusion, the computational model of lumen formation suggests that vacuolation and cell-cell repulsion work synergistically and that the discrepancy between observations of different experimental groups might be explained by the vessel sizes they are studying.

Chapter 5 proposes global sensitivity analysis as a tool to study and falsify morphogenesis models, using a model of vascular morphogenesis as a case study. The exact mechanisms that drive vasculogenesis *in vivo* are not yet clear. Our group has generated multiple cell-based models that support different mechanistic hypotheses. The proposed mechanisms for blood vessel formation may all be functional *in vivo*, but at different times in the process or under different environmental circumstances, or perhaps work simultaneously to reinforce one other. However, some mechanisms may merely be functional for blood vessel formation *in silico*. Despite many attempts for biological validation, we cannot give a final answer to this question. In Chapter 5, we suggest a global sensitivity analysis for such models as a new validation tool. In this chapter, we introduce a workflow to perform global sensitivity analysis on non-linear, multi-factorial models, using the cellular Potts-based model of contact-inhibited chemotaxis for network development as example. A global sensitivity analysis ranks the impact of parameters and their correlations on vascular network formation. Comparing the ranking of different models with knowledge derived from experimental data on the impact of the parameters can help to falsify models. Additionally, the sensitivity analysis results can be used to generate suggestions for validation experiments. The global sensitivity analysis for the contact inhibition model showed that *in silico* sprouting, measured by compactness, requires a combination of parameters that drive different mechanisms in the model. In contrast, the lacuna count of network depends only on the diffusion coefficient of the chemoattractant that is secreted by the endothelial cells. By a future study of each of the alternative models with this global sensitivity analysis approach, we hope to falsify some of the models and find the true operand mechanisms in vascular network development.

In summary, this thesis makes use of cell-based computational modeling to gain insight in different steps of angiogenesis and vasculogenesis, address-

6. Summary

ing questions that often originate from experimental observations. As a modeling philosophy, we study how mechanistic properties on the lower scale affect patterning of the higher scale, e.g. from cell shape to vascular networks, from proteolytic enzyme interactions to matrix invasion, and from fusion of subcellular vacuoles to lumens. In this thesis, we have shown that this modeling philosophy can help us to understand the counter-intuitive and unexpected phenomena in biology.

Samenvatting

Tijdens de embryogenese wordt een netwerk van bloedvaten in ons lichaam gevormd. Na de geboorte vormen bloedvaten vertakkingen naar zuurstof-arme gebieden, zoals een wond of een tumor, een proces dat we angiogenese noemen. Een beter begrip van angiogenese en van het vormen van vasculaire netwerken kan de ontwikkeling van medische therapieën en het creëren van bloedvaten in kunstmatige weefsels bevorderen. Computatieel modelleren helpt ons de mechanismes die bloedvatvorming aansturen te vinden en te begrijpen. In dit proefschrift dragen wij computationele modellen aan voor verschillende stappen in het complexe proces van angiogenese: bindweefselinvasie, de dynamica van bloedvatcellen (endotheelcellen) tijdens het vertakken en lumenvorming. Hoofdstuk 1 schetst de biologie van angiogenese en geeft een overzicht van de belangrijkste computationele modelleringstechnieken die gebruikt zijn in het veld.

Hoofdstuk 2 beschrijft een computationeel model van angiogenese-achtige invasie van endotheelcellen in bindweefsel bestaande uit fibrine. Koolwijk *et al.* (1996) hebben een experimenteel model ontwikkeld van bloedvatgroei in fibrineweefsel, wat de tijdelijke weefselstructuur vormt tijdens wondheling. Weijers *et al.* (2010) hebben laten zien dat de samenstelling van fibrine hierbij invloed heeft op de mate van bloedvatgroei; er is meer ingroei op hoog moleculair gewicht (HMW) fibrinogeen dan op laag moleculair gewicht (LMW) fibrinogeen. In hoofdstuk 2 hebben we, met behulp van een cel-gebaseerd computationeel model dat het *in vitro* model reproduceert, bestudeerd welke mechanismes de verminderde bloedvatgroei op LMW vergeleken met HMW veroorzaken. Op basis van de modelresultaten stellen wij voor dat een lokaal terugkoppelingsmechanisme cellen in de monolaag selecteert voor fibrineinvasie en vervolgens bloedvatgroei aandrijft. Hierbij zorgt plasmine-aangedreven fibrineafbraak door een ingroeïende cel ervoor dat transforming growth factor $\beta 1$ (TGF $\beta 1$) loslaat van fibrine. TGF $\beta 1$ stimuleert vervolgens de fibrineafbraak door die cel. Dit model reproduceert ook een verlaagde bloedvattingroei op LMW vergeleken met HMW wanneer er minder TGF $\beta 1$ gebonden is aan LMW dan aan HMW, zoals ook experimenteel geconstateerd is.

Hoofdstuk 3 bestudeert tipcelovernames in een computationeel model van dynamische bloedvatgroei en intercellulaire signalering. Tijdens angiogenese

differentiëren endotheelcellen in tip- en stalkcellen door laterale inhibitie afhankelijk van Delta-Notch-signalen. Tipcellen hebben lange filopodia om de lokale omgeving af te tasten en ze leiden de stalkcellen in het bloedvat. Voor lange tijd was gedacht dat, na het ontstaan van een gedifferentieerd tip- en stalkcelpatroon, de tipcel in de voorste punt van het bloedvat de leider bleef gedurende het hele proces van bloedvatgroei. Echter, recent is ontdekt dat cellen continu wisselen van positie in de spruit en concurreren om de spruitpuntpositie, een proces genaamd tipcelovername. De biologische functie van tipcelovername is onduidelijk. Wij vroegen ons af of tipcelovername slechts een neveneffect is van bloedvatgroei of dat het gereguleerd is door een signaleringsnetwerk van VEGF, Dll4 en Notch, en dus wellicht functioneel is. Daarom bestudeerden we twee bestaande computationele modellen van bloedvatgroei, waardoor we het effect van verschillende celdynamica tijdens bloedvatgroei op tipcelovername konden bestuderen. Zoals ook in experimenten is geobserveerd, bewegen cellen in onze modellen spontaan voorwaarts en achterwaarts in een vormende spruit als een neveneffect van de mechanismes die de vorming van het bloedvat aandrijven. Dit suggereert dat tipcelovernames en de celdynamica tijdens bloedvatgroei afhankelijk van elkaar zijn en, daarom, in combinatie met elkaar bestudeerd en geïnterpreteerd zouden moeten worden. In experimenten waarin bloedvaten groeien vanuit een celklont met twee verschillende cellijnen, hebben wild-type-cellen een hogere kans om de spruitpuntpositie in te nemen dan *Vegfr2*-haploïden, wat een indicatie is dat VEGF-Dll4-Notch-signalering misschien tipcelovernames reguleert. Overeenkomstig met deze experimenten nemen de wild-type-cellen, als gevolg van VEGF-Dll4-Notch-signalering, ook vaker de spruitpuntpositie in dan *Vegfr2*-haploïden in een van onze modellen. Dit komt simpelweg doordat wild-type-cellen vaker differentiëren in tipcellen die gunstige eigenschappen bezitten om op die positie te komen. Concluderend suggereren wij dat tipcelovernames een niet-functioneel neveneffect zijn van bloedvatvorming. Mogelijk is de functie van VEGF-Dll4-Notch-signalering ervoor te zorgen dat de cel die toevallig op de punt terecht komt het juiste tipcelphenotype krijgt.

Hoofdstuk 4 beschrijft een model van de volgende stap in bloedvatvorming: lumenvorming. Nadat bloedvaten zijn gevormd moeten ze hol worden zodat het bloed erdoorheen kan stromen. Het debat over de mechanismes van dit hol worden, ofwel lumenvorming, stamt uit de 19^{de} eeuw. Experimenteel onderzoek heeft geresulteerd in twee hoofdhypotheses: vacuolatie en cel-celafstoting. Tijdens vacuolatie zouden vacuoles gevormd worden door de fusie van pinocytotische blaasjes. Deze vacuoles vormen uiteindelijk een intracellulair lumen door de gehele cel te overspannen en te fuseren met het celmembraan aan beide kanten van de cel, of ze vormen extracellulaire lumens door gesecreteerd te worden tussen cellen. Tijdens cel-celafstoting

vormt een lumen tussen de cellen. Beide hypothesen worden ondersteund door sterke experimentele bewijzen, met als resultaat dat het debat voortduurt. In hoofdstuk 4 gaan we dit debat aan met een computationeel model van lumenvorming dat beide hypothesen representeert. In het model kunnen continue lumens gevormd worden in een vertakt bloedvat door vacuolatie en ook door cel-celafstoting. Echter, lumenvorming is veel robuuster voor veranderingen in de parameterwaarden van het model wanneer de twee mechanismes gecombineerd worden, wat suggereert dat de hypothesen synergetisch werken. Hoe kan het dan dat er experimenteel bewijs is gevonden voor elke afgezonderde hypothese en niet voor een samenwerking? Hiervoor is het belangrijk te beseffen dat vacuolatie vooral bestudeerd is in kleine vaten (intersegmentale vaten van zebrafissen), terwijl cel-celafstoting vooral bekeken is in grote vaten zoals de aortae van muizen. De modelresultaten lijken visueel op vacuolatie wanneer lumenvorming door een samenwerking van beide hypothesen plaatsvindt in een bloedvat bestaande uit één rij cellen, maar lijken visueel op cel-celafstoting wanneer dit gebeurt in een vat dat meerdere cellen dik is. Dus het computationele model van lumenvorming suggereert dat de twee hypothesen synergetisch werken en dat het verschil tussen de experimentele observaties van verschillende groepen wellicht verklaard zou kunnen worden door de verschillende vatgroottes die de onderzoekers bestudeerden.

Hoofdstuk 5 stelt een globale sensitiviteitsanalyse voor als instrument om morphogenese modellen te bestuderen en te falsificeren, waarbij een model van vasculaire morphogenese als een casestudie gebruikt is. De exacte mechanismes die *in vivo* bloedvatvorming aandrijven zijn niet bekend. Onze groep heeft meerdere modellen ontwikkeld die verschillende hypothesen voor bloedvatvorming ondersteunen. Deze voorgestelde hypothesen zouden allen functioneel kunnen zijn *in vivo*, maar op verschillende momenten in het proces of onder verschillende omgevingscondities, of wellicht werken ze wel synergetisch. Sommige van deze hypothesen zijn misschien echter alleen functioneel in het model en niet *in vivo*. Ondanks vele pogingen voor biologische validatie is hier nog geen antwoord op. In hoofdstuk 5 stellen we een globale sensitiviteitsanalyse voor als een nieuw hulpmiddel om modellen te falsificeren. We hebben een werkplan geïntroduceerd voor het toepassen van globale sensitiviteitsanalyses op niet-lineaire, multi-factoriale modellen, en we gebruiken het model van contact-geïnhibeerde chemotaxis voor bloedvatvorming als voorbeeld. Een globale sensitiviteitsanalyse rangschikt de impact van de parameters en van combinaties van parameters op bloedvatvorming. Een vergelijking van deze ranking van verschillende modellen met kennis uit experimentele data over de impact van de parameters kan helpen modellen te falsificeren. De globale sensitiviteitsanalyse van het voorbeeldmodel liet zien dat bloedvatvorming, gemeten door compactheid, afhan-

6. Samenvatting

kelijk is van een combinatie van parameters die verschillende mechanismes in bloedvatvorming aansturen. Het aantal lacunae in een netwerk wordt alleen bepaald door de diffusiecoëfficiënt van de chemoattractant die gesecreteerd wordt door de cellen zelf. In een toekomstige studie van globale sensitiviteitsanalyses van alle alternatieve modellen voor bloedvatvorming in onze groep, hopen we enkele modellen te falsificeren en de mechanismes die werkzaam zijn *in vivo* te achterhalen.

Samenvattend maakt dit proefschrift gebruik van cel-gebaseerde computationele modellen om inzichten te krijgen in verschillende stappen van angiogenese en vasculogenese door vragen te adresseren die ontstaan uit experimentele observaties. Wij werken vanuit een centrale vraag: hoe kunnen mechanistische eigenschappen op een lagere schaal patroonvorming op een hogere schaal beïnvloeden, bijvoorbeeld vanuit celvorm naar bloedvatnetwerken, vanuit interacties tussen proteolytische enzymen naar matrixinvasie en vanuit fusie van subcellulaire vacuoles tot lumens? In dit proefschrift hebben we laten zien dat we vanuit deze filosofie vaak tegenintuïtieve en onverwachte verschijnselen in de biologie kunnen begrijpen.

Dankwoord

Vijf jaar geleden zou ik nooit geloofd hebben dat ik met gebruik van computersimulaties zou promoveren aan het Mathematische Instituut Leiden. Ik wist niets van computers of programmeren en eerlijk gezegd heb ik nog steeds regelmatig moeite met het vinden van de aanknop. Maar toen ik Roeland vroeg of ik bij hem stage mocht lopen zonder enige kennis van programmeren of modelleren gaf hij mij de kans: "als je het maar wil leren". Hier zal ik hem altijd dankbaar voor zijn. Na het afronden van die stage vroeg hij mij een PhD bij hem te starten. Mede dankzij zijn aanstekelijke enthousiasme, zijn inspirerende inzichten en zijn brede kennis heb ik mij hierin kunnen ontwikkelen van bioloog tot computationeel bioloog.

Het is een cliché maar waar, een PhD-traject kent vele pieken en dalen. Ik wil twee mensen in het bijzonder bedanken voor de onvoorwaardelijke steun die ik heb gevoeld. Dit zijn mijn vriend Gerben, die me altijd weer aan het lachen kreeg, hoe verslagen ik er ook bijzat. En mijn vader, die mijn PhD denk ik net zo intens beleefd heeft als ikzelf. Hij heeft me ook inhoudelijk veel geholpen met het structureren van mijn artikelen en het plannen van mijn PhD. Daarnaast wil ik Suzanne bedanken voor alle lunches, waarin we onze PhD-ervaringen konden delen. Mijn zus, Ingrid, voor het stellen van een voorbeeld, ze heeft het PhD traject reeds doorlopen en is er zelfs enthousiaster en gepassioneerder voor haar onderwerp uitgekomen. En mijn moeder voor haar geloof in mij en haar stem achter in mijn hoofd die zegt dat het altijd allemaal weer goed komt.

Het CWI is een fantastische werkomgeving waar goed voor je gezorgd wordt. Zo kon ik altijd bij de IT, Maarten en Michael, binnenlopen voor welk computerprobleem dan ook. Maar wat het vooral fantastisch maakt is de gezellige sfeer en de leuke collega's en daar wil ik de gehele Life Sciences groep voor bedanken. Je kon altijd bij iedereen aankloppen voor advies of voor gezelligheid. Vooral met Margriet en Lisanne heb ik veel kopjes thee gedronken. Margriet begeleidde mij tijdens mijn stage en is daar eigenlijk nooit meer mee gestopt, ze weet alles! Ze is één van de meest behulpzame mensen die ik ken en mede dankzij haar kan ik nu programmeren en modelleren. Lisanne was de laatste twee jaar mijn kamergenoot op werk en ik mis onze gesprekken nu al. Beiden hebben ze mij zowel inhoudelijk als mentaal veel geholpen tij-

6. Dankwoord

dens mijn PhD en daarom was het voor mij ook een logische keuze om hen te vragen als mijn paranimfen.

Ook heb ik fijne wetenschappelijke samenwerkingen kunnen aangaan. Pieter, Ester en Marloes boden mij de kans om mijn werk ook experimenteel te toetsen. Zelfs heb ik samen met Ester op het lab gestaan. Het was een lastig project, waarin hun enthousiasme en vastberadenheid een grote steun waren. Daarnaast wil ik Joke en Maria bedanken voor een fijne en efficiënte samenwerking aan een meer wiskundig artikel.

Tot slot wil ik Chang bedanken, alle mooie foto's van mijn retina in dit boekje zijn aan haar te danken. Zij heeft geregeld dat Gerard de Graaf, medisch fotograaf, prachtige fundusfoto's voor mij heeft gemaakt om mijn boekje een wel heel persoonlijk tintje te kunnen geven!

Curriculum vitae

Sonja Boas is geboren op 6 augustus 1987 te Maastricht. Ze behaalde in 2005 *cum laude* haar Gymnasium diploma aan 't Baarnsch lyceum, met profiel Natuur & Gezondheid, aangevuld met Latijn, Wiskunde en Economie. Vervolgens heeft ze de Bachelor Biomedische wetenschappen gevolgd aan de UvA en wederom *cum laude* afgesloten. Tijdens een laboratoriumstage voor de master Life Sciences aan de UvA realiseerde ze zich dat ze meer aangetrokken werd door de wiskundige en analytische kant van de biologie. Met als doel een wiskundige basis te vormen heeft ze haar master onderbroken met vakken van de bachelor Econometrie en Operationele Research aan de VU. Daarna heeft ze de master Life Sciences vervolgd met computationeel biologische vakken en een stage op het Centrum voor Wiskunde en Informatica (CWI). Tijdens deze stage maakte ze kennis met het zogenaamde cell-based modelleren; ze bestudeerde welk celgedrag kan resulteren in het vormen van bloedvaten. Ze ronde haar master in 2011 *cum laude* af.

Hierna accepteerde ze een PhD-positie als vervolg van haar stage op het CWI. Gedurende haar PhD gebruikte ze cell-based modelleren om verschillende aspecten van bloedvatgroei te bestuderen. Tijdens haar projecten vormde ze een brug tussen verschillende vakgebieden in verschillende interdisciplinaire samenwerkingen, met zowel wiskundigen als biologen. Tenslotte heeft ze met veel plezier deelgenomen aan het PhD activity committee en de ondernemingsraad van het CWI. In december 2015 gaat ze als consultant werken bij Strategies in Regulated Markets (SiRM) in Den Haag.

Publications

Journal publications

- Sonja E. M. Boas and Roeland M.H. Merks, *Synergy of Cell-Cell Repulsion and Vacuolation in a Computational Model of Lumen Formation* (2014). J. R. Soc. Interface 11: 20131049. <http://dx.doi.org/10.1098/rsif.2013.1049>
- Sonja E. M. Boas and Roeland M.H. Merks, *Tip cell overtaking occurs as a side effect of sprouting in computational models of angiogenesis*. BMC Systems Biology (in press) arXiv:1507.06230
- Sonja E. M. Boas, Maria I. Navarro Jimenez, Roeland M.H. Merks and Joke G. Blom, *A global sensitivity analysis approach for morphogenesis models*. BMC Systems Biology (in press) arXiv: 1507.08504
- Sonja E. M. Boas, Marloes van den Broek, Ester M. Weijers, Pieter Koolwijk and Roeland M.H. Merks, *A local uPAR-plasmin-TGF β 1 positive feedback loop in a computational model of angiogenic sprouting explains the in vitro effect of fibrinogen variants*. (in preparation)

Book chapters and encyclopedia entry

- Sonja E. M. Boas, Margriet M. Palm, Pieter Koolwijk and Roeland M.H. Merks, *Computational Modeling of Angiogenesis: Towards a Multi-Scale Understanding of Cell-Cell and Cell-Matrix Interactions* (2013) Mechanical and Chemical Signaling in Angiogenesis, Studies in Mechanobiology, Tissue Engineering and Biomaterials Volume 12, 161-183
- M. G. Dallinga and Sonja E. M. Boas *et al.*, *Tip cells in angiogenesis* (2015) Tip Cells in Angiogenesis. In: eLS. John Wiley & Sons, Ltd: Chichester. DOI: 10.1002/9780470015902.a0025977
- Claudiu-Cristi Antonovici, Sonja E.M. Boas, Elisabeth G. Rens, Hannan Tahir, Roeland M.H. Merks *Multiscale analysis of morphogenesis* In: Ralph A. Bradshaw and Philip Stahl (Eds.) Encyclopedia of Cell Biology, Section 4, Doug Lauffenburger (Ed.) Systems Cell Biology. Elsevier (Amsterdam). ISBN:9780123944474 (in press)
- Sonja E.M. Boas, Yi Jiang, Roeland M.H. Merks, Sotiris A. Prokopiou and Elisabeth G. Rens *Cellular Potts model: applications to vasculogenesis and angiogenesis* In: Louis, P.-Y. and Nardi, F.R. (Eds.) Probabilistic Cellular Automata: Theory, Applications and Future Perspectives. Springer. (in press)